A Thesis entitled

Structure-Property Correlation Study of Transition Metal Oxides and Energetic Solids

Submitted to
University of Hyderabad

For the award of the degree of

Doctor of Philosophy

in

Physics

by

Subrata Mondal

(15ACPA01)

Under the Supervision of

Dr. G. S. Vaitheeswaran

हैदराबाद विश्वविद्यालय
University of Hyderabad

प्रतिष्ठित संस्थान
INSTITUTION OF EMINENCE
राष्ट्रीय अपेक्षाएँ, वैश्विक मानक
National Needs, Global Standards

Advanced Centre for Research in High Energy Materials (ACRHEM)
School of Physics
University of Hyderabad
Hyderabad-500046

(December, 2021)

Dedicated to

My Family & Friends

हैदराबाद विश्वविद्यालय
University of Hyderabad

प्रतिष्ठित संस्थान
INSTITUTION OF EMINENCE
राष्ट्रीय अपेक्षाएँ, वैश्विक मानक
National Needs, Global Standards

Declaration

I, ***Subrata Mondal*** hereby declare that, the work reported in this thesis entitled, *"Structure-Property Correlation Study of Transition Metal Oxides and Energetic Solids"*, is original and has been carried out by me under the supervision of *Dr. G. S. Vaitheeswaran*, ACRHEM, School of Physics, University of Hyderabad, Telangana, India, as per the Ph.D. ordinances of the University. I also declare that, this work is free from plagiarism and it has not submitted for the award of a research degree at any other University. I hereby agree that my thesis can be deposited in Shodhganga or INFLIBNET.

A report on plagiarism statistics from the university librarian is enclosed.

Subrata Mondal

(SUBRATA MONDAL)
Reg. No: 15ACPA01

G. Vaitheeswaran

(Dr. G. S. Vaitheeswaran)
Thesis Supervisor,
ACRHEM, School of Physics,
University of Hyderabad.

Dr. G.S. Vaitheeswaran
Associate Professor
School of Physics
University of Hyderabad
Hyderabad-500 046. (TS) INDIA

हैदराबाद विश्वविद्यालय
University of Hyderabad

प्रतिष्ठित संस्थान
INSTITUTION OF EMINENCE
राष्ट्रीय अपेक्षाएँ, वैश्विक मानक
National Needs, Global Standards

Certificate

This is to certify that, the thesis entitled *"Structure-Property Correlation Study of Transition Metal Oxides and Energetic Solids"*, submitted to the University of Hyderabad by *Mr. Subrata Mondal* bearing *Reg. No. 15ACPA01* in partial fulfilment of the requirements for the award of Doctor of Philosophy in Physics, is a bonafide work carried out by him under my supervision and guidance, which is a plagiarism free thesis. The thesis has not been submitted previously in part or in full to this or any other University or Institution for the award of any degree or diploma.

G. Vaitheeswaran

Dr. G.S. Vaitheeswaran
Associate Professor
School of Physics
University of Hyderabad
Hyderabad-500 046. (TS) INDIA

(Dr. G. S. Vaitheeswaran)
Thesis Supervisor,
ACRHEM, School of Physics,
University of Hyderabad.

Director,
ACRHEM,
University of Hyderabad.

Director
ACRHEM

M. Ghanashyam

I/c Dean,
School of physics,
University of Hyderabad.

DEAN
School of Physics
University of Hyderabad
Hyderabad-500 046. INDIA

हैदराबाद विश्वविद्यालय
University of Hyderabad

प्रतिष्ठित संस्थान
INSTITUTION OF EMINENCE
राष्ट्रीय अपेक्षाएँ, वैश्विक मानक
National Needs, Global Standards

Certificate of Course Work

This is to certify that the thesis entitled *"Structure-Property Correlation Study of Transition Metal Oxides and Energetic Solids"*, submitted to the University of Hyderabad by *Mr. Subrata Mondal* bearing *Reg. No. 15ACPA01*, in partial fulfilment of the requirements for the award of Doctor of Philosophy in Physics at ACRHEM, School of Physics, University of Hyderabad, is a bonafide work carried out by him under my supervision and guidance. This thesis is free from the plagiarism and has not been submitted previously in part or in full to this or any other University or Institution for the award of any degree or diploma.

Further, the student has the following publications before submission of the thesis for adjudication:

- **S. Mondal**, G. Vaitheeswaran, Brendan J Kennedy, Clarissa Chay, Sean Injac and Daniel Errandonea, *Crystal structure and phase transition of TlReO4: a combined experimental and theoretical study*, J. Phys.: Condens. Matter 33, 065403 (2021). (**Chapter 3**)

- **S. Mondal**, G. Vaitheeswaran, M K Gupta and Ranjan Mittal, *Structural, elastic, vibrational and optical properties of energetic material octanitrocubane studied from first-principles theory*, J. Phys.: Condens. Matter 32, 425502 (2020). (**Chapter 5**)

- **S. Mondal**, D. Rocca, S. Lebegue, G. Vaitheeswaran, *Structural, elastic, and quasi-particle bandstructure of 4,4-Bis(nitramino)azofurazan from first principles theory*, Computational Materials Science 169, 109081 (2019). (**Chapter 6**)

- **S. Mondal**, J. Prathap Kumar, E. Narsimha Rao, and G. Vaitheeswaran, *Structure-property correlations of bis(nitrofurazano) furazan(BNFF-1): A density functional theory study*, AIP Coference Proceedings 2115, 030391 (2019). (**Chapter 6**)

Manuscripts under preparation/review:

- **S. Mondal**, Sohan Lal, Neeraj Kumbhakarna, Arindrajit Chowdhury, Irishi N. N. Namboothiri and G. Vaitheeswaran, *Experimental and Theoretical Study on the Structural and Energetic Properties of Potassium Dinitromethane* (2021). (**Chapter**

4)

- **S. Mondal**, J. Prathap Kumar, and G. Vaitheeswaran, *Comparative DFT study of crystalline properties of Nitroformate-based energetic saltsComparative DFT study of crystalline properties of Nitroformate-based energetic salts* (2021). (**Chapter 4**)

Also, made presentations in the following conferences:

- **15th Indian Theoretical Chemistry Symposium** organized by School of Chemistry, University of Hyderabad during 14th Dec – 17th Dec, (**2016**). (POSTER)
- **National Conference on Recent Trends in Condensed Matter Physics** organized by Bose Institute during 31st Oct – 3rd Nov, (**2017**). (POSTER)
- **Sorbonne-JNCASR School on Advanced Computational Material Science** jointly organized by Sorbonne University, Paris and JNCASR, Bangalore, 29th Jan - 02nd Feb, (**2018**). (**Best Poster award**)

The following courses have taken as part of the course work:

Course No.	**Course offered at**	**Title of the Course**	**Credits**	**Pass/Fail**
PY801	School of Physics	Advanced Quantum Mechanics	4	Pass
PY804	School of Physics	Advanced Electromagnetic Theory	4	Pass
PY801	School of Physics	Research Methodology	4	Pass
PY804	School of Physics	Advanced Mathematical Methods	4	Pass

G. Vaitheeswaran

Dr. G.S. Vaitheeswaran
Associate Professor
School of Physics
University of Hyderabad
Hyderabad-500 046. (TS) INDIA

(Dr. G. S. Vaitheeswaran)
Thesis Supervisor,
ACRHEM, School of Physics,
University of Hyderabad.

Director,
ACRHEM,
University of Hyderabad.

Director
ACRHEM

M. Ghanashyam

I/c Dean,
School of physics,
University of Hyderabad.

DEAN
School of Physics
University of Hyderabad
Hyderabad-500 046, INDIA

Acknowledgments

असतो मा सद्गमय
तमसो मा ज्योतिर्गमय
मृत्योर्मामृतं गमय

"...let's follow THE PATH OF TRUTH... "

With immense pleasure, I would like to express my deepest and sincere gratitude to the following persons for their timely help and support towards the completion of my thesis work.

First of all, I have to mention about my supervisor *Dr. G. S. Vaitheeswaran* in this regard, as his motivation and encouragement made it possible for me to work on the topic of my interest. His constant support, from defining a problem to analysing and understanding any system properly, has helped me develop myself. His expertise, understanding, helpful guidance also helped me become insightful about the research work. From writing manuscripts to presentations, his unconditional assistance helped me improve at each point. Without his academic and personal support, I couldn't have finished my PhD work. Along with academic support, he has always stood by my side in my difficult times. I am really thankful to you, Sir, for introducing me to this research world.

I extend my sincere thanks to past and present *Director, ACRHEM*; *Dean, School of Physics* for their unconditional academic support.

I want to thank my doctoral committee members *Prof. Ashok Chatterjee* and *Dr. Ashok Vudayagiri*, for showing their straightforward approach regarding my research work. Their insightful questions have always motivated me to think more about the fundamental concepts of my research work. I am grateful for showing me the right direction.

I also like to thank all the faculties of ACRHEM and School of Physics for their constant support and teachings in the course work.

I am also thankful to my collaborators, Dr. Sebastien Lebegue from CNRS France; Prof. Brendan J Kennedy from University of Sydney, Australia; Prof. Daniel Errandonea from

ICMUV, Universitat de Valencia, Spain; Prof. Ranjan Mittal and Dr. M. K. Gupta from BARC, India; and Prof. Neeraj Kumbhakarna, Prof. Arindrajit Chowdhury and Prof. Irishi N. N. Namboothiri from IIT Bombay, India.

I would like to thank DRDO, Govt of India through ACRHEM for their financial support and office staff (ACRHEM and School of Physics) for their administrative support.

I have to mention my best thanks to my seniors for their consistent help in suggesting the systematic learning and presentation approaches. It has been a very pleasant experience to work in the warm and friendly atmosphere with my senior lab-mates: *Dr. Appalakondaiah*, who gave initial training on computational approaches; *Dr. Narsimha Rao*, who helped me to understand various topics of our research work through rigorous discussion; *Dr. N. Yedukondalu*, who shared his research experiences with me which led me to the understand various aspects of research;

I also express my thanks to my lab-mates: *J. Prathap Kumar, Adibaiah, Dr. B. Moses Abraham and Juniors' Supratik Mukherjee, and T. Aiswarya*. I must thank all my energetic friends *Hemant Kumar Sharma, Pawan Kumar, Vineet Sharma, Sarthak*. I would like to thank all my ACRHEM and School of Physics friends for helping and supporting me unconditionally on this long and sometimes difficult journey.

I would like to give my lovely heartfelt wishes and blessings to my younger sister for her support and a special thanks to friends in my village for giving an invaluable memories from my childhood. I will utilize this opportunity to specially thank my parents for their continuous blessings and for giving me full freedom and having faith in me to achieve my dreams.

Subrata Mondal

Subrata Mondal

Table of Contents

List of Figures

List of Tables

CHAPTER 1

Introduction

Computer simulation has become an indispensable part of different disciplines of modern scientific research and technological advancements. By providing a new extent of understanding of various scientific phenomena, these simulation techniques have proven their potential as exciting investigation tools as necessary as the conventional experimental and theoretical approaches. Numerical simulations not only bridge the theoretical and experimental understanding of any physical phenomena but also help to carry out scientific research in extreme conditions that are not feasible in the laboratory. Due to different computational techniques' success, these studies have established an interdisciplinary research method named computational physics or computational materials science. Diverse areas of study, including biology, chemistry, mathematics, physics, and even medicine, and engineering, usually are being carried out through this approach [1, 2, 3, 4, 5, 6, 7]. Generally, two sorts of simulations techniques are considered for three purposes which are understanding, exploration, and prediction. Among these, equation-based simulation techniques are typically used in material or physical sciences. On the other hand, agent-based simulations are used in the context of behavioural or social science. From the materials science perspective, these techniques play an increasingly crucial role. These techniques helped to improve different experimental conditions to a greater extent and design novel materials. These simulation techniques not only improve other experimental conditions but also help to get rid of rough, experimental conditions, reduce production time by guiding experiments, product quality, productivity, and accurate feedback information for guiding production [8, 9, 10, 11, 12]. The application of computer simulation technology is widely used in material microstructure, heat treatment, corrosion and protection, materials design, etc.

1.1 Different types of simulation techniques

Various systems in materials science show different characteristics in different time and length scales. The involvement of these multiple scales makes it more fascinating to have a proper understanding of processes associated with these systems. Some of these processes, occurring at a lower scale, are found to govern the system's behaviour at several scales. The study of this notion in materials science is known as structure-property correlation study, where the present microscopic interactions determine materials behaviour at continuum level [13, 14, 15]. Due to the complexity of multiple scales involved, a single physical or computational model is not enough to explain materials behaviour using one unified method. As a result, different simulation techniques usually are being used. The first-ever scientific simulation techniques developed as well as implemented were Monte Carlo (MC), and Molecular Dynamics (MD) methods, fully rooted in classical physics [16, 17, 18]. Other simulation models, such as multiscale simulation models and couple modelling methods, were developed to overcome the problems associated with these techniques. These methods can involve MD, quantum mechanics, or both. In the case of mesoscopic scale, continuum theory-based methods are used, like finite element methods (FEM) [19, 20, 21]. In this connection, quantum mechanics-based density functional theory (DFT) has shown its importance in predicting the properties of materials.

1.2 Importance of Density Functional Theory

DFT has played an important role in computing and predicting crystalline properties of solids accurately at the electronic scale by helping create the high-throughput (HT) calculation frameworks. This kind of study of materials properties is only possible through sophisticated experiments.[22] Till now, these DFT computations have produced a large number of data sets related to the properties of materials. These data sets, obtained from various sophisticated experiments [23] as well as simulations guided to a new scientific paradigm known as data-driven science, followed by experiment, theory in addition to computational simulation. In the case of materials science, this sort of study has shown a tremendous impact by accelerating the design or discovery of novel materials with desired properties and hence, known to start a newly emerging field of materials informatics.[24, 25, 26, 27, 28, 29, 30, 31, 32, 33, 34, 35, 36, 37, 38, 39, 40, 41, 42, 43, 44, 45, 46, 47, 48]. This advancement of computational materials science has mainly been possible because of the rapid improvement of computational capabilities along with the accomplishment of DFT.

DFT based *ab initio* methods are considered as the most potent computational tools for obtaining an accurate understanding of material systems containing many electrons. Along with different practical systems like atoms, molecules, clusters, amorphous systems, consideration of translational symmetry through Bloch's theorem [49] allowed DFT to study other extended systems like solid crystals, surfaces, etc. Since its first implementation, the evolution of DFT from constrained computational capabilities of producing approximate understanding to more accurate results has made it a robust predictive method commonly used in various applications such as drug designing, material designing related to water spitting, solar cell etc. This DFT application landscape is vast, consisting of various features and applicable for a wide variety of systems. Many technics, generally known as the post-Kohn-Sham (KS) approaches, have been considered for overcoming different DFT deficiencies. Among these, time-dependent density functional theory (TDDFT) [50, 51, 52] was proposed to study excited states, Dynamical Mean Field Theory (DMFT) [55, 56] and the Hubbard U parameter [53, 54] were considered to tackle systems related strongly correlated electrons and for exciton dynamics, the GW approximation [57, 58] was proposed. In conclusion, DFT is considered a well-established theory currently available to study the electronic structure of materials.

In addition to studying various systems from atoms[59], molecules[60, 61], 0-D system[64, 65, 66] arrangement to extended systems like 1-D[67, 68, 69, 70, 71, 72, 73], 2-D[74], surface[62], 3-D crystals and defects[63], the use of DFT can also be applied to understand various properties such as structural[75], thermal[78, 79, 80], electronic/transport[76, 77], optical[82], electron-phonon[81], magnetic[84, 85, 86], catalytic[83], topological[87, 88, 89] and many more. The use of DFT calculations in geology and the earth sciences have the ability to simulate conditions in the Earth's interior. Successful application of DFT could be observed in a wide range of materials science research. The structure and optoelectronic property relationship of organic compounds is well understood through this approach. For designing novel photovoltaic donor material, DFT has benefited researchers to a great extent by providing information that is inaccessible experimentally. This kind of Organic Semiconductors (OSC) research has clearly shown the power of DFT in understanding and predicting essential properties of organic materials. In the case of energy-related materials, successful prediction of important properties through DFT studies is worth mentioning as these predictions were subsequently found to be verified experimentally.

Computational designing of potent materials related to lithium-ion batteries, hydrogen storage and production, superconductors, thermoelectric, and photovoltaic indicates the significance of DFT. The importance of DFT studies can also be seen in other applications along with renewable energy applications, including magnetic materials, multiferroic materials, etc. To fill the knowledge gap associated with new as well as exciting novel materials in different research areas, these computational techniques are found to be very useful. These materials also enable various technological advancements, which help overcome different social challenges. Moreover, it has been estimated that this development of novel materials enables nearly 67 % of growth in the computation field. This development also powers the transformation of other industries, such as energy storage[90].

Storage of energy in materials can be obtained in so many ways, which are in terms of electrical, electromagnetic, biological, electrochemical, to chemical energy form. Among these, capacitor, superconducting, magnetic energy storage is known for electrical and electromagnetic energy storage, rechargeable batteries are known for electrochemical energy storage, hydrogen storage and energetic materials are known for chemical energy storage. So, the prediction of novel materials in these fields can help in different technological advancements associated with energy storage. Experimental as well as DFT studies have confirmed the importance of transition-metal oxide (TMO) semiconductors as electrochemical and energetic materials as chemical energy storage materials.

1.3 DFT and transition metal oxides

TMOs constitute a significant class of materials by showing the properties of insulators, semiconductors, conductors and superconductors. These materials are also known for their interesting piezoelectric, ferroelectric, antiferroelectric, and magnetic properties. These compounds are considered as essential minerals as well as the significant part of rocks [91]. These compounds are known to show various technological aspects due to their potential use in devices related to energy conversion, particularly in photoelectrochemistry, photocatalysis, and photovoltaics[92, 93, 94, 95]. As these materials are relatively abundant with low-production costs and stable in an aggressive chemical environment or ultraviolet (UV) light, they are attractive candidates for considerably large-scale applications. Different properties of these materials, such as structural, elastic, energetic, and magnetic properties, have been studied and understood thoroughly using numerous investigations[96, 97, 98, 99, 100, 101, 102, 103]. Though, the proper behaviour of the electronic structure of these materials is not entirely understood yet within the theoretically existing models. Partially filled d-states, considerable effects of correlation, open-shell character, and spin configuration variation in a restricted-energy range made these materials more exciting and challenging electronic systems to understand.

Strongly correlated electronic systems are well known for their rich physics and offer unique optical, transport, and magnetic properties. To assess the usefulness of TMO-related compounds in conversion devices related to solar energy, exact and effective technics are needed for determining band-gap and band-edge positions. Information about these parameters helps in the rough screening of potential materials for efficient photocatalysts or photoelectrodes. Electronic band structure calculation of these materials are found to be very demanding due to the presence of strong interactions in highly localized d-electrons[104]. This leads to errors in calculating band-gap energies with normal DFT functional. However, similar schemes successfully predict the structural properties, stability and other properties of molecules and solids. This suggests a considerable constraint of DFT in predicting an accurate picture of the electronic band structure for strongly correlated electrons[105, 106, 107]. To overcome this limitation, hybrid DFT functionals[108, 109, 110, 111, 112] were used extensively for reducing the error associated to self-interaction. This is usually achieved by adding non-local exact Hartree-Fock (HF) exchange with local or semi-local exchange contribution.

DFT+U approach, which uses the intra-atomic effective coulomb parameter (U), has shown its potential to be a more economically alternative approach in this connection[113, 114, 115, 116, 117]. Among all these techniques, computationally expensive GW approximation can also be considered, which is known as the most accurate method for calculating electronic band structure to date[118, 119]. Among other less expensive computation techniques, use of HSE06 XC functional[111, 112] and the TB-mBJ XC[120] potential can also be used in this purpose. Along with all these developments, it usually is being mentioned that the most encouraging theoretical method regarding the analysis of the catalytic process is DFT. Due to the ability to change the states of oxidation and hence form or break bonds with reactants, oxides of transition metals are used broadly as catalysts. In case of selective oxidation of alcohols [122, 123] or hydrocarbons [121], nitric oxide reduction[124, 125], the sulfur dioxide oxidation[126], and the splitting of water, photochemically or electrochemically, for producing oxygen and hydrogen[127, 128], use of these metal oxides worth mentioning. This kind of materials form an important class known as reducible transition metal oxides (RTMOs). Among various TMOs, binary TMOs are rigorously investigated strongly correlated systems[129, 130, 131, 132, 133, 134, 135, 136, 137, 138, 139, 140, 141, 142, 143, 144, 145]. In this regard, understanding of photocatalytic properties of sensitized and doped TiO_2 can be mentioned[146, 147, 148, 149, 150]. Among other noteworthy studies, recent reports on Mn-doped rutile TiO_2 band structure[151] and the nucleation, and associated adsorption of TM clusters on (101) plane of anatase TiO_2[152, 153] are of specific interest. Another interesting use of DFT calculation is to compute energy levels and charge state of hydrogen situated in interstitial space of oxides ZnO, CdO, HfO_2, TiO_2, ZrO_2, $SrTiO_3$, $SrZrO_3$, $PbTiO_3$ and $ZrSiO_4$[154, 155]. DFT calculations have also been used to other complex crystalline solids such as HCP iron [156, 157], ternary $PbTiO_3$ perovskites [158, 159, 160] and ABO_4 type materials. Among different transition metal oxides, the influence of catalytic behaviour of vanadium oxide in numerous heterogeneous processes related to the industrial application is worth-mentioning. The fundamental character of group 7 elements in the periodic table is the availability of high-spin d-states of electrons followed by the oxidation in an appropriate weak field. Manganese has shown its specific significance among these elements as this TM can be found to take part in the photosynthesis process. In this connection, the study of possible reaction pathways of alkylidenes $MO_2(CH_2)(CH_3)$ related to group 7 elements with ethylene by Haunschild et al. is noteworthy[161] where M stands for Re, Tc, and Mn. Proper understanding of CH_4 dissociation through DFT calculation on Ru(0001), Tc(0001), Pd(111), Cu(111), Pt(111), and three surfaces of crystalline PdO are well known. Also, the C-C bond formation mechanism has been studied through DFT on Fe, Re, Ru, Rh, and Co[162, 163]. In this connection, studies of different properties of ABO_4 type ternary transition metal oxides are found to be significantly less. This has motivated us to study other crystalline properties of ABO_4 type transition metal oxides, especially those related to group 7 transition metals.

1.4 DFT and Energetic materials

Along with TMOs, we have also studied the crystalline properties of energetic materials (EMs) in this work. EMs are defined as considerable amounts of controllable chemical energy storage systems. These materials show their importance in pyrotechnics, propellants, fuels, and explosives. This class of materials are mainly divided into primary and secondary EMs[164, 165]. Primary explosives are known to detonate with relatively lower perturbation in the shock or heat form. On the other hand, secondary EMs are more powerful and require a more vital impulse for detonation initiation. As a result, primary EMs are usually used to trigger the detonation initiation of powerful secondary EMs. Organic molecules typically form secondary explosives. These EMs can be obtained in molecular liquids or solids under normal conditions. Example of some typical secondary EMs are nitromethane[169], Cyclotrimethylene trinitramine (RDX)[168], Cyclotetramethylene tetranitramine (HMX)[167], and Pentaerythritol tetranitrate (PETN)[166], etc.

The main feature of these EMs is their detonation ability which is nothing but the process of combustion at a much faster rate. Consequently, this creates a shockwave that travels at supersonic speed. These self-sustaining chemical reactions release a tremendous amount of gaseous products along with high temperature and pressure, resulting in the effect of destruction. Hence, these materials are very much useful for the commercial purpose of reconstruction and in warfare. Studies of these EMs are mainly concerned to find new materials with less sensitivity and high density in addition to low toxicity[170, 171, 172, 173, 174, 175]. The sensitivity of such materials depends on a lot of parameters that can release the stored chemical energy from these materials by initiating the detonation process, and these various means of stimuli could be electrostatic discharge, friction, heat, impact, shock, etc.[175, 176, 177, 178, 179, 180]. As a consequence, less sensitive EMs could be very useful with reduced risk of handling as well as transportation. Which eventually reduces the cost associated with these materials. The main drawback of designing insensitive EMs is the incomplete understanding of the associated microscopic phenomena, which eventually initiates detonation. In this consideration, simulation and modelling can help to understand these phenomena of detonation initiation at lower length and time scales. The first-principles calculation plays a significant role in this connection by predicting the precise Equation of States (EOS) for EMs. As these materials are highly reactive in nature, this kind of study reduces the damage as well as the cost associated with the experiment. As these materials are basically molecular solids, the incorporation of van der Waals (vdW) corrected schemes to DFT is very necessary[181, 182, 183, 184, 185, 186]. This kind of study also helps to understand such materials' anisotropic behaviour under compression.

Among different simulations of EMs, hydrostatic compression study of PETN through DFT calculations are worth mentioning[187, 188]. Among other investigations, the hydrostatic pressure study of HMX is also well reported. A similar DFT study on RDX can also be obtained from literature[189]. In this connection, the large unit cell of EMs is prohibitive in carrying out thorough DFT calculations. In contrast to the large crystal cell of RDX, the small size of the unit of solid nitromethane's (NM) crystal cell has given DFT calculations a significant advantage over different types of calculations. A large number of calculations have been reported related to NM, which is commonly considered as a prototype EM[190, 191, 192]. This sort of simulation technique not only helps us to understand the stiffness of EMs but also provides information about directional sensitivity through the elastic properties of such materials. Further, understanding of electronic band structure and electronic bandgap under compression can give information about the initiation of detonation. These initial estimations can furnish helpful guidelines regarding the selection of appropriate methods for investigating various chemical as well as physical properties of EMs.

Proper understanding of these EMs has clearly shown the importance of the NO_2 group in such materials. In this consideration, it has been observed that a proper balance of different functional groups present in these materials can help to achieve high performance with less sensitivity. The use of the heterocyclic group instead of the NO_2 group has also shown tremendous impact in this regard. This has motivated us to carry out a structure-property correlation study of EMs with different molecular structures. In this study, we have considered prototype NM based, cage structure-based and heterocyclic structure-based EMs for a comparative understanding of such materials.

1.5 Thesis Organization

This thesis provides the microscopic understanding of structural, elastic, electronic and Γ-point vibrational properties of EMs along with structural, Γ-point vibrational properties and IR spectra of ABO_4 type transition metal oxides ($TlTcO_4$ and $TlReO_4$). All calculations are done at 0 K as DFT is valid at 0 K (ground state). The whole thesis is organized into seven chapters, including this introduction chapter, theoretical details, four chapters with computationally obtained results regarding this thesis work, and a conclusion chapter. A brief description of the contents in the chapters is given below.

Chapter 1

This chapter gives the general introduction of computational simulations along with the importance and success of DFT in predicting different properties of materials for various applications. Then this discussion is followed by the use of DFT for predicting energy-storing material and the significance of transition metal oxides and energetic solids. Later, the organization of thesis chapters with a brief description is presented.

Chapter 2

This chapter provides a brief description of basic knowledge of DFT and associated methods involved in this thesis work. A brief discussion about different approximations, pseudopotential approach, projector augmented wave (PAW) method, linear augmented plane wave (LAPW) method along with vdW corrected DFT has been provided.

Chapter 3

This chapter deals with a comparative study of crystalline properties of thallium based pertechnetate and perrhenate. The crystal structure of the orthorhombic phase of $TlTcO_4$, the low- and room-temperature phases, along with the previously reported hypothetical phase of $TlReO_4$, have been considered in this study. After providing the importance and motivation behind selecting these materials for a thorough DFT study, experimentally obtained basic crystal structure information of these materials have been used as the input. The plane-wave pseudo-potential formalism (PW-PP) has been considered for getting the correct theoretical ground-state crystal structures. In order to obtain more accurate results for ground-state structural parameters, van der Waals (vdW) corrected DFT along with standard DFT functionals has also been considered. The importance of DFT total energy calculation has been verified in this chapter by predicting the correct ground state structure of $TlReO_4$. After getting the exact theoretical ground-state crystal structure, density functional perturbation theory (DFPT) calculation has been performed for computing Born Effective Charge (BEC) values as well as the vibrational properties of these materials. BEC values provide knowledge about the bonding nature present in these materials. This chapter also provides knowledge about the IR spectra and associated important vibrational modes of these materials.

Chapter 4

Crystalline properties of nitromethane related di- and trinitromethane based energetic salts have been discussed in this chapter. As the structure-properties correlation is linked with electronic structure and different interactions present in these materials, a lot of information can be obtained from such studies, which help in designing potential new energetic materials. Here, we have attempted to understand different properties of dinitromethane based potassium dinitromethane (KDNM) and trinitromethane based formamidinium nitroformate (FNF), methylhydrazinium nitroformate (MHNF), and potassium nitroformate (KNF). Along with available experimental reports, our comparative theoretical study on these materials will provide a deep insight about such materials and help to design well desired energetic materials.

Here we have performed PW-PP method based DFT calculations for obtaining a proper theoretical understanding of different properties of studied materials. In addition with standard exchange-correlation functional like (GGA) and (LDA), we have also considered various schemes of vdW corrected methods to obtain accurate structural properties. As a next step, a high-pressure study has been performed on FNF, MHNF and KNF to understand the pressure variation of structural parameters. Calculated pressure coefficient values of lattice parameters help us to understand the compressibility of these crystals. After a detailed understanding of the structural properties of studied materials, knowledge about these materials' elastic properties can help us to have a deep insight into the present intermolecular interactions in these materials. Elastic properties of energetic materials are correlated to their sensitivity towards explosion as they are linked with the intermolecular interactions present in such materials. Information about these properties also helps us to have a proper understanding of the mechanical stability of such materials. Keeping this in mind, we have considered the stress-strain method to calculate the elastic constant of studied materials. Linear response theory-based DFPT implemented in CASTEP code has been considered for calculating the born effective charge tensor of our studied materials, allowing us to know more about vibrational and optical properties. This quantity also helps us to predict the presence of different bonding in these materials. IR spectra of these materials have also been computed. Pressure variation of IR spectra of nitroformate based materials provides more insight into these materials.

Chapter 5

This chapter presents a thorough understanding of the crystalline properties of potential cage-structured EM octanitrocubane (ONC). After providing basic information about the importance of cage-structured materials compared to non-caged compounds, a detailed understanding of ONC has been given here. Though many molecular level theoretical studies have been performed on this material to date, rigorous analysis of the crystalline properties has not been done yet, indicating this study's significance.

The structural, elastic and zone-centred vibrational frequencies of ONC have been evaluated through the projector augmented wave (PAW) formalism. On the other hand, the full-potential LAPW approach has been used for calculating the electronic and optical properties of this material. The vdW corrected DFT schemes initially have addressed the structural properties of layered ONC. After obtaining the most accurate ground-state structural parameters, a high-pressure study has been considered to understand different crystallographic axes' compressibility properly. We have also computed the elastic properties of this material to understand the sensitivity of ONC regarding shock initiated detonation. After that, BEC values of the constituent elements of ONC and the Γ-point phonon frequencies along with the TB-mBJ bandgap of ONC have been reported. And finally, optical properties calculated with TB-mBJ potential of studied material were provided in this chapter.

Chapter 6

This chapter gives a clear idea about the solid-state structure-property correlation of heterocyclic furazan based EMs 4,4′-Bis(nitramino)azofurazan, known as DNAF and Bis(nitrofurazano)furazan, known as BNFF-1. As a first step, the significance of the heterocyclic group over the conventional use of EMs have been discussed. Then mentioning the earlier reports and importance of furazan based EMs, a brief discussion for our studied materials has been provided. A complete structure-property relation study on these compounds is given after furnishing the significance and motivation behind considering these materials. To obtain the different properties of these materials, the PAW approach has been considered. A thorough understanding of bond angles and lengths of DNAF, especially intra-, intermolecular hydrogen bonds of this compound, has also been presented along with lattice parameters and unit cell volume. After obtaining these materials' ground state structural parameters, a pressure variation study has been performed to understand the compressibility nature of different structural parameters. The understanding of present intermolecular interactions in DNAF has also been supported by a Hirshfeld surface analysis study. As it is a well-known fact that DFT always underestimates the bandgap, the electronic band structure of DNAF and BNFF-1 has been studied using GW approximation and TB-mBJ potential, respectively.

Chapter 7

This chapter summarizes the whole thesis work where the conclusion of our study has been focused. The future scope and possible expansion of this current work have been included at the end this thesis.

References

[1] R. Hockney and J. Eastwood, McGraw-Hill, New York, NY, USA, (1981).

[2] G. Ciccotti, G. Frenkel and I.R. McDonald, North-Holland: Amsterdam, The Netherlands, (1987).

[3] R. Hockney, Methods Comp. Phys. 9, 136-211 (1970).

[4] M. Allen and D. Tildesly, Oxford University Press: Oxford, UK, (1991).

[5] G.R. Liu and M.B. Liu, World Scientific Co. Pte. Ltd.: Singapore, (2003).

[6] T. Gates, G. Odegard, S. Frankland and T. Clancy, Compos. Sci. Technol. 65, 2416–2434 (2005).

[7] M. Steinhauser, M. Kuhn, A. Khan, S. Kohei and R. Amir, Eds.; Neat Press, Fulton, Maryland, USA, pp. 634–636 (2006).

[8] W. Scholz, W. Suss and T. Schrefl, Comput. Mat. Sci. (2000).

[9] SENG Dewen and LI Zhongxue., Journal of Liaoning Technical University, Vol.27(1), pp.9-12, (2008).

[10] G. Lannacone and P. Coli, Appl. Phys. Lett., 78(14), 204 (2001).

[11] D. SENG, Z. SONG and H. WANG, Proc. of SPIE Vol. 7143, (2008).

[12] J. Schiotz, F.D. Tolla and W. Jacobsen, Nature, 391: 561 (1998).

[13] R. Phillips, Cambridge University Press: Cambridge, UK, (2001).

[14] S., Yip, Ed., Springer: Berlin, Germany, (2005).

[15] M.O. Steinhauser, Springer: Berlin/Heidelberg/New York, Germany/USA, (2008).

[16] M. Finnis and J. Sinclair, Phil. Mag. A 50, 45 (1984).

[17] W. Kohn and L. Sham, Phys. Rev. 140, 1133–1138 (1965).

[18] R. Car and M. Parinello, Phys. Rev. Lett. 55, 2471 (1985).

[19] R. Courant, Bull. Amer. Math. Soc. 49, 1–23 (1943).

[20] J. Bishop and R. Hill, Philos. Mag. 42, 414–427 (1951). Int. J. Mol. Sci. 10, 5205 (2009).

[21] X. Markenscoff, A. Gupta, Eds. Collected Works of J.D. Eshelby; Springer: New York, NY, USA, (2006).

[22] W. Kohn, Rev. Modern Phys. 71, 1253 (1999).

[23] (SGTE), S.G.T.E. et al., Landolt-Boernstein New Series, Group IV (1999).

[24] Z.D. Pozun et al., J. Chem. Phys. 136, 174101 (2012).

[25] G. Montavon et al., N.J. Phys., Focus Issue, Novel Materials Discovery (2013).

[26] A. Agrawal et al., Integr. Mater. Manuf. Innov. 3, 1–19 (2014).

[27] B. Meredig et al., Phys. Rev. B 89, 094104 (2014).

[28] A.G. Kusne et al., Sci. Rep. 4, 6367 (2014).

[29] M. Fernandez, P.G. Boyd, T.D. Daff, M.Z. Aghaji & T.K. Woo, J. Phys. Chem. Lett. 5, 3056–3060 (2014).

[30] C. Kim, G. Pilania & R. Ramprasad, Chem. Mater. 28, 1304–1311 (2016).

[31] D. Xue et al., Nat. Commun. 7, 11241 (2016).

[32] F.A. Faber, A. Lindmaa, O.A. VonLilienfeld & R. Armiento, Phys. Rev. Lett. 117, 135502 (2016).

[33] A.O. Oliynyk et al., Chem. Mater. 28, 7324–7331 (2016).

[34] P. Raccuglia et al., Nature 533, 73–76 (2016).

[35] L. Ward, A. Agrawal, A. Choudhary & C. Wolverton, npj Comput. Mater. 2, 16028 (2016).

[36] L. Ward et al., Phys.Rev. B 96, 024104 (2017).

[37] O. Isayev et al., Nat. Commun. 8, 15679 (2017).

[38] F. Legrain, J. Carrete, A. van Roekeghem, S. Curtarolo & N. Mingo, Chem. Mater. 29, 6220–6227 (2017).

[39] D. Jha et al., Microsc. Microanal. 24, 497–502 (2018).

[40] V. Stanev et al., npj Comput. Mater. 4, 29 (2018).

[41] R. Ramprasad, R. Batra, G. Pilania, A. Mannodi-Kanakkithodi & C. Kim, npj Computat. Mater. 3, 54 (2017).

[42] A. Seko, H. Hayashi, K. Nakayama, A. Takahashi & I. Tanaka, Phys. Rev. B 95, 144110 (2017).

[43] M. De Jong et al., Sci. Rep. 6, 34256 (2016).

[44] E. W. Bucholz et al., Tribol. Lett. 47, 211–221 (2012).

[45] D. Jha et al., Sci. Rep. 8, 17593 (2018).

[46] A. Agrawal & A. Choudhary, APL Mater. 4, 1–10 (2016).

[47] A. Agrawal & A. Choudhary, MRS Commun. 9, 1–14 (2019).

[48] D. Jha et al., ACM (2019).

[49] F. Bloch, Zeitschrift für Phys. 52 555 (1929).

[50] E. Runge and E.K.U. Gross, Phys. Rev. Lett. 52 997 (1984).

[51] M. Petersilka, U.J. Gossmann and E.K.U. Gross, Phys. Rev. Lett. 76 1212 (1996).

[52] C.A. Ullrich and Hui Yang Z, Brazilian J. Phys. 44 154 (2014).

[53] A.I. Liechtenstein, V.I. Anisimov and J. Zaanen, Phys. Rev. B 52 R5467 (1995).

[54] S. Dudarev and G. Botton, Phys. Rev. B 57 1505 (1998).

[55] G. Kotliar, S.Y. Savrasov, K. Haule, V.S. Oudovenko, O. Parcollet and C.A. Marianetti, Rev. Mod. Phys. 78 865 (2006).

[56] A. Paul and T. Birol, Annu. Rev. Mater. Res. accepted (https://doi.org/10.1146/annurev-matsci-070218-121825) (2019).

[57] L. Hedin, Phys. Rev. 139, A796 (1965).

[58] F. Aryasetiawan and O. Gunnarsson, Reports Prog. Phys. 61, 237 (1998).

[59] J.P. Perdew, J.A. Chevary, S.H. Vosko, K.A. Jackson, M.R. Pederson, D.J. Singh and C. Fiolhais, Phys. Rev. B 46, 6671 (1992).

[60] R.G. Parr and W. Yang, Annu. Rev. Phys. Chem. 46, 701 (1995).

[61] G.R. Schleder, A. Fazzio and J.T. Arantes, J. Comput. Chem. 38, 2675 (2017).

[62] B. Hammer and J. Nørskov, Theoretical surface science and catalysis—calculations and concepts Impact of Surface Science on Catalysis (Advances in Catalysis vol 45) ed B.C. Gates and H.Knozinger (New York: Academic) pp 71–129 (2000).

[63] C. Freysoldt, B. Grabowski, T. Hickel, J. Neugebauer, G. Kresse, A. Janotti and C.G. Van de Walle, Rev. Mod. Phys. 86, 253 (2014).

[64] F. Baletto and R. Ferrando, Rev. Mod. Phys. 77, 371 (2005).

[65] A.S. Barnard, Reports Prog. Phys. 73, 086502 (2010).

[66] G.R. Schleder, A. Fazzio and J.T. Arantes, Int. J. Quantum Chem. 119, e25874 (2018).

[67] B.R. Sharma, A. Manjanath and A.K. Singh, Sci. Rep. 4, 7164 (2014).

[68] S.B. Fagan, R.J. Baierle, R. Mota, A.J.R. da Silva and A. Fazzio, Phys. Rev. B 61, 9994 (2000).

[69] T.M. Schmidt, R.J. Baierle, P. Piquini and A. Fazzio, Phys. Rev. B 67, 113407 (2003).

[70] E.Z. da Silva, F.D. Novaes, A.J.R. da Silva and A. Fazzio, Phys. Rev. B 69, 115411 (2004).

[71] S.B. Fagan, A.J.R. da Silva, R. Mota, R.J. Baierle and A. Fazzio, Phys. Rev. B 67, 033405 (2003).

[72] R.G. Amorim, A. Fazzio, A. Antonelli, F.D. Novaes, and A.J.R. da Silva, Nano Lett. 7, 2459 (2007).

[73] S.B. Fagan, R. Mota, A.J.R. da Silva and A. Fazzio, Nano Lett. 4, 975 (2004).

[74] J.T. Paul et al, J. Phys.: Condens. Matter 29, 473001 (2017).

[75] R. Wu, A.J. Freeman and G.B. Olson, Science 265, 376 (1994).

[76] T.B. Martins, R.H. Miwa, A.J.R. da Silva and A. Fazzio, Phys. Rev. Lett. 98, 196803 (2007).

[77] J.E. Padilha, A. Fazzio and A.J.R. da Silva, Phys. Rev. Lett. 114, 066803 (2015).

[78] S. Baroni, S. de Gironcoli, A. Dal Corso and P. Giannozzi, Rev. Mod. Phys. 73, 515 (2001).

[79] A. Torres, R.B. Pontes, A.J.R. da Silva and A. Fazzio, Phys. Chem. Chem. Phys. 17, 5386 (2015).

[80] E.O. Wrasse, A. Torres, R.J. Baierle, A. Fazzio and T.M. Schmidt, Phys. Chem. Chem. Phys. 16, 8114 (2014).

[81] F. Giustino, Rev. Mod. Phys. 89, 015003 (2017).

[82] F. Tian and C. Liu, The Journal of Physical Chemistry B 110, 17866 (2006).

[83] J.K. Nørskov, T. Bligaard, J. Rossmeisl and C.H. Christensen, Nat. Chem. 1, 37 (2009).

[84] T. Burkert, L. Nordström, O. Eriksson and O. Heinonen, Phys. Rev. Lett. 93, 027203 (2004).

[85] M. Costa, A.T. Costa, J. Hu, R.Q. Wu and R.B. Muniz, J. Phys.: Condens. Matter 30, 305802 (2018).

[86] M. Bode, M. Heide, K. von Bergmann, P. Ferriani, S. Heinze, G. Bihlmayer, A. Kubetzka, O. Pietzsch, S. Blügel and R. Wiesendanger, Nature 447, 190 (2007).

[87] A. Bansil, H. Lin and T. Das, Rev. Mod. Phys. 88, 021004 (2016).

[88] C.M. Acosta, M.P. Lima, R.H. Miwa, A.J.R. da Silva and A. Fazzio, Phys. Rev. B 89, 155438 (2014).

[89] C. Mera Acosta, O. Babilonia, L. Abdalla and A. Fazzio, Phys. Rev. B 94, 041302 (2016).

[90] C.L. Magee, Complexity 18, 10 (2012).

[91] C.M. Rignanese, J. Phys.: Condens. Matter 17, R357 (2005).

[92] A. Fujishima and K. Honda, Nature 238, 37-38 (1972).

[93] A. Kudo and Y. Miseki, Chem. Soc. Rev. 38, 253-278 (2009).

[94] B. Coelho, A.C. Oliveira and A. Mendes, Energy Environ. Sci. 3, 1398-1405 (2010).

[95] S. Shen, J. Shi, P. Guo and L. Guo, Int. J. Nanotechnol. 8, 523-591 (2011).

[96] P.E.M. Siegbahn, Chem. Phys. Lett. 201, 15-23 (1993).

[97] P.E.M. Siegbahn and M. Svensson, Chem. Phys. Lett. 216, 147-154 (1993).

[98] G.L. Gutsev, L. Andrews, C.W. Bauschlicher, Theor. Chem. Acc. 109, 298-308 (2003).

[99] X. Wang, F.X. Zhang, I. Loa, K. Syassen, M. Hanfland and Y.L. Mathis, Phys. Status Solidi B 241, 3168-3178 (2004).

[100] L.A. Errico, M. Renteria and M. Weissmann, Phys. Rev. B 72, 184425-1-184425-8 (2005).

[101] M.H. Kane, W.E. Fenwick, M. Strassburg, B. Nemeth, R. Varatharajan, Q. Song, D.J. Keeble, H. El-Mkami, G.M. Smith, Z.J. Zhang, J. Nause, C.J. Summers and I.T. Ferguson, Phys. Status Solidi B 244, 1462-1467 (2007).

[102] C.J. Cramer and D.G. Truhlar, Phys. Chem. Chem. Phys. 11, 10757-10816 (2009).

[103] N. Mehtougui, D. Rached, R. Khenata, H. Rached, M. Rabah and S. Bin-Omran, Mater. Sci. Semicond. Process. 15, 331-339 (2012).

[104] A.J. Cohen, P. Mori-Sanchez and W. Yang, Science 321, 792-794 (2008).

[105] J. Zaanen, G.A. Sawatzky and J.W. Allen, Phys. Rev. Lett. 55, 418-421 (1985).

[106] S. Hufner, Adv. Phys. 43, 183-356 (1994).

[107] V.I. Anisimov, F. Aryasetiawan and A.I. Lichtenstein, J. Phys.: Condens. Matter 9, 767-808 (1997).

[108] A.D. Becke, J. Chem. Phys. 98, 1372-1377 (1993).

[109] J.P. Perdew, M. Emzerhof, K. Burke, J. Chem. Phys. 105, 9982-9985 (1996).

[110] C. Adamo and V. Barone, Chem. Phys. Lett. 274, 242-250 (1997).

[111] J. Heyd, G.E. Scuseria and M. Ernzerhof, J. Chem. Phys. 118, 8207-8215 (2003).

[112] J. Heyd, G. Scuseria and M. Ernzerhof, J. Chem. Phys. 124, 219906 (2006).

[113] V.I. Anisimov, J. Zaanen and O.K. Andersen, Phys. Rev. B 44, 943-954 (1991).

[114] M.T. Czyzyk and G.A. Sawatzky, Phys. Rev. B 49, 14211-14228 (1994).

[115] A.I. Liechtenstein, V.I. Anisimov and J. Zaanen, Phys. Rev. B 52, R5467-R5470 (1995).

[116] S.L. Dudarev, G.A. Botton, S.Y. Savrasov, C.J. Humphreys and A.P. Sutton, Phys. Rev. B 57, 1505-1509 (1998).

[117] M. Cococcioni and S. de Gironcoli, Phys. Rev. B 71, 035105 (2005).

[118] L. Hedin, Phys. Rev. 139, A796-A823 (1965).

[119] W.G. Aulbur, M. Stadele and A. Gorling, Phys. Rev. B 62, 7121-7132 (2000).

[120] F. Tran and P. Blaha, Phys. Rev. Lett. 102, 226401 (2009).

[121] S. Albonetti, F. Cavani and F. Trifiro, Catal. Rev.: Sci. Eng. 38 (4), 413-438 (1996).

[122] W.C. Vining, A. Goodrow, J. Strunk and A.T. Bell, J. Catal. 270 (1), 163-171 (2010).

[123] W. Zhang, A. Desikan and S.T. Oyama, J. Phys. Chem. 99, 11468-11476 (1995).

[124] L. Chen, J. Li, M. Ge and R. Zhu, Catal. Today 153 (3-4), 77-83 (2010).

[125] L. Lietti, P. Forzatti and F. Bregani, Ind. Eng. Chem. Res. 35, 3884-3892 (1996).

[126] J.P. Dunn, H.G. Stenger Jr. and I.E. Wachs, J. Catal. 181 (2), 233-243 (1999).

[127] A. Kudo and Y. Miseki, Chem. Soc. Rev. 38, 253-278 (2009).

[128] M. Batzill, Energy Environ. Sci. 4, 3275-3286 (2011).

[129] V.I. Anisimov, F. Aryasetiawan & A.I. Lichtenstein, J. Phys. Conden. Matter 9, 767-808 (1997).

[130] B. Himmetoglu, A. Floris, S. de Gironcoli & M. Cococcioni, Int. J. Quant. Chem. 114, 14-49 (2013).

[131] P. Gopal et al., J. Phys. Condens. Matter 29, 444003 (2017).

[132] F. Tran, P. Blaha, K. Schwarz & P. Novák, Phys. Rev. B 74, 155108 (2006).

[133] H. Jiang, R.I. Gomez-Abal, P. Rinke & M. Scheffler, Phys. Rev. B 82, 045108 (2010).

[134] Q. Yin, A. Gordienko, X. Wan & S.Y. Savrasov, Phys. Rev. Lett. 100, 066406 (2008).

[135] A. Hariki, T. Uozumi & J. Kunes, Phys. Rev. B 96, 045111 (2017).

[136] D.-H. Seo, A. Urban & G. Ceder, Phys. Rev. B 92, 115118 (2015).

[137] M. Takahashi & J.-I. Igarashi, Phys. Rev. B 54, 13566–13574 (1996).

[138] R.E. Cohen, I.I. Mazin & D.G. Isaak, Science 275, 654–657 (1997).

[139] K. Ohta et al., Phys. Rev. Lett. 108, 026403 (2012).

[140] J. Kuneš, V.I. Anisimov, S.L. Skornyakov, A.V. Lukoyanov & D. Vollhardt, Phys. Rev. Lett.

99, 156404 (2007).

[141] Z.-X. Shen et al., Phys. Rev. B 44, 3604–3626 (1991).

[142] J. van Elp, R.H. Potze, H. Eskes, R. Berger & G.A. Sawatzky, Phys. Rev. B 44, 1530–1537 (1991).

[143] G.A. Sawatzky & J.W. Allen, Phys. Rev. Lett. 53, 2339–2342 (1984).

[144] J. van Elp et al., Rev. B 44, 6090–6103 (1991).

[145] R. Zimmermann et al., J. Phys. Condens. Matter 11, 1657–1682 (1999).

[146] F. De Angelis, A. Tilocca and A. Selloni, J. Am. Chem. Soc. 126, 15024 (2004).

[147] C. Di Valentin, E. Finazzi, G. Pacchioni, A. Selloni, S. Livraghi, A.M. Czoska, M.C. Paganini and E. Giamello, Chem. Mater. 20, 3706 (2008).

[148] A.M. Czoska, S. Livraghi, M. Chiesa, E. Giamello, S. Agnoli, G. Granozzi, E. Finazzi, C.D. Valentin and G. Pacchioni, J. Phys. Chem. C 112, 8951 (2008).

[149] K. Yang, Y. Dai, B. Huang and M.-H. Whangbo, Chem. Mater. 20, 6528 (2008).

[150] C. Di Valentin, G. Pacchioni, H. Onishi and A. Kudo, Chem. Phys. Lett. 469, 166 (2009).

[151] G. Shao, J. Phys. Chem. C 112, 18677 (2008).

[152] X.-Q. Gong, A. Selloni, O. Dulub, P. Jacobson and U. Diebold, J. Am. Chem. Soc. 130, 370 (2008).

[153] J. Zhang, M. Zhang, Y. Han, W. Li, X. Meng and B. Zong, J. Phys. Chem. C 112, 19506 (2008).

[154] J. Robertson, K. Xiong and S.J. Clark, Thin Solid Films 496, 1 (2006).

[155] K. Xiong, J. Robertson and S.J. Clark, J. Appl. Phys. 102, 083701 (2007).

[156] C.M.S. Gannarelli, D. Alfe´ and M.J. Gillan, Phys. Earth Planet. Interiors 152, 67 (2005).

[157] D.F. Johnson and E.A. Carter, J. Chem. Phys. 128, 104703 (2008).

[158] S. Piskunov, E. Heifets, R.I. Eglitis and G. Borstel, Comput. Mater. Sci. 29, 165 (2004).

[159] P. Baettig, C.F. Schelle, R. LeSar, U.V. Waghmare and N.A. Spaldin, Chem. Mater. 17, 1376 (2005).

[160] S.M. Hosseini, T. Movlasooy and A. Kompany, Phys. B 391, 316 (2007).

[161] R. Haunschild and G. Frenking, J. Organomet. Chem. 693, 3627 (2008).

[162] J. Cheng, P. Hu, P. Ellis, S. French, G. Kelly and C.M. Lok, J. Phys. Chem. C 112, 6082 (2008).

[163] J. Cheng, P. Hu, P. Ellis, S. French, G. Kelly and C.M. Lok, J. Catal. 257, 221 (2008).

[164] A.K. Sikder, G. Maddala, J.P. Agrawal et al., J. Hazard Mater 84, 1–26 (2001).

[165] D.M. Badgujar, M.B. Talawar, S.N. Asthana et al., J. Hazard Mater. 151, 289–305 (2008).

[166] A. Booth and F. Llewellyn, J Chem Sci (Resumed). 163, 837–846 (1947).

[167] C.S. Choi and H.P. Boutin, Acta Crystallogr Sec B. 26, 1235–1240 (1970).

[168] C.S. Choi and E. Prince, Acta Crystallogr Sec B. 28, 2857–2862 (1972).

[169] S. Trevino, E. Prince and C. Hubbard, J Chem Phys. 73, 2996–3000 (1980).

[170] H. Brand, P. Mayer, A. Schulz and J.J. Weigand, Angew. Chem., Int. Ed. 44, 3929 (2005).

[171] M.H.V. Huynh, M.A. Hiskey, D.E. Chavez, D.L. Naud and R.D. Gilardi, J. Am. Chem. Soc. 127, 12537 (2005).

[172] R.P. Singh, R.D. Verma, D.T. Meshri and J.M. Shreeve, Angew. Chem., Int. Ed. 45, 3584 (2006).

[173] Y.-H. Joo and J.M. Shreeve, Angew. Chem., Int. Ed. 48, 564 (2009).

[174] R. Wang, H. Xu, Y. Guo, R. Sa, and J.M. Shreeve, J. Am. Chem. Soc. 132, 11904 (2010).

[175] A.A. Dippold and T.M. Klapötke, Chem. - Eur. J. 18, 16742 (2012).

[176] C. Weir, M.L. Pantoya, G. Ramachandran, T. Dallas, D. Prentice and M. Daniels, J. Electrost. 71, 77 (2013).

[177] P.C. Hsu, G. Hust, M.X. Zhang, T.K. Lorenz, J.G. Reynolds, L. Fried, H.K. Springer and J.L. Maienschein, J. Phys.: Conf. Ser. 500, 052019 (2014).

[178] D. Skinner, D. Olson and A. Block-Bolten, Propellants, Explos., Pyrotech. 23, 34 (1998).

[179] P.M. Dickson, G.R. Parker, L.B. Smilowitz, J.M. Zucker and B.W. Asay, AIP Conf. Proc. 845, 1057 (2006).

[180] G.G. Savenkov, V.A. Morozov, A.S. Mazur and A.A. Lukin, Russ. J. Phys. Chem. B 9, 710 (2015).

[181] A.N. Ali, M.M. Sandstrom, D.M. Oschwald, K.M. Moore and S.F. Son, Propellants, Explos., Pyrotech. 30, 351 (2005).

[182] S. Appalakondaiah, G. Vaitheeswaran and S. Lebègue, J Chem Phys. 138, 1601–1601 (2013).

[183] M. Conroy, I. Oleynik, S. Zybin et al., J Phys Chem A. 113, 3610–3614 (2009).

[184] S. Hunter, P.L. Coster, A.J. Davidson et al., J Phys Chem C. 119, 2322–2334 (2015).

[185] S. Hunter, T. Sutinen, S.F. Parker et al., J Phys Chem C 117, 8062–8071 (2013).

[186] I.A. Fedorov and Y.N. Zhuravlev, Chem Phys. 436, 1–7 (2014).

[187] A.C. Landerville, M.W. Conroy, M.M. Budzevich et al., Appl Phys Lett. 97, 251908 (2010).

[188] C.K. Gan, T.D. Sewell and M. Challacomb, Phys. Rev. B 69 (2004).

[189] E.F.C. Byrd and B.M. Rice, J. Phys. Chem. C 111, 2787 (2007).

[190] D. Lian et al., Chinese Phys. Lett. 25 (2008).

[191] F.J. Zerilli, J.P. Hooper and M.M. Kuklja, J. Chem. Phys. 126 (2007).

[192] H. Liu et al., J. Chem. Phys. 124 (2006).

[193] E.J. Reed, J.D. Joannopoulos and L.E. Fried, Phys. Rev. B 62, 16500 (2000).

CHAPTER 2

Theoretical methods and their Implementation

Details of theoretical methods and their implementations involved in computing different material properties associated with this thesis work have been discussed in this chapter. A brief history of solving the many-body problem through the wave function approach has been discussed, followed by the DFT approach. Along with the central concept of the DFT approach, different approximations for considering electronic exchange-correlation contributions, like the local density as well as the generalized gradient approximations, are discussed. Details about the implementation of DFT through different packages and schemes related to this thesis work have been mentioned after that. Other essential concepts, such as basis set and pseudopotential (PP), associated with these packages for DFT calculations were also explained. After discussing the implementation of standard DFT calculation, semi-empirical dispersion corrected DFT has been presented. Analysis of elastic properties through the stress-strain method is discussed briefly. Linear response theory-based density functional perturbation theory (DFPT), used for calculating lattice dynamical properties and IR spectra of studied materials, was discussed after that. In the end, different approaches have been discussed regarding the calculation of the correct electronic band structure of materials.

2.1 Many-body problem through wave function approach

The very basic concept of solving many-body problem quantum mechanically is based on the single-particle Schrödinger equation. Though the structure of the equation looks simple for a single particle and solution can be easily obtained, a solution for a many-body particle system using the same equation will become more complicated. This complex and challenging nature of the equation arises due to the complicated form of the wave function and the presence of interaction between particles of the system. From the materials perspective, this situation can be compared with the much more straightforward solution of the hydrogen atom with the solution of more complicated systems such as atoms with higher atomic numbers, molecules and extended systems like solid. The generalized form of the many-body Hamiltonian in this connection is

$$\begin{aligned} H = &-\sum_i \frac{\hbar^2\nabla_i^2}{2M_i} + \frac{1}{2}\sum_{i,j}\frac{Z^2e^2}{|\mathbf{R}_i - \mathbf{R}_j|} \\ &-\sum_k \frac{\hbar^2\nabla_k^2}{2m_k} + \frac{1}{2}\sum_{k,l}\frac{e^2}{|\mathbf{r}_k - \mathbf{r}_l|} - \sum_{k,i}\frac{Ze^2}{|\mathbf{r}_k - \mathbf{R}_i|} \end{aligned} \tag{2.1}$$

Here the mass of the kth electron and the mass of the ith nucleus have been denoted by m$_k$ and M$_i$, respectively. The position vector of the kth electron and the ith ion have been marked using $\mathbf{r}_k$ and $\mathbf{R}_i$. The atomic number is denoted by Z. The Hamiltonian operator $\hat{H}$, generally described by the summation of any system's potential and kinetic energy operators, consists of 5 terms for a many-body system. The kinetic energy operator for nuclei or ions (T$_N$) and for electrons (T$_e$) can be expressed by the first and third terms of Equation 2.1, respectively. On the other hand, 2nd and 4th terms denote the potential energy related to Coulomb repulsion of nuclear-nuclear (V$_{NN}$) and electron-electron (V$_{ee}$) interaction. The last term of the equation denotes the attractive Coulomb potential related to the nuclear-electron interaction (V$_{Ne}$). As the solution of the above equation gets more complicated for the system with a higher number of electrons, different approximations are being used to simplify the Hamiltonian operator.

2.1.1 Born-Oppenheimer Approximation

For reducing the complex nature of the many-body Hamiltonian operator, Born-Oppenheimer approximation [1] is normally being considered first to simplify the Hamiltonian by separating nuclear and electronic contribution. As a result of the considerable mass difference between electrons and nuclei, the many-body Hamiltonian can be expressed as

$$H = -\sum_k \frac{\hbar^2\nabla_k^2}{2m_k} + \frac{1}{2}\sum_{k,l}\frac{e^2}{|\mathbf{r}_k - \mathbf{r}_l|} - \sum_{k,i}\frac{Ze^2}{|\mathbf{r}_k - \mathbf{R}_i|} \tag{2.2}$$

2.1.2 Hartree Approximation

Though the complexity of the given complex Hamiltonian is reduced by the Born-Oppenheimer approximation up to some extent, it is still complex. This complexity comes from electron-electron interaction. The approximation for minimising this kind of complexity to obtain the solution of the Schrödinger wave equation of a system was given by Hartree. According to this approximation, [2] expression of many-body system's wave function becomes

$$\Psi(\mathbf{r}_1\sigma_1, \mathbf{r}_2\sigma_2, ..., \mathbf{r}_N\sigma_N) = \prod_i^N \psi_i(\mathbf{r}_i\sigma_i) \tag{2.3}$$

Where σ's and $\mathbf{r}$'s denotes the spin and the space coordinates, respectively. Using this Hartree approximation, one can say that the position of other electrons controls the potential in which certain electrons perceive. As a result, single-particle averaged potential can be used for the approximated potential of the studied system.

$$V_H(\mathbf{r}_i) = \sum_{j \neq i} \frac{|\psi_j(\mathbf{r}_j)|^2}{|\mathbf{r}_i - \mathbf{r}_j|} \tag{2.4}$$

Here, $\psi_j(\mathbf{r}_j)$ means the wave function of a single-particle (solution of wave equation associated to single-particle) and the Hartree potential is denoted by V$_H$. Now the Schrödinger equation can be written as

$$[-\sum_k \frac{\hbar^2 \nabla_k^2}{2m_k} + V_{ext} + V_H(\mathbf{r}_i)]\psi_i(\mathbf{r}_i) = \epsilon_i \psi_i(\mathbf{r}_i) \tag{2.5}$$

This simplification leads to a set of separable equations. Though a self-consistent iterative process is still required to obtain the solution of these equations more due to their non-linear nature. As no two electrons are allowed to acquire the same quantum state according to the exclusion principle of Pauli, antisymmetric nature should be followed by the wave function of any system. Interchange electron coordinates in the above wave function show that this antisymmetric nature could not be found. In order to solve this kind of problem Hartree-Fock [3] theory comes into the picture.

2.1.3 Hartree-Fock Approximation

Though the many-body wave function is normally written as the product of constituent particle's wave function in the Hartree method, the same is expressed as the slater determinants of the wave function of constituent particles in the Hartree-Fock approach[3]. According to this method, the wave function can have the form as

$$\Psi(\mathbf{r}_1\sigma_1, ..., \mathbf{r}_N\sigma_N) = \frac{1}{\sqrt{N!}} \begin{pmatrix} \psi_1(\mathbf{r}_1\sigma_1) & \psi_1(\mathbf{r}_2\sigma_2) & . & . & \psi_1(\mathbf{r}_N\sigma_N) \\ \psi_2(\mathbf{r}_1\sigma_1) & \psi_2(\mathbf{r}_2\sigma_2) & . & . & \psi_2(\mathbf{r}_N\sigma_N) \\ . & . & . & . & . \\ . & . & . & . & . \\ \psi_N(\mathbf{r}_1\sigma_1) & \psi_N(\mathbf{r}_2\sigma_2) & . & . & \psi_N(\mathbf{r}_N\sigma_N) \end{pmatrix} \tag{2.6}$$

Here, the total electron number of the many-body system is denoted by N. This slater determinant is nothing but the linear combination of Hartree products given in Equation 2.3. The Hartree-Fork equation that follows from the energy minimization can be expressed as

$$\begin{split} &[-\frac{\hbar^2}{2m}\nabla^2 + V_{ext} + V_H(\mathbf{r}_i)]\psi_i(\mathbf{r}_i) \\ &\qquad - \sum_j \delta_{\sigma_i\sigma_j} \int d\mathbf{r}' \frac{\psi_j^*(\mathbf{r}')\psi_i(\mathbf{r}')}{|\mathbf{r} - \mathbf{r}'|} \psi_j(\mathbf{r}) = \epsilon_i \psi_i(\mathbf{r}_i) \end{split} \tag{2.7}$$

The last term associated with the left side of the Equation 2.7 is due to the Hartree-Fock wave function. Interaction between electrons with the same spin is involved in this term, known as the exchange term. Due to the antisymmetric nature of the wave function, a specific type of interaction is also present between the electrons. This kind of interaction is called the correlation interaction. The energy difference between the Hartree-Fock limit and the exact energy is usually considered the correlation energy.

2.2 Thomas-Fermi Theory

Nearly at the same time as Hartree(1927-1928), Thomas and Fermi[10, 11] proposed a different line of thought. They suggested considering the main variable of the many-body system as the total electron density instead of the many-body wave function. Using this concept, they evaluated the total energy of the system. To obtain the system's total energy, different contributions such as the kinetic, electrostatic interaction potential and external potential energy parts have been taken from homogeneous electron gas. The main idea of this study was to obtain similar quantities related to the inhomogeneous system.

$$E_\alpha[\rho] = \int \rho(\mathbf{r})\epsilon_\alpha[\rho(\mathbf{r})]d^3r \tag{2.8}$$

The α contribution to the energy density is given by $\epsilon_\alpha[\rho(\mathbf{r})]$. Here, the parameter α denotes the kinetic, electrostatic and external contribution. This calculation has been done locally for the assumed density value at each point of space. The famous local density approximation was proposed for the first time during this time. The functional dependence of energy density and the total energy on the density of electrons has been indicated by the square brackets. This electron density is dependent on the Fermi energy (ϵ_F) in the case of homogeneous gas, and the relation is given by

$$\rho = \frac{1}{3\pi^2}(\frac{2m}{\hbar^2})^{\frac{3}{2}}\epsilon_F^{\frac{3}{2}} \tag{2.9}$$

Therefore the expression of the kinetic energy density is as follows

$$t[\rho] = \frac{3}{5}\frac{\hbar^2}{2m}(3\pi^2)^{\frac{2}{3}}\rho^{\frac{2}{3}} \tag{2.10}$$

So the LDA kinetic energy is

$$T_{TF} = C_k \int \rho(\mathbf{r})^{\frac{5}{3}}d^3r, \tag{2.11}$$

with $C_k = 2.871$ hartree (unit of energy). The implementation of exchange into the above equation can be achieved using Slater's expression in the homogeneous electron gas case. After consideration of exchange, this theory is known as the Thomas-Fermi-Dirac (TFD). Application of local approximation for the homogenous system of electron gas can also help to incorporate the contribution of correlation, which was proposed by Wigner.

Replacement of these approximations into the typical expression of the energy for an inhomogeneous electron gas system leads to the energy expression related to TFD:

$$\begin{aligned} E_{TFD}[\rho] = C_k \int \rho(\mathbf{r})^{\frac{5}{3}} d^3r + \int \rho(\mathbf{r}) v_{ext}(\mathbf{r}) d^3r + \frac{1}{2} \int \int \frac{\rho(\mathbf{r})\rho(\mathbf{r}')}{|\mathbf{r}-\mathbf{r}'|} d^3r d^3r' \\ - C_X \int \rho(\mathbf{r})^{\frac{4}{3}} d^3r \end{aligned} \tag{2.12}$$

Here C_X denotes the exchange constant. From the above expression, it can be clearly seen that the E_{TFD} is mainly dependent on the electronic density. This made us conclude that this quantity is functional. Now one needs to find suitable density $\rho(\mathbf{r})$ for which $E_{TFD}[\rho]$ is going to be minimized by assuming some variational principle intuitively. In such a case, we have to consider the condition that the total electron number of the system should be equal to the full charge of the system: $\int \rho(\mathbf{r}) dr = N$. This sort of variation is related to a function, density $\rho(\mathbf{r})$, instead of a parameter. Due to this, the minimization scheme tries to obtain a function in the 3-D space that provides the minimized stationary energy state for density variations.

2.3 Density Functional Theory(DFT)

Density Functional Theory is very useful for handling the aforementioned many-body system differently. This is basically a quantum mechanical computational method used for investigating the electronic structure-property (principally the ground state) of many electron systems. The fundamental concept of DFT [4, 5, 6, 7, 8, 9] is to represent an interacting electronic system in terms of its density instead of its associated wave function. This theory is found to be very useful for obtaining various properties of materials by solving the many-electron problem using different functionals, generally referred to as the function of a function. The electron density of the system, which is mainly dependent on the spatial coordinates, play a crucial role in this connection.

Although the Thomas-Fermi model provides its first conceptual roots, the existence of DFT has mainly been possible due to the Hohenerg-Hohn theorems[12]:

The Hohenberg–Kohn theorems can adequately describe the many-electron system in an external potential.

Theorem 1. The external potential, hence the total energy, is a unique functional of the electron density.

Theorem 2. The functional that delivers the ground-state energy of the system provides the minimized energy if and only if the input density is the actual ground-state density.

The expression for the main variable of DFT, which is particle density $\mathrm{n}(\mathbf{r})$, can be written in terms of the wave function as

$$n(\mathbf{r}) = N \int d^3\mathbf{r}_2 \int d^3\mathbf{r}_3 ... \int d^3\mathbf{r}_N \Psi^*(\mathbf{r}, \mathbf{r}_2, ..., \mathbf{r}_N) \Psi(\mathbf{r}, \mathbf{r}_2, ..., \mathbf{r}_N). \tag{2.13}$$

Here Ψ is the normalized total wave function of the system. In another way, we can say that we can calculate the ground state wave function $\Psi_0(\mathbf{r}_1, ..., \mathbf{r}_N)$ of any system from its corresponding ground state density $n_0(\mathbf{r})$. This tells us Ψ_0 is a unique functional of n_0.

$$\Psi_0 = \Psi_0[n_0] \tag{2.14}$$

From this, we can also predict that the expectation value of any observable in the ground state is a functional of n_0. This is also true for the system's energy in the ground state. The expression of the ground state energy in this connection can be written as

$$E_0 = E[n_0] = \langle \Psi_0[n_0] | \hat{T} + \hat{V} + \hat{U} | \Psi_0[n_0] \rangle \tag{2.15}$$

Here we can write the contribution from the external potential using the density n_0 of the ground state. In general, this contribution can be expressed concerning the density, n as

$$V[n] = \int V(\mathbf{r}) n(\mathbf{r}) d^3\mathbf{r} \tag{2.16}$$

Though the U[n] and T[n] functionals are referred to as the universal functionals, the V[n] functional is considered as non-universal as it depends on the system which we are studying. If we account for a system for which V is specified, then the functional E[n] has to be minimised concerning $n(\mathbf{r})$ where E[n] can be expressed as

$$E[n] = T[n] + U[n] + \int V(\mathbf{r}) n(\mathbf{r}) d^3\mathbf{r} \tag{2.17}$$

Here we have to assume that the expressions for U[n] and T[n] are reliable. After minimizing the above functional successfully, we can get the density n_0 and other desired observables associated with the ground state. The Lagrange undermined multiplier approach is found to be very useful for solving the minimization problem. First of all, we have to take an energy functional, which does not contain energy term related electron-electron interaction,

$$E_s[n] = \langle \Psi_s[n] | \hat{T} + \hat{V}_s | \Psi_s[n] \rangle \tag{2.18}$$

Here $\hat{T}$ is related to kinetic energy, and $\hat{V}_s$ is associated with the effective external potential. Now the Kohn-Sham [13] equations related to the auxiliary non-interacting system can be solved where the equation is given as

$$[-\frac{\hbar^2}{2m}\nabla^2 + V_s(\mathbf{r})]\phi_i(\mathbf{r}) = \epsilon_i \phi_i(\mathbf{r}) \tag{2.19}$$

After solving this, we will get ϕ_i and from which we will be able to get the density $n(\mathbf{r})$ related to the actual many-body system. Now the single-particle effective potential can be expressed more explicitly as

$$V_s = V_{Ext} + V_H + V_{XC}[n_s(\mathbf{r})] \tag{2.20}$$

where

$$V_H = \int \frac{e^2 n_s(\mathbf{r}')}{|\mathbf{r} - \mathbf{r}'|} d^3r' \tag{2.21}$$

is called the Hartree term, which represents the Coulomb repulsion and the potential $V_{XC}[n_s(\mathbf{r})]$ is known to be related to the exchange-correlation part associated with electron-electron interaction. The Hartree and the exchange-correlation terms are dependent on $n(\mathbf{r})$ and, as a consequence, depends on ψ_i, which also in tern depends on V_s. As a result, a self-consistent approach has to be considered to obtain the solution of the Kohn-Sham equation[13]. Due to this fact, these steps have to be followed. Firstly an initial guess of density $n(\mathbf{r})$ has to be considered, and then the corresponding V_s has to be evaluated. After this, the Kohn-Sham equation has to be solved using those values for the ψ_i. As a next step, these steps have to perform followed by the calculation of new density. These steps need to continue until convergence is reached.

2.4 Approximations

In the above approach, Hartree term includes the long-range interaction, and the T[n] functional contains kinetic energy. This also tells that the energy regarding the exchange-correlation part can be considered somewhat local functional of the electron density. As a result, E_{XC} can be expressed as $E_{XC} = \int \epsilon_{XC}([n], \mathbf{r}) n(\mathbf{r}) d\mathbf{r}$. Here ϵ_{XC} is the single particle energy which is dependent on $n(\mathbf{r})$ close to $\mathbf{r}$. Now it is quite reasonable to approximate $\epsilon_{XC}([n], \mathbf{r})$ locally by an energy functional of a system of constant density ($n(\mathbf{r}) = n = constant$) for a slowly varying $n(\mathbf{r})$. Instead of finding $\epsilon_{XC}([n], \mathbf{r})$ related to any shape on $n(\mathbf{r})$ it will be enough to have $\epsilon_{XC}([n], \mathbf{r})$ associated to a series of constant density, n, which is known as the basic idea of the LDA or Local Density Approximation [14]. Taking also into account the gradient of the density would be a way to improve LDA. Realization of the use of other general functions related to $n(\mathbf{r})$ and $\nabla n(\mathbf{r})$ helped in achieving this major breakthrough. Which led to the new approximation known as GGA or Generalized Gradient Approximation [15] and can be expressed as $E_{XC}^{GGA}[n] = \int f(n(\mathbf{r}), \nabla n \mathbf{r}) d\mathbf{r}$.

2.5 Some basic parameters

Different basic essential parameters, such as basis set and pseudopotential (PP) associated with these computational techniques for carrying out DFT calculations, have been explained here.

2.5.1 Basis set

The basis set in density-functional theory or Hartree–Fock method is usually referred to as a set of basis functions used to represent electronic wave function. The main advantage of using a basis set in such calculations is to turn related partial differential equations into suitable algebraic equations, which in turn help in the computer implementation. Among various choices of basis sets, using a linear combination of atomic orbitals is commonplace in the community related to quantum chemistry. In contrast, the solid-state community

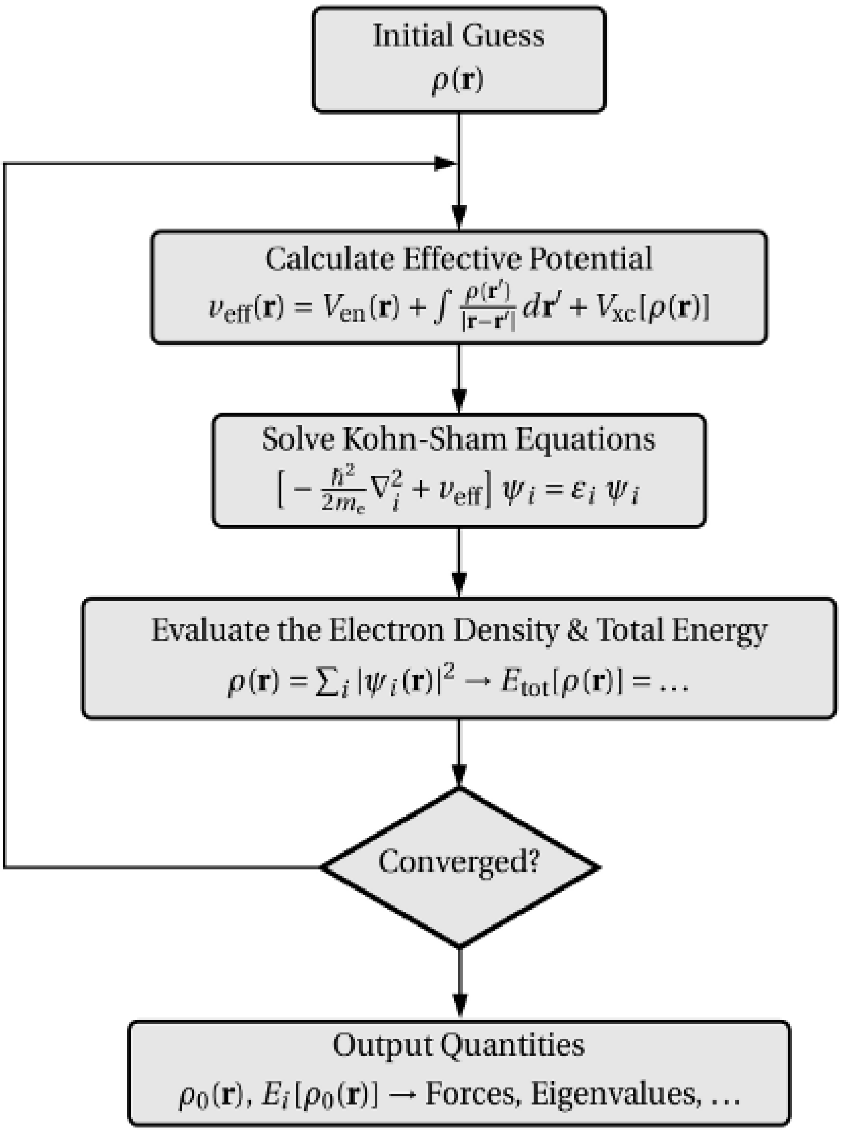

Figure. 2.1 DFT Algorithm

typically uses the plane-wave basis set.

In the case of extended systems like crystalline solids, the electronic wave function spans over the entire crystal. Hence, the required basis set is also infinite for expanding the Kohn-Sham orbital. But as the crystalline solids are known to follow periodic boundary conditions, Bloch's theorem helps connect the electronic properties in an infinite periodic system with the electrons in a unit cell. According to this theorem, the single-particle solution in a periodic potential, which is U($\mathbf{r}$)=U($\mathbf{r}$+$\mathbf{R}$), will have the form of

$$\phi_i(\mathbf{k}, \mathbf{r}) = e^{i\mathbf{k}.\mathbf{r}} u_i(\mathbf{k}, \mathbf{r}) \tag{2.22}$$

Here $u_i(\mathbf{k}, \mathbf{r}) = u_i(\mathbf{k}, \mathbf{r} + \mathbf{R})$. This implies

$$\phi_i(\mathbf{k}, \mathbf{r} + \mathbf{R}) = \phi_i(\mathbf{k}, \mathbf{R}) e^{i\mathbf{k}.\mathbf{R}} \tag{2.23}$$

By substituting this in the central equation of Kohn-Sham DFT, a new eigenvalue equation can be obtained regarding each given $\mathbf{k}$. So, an electronic state is being occupied by each electron with a definite wave vector $\mathbf{k}$. Consequently, the problem of getting a solution for an extended system containing infinite electrons becomes the problem related to finite electronic bands but at the infinite k-points of a single unit cell in reciprocal space. This, in principle, leads to calculations of unlimited numbers due to the contribution of occupied states for each k-point to electronic potential. The wave function at closed k-points will almost be identical. As a result, the wave functions around some particular k-point of a small region in reciprocal space can be replaced with the wave function at that k-point. This solves the problem of infinite k-points to finite k-points. In order to solve the Kohn-Sham equations numerically, well-defined basis sets are normally being used for expanding these Kohn-Sham orbitals. As already mentioned previously, the plane-wave basis set is typically considered for crystalline materials. Expansion of Kohn-Sham orbitals $\phi_i(\mathbf{k},\mathbf{r})$ through plane-wave basis set is as follows

$$\phi_i(\mathbf{k},\mathbf{r}) = e^{i\mathbf{k}.\mathbf{r}} u_i(\mathbf{k},\mathbf{r}) = \frac{1}{\sqrt{V}} \sum_G C_{i,\mathbf{K}+\mathbf{G}} e^{i(\mathbf{K}+\mathbf{G})\mathbf{r}} \tag{2.24}$$

Here the lattice vector in reciprocal space and the expansion coefficient are defined by 'G' and $C_{\mathbf{K}+\mathbf{G}}$, respectively. In principle, one should use an infinite basis set for expanding these Kohn-Sham orbitals, $u_i(\mathbf{k},\mathbf{r})$. Though in practice, truncation of infinite basis set is possible by including only plane waves with less kinetic energies compared to a defined cut-off

$$\frac{1}{2}|\mathbf{K}+\mathbf{G}|^2 < E_{cut-off} \tag{2.25}$$

The calculated energy of any system will show some error because of the improper plane-wave basis set truncation. So, one can systematically reduce the magnitude of the error by using a larger energy cut-off value. In practice, the cut-off energy increment should be allowed until the required tolerance of the calculated total energy.

2.5.2 Pseudopotential

Pseudopotential, which is also known as effective potential in physics, usually is being used to simplify the description of a complex system. This approximation helps to find an effective potential for an atom by replacing its all-electron potential or full potential. As most of the physical properties of any chemical compound are less dependent on core electrons and mainly dependent on valence electrons, the core electronic states are eliminated in this approach and pseudo-wavefunction with fewer nodes is used to describe the chemically active valence electrons. This allows the practical use of plane-wave basis sets as few Fourier modes are enough to describe the pseudo-wavefunctions. From the implementation perspective, two main drawbacks are considered for expanding all the electrons' Kohn-Sham wave function through a plane-wave basis set. Among these, the first one is considered rapid oscillation of wave function of valence electrons near the core region for maintaining the orthogonality to the wave functions of core electrons. The second one is the accurate description of the deep potential near nuclei. Due to these two factors, many plane-wave basis sets are required to expand the Kohn-Sham wave functions of all the electrons, especially near nuclei. So the use of pseudopotential for describing electron-ion interaction reduces the electron number of the system. Also, a reduced plane-wave basis set size is needed to explain the much softer as well as smoother pseudo valence wave functions. In turn, this helps to perform faster calculations and consider the bigger system. Though pseudopotential replaces the all-electron potential with a smoother one near the core region, it provides the actual valence charge density outside of the core region. Depending on different parameters, different types of pseudopotential schemes are available for practical applications. Pseudopotentials with larger cut-off radius are softer, which are easily convergent but less transferable. In the case of norm-conserving pseudopotentials, a relatively large number of plane waves are required for more accurate results. This is associated with the fact that a considerable energy cut-off value is needed for such kind of pseudopotential. On the other hand, ultra-soft pseudopotentials are known for specific relaxed requirements. Consequently, a much smaller plane-wave basis set is needed for the convergence and is much faster than norm-conserving pseudopotentials.

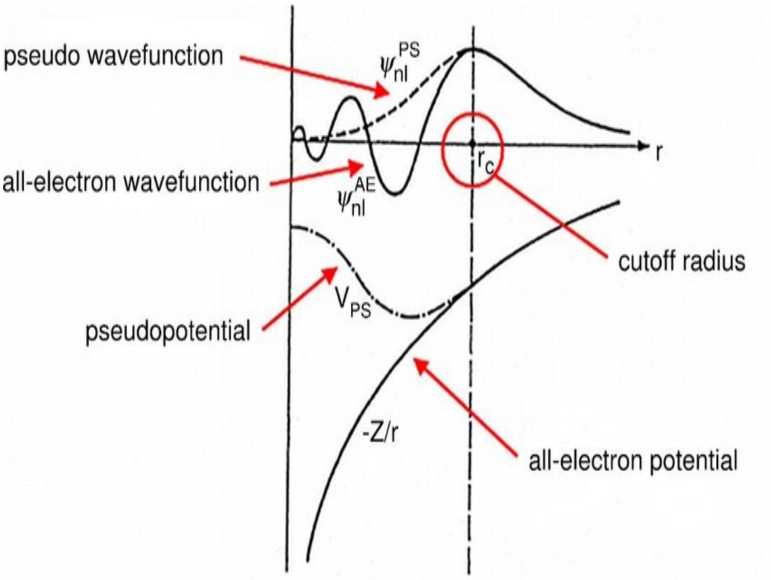

Figure. 2.2 Pseudopotential and pseudo wave-function

2.6 Implementation of DFT through different approaches

Implementation of DFT calculation through different schemes associated with this thesis work has been discussed here.

2.6.1 CAmbridge Sequential Total Energy Package

Cambridge Sequential Total Energy Package or CASTEP is basically designed for the quantum mechanical study of solid-state materials. This package mainly uses the plane-wave pseudopotential method to execute density functional theory-based calculations to explore crystalline materials' different properties. Among these properties, analysis of structural properties, elastic properties, electronic band structure, the partial and total density of states as well as the optical properties of solid materials are worth mentioning. Along with these, vibrational properties such as the zone-centred phonon frequencies, the complete phonon dispersion, the phonon density of states and the associated thermodynamic properties can also be calculated with the help of linear response theory or finite displacement technique implemented in this code. A brief discussion about different tasks performed using this code has been provided here. As a first step, a theoretical equilibrium crystal structure can be obtained by performing the Geometry Optimization task. This task is based on the reduction of the magnitude of the forces and stresses obtained at each step of calculations to a specific convergence tolerance limit. After obtaining the optimized crystal structure, electronic eigenvalues along different high symmetry Brillouin zone points can be calculated using the properties task. Using a fine Monkhorst-Pack grid and non-self consistent calculation, these electronic eigenvalues for both the conduction as well as the valence bands can be calculated, which produces the density of states and the electronic band structure. This code can also determine the electron charge density difference in any structure. Application of volume conserving finite strain technique through this code can also help find the elastic constants and associated mechanical properties of materials. Optical properties can also be calculated along with the density of states and the electronic band structure of studied materials. The linear response theory implemented in this code helps obtain the second derivative of total energy concerning atomic displacement. It hence helps in calculating the dynamical matrix for a set of q-vectors. The force constant matrix can be obtained from the dynamical matrices using Fourier transformation. This can be further useful to get the vibrational frequencies, IR and Raman modes.

2.6.2 PAW Method and its implementation

The Projector Augmented Wave (PAW)[16] formalism has shown tremendous success now-a-days for implementing Density Functional Theory. The basic concept of this method is based on the generalization of the ultrasoft-pseudopotential in addition to the linearized augmented plane-wave (LAPW) formalism. This method is highly efficient for more excellent computational performance. The valence wave functions are required to be orthogonal to core states which lead to the rapid oscillations of valence wave function near ion cores. This sort of situation is very problematic because it requires many Fourier components to describe the wave functions accurately. The PAW approach addresses this issue by transforming these oscillatory wave functions to smooth wave functions. These smooth wave functions are more convenient in computation, providing a direction for calculating properties related to all-electron wave functions. This method is quite similar to changing the Heisenberg picture from the Schrodinger picture. Concept of pseudo-potential dates from the 1930s, when Fermi and Hellmann proposed the solution mechanism of the Schrödinger equation regarding the valence electrons orthogonal to the core electronic states. The extension of this concept offers the development of different pseudopotential schemes from 'norm-conserving'[17] to ultra-soft[18, 19, 20] and finally to the PAW formalism[16]. The PAW formalism, which Blöchl introduces, is based on the projector functions that map complex wave functions onto 'pseudo' wave functions. Using this approach, the modelling of core electrons is being considered by neglecting these electrons but by considering the difference between the 'true' wave function and the obtained pseudo-wave function. The expression of the Schrödinger equation becomes

$$\tau^* H \tau \tilde{\Psi} = E \tau^* \tau \tilde{\Psi} \tag{2.26}$$

Where $\tilde{\Psi}$ is the pseudo wave function, τ is the transformation operator that connects the exact (Ψ) and the pseudo ($\tilde{\Psi}$) wave function. To determine the 'pseudo' wave functions, the Schrödinger equation is being solved first in DFT, and then projectors enable us to obtain the exact density. The high performance of this formalism has already been established for studying systems like molecules, solids ad surfaces. This kind of method where energy- and potential-independent wave functions are used is mainly used in packages such as GAPW, CP-PAW, VASP [21], ABINIT, NWCHEM, PWPAW, ESPRESSO [22], etc.

2.6.3 Full Potential Linearized Augmented Plane Wave (FP-LAPW) method

The Khon-Sham equation can also be solved without separating the core and the valence electronic wave function, as discussed in the pseudopotential method. In such an approach, all electrons are considered in an explicit way for the computation and are known as the all-electron method. Among these methods, the most accurate electronic structure calculation approach is known as the linearized augmented plane-wave or LAPW method. This approach basically divides the whole unit cell into the interstitial and non-overlapped atomic sphere regions. Non-overlapping atomic sphere with radius R uses the wave function as the multiplication of spherical harmonics $Y_{lm}(\mathbf{r})$ with radial functions linear combination.

$$\phi_{kn} = \sum_{lm} [A_{lm,kn} u_l(\mathbf{r}, E_l) + B_{lm,kn} \dot{u}_l(\mathbf{r}, E_l)] Y_{lm}(\mathbf{r}) \tag{2.27}$$

Here, the radial part solution with the energy E_l has been denoted by $u_l(\mathbf{r}, E_l)$. This is typically chosen at the midpoint of the corresponding band of l-like characters. The derivative of the radial part with respect to energy at E$_l$ energy denotes the potential's spherical part, $\dot{u}_l(\mathbf{r}, E_l)$, inside the sphere. The linear combination of the radial and its energy derivative function is used to obtain the linearized radial wave function inside the sphere, which can be achieved by numerically integrating the radial part of the function using a radial mesh. The coefficients of the Equation 2.27, A$_{lm}$ and B$_{lm}$, are known as functions of k$_n$. The k$_n$ can also be represented by k+K$_n$. Where K$_n$ refers to the lattice vectors in reciprocal space, k is known as the wave vector regarding the first Brillouin zone. This wave vector k can be determined using the condition that the corresponding basis function should match for functions of the inside sphere with each plane wave of the interstitial region. The expansion of the plane wave in the interstitial area is used as

$$\phi_{kn} = \frac{1}{\sqrt{\omega}} e^{ik_n r} \tag{2.28}$$

The augmentation of every plane wave is achieved using an atomic-like function for each atomic sphere. In accordance with the linear variational approach, the Kohn-Sham solutions can be expanded in terms of combined basis set regarding the linear augmented plane waves.

$$\psi_k = \sum_n c_n \phi_{kn} \tag{2.29}$$

Here the coefficients, c$_n$, can be determined using the Rayleigh-Ritz variational principle method. A cutoff parameter of R$_{mt}$K$_{max}$ = 6 to 9 controls the convergence related to this basis set. Here R$_{mt}$ defines the radius of the smallest atomic sphere in the unit cell, whereas K$_{max}$ is related to the magnitude regarding the largest K vector.

2.7 Semi-empirical dispersion correction

After the implementation of standard DFT calculation, semi-empirical dispersion corrected DFT has been presented. The main drawback of standard DFT is the inability to capture dispersion correction or van der Waals interaction using semi-local density functional. The inclusion of this correction using non-local correlation functional to the total energy is considered a significant development of DFT calculation. A cheap and straightforward solution to this problem has been achieved by incorporating an empirical potential in the form of $-C_6/R^6$. Here, the coefficient C$_6$ denotes the pairwise atomic parameter. This approach is referred to as the dispersion-corrected DFT or the DFT-D method and provides an alternative path of dispersion correction without using the non-local correlation functional. DFT-D2 scheme is known as the oldest scheme in this regard and uses -$\frac{C}{R^6}$ pairwise atomic term for the empirical dispersion potential.

$$E^{D2}_{disp} = -s_6 \sum_A \sum_{B<A} \left(\frac{C_{6,AB}}{R^6_{AB}}\right) f^{D2}_{damp}(R_{AB}) \tag{2.30}$$

At short range, this function is damped, where R^{-6}_{AB} diverges, via

$$f^{D2}_{damp}(R_{AB}) = [1 + e^{-d(\frac{R_{AB}}{R_{0,AB}}-1)}]^{-1} \tag{2.31}$$

This also helps avoid double-counting effects related to electron correlation, as the correlation of short- to medium-range has been incorporated using the density functional. Here, quantity $R_{0,AB}$ denotes the van der Waals radii sum of atoms A and B, whereas d is used for an additional parameter. The atomic coefficient $\mathrm{C}_{6,A}$ is known as the primary parameter, and the geometric means of these parameters provides the pairwise parameters used in Equation 2.30.

$$C_{6,AB} = (C_{6,A}C_{6,B})^{\frac{1}{2}} \tag{2.32}$$

The expression of the DFT-D2 total energy is

$$E_{DFT-D2} = E_{KS-DFT} + E_{disp}^{D2} \tag{2.33}$$

2.8 Approaches used for calculating materials properties

Stress-Strain approach

In order to calculate elastic constants of materials accurately, two approaches usually are being used: energy-strain and stress-strain approach. Among these methods, the stress-strain process depends on using lesser strain sets with more accurate calculations of stresses. This leads to the need for a higher energy cut-off with a denser k-mess. This method is usually preferred instead of its expensive computational nature due to its straightforward implementation. In this regard, the elastic tensor is evaluated by obtaining the stress tensor related to several distorted crystal structures and the strain-stress relationship. Considering the fixed lattice parameters, internal coordinates have been optimized in each run. The accuracy of obtained elastic constant values depends significantly on the achieved convergence of each distorted crystal structure.

Density functional perturbation theory (DFPT)

DFPT or linear response method is considered the most desired approach for calculating lattice dynamics of materials through ab initio calculation. Analytical computation of the second order derivative of the total energy concerning a certain perturbation is known to be provided by this method. Based on the type of perturbation, different properties of materials are being evaluated. The phonon frequencies and the associated dynamical matrix can be obtained from the perturbation of ionic positions. The force constants matrix is obtained using the differentiation of Hellmann-Feynman forces for each atom regarding ionic coordinates. This procedure clearly explains that the force constants matrix is dependent on the electronic charge density at its ground-state and its linear response related to an atomic distortion. As the formalism of density functional theory maintains the variational principle, the second-order energy change is dependent on the first-order change of the electronic charge density. The formalism of DFT and DFPT is found to be very much similar to each other in this respect. As DFT equations can be solved by implementing total energy minimization. Solution of DFPT problem can also be achieved by reducing the second-order perturbation of total energy, known to be associated to the first-order density, potential and wavefunction change, and can be implemented through

$$\begin{aligned} E^{(2)} = \sum_{k,n} [\langle \Psi^{(1)}_{k,n} | H^{(0)} - \epsilon^{(0)}_{k,n} | \Psi^{(1)}_{k,n} \rangle + \langle \Psi^{(1)}_{k,n} | V^{(1)} | \Psi^{(0)}_{k,n} \rangle + \langle \Psi^{(0)}_{k,n} | V^{(1)} | \Psi^{(1)}_{k,n} \rangle] \\ + \frac{1}{2} \int \frac{\delta^2 E_{xc}}{\delta n(r) \delta n(r')} n^{(1)}(r) n^{(1)}(r') + \sum_{k,n} \langle \Psi^{(0)}_{k,n} | V^{(2)} | \Psi^{(0)}_{k,n} \rangle \end{aligned} \tag{2.34}$$

Electronic band structure correction methods

In the end, different approaches have been discussed in order to calculate the more accurate electronic band structure of studied materials. **Tran-Blaha-modified Becke-Johnson (TB-mBJ) potential**

There are various approaches for calculating the exact experimental bandgap of any material that lies inside or outside the framework of KS formalism. The Becke and Johnson potential (BJ) is a computationally less expensive semilocal method within the KS framework.

$$v^{BJ}_{x,\sigma}(\mathbf{r}) = v^{BR}_{x,\sigma}(\mathbf{r}) + \frac{1}{\pi}\sqrt{\frac{5}{6}}\sqrt{\frac{t_\sigma(\mathbf{r})}{\rho_\sigma(\mathbf{r})}} \tag{2.35}$$

The self-consistent implementation of this BJ exchange potential into wien2k code has provided the platform for calculating nearly exact bandgap of periodic solids. However, this potential improves LDA or GGA bandgap the improvement was diminished. This limitation of BJ potential can be removed by using the modified version of this potential, TB-mJ.

$$v^{TB-mBJ}_{x,\sigma}(\mathbf{r}) = c v^{BR}_{x,\sigma}(\mathbf{r}) + (3c-2)\frac{1}{\pi}\sqrt{\frac{5}{6}}\sqrt{\frac{t_\sigma(\mathbf{r})}{\rho_\sigma(\mathbf{r})}} \tag{2.36}$$

This could be achieved by introducing a parameter that changes the relative contribution of terms of BJ potential.

$$c = \alpha + \beta \left(\frac{1}{V_{cell}} \int_{cell} \frac{|\delta\rho(\mathbf{r}')|}{\rho(\mathbf{r}')} d^3r' \right)^{\frac{1}{2}} \tag{2.37}$$

As this TB-mBJ potential cannot be written as a functional derivative, this potential cannot be considered for force calculation and is the main drawback.

GW approximation

The significant underestimation in the DFT band gap is attributed to the fact that quasi-particle excitations are being neglected in such calculations. In this connection, eigenvalue correction of the Kohn-Sham states can be obtained by implementing the Green function techniques along with the GW approximation related to electronic self-energy, $\Sigma = -i\hbar GW\Gamma$. This Σ contains all many-body effects of correlation and exchange beyond the Hartree potential and considers all the dynamic processes related to many-electron system. The proper understanding of this GW approximation can be obtained from the qusiparticle equation which is expressed as

$$(T + V_{ext} + V_h)\phi_{nk}(\mathbf{r}) + \int d\mathbf{r}\Sigma(\mathbf{r}, \mathbf{r}', \omega = E_{nk})\phi_{nk}(\mathbf{r}') = E_{nk}\phi_{nk}(\mathbf{r}) \tag{2.38}$$

Here, the kinetic energy, the external potential of the nuclei, and the Hartree potential have been denoted by T, V_{ext}, and V_h, respectively. E_{nk} and ϕ_{nk} denote the quasiparticle energies and the associated states. In this regard, it can be said that the many-body self-energy Σ has replaced the exchange-correlation potential of DFT in the above equation. As this self-energy Σ is dependent on the the Green's function G, the screened Coulomb interaction W, the irreducible polarizability χ, and the irreducible vertex function Γ, a self-consistent procedure should be used. These functions can be obtained using Hedin equations and are given as follows:

$$G(1,2) = G_0(1,2) + \int d(3,4)G_0(1,3)\sum(3,4)G(4,2) \tag{2.39}$$

$$\chi(1,2) = \int d(3,4)G(1,3)G(4,1)\Gamma(3,4;2) \tag{2.40}$$

$$W(1,2) = V(1,2) + \int d(3,4)V(1,3)\chi(3,4)W(4,2) \tag{2.41}$$

$$\Sigma(1,2) = \int d(3,4)G(1,3)\Gamma(3,2;4)W(4,1) \tag{2.42}$$

$$\Gamma(1,2;3) = \delta(1,2)\delta(1,3) + \int d(4,5,6,7)\frac{\delta\sum(1,2)}{\delta G(4,5)}G(4,6)G(7,5)\Gamma(6,7;3) \tag{2.43}$$

The bare Coulomb interaction has been denoted through V and the numbers have been used to denote position and time such as $1 = (\mathbf{r}_1, t_1), 2 = (\mathbf{r}_2, t_2), ...$ Though these equations are known to be exact, approximations are required for solving real systems. This can be achieved by using the bare vertex instead the vertex function and is known as the GW approximation.

$$\Gamma(1,2;3) = \delta(1,2)\delta(1,3) \tag{2.44}$$

This leads to the reduced equations for polarizability and self-energy

$$\chi(1,2) = G(1,2)G(2,1) \tag{2.45}$$

$$\sum(1,2) = G(1,2)W(2,1) \tag{2.46}$$

In this approximation, the Green's function and the screened potential are normally considered. However, these equations are practically solved in reciprocal space

$$W_{GG'}(\mathbf{q},\omega) = [\delta_{GG'} - \chi_{GG'}(\mathbf{q},\omega)V_{GG'}(\mathbf{q})]^{-1}V_{GG'}(\mathbf{q}) \tag{2.47}$$

$$G_{GG'}(\mathbf{q},\omega) = [\delta_{GG'} - \sum_{GG'}(\mathbf{q},\omega) G^{(0)}_{GG'}(\mathbf{q})]^{-1} G^{(0)}_{GG'}(\mathbf{q}) \tag{2.48}$$

Principally these equations have to be solved in a self-consistent way and the non-interacting Green's function $G^{(0)}$ can be obtained in the first iteration.

$$G^0(\mathbf{r},\mathbf{r}',\omega) = \sum_{nk} \frac{\phi^{*(0)}_{nk}(\mathbf{r})\phi^{(0)}_{nk}(\mathbf{r}')}{\omega - E^{(0)}_{nk}} \tag{2.49}$$

Here $\phi^{(0)}_{nk}$ and $E^{(0)}_{nk}$ are one-electron orbital set and the corresponding energies. As a next step, $\chi^{(0)}$ is obtained, followed by $W^{(0)}$ and $\Sigma^{(0)}$. This tells that a first guess of one-electron eigen-system is required for GW calculations, which is normally taken from a preceding DFT calculation. Principally, all steps should be repeated by updating the Green's function using the Dyson equation in each iteration till the self-consistency is reached.

References

[1] M. Born and J.R. Oppenheimer, Ann. Phys. 84, 457 (1927).

[2] D.R. Hartree, Proc. Cambridge Phil. Soc. 24, 89 (1928).

[3] V. Fock, Z. Physik 61, 126 (1930).

[4] R.G. Parr, Ann. Rev. Phys. Chem. 34, 631 (1983).

[5] T. Ziegler, Chem. Rev. 91, 651 (1991).

[6] P. Geerlings, F.D. Proft and W. Langenaeker, Chem. Rev. 103, 1793 (2003).

[7] R.O. Jones and O. Gunnarsson, Rev. Mod. Phys. 61, 689 (1989).

[8] R.G. Parr and W. Yang, Density-Functional Theory of Atoms and Molecules (Oxford University Press, New York, 1989).

[9] M.R. Dreizler and E.K.U. Gross, Density Functional Theory: An Approach to the Quantum Many-Body Problem (Springer, Berlin, 1990).

[10] L.H. Thomas, Proc. Camb. Phil. Soc. 23, 542 (1927).

[11] E. Fermi, Rend. Accad. Lincei. 6, 602 (1927).

[12] P. Hohenberg and W. Kohn, Phys. Rev. 136, B864 (1964).

[13] W. Kohn and L.J. Sham, Phys. Rev. 140, A1133 (1965).

[14] J.P. Perdew, A. Zunger, Phys. Rev. B. 23, 5048 (1981).

[15] J.P. Perdew, K. Burke, M. Ernzerhof, Phys. Rev. Lett. 77, 3865 (1996).

[16] P.E. Blöchl, Phys. Rev. B 50, 17953 (1994).

[17] D.R. Hamann, M. Schlüter and C. Chiang, Phys. Rev. Lett. 43, 1494-1497 (1979).

[18] D. Vanderbilt, Phys. Rev. B 41, R7892 (1990).

[19] K. Laasonen, R. Car, C. Lee, and D. Vanderbilt, Phys. Rev. B 43, 6796 (1991).

[20] K. Laasonen, A. Pasquarello, R. Car, C. Lee, and D. Vanderbilt, Phys. Rev. B 47, 10142 (1993).

[21] G. Kresse and J. Furthmüller, Phys. Rev. B 54, 11169 (1996).

[22] P. Giannozzi et al., J. Phys. Condens. Matter, 21, 5502 (2009).

CHAPTER 3

Crystalline properties of transition metal oxides

A comparative study of crystalline properties of transition metal oxides thallium pertechnetate and perrhenate has been presented. The structural and vibrational properties along with IR and Raman frequencies of these materials are mainly discussed. DFT total energy calculation has been found to be very helpful for finding the correct ground state structure of $TlReO_4$. *Inclusion of vdW correction to the standard DFT calculation is found to improve the agreement with the obtained structural and vibrational properties for both materials. Born effective charge values provide knowledge about the bonding nature present in these materials. Calculations of zone-center phonon frequencies for both materials are mainly found to be divided into three regions following the usual trend of* ABO_4 *type materials. The most substantial infrared peak is associated with the internal asymmetric stretching of* BO_4, *whereas the strongest Raman peak is associated with the internal symmetric stretching of* BO_4.

3.1 Introduction

ABO_4 type ternary transition metal oxides where A and B cations can be found in multivalent states are known to crystallize in various crystalline structures. Due to this kind of structural malleability present in these materials, a diverse range of electronic as well as physical properties along with a wide variety of applications of these compounds are well known. As a result, study of these materials has obtained utmost interest from Earth Science [1], Material Science [2, 3, 4] and also from fundamental physics point of view [5]. In this connection, silicates, arsenates, phosphate, chromates and vanadates are normally found in zircon type structure [6] whereas phosphates and arsenates are found in quartz type of structures [7]. Germanates, molybdates, tungstates and periodates are found in isomorphic to scheelite [8] and molybdates, tungstates and tantalates are found in wolframite structure [9]. Other important type of structures is monazite [12], M-fergusonite, which is monoclinic distorted scheelite [10] and pseudo scheelite, which is orthorhombic distorted scheelite [11] structure. These oxides have shown wide range of applications as scintillators ($CdWO_4$ and $PbWO_4$), phosphors ($ZrGeO_4$ and $HfGeO_4$), good laser-host materials ($BaWO_4$, YVO_4 and $GdTaO_4$) and in battery use ($CaMoO_4$ and $SrWO_4$) [13]. These sorts of materials have also found their use as nuclear waste storage processes as well as in photocatalysis applications [14, 15, 16, 17, 18]. Oxides of Ru and Os with scheelite structure, d^1 electron configuration and with TM cations in distorted tetrahedron are mainly known for special interest related to magnetic properties. These sorts of systems provide a great deal of information in between spin, spin-orbit coupling and crystal field present in those systems [19, 20, 21]. Along with these diverse technological applications, these materials are also known for showing pressure-induced structural transformation and hence exist in different polymorphic phases [13, 14]. A combined study using quantum chemistry-based computer simulation along with proper crystal-chemistry arguments has shown fruitful for having a proper understanding of high-pressure behaviour of these materials [22, 23]. In this connection, the main goal of this chapter is to provide a detailed knowledge of the structure-property correlation of pertechnetates and perrhenates by means of quantum chemistry-based density functional theory calculation. These families of ABO_4 type transition metal oxides are a less studied class of materials, and this kind of study on pertechnetates and perrhenates will contribute to the understanding influence of cation substitution on the structural properties of ABO_4 type materials [23, 24]. Among synthesized elements, technetium (Tc) is known for being the first-ever synthesized transition metal which is the lightest element and shows radioactivity. Instead of its main involvement in nuclear processes, application of this element can also be found as a corrosion inhibitor in the steel industry, as environmental water tracer [25, 26] and as low-temperature superconductor [27]. Understanding of heavy element solar production can also be obtained from the presence of this element in a variety star spectrum [28, 29]. By providing the knowledge of oxyanion formation in between rhenium and chromium transition metals, it fills the knowledge gap of transition metals which is very important in terms of chemistry point [30]. Though this element is known as synthesized, ^{99}Tc is known to be the natural, most abundant and common isotope of its 21 isotopes which is an appreciable by-product in uranium and plutonium fission reaction. This isotope is also known to form a daughter product from its metastable isomer ^{99m}Tc, which found its important place in radiopharmaceutical [31]. Though the half-life of ^{99m}Tc is 6h, half-life of ^{99}Tc is nearly 2.1×10^5 years with 0.29 MeV β_{max} energy. Hence being a weak beta emitter, ^{99}Tc is found to be a major source of radioactivity in spent nuclear materials

[32, 33]. Oxidation state 7^+, among other states ranging from 1^- to 7^+ state, is found to be responsible for the formation of pertechnetate anion (TcO_4^-), which is a dominant form of this element in an oxidizing environment. This form is known to adsorb onto the mineral surface and shows high mobility in aqueous solution and hence considered as significant environmental hazard by posing challenges regarding the management of this nuclear waste. This is the sole reason for carrying out research in solution rather than solid phase. First isolated Tc oxides were seen to crystallize in tetragonal scheelite type $CaWO_4$ crystal structure with $I4_1/a$ space group [34, 36] (NH_4TcO_4, $KTcO_4$ and $AgTcO_4$) and orthorhombic structure with space group Pnma ($CsTcO_4$) [37, 38]. Though the study on $RbTcO_4$ is very less except from the context of alkali pertechnetates, it has been confirmed to crystallize in tetragonal structure [39, 40, 41, 42]. Due to its link with Tc volatility at the time of vitrification, more attention has been received by $CsTcO_4$ [43, 44]. Also, reports regarding temperature-induced phase transition of $CsTcO_4$ and $TlTcO_4$ from orthorhombic to tetragonal phase can be seen in literature [45]. Alkali-metal pertechnetate salts are reported to be isomorphic with analogous rhenium salts [46] and reported chemical properties for both these oxides are found to be very similar. $AReO_4$ type perrhenates (A = alkali metal, silver, thallium or ammonium) crystallize in scheelite or pseudo-scheelite structure and are famous for showing temperature or pressure-induced phase transition in these materials [47]. Among these perrhenates, thallium perrhenate has obtained special attention for its high pressure structural as well as an electronic phase transition. A great amount of study based on electron diffraction [48], X-ray diffraction (XRD) [49, 50], Raman spectroscopy [51, 52] and x-ray near-edge absorption spectroscopy [53] have already been carried out on this material which confirms that it crystallizes in pseudo scheelite structure at normal conditions [47]. These studies reveal that this material undergoes temperature-induced phase transition at 200 and 400 K [49, 54] and pressure-induced phase transition at 0.5, 1.9 and 9.7 GPa [52, 55]. A colour change of this material is caused by the last pressure-dependent phase transition at 9.7 GPa [52]. Though an electronic transition mechanism has been proposed regarding this phenomenon, very less information is available till now of properties of this material [51, 52, 53]. In case of $TlTcO_4$ also, multiple characterization techniques, including X-ray absorption spectroscopy (XAS), Raman spectroscopy, and X-ray diffraction (XRD), have been used to determine the chemistry of ^{99}Tc in technetium-bearing glasses [56, 57, 58, 59, 60, 61, 62, 63]. Recently, $KTcO_4$ and $NaTcO_4$, two other common Tc standards, have been used in Raman analysis of Tc-doped glasses to investigate ion exchange between pertechnetate species in glass [57]. Another significant use of alkali pertechnetates is the application of $KTcO_4$ as a common initial material in synthesizing Tc-based radiopharmaceuticals. A lot of modern study of the structure along with localized chemistry of solid sodium, potassium, rubidium, and caesium pertechnetates have been performed, using X-ray absorption spectroscopy (XAS), extended Xray absorption

fine structure (EXAFS) analysis, including Tc K-edge X-ray absorption near-edge spectroscopy (XANES), high-resolution Raman spectroscopy, neutron diffraction (ND), and ^{99}Tc solid-state nuclear magnetic resonance (NMR). The Raman spectra of pertechnetate (TcO_4^-) in solution have been made by various studies [64, 65, 66, 67, 68, 69]. However, there have been few reports of the Raman spectrum of $KTcO_4$ [66, 70, 71] and only one of $NaTcO_4$ [72]. Although these earlier reported experimental results provide a lot of information about these materials, extensive research on these materials is not yet done. Such as the crystal and vibrational properties of $TlReO_4$ and almost all crystalline properties of $TlTcO_4$ have still not been evaluated correctly. At the same time, the lack of theoretical studies of these compounds makes it very difficult to interpret the available experimental results. In this connection, a systematic density functional theory based theoretical study can provide a deep insight into the physical properties of these compounds [73, 74, 75, 76, 77]. As this kind of theoretical study has not been reported till now for studied materials, we think it is timely to carry out the theoretical calculation on these materials. In order to execute our theoretical study, basic crystal structure information of these materials have been used as the input in our calculation. After obtaining the correct theoretical ground-state crystal structure, we have performed other calculations for getting other properties of these materials.

This chapter has been arranged as: computational details involved in this study are discussed in the next section. After that, the structural and dynamical properties are presented and discussed. Finally, the conclusions of this study are presented.

3.2 Computational Details

Density Functional Theory (DFT) [78, 79, 80] based plane-wave pseudo-potential approach (PW-PP) implemented in the CASTEP code [81, 82] has been considered to execute the theoretical study of structural property as well as vibrational properties of $TlTcO_4$ and $TlReO_4$. In addition, with local density approximation (LDA) [83] and generalized gradient approximation (GGA) [84, 85] for treating electronic exchange-correlation interaction, van der Waals (vdW) interaction has also been considered through TS scheme [86] which is well-known for incorporating polarizability of inter-atomic bonds for obtaining correct structural parameters [84, 86]. The structural properties of $TlTcO_4$ have been calculated using ultra-soft pseudo-potential with 600 eV energy cut-off and k-points spacing of 0.02 $Å^{-1}$ with k-grids of 7×7×3. Convergence criteria for obtaining its ground state structure were set to < 0.01 eV $Å^{-1}$ as force minimization criterion and $< 5\times10^{-6}$ eV as energy minimization criterion on each atom. In case of $TlReO_4$, the norm-conserving pseudo-potential method (NC-PP) have been implemented through the Monkhorst-Pack scheme, where 800 eV energy cut-off is used throughout the calculations. Brillouin zone sampling for this material was done using Monkhorst-Pack scheme [87] with the k-point spacing of 0.03 $Å^{-1}$ and with k-grids of 2×3×6 for the monoclinic, 6×6×3 for the tetragonal and 6×6×3 for the hypothetical orthorhombic $TlReO_4$ structures. Similar convergence criteria as $TlTcO_4$ have been implemented for obtaining ground-state structure. Geometry optimization of these structures have been obtained using Broyden–Fletcher–Goldfarb–Shanno (BFGS) algorithm [88]. After obtaining the exact theoretical ground-state crystal structure of these materials, density functional perturbation theory (DFPT) based on linear response theory was used to compute the Born effective charge (BEC) tensor and zone-centered phonon frequencies of the orthorhombic $TlTcO_4$ and the low- and room-temperature phases of $TlReO_4$.

3.3 Results and Discussion

3.3.1 Comparative understanding of structural property of $TlReO_4$ and $TlTcO_4$

$TlReO_4$ was initially reported to crystallize in orthorhombic pseudo-scheelite type structure under ambient condition with *Pnma* space group [11, 50]. Our recent report[100] has shown that it actually crystallizes in monoclinic crystal structure with $P2_1/c$ space group at room temperature rather than orthorhombic structure which supports the findings of Rogner and Range [8]. This study on $TlReO_4$ has also shown that it transforms to tetragonal crystal structure with $I4_1/a$ space group at high and low temperature. The schematical representation of these structures are given in the Figure 3.1. Here, tetragonal $TlReO_4$ at 50 K, monoclinic $TlReO_4$ at 290 K and tetragonal $TlReO_4$ at 450 K were shown by Figure 3.1a, 3.1c and 3.1d, respectively. Figure 3.1b represents the earlier proposed orthorhombic crystal structure of $TlReO_4$. The only common feature among these structures is that the Tl coordination polyhedra are connected by isolated ReO_4 tetrahedra. The temperature effect on these tetrahedra is significantly less as they are rigid. Also, distortion can be seen in these units, with an average distance between Re and O atoms being near to 1.66 Å. Table 3.1 represents structural information of these phases from our reported result as well as earlier reports for orthorhombic phase [11]. The possible reason regarding mis-assignment of crystal structure of $TlReO_4$ in case of previous reports could be as follows [11, 24, 90]. The orthorhombic structure of the earlier studies is known to be symmetrized version of our monoclinic structure. Actually, this structure is isomorphic to $CsReO_4$ crystal structure [89]. A relation related to group-subgroup can be seen in between these structures where monoclinic ($P2_1/c$) $TlReO_4$ forms a subgroup of *Pnma* orthorhombic structure. In this connection, one can find that a and c unit-cell parameters of the orthorhombic structure are identical to b and c parameters of the monoclinic structure. It can also be seen that the unit-cell parameter a of monoclinic $TlReO_4$ found to be three times with respect to the unit-cell b parameter of orthorhombic structure and monoclinic angle β is nearly equal to 90°. So monoclinic structure can be considered as superstructure of orthorhombic structure and can be obtained using a klassengleiche subgroup transformation by multiplying orthorhombic unit-cell parameter

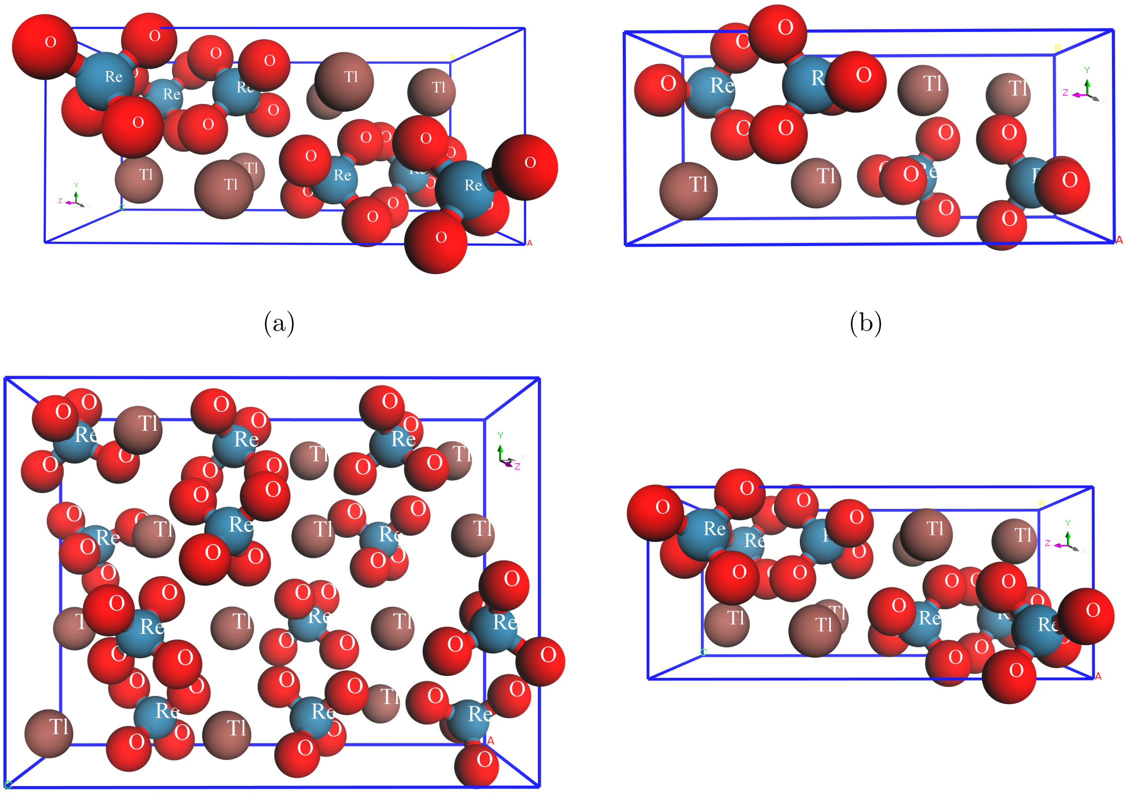

(a)

(b)

(c)

(d)

Figure. 3.1 Crystal structure of $TlReO_4$ in different conditions. (a) denotes the crystal alignment of $TlReO_4$ at 50 K (Tetragonal), (b) shows the hypothetical orthorhombic arrangement of $TlReO_4$ as reported in Ref.[11], (c) Shows the monoclinic crystal arrangement observed at room temperature and (d) depicts the tetragonal arrangement of $TlReO_4$ at 450 K.

b with 3 and subsequent breaking of symmetry by means of translationengleighe transformation. This reduces symmetry to monoclinic from orthorhombic structure $P2_1/c \subset Pnma$. Due to this reason, common Bragg peaks could have been seen for both structures leading to misidentification of room temperature crystal structure in previously reported low-resolution diffraction studies. These kinds of experimental discrepancies are known to be well addressed through DFT based theoretical study. That is the sole reason to perform total-energy DFT calculations for having a deep insight about this material. The effect of different exchange-correlation functional along with van der Waals (vdW) interaction have been tested initially for both these before mentioned structures of $TlReO_4$ at room temperature. The energy difference between these structures is found to be 93.52 meV using LDA functional where monoclinic crystal structure shows more favourable energetically than previously reported orthorhombic structure. In a similar way, GGA functional PBE and vdW corrected PBE + TS methods also support the fact obtained from LDA

Table 3.1 Refined structural parameters for $TlReO_4$ at 50, 290 and 450 K. The values previously reported for the proposed orthorhombic structure, taken from Ref.[11] are also shown. The numbering scheme of the various cations correspond to the values given by Chay et al.[89]

Parameters	Orthorhombic	50 K phase	290 K phase	450 K phase
Space group	$Pnma$	$I4_1/a$	$P2_1/c$	$I4_1/a$
Atoms/cell	24	24	72	24
f.u./cell	4	4	12	4
a (Å)	5.62	5.79	17.40	5.78
b (Å)	5.79	5.79	13.31	5.78
c (Å)	13.30	12.87	5.63	13.40
β (°)			90.169	
V (Å^3)	432.92	430.99	1304.06	447.34
Tl1	(0.025,0.75,0.127)	(0.0,0.25,0.125)	(0.079,0.372,0.472)	(0.0,0.25,0.625)
Tl2		(0.247,0.627,0.480)		
Tl3		(0.414,0.373,0.497)		
Re1	(0.038,0.25,0.380)	(0.0,0.25,0.625)	(0.251,0.375,-0.017)	(0.0,0.25,0.125)
Re2		(0.418,0.625,-0.001)		
Re3		(0.084,0.615,0.027)		
O11	(0.822,0.25,0.084)	(0.119,0.036,0.201)	(0.281,0.456,-0.223)	(0.088,0.025,0.198)
O12	(0.856,0.25,0.474)		(0.211,0.436,0.215)	
O13	(0.012,0.515,0.686)		(0.186,0.301,-0.154)	
O14			(0.324,0.302,0.038)	
O21			(0.3815,0.5531,0.230)	
O22			(0.451,0.550,-0.236)	
O23			(0.487,0.705,0.109)	
O24			(0.347,0.703,-0.110)	
O31			(0.173,0.668,-0.004)	
O32			(0.006,0.690,-0.062)	
O33			(0.075,0.582,0.323)	
O34			(0.082,0.508,-0.139)	

functional except the different energy differences of these structures, which are 59.9 meV from PBE and 24.63 meV from PBE + TS. Our calculations using DFT validated our XRD experiments and also provided well described structural details. As it is well known

Table 3.2 Calculated total energy per formula unit (in eV) of the previously proposed orthorhombic and experimentally observed monoclinic structures of $TlReO_4$.

	Orthorhombic	Monoclinic
LDA	-3364.23198	-3364.32550
PBE	-3369.91988	-3369.97978
PBE+TS	-3371.11530	-3371.13993

that temperature cannot be included in the DFT calculation, we have not considered the second transition from monoclinic to the tetragonal structure. Though it can be well speculated that the high symmetry tetragonal phase could be possible by entropic effect at high temperature [91, 92]. Structural parameters obtained from our calculations have been given in Tables 3.3 and 3.4. The main limitation known for normal LDA and GGA functionals is to produce underestimated and overestimated structural parameters.

Table 3.3 Calculated structural properties of low-temperature tetragonal phase of $TlReO_4$ with different functionals.

Tetragonal $TlReO_4$ (50 K phase)

Parameters	LDA	GGA	GGA+TS	Experimental
a (Å)	5.65	5.94	5.77	5.787
b (Å)	5.65	5.94	5.77	5.787
c (Å)	12.05	13.22	12.90	12.872
Volume (Å^3)	384.60	466.64	429.98	431.00
Tl(x,y,z)	(0.0,0.25,0.625)	(0.0,0.25,0.625)	(0.0,0.25,0.625)	(0.0,0.25,0.625)
Re(x,y,z)	(0.0,0.25,0.125)	(0.0,0.25,0.125)	(0.0,0.25,0.125)	(0.0,0.25,0.125)
O(x,y,z)	(0.138,0.034,0.208)	(0.117,0.037,0.201)	(0.115,0.027,0.203)	(0.119,0.036,0.201)

Table 3.4 Calculated structural properties of room-temperature monoclinic phase of $TlReO_4$ with different functionals.

Monoclinic $TlReO_4$ (290 K phase)

Parameters	LDA	GGA	GGA+TS	Experimental
a(Å)	16.855	17.765	17.446	17.396
b(Å)	12.431	13.460	13.009	13.313
c (Å)	5.475	5.841	5.644	5.631
β (°)	90.851	90.726	90.117	90.169
Volume (Å^3)	1147.09	1396.65	1280.82	1304.06

Obtained underestimated structural parameters are found in a comparable range with reported other similar oxides [10]. So, to obtain the correct structural parameters of this material, vdW corrected TS scheme along with PBE functional has been considered, which is found to produce theoretical results of structural parameters of this material in good agreement with experimentally reported results. Though one can think of including spin-orbit coupling contribution energy for obtaining more accurate structural parameters due to the presence of Re atom in the system, it has been observed that the SOC does not affect much in the case of structural properties for similar compounds [93]. Instead, this kind of effect contribute more to electronic band structure and associated electronic and optical properties. As a result, we have not considered the SOC effect in calculating the structural properties of this material.

In the case of $TlTcO_4$, also we did not consider the SOC effect for calculating structural parameters due to the above-mentioned reason. Unlike $TlReO_4$, $TlTcO_4$ does not report to have any structural discrepancies, and it is found to crystallize in orthorhombic *Pnam* crystal structure which is similar to $CsTcO_4$ but different from other mostly crystallized pertechnetate compounds crystallized in $CaWO_4$ type scheelite structure. Figure 3.2 shows the crystal structure of $TlTcO_4$ in different orientation. Initially, the experimental crystal structural details have been considered as the input parameter for our calculations where we have considered LDA and GGA functional like $TlReO_4$ to incorporate exchange-correlation interaction. Similar to $TlReO_4$ calculations, incorporation van der Waals interaction has also been considered for this material. Structural parameters for $TlTcO_4$ obtained from our calculations at ambient condition and using various schemes along with experimental results are given in Table 3.5. The results provided in this table clearly shows the expected trend of underestimation and overestimation of structural parameters obtained using LDA and GGA functionals, respectively. Incorporation of van der Waals correction with GGA shows a decrease in volume error, on the other hand it is found to be increased with LDA functional. From all possible use of functional, the combination of PBE functional and TS scheme shows the more accurate structural properties of this material like $TlReO_4$.

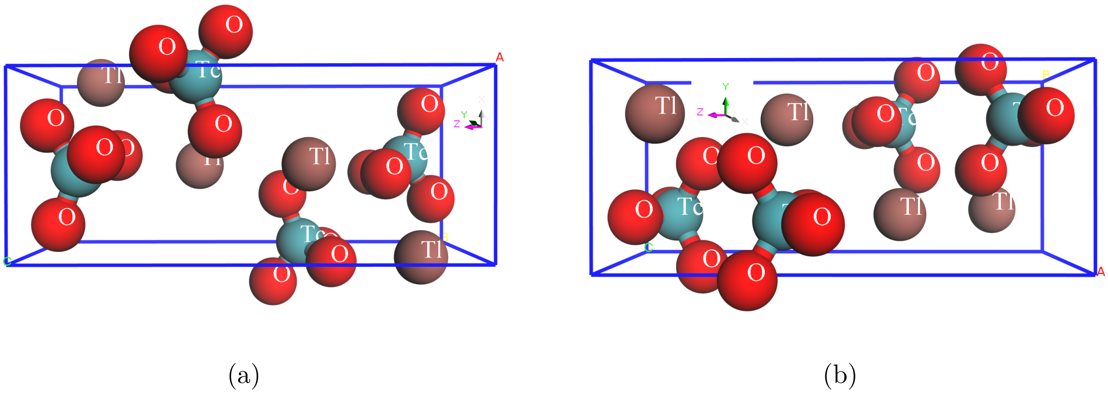

(a)

(b)

Figure. 3.2 Crystal structure of $TlTcO_4$ in xz-plane (a) and in yz-pane (b)

3.3.2 Born effective charge (BEC) of $TlReO_4$ and $TlTcO_4$ and bonding nature

The Born effective charge (BEC) is known as a very useful rudimentary quantity which provides a profound understanding of material properties particularly related to vibrational as well as optical properties of such material. Mainly the coupling between lattice displacement and electrostatic field is defined by this quantity. Computation of this quantity was done using the linear response method established in the CASTEP code for the above-mentioned materials. This calculation is found to satisfy well known acoustic sum

Table 3.5 Ground state structural details of $TlTcO_4$ with different functional as well as with other van der Waals corrected schemes and experimental data:

	Expt.	LDA	LDA+OBS	PBE	PBE+TS	PW91	PW91+OBS
Space Group	*Pnma*						
atoms	24						
f.u./cell	4						
a (in Å)	5.49536	5.19	5.12	5.76	5.51	5.75	5.64
b (in Å)	5.74218	5.62	5.61	5.94	5.86	5.93	5.88
c (in Å)	13.4505	12.92	12.85	13.73	12.98	13.67	13.60
Vol (in Å^3)	424.75	377.24	369.13	469.31	419.01	465.46	451.31
Error %		-11.19%	-13.10%	+10.49%	-1.35%	+9.59%	+6.25%

rule: $\sum_k Z^*_{k,ij} = 0$. Results of this calculation are given in the Table 3.6, 3.7 and 3.8. All components of BEC for O1 atoms in the low-temperature phase of $TlReO_4$ show non-zero values, whereas off-diagonal components except Z^*_{12} and Z^*_{21} for Tl and Re atoms show no contribution. The result present in these tables clearly shows a nearly doubled BEC of Tl atom compared to their nominal charge. A large reduction of xx, yy and zz components of BECs from their nominal charge of Re atom can also be observed. It is also found that $Z^*_{11} = Z^*_{22} \neq Z^*_{33}$ relation is true for Tl and Re of $TlReO_4$. In the case of monoclinic $TlReO_4$, all components of BEC for all elements are found to be present. Instead of the presence of small differences, the BEC value of crystallographically different Tl and Re atoms in monoclinic crystal matches quite well to that the values obtained for tetragonal structure, and this shows that the charge transfer between different present atoms did not take place during the transition [52]. The presence of the mixed ionic and covalent character of bonding is pretty much evident in studied crystals as the same can be suggested from the deviation of BEC's of constituting elements from their nominal charges. Normally covalent character of any bond is interpreted as charge transfer due to atomic displacement of those considered bonds [94, 95]. In this context, a notable amount of deviation in BEC of all present elements of $TlReO_4$ from their nominal charge helps us to make a conclusion that both the $TlReO_4$ phases possess appreciable covalent nature. A huge reduction of the nominal charge of Re atom in ReO_4 anion confirms the strong

Table 3.6 Calculated BECs of Tl, Re and O atoms in low-temperature tetragonal phase of $TlReO_4$.

Atoms	Ionic	Z^*_{11}	Z^*_{22}	Z^*_{33}
Tl1	1	1.93	1.93	2.07
Re1	7	3.36	3.36	3.33
O1	-2	-0.94	-1.71	-1.35

covalent character of this block. However, the presence of a smaller reduction of the nominal charge of oxygen atoms introduces ionicity in this block. The earlier comment is supported by the fact the off-diagonal elements of oxygen atoms are present. Also, the nearly doubled value of BEC of Tl atoms signals towards a possible hybridization of Tl and nearby oxygen atoms.

Table 3.7 Calculated BECs of Tl, Re and O atoms in room-temperature monoclinic phase of $TlReO_4$.

Atoms	Ionic	Z^*_{11}	Z^*_{22}	Z^*_{33}
Tl1	1	2.08	1.98	1.89
Tl2	1	1.90	2.16	1.88
Tl3	1	1.89	2.08	1.90
Re1	7	3.28	3.22	3.33
Re2	7	3.32	3.40	3.44
Re3	7	3.20	3.03	2.92
O11	-2	-0.81	-1.55	-1.67
O12	-2	-0.97	-1.17	-1.73
O13	-2	-1.61	-1.40	-0.91
O14	-2	-1.83	-1.29	-0.85
O21	-2	-0.98	-1.32	-1.68
O22	-2	-0.96	-1.40	-1.67
O23	-2	-1.69	-1.31	-0.97
O24	-2	-1.68	-1.39	-1.03
O31	-2	-2.07	-1.14	-0.66
O32	-2	-1.81	-1.28	-0.78
O33	-2	-0.74	-0.78	-2.39
O34	-2	-0.53	-1.85	-1.02

Table 3.8 Calculated BECs of Tl, Tc and O atoms in orthorhombic crystalline phase of $TlTcO_4$.

Atoms	Ionic	Z^*_{11}	Z^*_{22}	Z^*_{33}
O1	-2	-0.63	-2.01	-1.23
O2	-2	-2.43	-0.56	-0.82
O3	-2	-0.97	-0.33	-1.69
Tc	7	2.78	2.96	2.78
Tl	1	1.87	1.95	2.19

A similar trend can also be observed in the case of BEC values of $TlTcO_4$, where the

Tl atom shows a nearly doubled value of BEC with respect to its nominal charge. A significant amount of reduction of charge from its nominal charge can be seen for the Tc atom. In this case a large deviation of BEC of Tc can be observed from its nominal charge in comparison to the Re atom of $TlReO_4$ indicates a more covalent nature of TcO_4 block than ReO_4 unit. Also, the highly anisotropic nature of BEC of this material can be found, which shows the relation $Z^*_{11} \neq Z^*_{22} \neq Z^*_{33}$ for all present elements of $TlTcO_4$. In comparison to Tl atoms of $TlReO_4$, Tl atoms of $TlTcO_4$ shows the higher value of BEC and hence can be considered to have more hybridization of Tl by its neighbouring oxygen atoms, which is well anticipated as this TcO_4^- anion is known to adsorb onto the mineral surface and shows high mobility in aqueous solution.

3.3.3 Vibrational properties of $TlReO_4$ and $TlTcO_4$

Optimized crystal structures with vdW corrected PBE + TS scheme were used for calculating zone-centered phonon frequencies together with IR and Raman frequencies of these studied materials. In this consideration, linear response theory realized through density functional perturbation theory (DFPT) has been used. As the primitive unit cells of tetragonal and monoclinic phases of $TlReO_4$ and orthorhombic crystal cell of $TlTcO_4$ contain 12, 72, and 24 numbers of atoms, a sum of 36, 216 and 72 number of Γ-point phonon frequencies can be obtained for these respective materials. Among these frequencies, three modes are acoustic, and the rest are optical in nature which are further IR active, Raman active and silent modes. In case of low-temperature tetragonal phase of $TlReO_4$, these modes are as follows: E_u and A_u (IR-active modes); B_g, E_g and A_g (Raman-active modes) and B_u (silent modes). In between these modes, 15 modes are corresponding to lattice vibration related external modes whereas 18 modes are related to the internal vibrations of ReO_4 unit. Irreducible representation of this material is denoted as $\Gamma = 5E_u + 5A_u + 5B_g + 5E_g + 3A_g + 3B_u$ where E_u and E_g are double degenerate modes. For monoclinic $TlReO_4$, $\Gamma = 54A_u + 54B_u + 54A_g + 54B_g$ is the irreducible representation and acoustic modes are denoted by A_u and $2B_u$. The total number of optical modes for this material is 213, and out of these modes, the number of external modes is 91 while the rest are connected with internal modes. Among present modes of this material, IR active modes are denoted by A_u and B_u while Raman active modes are distinguished by A_g and B_g. Available modes in orthorhombic $TlTcO_4$ are B_{1u}, B_{2u}, B_{3u} (IR-active), A_u(silent) and A_g, B_{1g}, B_{2g}, B_{3g} (Raman active) and the irreducible representation of gamma point phonon modes is expressed as $\Gamma = 11\ B_{1u} + 7\ B_{2u} + 11\ B_{3u} + 7\ A_u + 11\ A_g + 7B_{1g} + 11\ B_{2g} + 7\ B_{3g}$. After consideration of phonon degeneracy, possible Raman-active modes for low-temperature tetragonal $TlReO_4$ is thirteen. Among these modes, only eight modes have been reported to be detected [49] till now without symmetry assignment of these modes due to un-polarized configuration used in those experiments. Table 3.9 contains our calculated Raman frequencies of low temperature tetragonal $TlReO_4$ compared with reported literature values [49]. The difference between calculated and measured frequencies is found to be less than 6%. Overestimation of our calculated frequencies, especially in the high-frequency range for internal modes of ReO_4 is typical for DFT calculations [96]. So, phonon frequencies obtained from our calculations can be thought of as well-predicted for those modes which were not reported yet.

Table 3.9 Calculated Raman-active modes of low-temperature tetragonal phase of $TlReO_4$. The mode assignment, symmetry and frequencies are reported. Frequencies are compared with experiment at 90K. [Rot. = Rotation, Trans. = Translational, Rock. = Rocking, Wagg.= Wagging, Twist. = Twisting, Sci. = Scissoring, Asym. Str. = Asymmetric stretching and Sym. Str. = Symmetric Stretching]

Symmetry	Assignment	Frequency (cm^{-1})	Exp. Frequency (cm^{-1})[49]
B_g	Trans. of (Tl, ReO_4)	28.81	
E_g	Trans. of only Tl atoms	42.36	40
B_g	Trans. of (Tl, ReO_4)	61.37	
E_g	Rot. of ReO_4	63.97	63
A_g	Rot. of ReO_4	102.8	
E_g	Rot. of ReO_4	110.04	
B_g	Sci. in ReO_4	310.92	
A_g	Sci. in ReO_4	319.21	324
E_g	Wagg., Rock. in ReO_4	328	332
B_g	Sci., Twist. in ReO_4	335.93	341
E_g	Asym. Str. of Re-O bonds	929.29	878
B_g	Asym. Str. of Re-O bonds	941.83	891
A_g	Sym. Str. of all bonds in ReO_4	1000.61	957

Along with the prediction of these new modes of this material, assignment of these modes is also possible from our calculations. Besides predicting unknown Raman modes, we have reported IR-active modes of the tetragonal phase of $TlReO_4$. Results regarding IR modes of this material can be obtained in Table 3.10 and can be used as a reference for future experiments. Corresponding results for room temperature monoclinic phase of $TlReO_4$ have been provided in Tables 3.11 and 3.12. Table 3.12 particularly contains Raman frequencies as well as the assignment of these modes. These calculated Raman frequencies are found to match well with the experimental Raman frequencies reported in our recent report[100].

Table 3.10 Calculated IR-active modes of low-temperature tetragonal phase of $TlReO_4$. The mode assignment, symmetry and frequencies are reported. [Rot. = Rotation, Trans. = Translational, Rock. = Rocking, Wagg.= Wagging, Twist. = Twisting, Sci. = Scissoring, Asym. Str. = Asymmetric stretching and Sym. Str. = Symmetric Stretching]

Symmetry	Mode	Frequency (cm^{-1})	Assignment
A_u	IR	45.42	Trans. of Tl and ReO_4 in opposite direction
E_u	IR	45.81	Trans. of Tl and ReO_4 in opposite direction
E_u	IR	64.94	Rot. of ReO_4
B_u	Silent	144.65	Rot. of ReO_4
A_u	IR	284.96	Sci. in ReO_4
E_u	IR	293.88	Wagg., Rock. in ReO_4
B_u	Silent	335.12	Wagg., Rock. in ReO_4
A_u	IR	344.65	Twist., Sci. in ReO_4
A_u	IR	934.33	Sym. Str. of Re-O bond
E_u	IR	936.76	Asym. Str. of Re-O bond
B_u	Silent	1002.34	Sym. Str. of all bonds in ReO_4

Table 3.11 Calculated IR-active modes of room-temperature monoclinic phase of $TlReO_4$. The mode assignment, symmetry and frequencies are reported. [Rot. = Rotation, Trans. = Translational, Rock. = Rocking, Wagg.= Wagging, Twist. = Twisting, Sci. = Scissoring, Asym. Str. = Asymmetric stretching and Sym. Str. = Symmetric Stretching]

Sym.	**Frequency (cm^{-1})**	**Assignment of Modes**
A_u	19.13	Different combination of Trans. of Tl and ReO_4 along y axis
B_u	22.43	Different combination of Trans. of Tl and ReO_4 along z axis
A_u	27.51	Different combination of Trans. of Tl and ReO_4
A_u	31.38	Trans. of Tl and ReO_4 opposite direction
B_u	32.37	Rock. in ReO_4
A_u	32.98	Trans. of Tl and ReO_4 in opposite direction
B_u	36.53	Trans. of Tl and ReO_4 in opposite direction
A_u	38.02	Trans. of Tl and ReO_4 in opposite direction
A_u	41.02	Trans. of Tl in opposite direction, Rock. in ReO_4
B_u	41.29	Trans. of Tl in opposite direction, Rot. in ReO_4
B_u	42.19	Trans. of Tl in opposite direction, Rot. in ReO_4

Continued on next page

Table 3.11 – *Continued from previous page*

Sym.	**Frequency (cm^{-1})**	**Assignment of Modes**
A$_u$	43.44	Trans. of Tl and ReO$_4$
B$_u$	45.36	Trans. of ReO4, Rot. of ReO$_4$
A$_u$	46.37	Trans. of Tl and ReO$_4$
B$_u$	47.1	Rock., Rot. in ReO$_4$
B$_u$	50	Trans. of Tl and ReO$_4$
A$_u$	50.89	Trans. of Tl, Rock., Rot. In ReO$_4$
A$_u$	52.53	Trans. of Tl in opposite and ReO$_4$ in same direction
A$_u$	53.75	Trans. of Tl and ReO$_4$ in opposite direction
B$_u$	53.84	Trans. of Tl, Rock. in ReO$_4$
A$_u$	56.57	Trans. of Tl and ReO$_4$ in opposite direction
B$_u$	56.76	Trans. of Tl and ReO$_4$ in opposite direction
B$_u$	58.64	Trans. of Tl and ReO$_4$ in same direction
B$_u$	59.22	Trans. of ReO$_4$ in opposite direction
A$_u$	60.61	Trans. of Tl and ReO$_4$ in opposite direction
B$_u$	62.71	Trans. ReO$_4$ in opposite direction
A$_u$	63.16	Trans. of Tl and ReO$_4$ in opposite direction
A$_u$	66.31	Trans. of ReO$_4$ in opposite direction
B$_u$	67.38	Trans. of Tl in opposite and ReO$_4$ in same direction
A$_u$	67.79	Trans. of ReO$_4$ in opposite direction
B$_u$	68.31	Trans. of Tl and ReO$_4$ in opposite direction
B$_u$	68.98	Trans. of ReO$_4$ in opposite direction
A$_u$	69.99	Trans. of ReO$_4$ in same direction
B$_u$	73.47	Rot. of ReO$_4$
A$_u$	75.55	Trans. of ReO$_4$ in same direction
B$_u$	80	Rot. of ReO$_4$
B$_u$	82.05	Rot. of ReO$_4$
B$_u$	85.08	Rot. of ReO$_4$
A$_u$	87.46	Rot. of ReO$_4$
B$_u$	96.53	Rock., Wagg. in ReO$_4$
A$_u$	97.21	Rot. of ReO$_4$
B$_u$	105.84	Rot. of ReO$_4$
B$_u$	110.82	Rot. of ReO$_4$
A$_u$	112.31	Rot. of ReO$_4$
B$_u$	115.52	Rock. in ReO$_4$

Continued on next page

Table 3.11 – *Continued from previous page*

Sym.	**Frequency (cm^{-1})**	**Assignment of Modes**
A_u	117.37	Rot., Rock. in ReO_4
A_u	119.86	Rock. in ReO_4
B_u	120.86	Rock., Rot. in ReO_4
A_u	131.78	Rock., Wagg. in ReO_4
A_u	143.55	Twist. in ReO_4
A_u	147.28	Twist. in ReO_4
A_u	287.39	Wagg. in ReO_4
A_u	289.61	Rock., Sci. in ReO_4
B_u	289.84	Rock., Wagg. in ReO_4
B_u	290.96	Sci. in ReO_4
B_u	293.73	Rock., Wagg. in ReO_4
A_u	294.22	Sci., Rock., Wagg. in ReO_4
A_u	295.48	Sci., Rock., Wagg. in ReO_4
B_u	298.46	Sci., Rock., Wagg. in ReO_4
B_u	301.77	Wagg. in ReO_4
B_u	310.63	Sci. in ReO_4
B_u	314.12	Sci. in ReO_4
A_u	314.14	Sci. in ReO_4
B_u	316.63	Sci. in ReO_4
A_u	317.29	Sci. in ReO_4
A_u	318.56	Sci., Wagg. in ReO_4
B_u	319.99	Sci. in ReO_4
B_u	324.52	Sci., Twist. in ReO_4
A_u	326.01	Sci., Twist. in ReO_4
B_u	327.82	Sci. in ReO_4
B_u	328.75	Sci., Twist. in ReO_4
A_u	329.02	Sci., Wagg. in ReO_4
A_u	332.24	Sci., Wagg. in ReO_4
B_u	334.2	Sci., Wagg., Twist. in ReO_4
A_u	334.23	Sci., Twist. in ReO_4
B_u	337	Sci., Wagg. in ReO_4
A_u	340.68	Twist. in ReO_4
A_u	340.77	Twist. in ReO_4
B_u	341.78	Twist. in ReO_4
A_u	343.3	Twist. in ReO_4
A_u	344.59	Twist. in ReO_4

Continued on next page

Table 3.11 – *Continued from previous page*

Sym.	**Frequency (cm^{-1})**	**Assignment of Modes**
A$_u$	927.86	Asym. Str. of Re-O bond
A$_u$	929.16	Asym. Str. of Re-O bond
B$_u$	931.11	Sym., Asym. Str. of Re-O bond
A$_u$	933.0	Asym. Str. of Re-O bond
A$_u$	934.03	Asym. Str. of Re-O bond
B$_u$	934.2	Asym. Str. of Re-O bond
B$_u$	935.5	Asym. Str. of Re-O bond
A$_u$	936.16	Sym., Asym. Str. of Re-O bond
A$_u$	937.07	Asym. Str. of Re-O bond
B$_u$	937.85	Sym., Asym. Str. of Re-O bond
A$_u$	940.6	Sym., Asym. Str. of Re-O bond
B$_u$	941.26	Asym. Str. of Re-O bond
B$_u$	946.07	Asym. Str. of Re-O bond
A$_u$	949.55	Sym. Str. of Re-O bond
A$_u$	955.12	Asym. Str. of Re-O bond
B$_u$	967.17	Sym., Asym. Str. of Re-O bond
B$_u$	978.05	Sym., Asym. Str. of Re-O bond
B$_u$	980.46	Sym., Asym. Str. of Re-O bond
B$_u$	1002.16	Sym. Str. of Re-O bond
A$_u$	1003.04	Sym. Str. of Re-O bond
B$_u$	1004.53	Sym. Str. of Re-O bond
A$_u$	1004.91	Sym. Str. of Re-O bond
A$_u$	1007.98	Sym. Str. of Re-O bond
B$_u$	1009.18	Sym. Str. of Re-O bond

Table 3.12 Calculated Raman-active modes of room-temperature phase of TlReO$_4$. The mode assignment, symmetry and frequencies are reported. [Rot. = Rotation, Trans. = Translational, Rock. = Rocking, Wagg.= Wagging, Twist. = Twisting, Sci. = Scissoring, Asym. Str. = Asymmetric stretching and Sym. Str. = Symmetric Stretching]

Sym.	**Frequency (cm^{-1})**	**Assignment of Modes**
A$_g$	20.36	Trans. of Tl and ReO$_4$ along z axis
A$_g$	22.72	Trans. of Tl and ReO$_4$ along x axis

Continued on next page

Table 3.12 – *Continued from previous page*

Sym.	**Frequency (cm^{-1})**	**Assignment of Modes**
B$_g$	23.9	Trans. of Tl and ReO$_4$ along y axis
B$_g$	31.65	Trans. of Tl and ReO$_4$ in opposite direction
A$_g$	32.22	Trans. of Tl and ReO$_4$ in opposite direction
B$_g$	36.6	Trans. of Tl, Rot. Of ReO$_4$
A$_g$	37.12	Trans. of Tl and ReO$_4$
A$_g$	38.88	Trans. of Tl and ReO$_4$
A$_g$	41.01	Trans. of Tl and ReO$_4$
B$_g$	41.27	Trans. of Tl in opposite and ReO$_4$ in same direction
B$_g$	42.35	Trans. of Tl in opposite direction, Rock. in ReO$_4$
A$_g$	43.02	Trans. of Tl in opposite direction, Rock. in ReO$_4$
A$_g$	44.18	Trans. of Tl in opposite direction
A$_g$	44.98	Trans. of Tl and ReO$_4$
B$_g$	45.17	Trans. of Tl in opposite direction
B$_g$	47	Trans. of Tl in same direction and Rock. in ReO$_4$
B$_g$	48.51	Trans. of Tl and ReO$_4$ in opposite direction
B$_g$	49.97	Trans. of Tl, Rock., Rot. in ReO$_4$
A$_g$	52.3	Trans. of Tl and ReO$_4$ in opposite direction
B$_g$	53.3	Trans. of Tl and ReO$_4$
A$_g$	54.58	Trans. of Tl and ReO$_4$
A$_g$	55.68	Trans. of Tl and ReO$_4$, Rock. in ReO$_4$
B$_g$	56.18	Trans. of Tl and ReO$_4$ in same direction
B$_g$	757.58	Trans. of Tl and ReO$_4$ in opposite direction
A$_g$	59.6	Trans. of Tl and ReO$_4$ in opposite direction
B$_g$	60.64	Rock. in ReO$_4$
B$_g$	63.1	Trans. of Tl and ReO$_4$, Rock. in ReO$_4$
A$_g$	63.59	Trans. of Tl and ReO$_4$, Rock., Rot. in ReO$_4$
B$_g$	64.46	Trans. of Tl and ReO$_4$
A$_g$	64.75	Trans. of Tl and ReO$_4$, Rock., Rot. in ReO$_4$
A$_g$	66.89	Trans. of ReO$_4$
B$_g$	69.56	Trans. of ReO$_4$
A$_g$	70.63	Rot. in ReO$_4$
B$_g$	71.39	Trans. of ReO$_4$
A$_g$	71.52	Rot., Rock. in ReO$_4$
B$_g$	72.68	Rot. of ReO$_4$
A$_g$	79.82	Rot. of ReO$_4$
B$_g$	79.99	Rot. of ReO$_4$

Continued on next page

Table 3.12 – *Continued from previous page*

Sym.	**Frequency (cm^{-1})**	**Assignment of Modes**
A_g	82.41	Rot. of ReO_4
A_g	96.62	Rot. of ReO_4
A_g	97.75	Rot. of ReO_4
B_g	98.42	Rot. of ReO_4
B_g	100.96	Rot. of ReO_4
A_g	101.88	Rot. of ReO_4
A_g	105.03	Twist. in ReO_4
A_g	111.04	Rot. of ReO_4
B_g	114.04	Rot. of ReO_4
A_g	114.99	Twist. in ReO_4
A_g	121.14	Rock. in ReO_4
B_g	122.72	Rot. of ReO_4
B_g	126.89	Rock., Twist. in ReO_4
B_g	130.34	Rock. in ReO_4
B_g	135.25	Rock., Wagg. in ReO_4
B_g	140.57	Rock. in ReO_4
A_g	289.94	Rock., Wagg. in ReO_4
B_g	290.73	Sci. in ReO_4
A_g	293.08	Sci. in ReO_4
B_g	293.89	Sci. in ReO_4
A_g	300.29	Sci., Rock., Wagg. in ReO_4
A_g	303.79	Wagg. in ReO_4
B_g	308.25	Sci. in ReO_4
A_g	308.73	Sci. in ReO_4
A_g	312.8	Sci. in ReO_4
A_g	314.73	Sci. in ReO_4
B_g	315.74	Sci. in ReO_4
B_g	316.72	Sci. in ReO_4
A_g	318.64	Sci., Wagg. in ReO_4
A_g	320.59	Sci. in ReO_4
B_g	322.59	Sci. in ReO_4
A_g	325.23	Sci., Wagg. in ReO_4
B_g	325.35	Sci. in ReO_4
B_g	327.15	Sci. in ReO_4
B_g	328.01	Sci., Wagg. in ReO_4
A_g	328.08	Sci., Twist. in ReO_4

Continued on next page

Table 3.12 – *Continued from previous page*

Sym.	**Frequency (cm^{-1})**	**Assignment of Modes**
B_g	330.53	Sci., Wagg. in ReO_4
A_g	330.94	Sci., Wagg. in ReO_4
B_g	333.06	Sci., Wagg. in ReO_4
B_g	334.16	Sci., Wagg., Twist. in ReO_4
A_g	334.73	Sci. in ReO_4
B_g	336.76	Twist. in ReO_4
A_g	337.35	Sci., Wagging in ReO_4
A_g	338.48	Sci., Wagg. in ReO_4
B_g	343.84	Twist. in ReO_4
B_g	345.41	Twist. in ReO_4
B_g	928.55	Asym. Str. of Re-O bond
A_g	929.61	Asym. Str. of Re-O bond
B_g	931.11	Asym. Str. of Re-O bond
A_g	932.15	Asym. Str. of Re-O bond
B_g	932.27	Asym. Str. of Re-O bond
B_g	933.2	Asym. Str. of Re-O bond
A_g	935.36	Asym. Str. of Re-O bond
B_g	935.66	Asym. Str. of Re-O bond
B_g	936.85	Sym., Asym. Str. of Re-O bond
A_g	938.3	Asym. Str. of Re-O bond
A_g	941.78	Asym. Str. of Re-O bond
A_g	944.66	Asym. Str. of Re-O bond
B_g	946.79	Asym. Str. of Re-O bond
A_g	949.22	Sym., Asym. Str. of Re-O bond
B_g	952.16	Sym., Asym. Str. of Re-O bond
B_g	963.35	Asym. Str. of Re-O bond
A_g	973.35	Asym. Str. of Re-O bond
A_g	981.69	Asym. Str. of Re-O bond
A_g	1001.59	Sym. Str. of all bonds in ReO_4
B_g	1002.83	Sym. Str. of all bonds in ReO_4
A_g	1004.49	Sym. Str. of all bonds in ReO_4
B_g	1004.98	Sym. Str. of all bonds in ReO_4
B_g	1006.78	Sym. Str. of all bonds in ReO_4
A_g	1007.02	Sym. Str. of all bonds in ReO_4

A common feature that is typical for scheelite oxides could be observed for all these studied materials, as the Raman frequencies are mainly divided into three regions with phonon gaps [89]. Below 150 cm^{-1} frequencies are mainly obtained due to external modes present in these compounds where ReO_4 unit act as rigid block and movement of Tl atoms and ReO_4 block as a whole unit is involved in such modes. Because of the heavy mass of these two units of studied compounds and as the vibrational frequencies are inversely proportional to the square root of mass, the involvement of these units in the low-frequency range is quite logical. Participation of Re-O bonds of ReO_4 rigid units in wagging, rocking, scissoring, and twisting can be observed in the middle frequency range from 300 to 350 cm^{-1}. The high-frequency range is mainly obtained due to the internal stretching present in ReO_4 block, where oxygen atoms are found to show the main movement. As the Re-O bonds are the shortest bonds present in these materials, restoring forces related to stretching modes should show the largest value. Raman active modes are considered to arise due to change in polarizability. Our calculated vibrational frequencies along with our reported experimental Raman spectra of $TlReO_4$[100] helps us to obtain the high-intensity Raman mode of low-temperature tetragonal phase of $TlReO_4$, which is obtained at 1000.61 cm^{-1} due to symmetric stretching present in ReO_4. In the case of the monoclinic phase, the high-intensity mode can be obtained at 1001.59 cm^{-1}. From this report it can also be noted that the intensity of high-intensity Raman mode at 1000.61 cm^{-1} is nearly five times the second high-intensity modes present in tetragonal $TlReO_4$. This kind of property is quite common for scheelite-type materials [96] and is normally being considered for developing Raman lasers [97]. Another interesting observation is that internal symmetric stretching A_g mode has a measured frequency of 957 cm^{-1}. This frequency agrees within 2% with the values observed for the same mode in $AgReO_4$, $CsReO_4$, $KReO_4$, and $RbReO_4$ [55, 98]. The reason behind not obtaining all modes experimentally in earlier reported experiments could be the near degeneracy of frequencies for the tetragonal phase. In this context, the use of polarized Raman scattering could help for identifying all present modes of this material. Along with Raman frequencies of this material, we have also calculated the IR spectra of this material which was not reported earlier, and in this connection, our predicted results can guide future experimental study of IR spectra. IR modes of the low-temperature phase of $TlReO_4$ obtained from our study have been provided in Table 3.10. The same for the monoclinic phase has been given in Table 3.11. The IR spectra of both the phases are shown in Figure 3.3. As the monoclinic phase contains a larger atomic contribution than the tetragonal phase, we can observe an overall higher value of intensity for the monoclinic phase. IR peaks of the monoclinic phase are found to be larger compared to the tetragonal phase. It can also be noticed that the most intense peak for both the structures arises due to the internal stretching modes of ReO_4. The distribution of these IR modes also follows a similar trend as that of Raman modes for these materials. Particularly, external vibration related modes can be

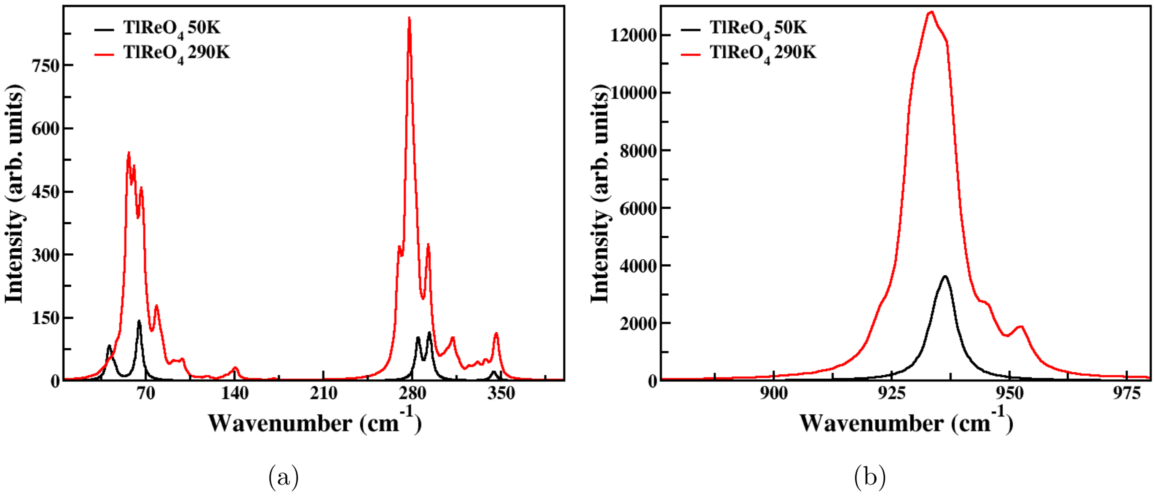

(a) (b)

Figure. 3.3 Calculated IR spectrum of tetragonal and monoclinic phase of TlReO$_4$ in two different frequency ranges.

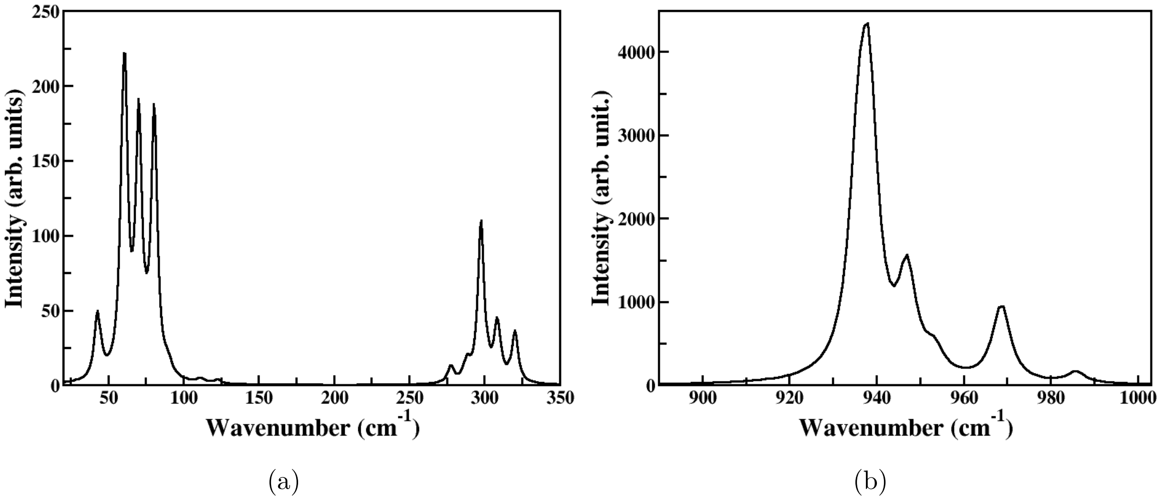

(a) (b)

Figure. 3.4 Calculated IR spectrum of orthorhombic TlTcO$_4$ divided in two different frequency ranges.

observed below 150 cm^{-1}, internal modes associated with the stretching of bonds in ReO_4 can be found to see above 920 cm^{-1} and other internal vibrational modes linked with wagging, scissoring, rocking and twisting present in ReO_4 block can be observed from 270 to 350 cm^{-1}. Obtained IR spectrum of these materials matches quite well with another scheelite type perrhenate structure $AgReO_4$ [99].

Figure 3.4 and 3.5 clearly depict the IR and Raman spectrum of $TlTcO_4$, respectively. Though Figure 3.4 is mainly divided into two regions, this figure clearly indicates that IR frequency distribution can be further subdivided into different regions. Frequencies below 130 cm^{-1} are mainly due to rotation, translation of Tl atom and pertechnetate group. The intensity of the frequencies from 277 to 326 cm^{-1} is very less, which is mainly attributed to rocking, wagging, scissoring, twisting present in the pertechnetate group. The region from 926 to 986 cm^{-1} is mainly due to the stretching of Tc-O bond in TcO_4 group. The highest intensity IR peaks in this high-frequency range are found due to the asymmetric stretching of the Tc-O bond. Figure 3.5 shows mainly three regions of the Raman spectra. Among these, the first region below 200 cm^{-1} is mainly due to the translational and rotational motion of different blocks in this material. The second region from 200 to 400 cm^{-1} is attributed due to wagging, rocking, scissoring of pertechnetate block, and the high-frequency region is due to the presence of stretching in Tc-O bonds. The High-intensity Raman peak of this material is obtained due to the symmetric stretching of the Tc-O bond where O3 type of atoms are involved which is similar for high-intensity IR mode. An interesting point between the IR spectra of $TlReO_4$ and $TlTcO_4$ could be noticed as the lower intensity value of the middle region of $TlTcO_4$ compared to $TlReO_4$. On the contrary, a reasonable intensity value of this middle region could be seen for the Raman spectra of $TlTc_4$. This indicates that $TlTcO_4$ is more polarizable compared to $TlReO_4$ which is found to be consistent with the BEC values of these materials. Figure 3.6, 3.7 and 3.8 depict a high intensity IR and Raman modes of $TlTcO_4$ and two phases of $TlReO_4$,

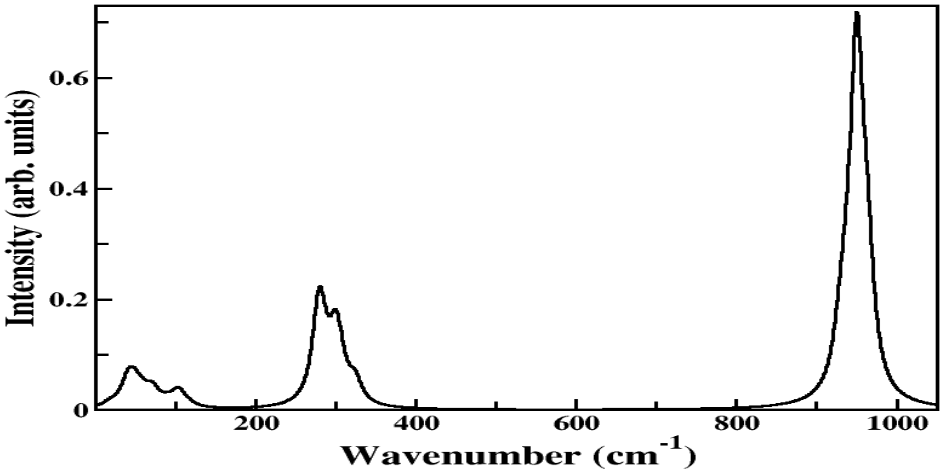

Figure. 3.5 Calculated Raman spectrum of orthorhombic $TlTcO_4$.

respectively.

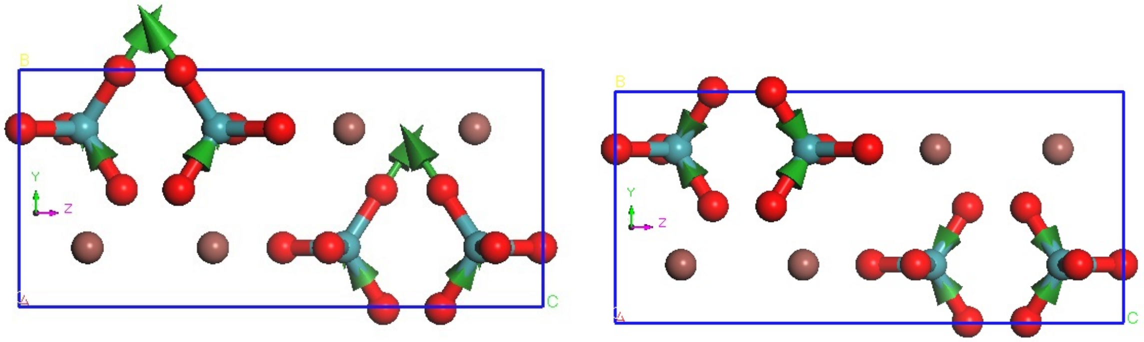

(a) (b)

Figure. 3.6 High intensity IR mode (shown in a) and Raman mode (shown in b) of $TlTcO_4$.

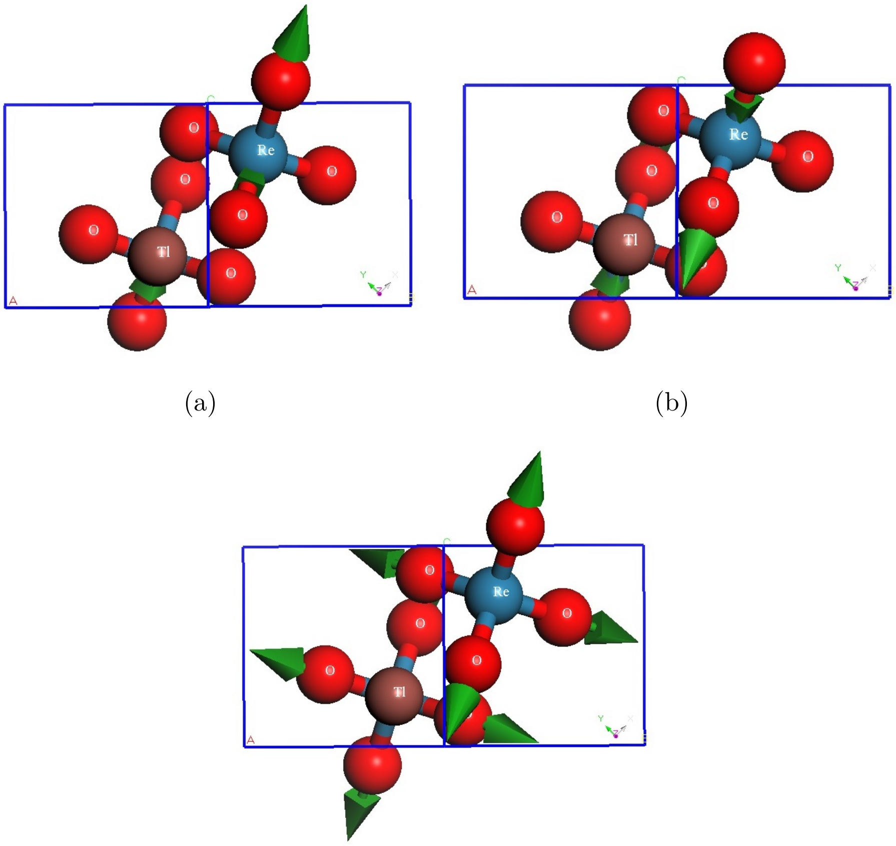

(a) (b)

(c)

Figure. 3.7 Lattice vibration of tetragonal $TlReO_4$ corresponding to high intensity IR modes at (a) 936.76, (b) second high intensity Raman mode at 929.29 and (c) high intensity Raman modes at 1000.61 cm^{-1}.

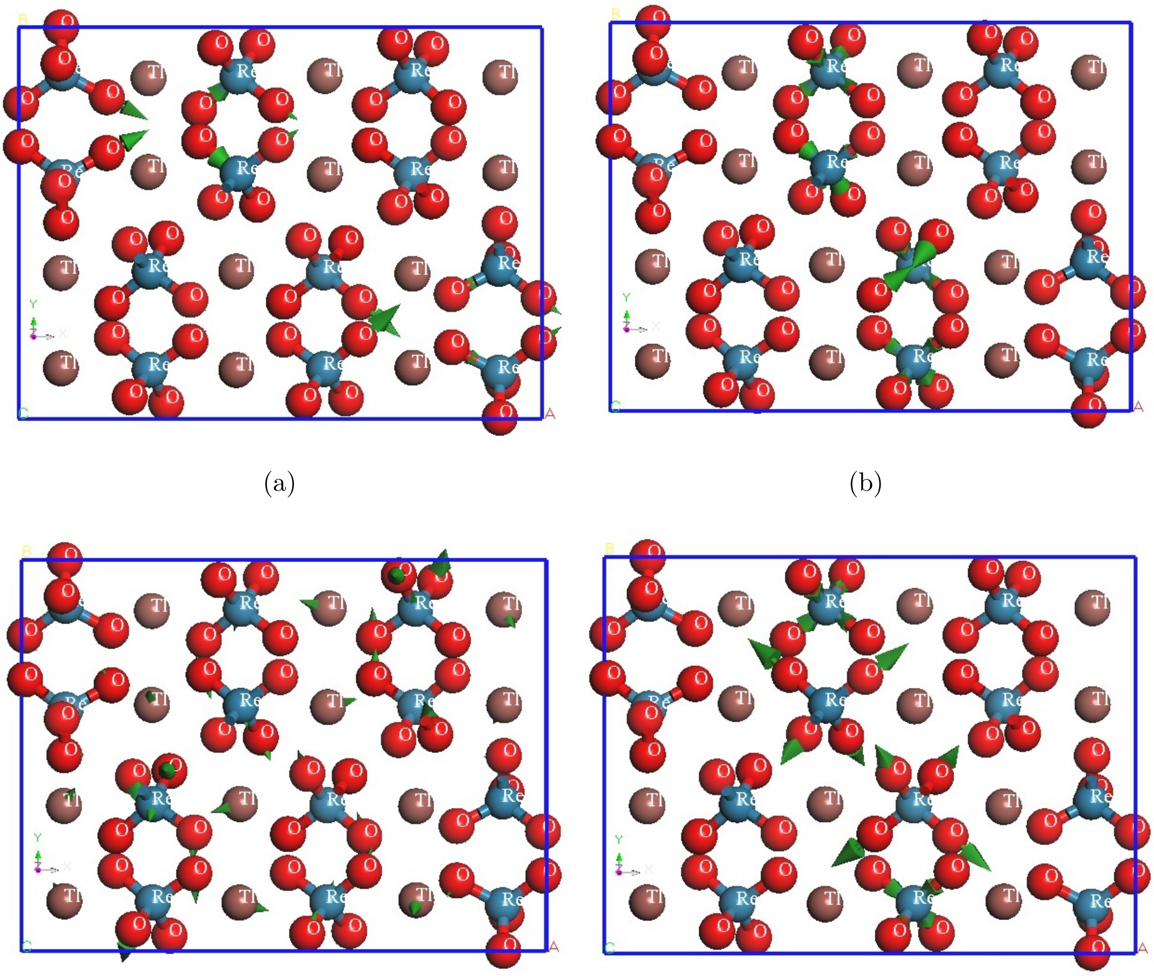

(a) (b)

(c) (d)

Figure. 3.8 Lattice vibration of monoclinic $TlReO_4$ corresponding to (a) high intensity IR mode at 937.85 cm^{-1} and other significant Raman modes at (b) 1001.59, (c) 41.27 and (d) 1002.83 cm^{-1}.

Table 3.13 Calculated zone-centered vibrational phonon frequencies of orthorhombic $TlTcO_4$. The mode assignment, symmetry and frequencies are reported. [Rot. = Rotation, Trans. = Translational, Rock. = Rocking, Wagg.= Wagging, Twist. = Twisting, Sci. = Scissoring, Asym. Str. = Asymmetric stretching and Sym. Str. = Symmetric Stretching]

Frequency (cm^{-1})	**Symmetry**	**Mode**	**Assignment**
18.09	B_{1g}	Raman	Rot.
32.36	B_{1g}	Raman	Trans.
35.25	A_u	Silent	Trans.

Continued on next page

Table 3.13 – *Continued from previous page*

Frequency (cm^{-1})	**Symmetry**	**Mode**	**Assignment**
40.97	A_g	Raman	Trans.
41.29	B_{3g}	Raman	Trans. of Tl + Rot. of TcO_4
42.87	B_{2u}	IR	Rot.
43.70	B_{1u}	IR	Trans.
48.76	B_{3u}	IR	Trans. of Tl + Rot. of TcO_4
49.45	A_g	Raman	Trans. of Tl
51.14	B_{2g}	Raman	Trans. of Tl + Rot. of TcO_4
52.80	A_u	Silent	Trans. of Tl + Rot. of TcO_4
59.81	B_{2g}	Raman	Trans.
60.54	B_{1u}	IR	Trans.
67.18	B_{3u}	IR	Trans. of Tl + Rot. of TcO_4
70.35	B_{2u}	IR	Trans.
70.66	A_g	Raman	Trans.
80.43	B_{3g}	Raman	Trans. of Tl + Rot. of TcO_4
80.48	B_{3u}	IR	Rot. of TcO_4
88.42	A_u	Silent	Rot. of TcO_4
89.12	B_{2g}	Raman	Rot. of TcO_4
89.49	B_{1u}	IR	Trans. of Tl + Rot. of TcO_4
91.32	B_{1g}	Raman	Trans.
92.30	B_{3g}	Raman	Rot. of TcO_4
93.97	B_{3g}	Raman	Rot. of TcO_4
95.89	B_{2g}	Raman	Trans. of TcO_4
99.89	A_u	Silent	Rot. of TcO_4
102.11	A_g	Raman	Rot. of TcO_4
110.22	A_g	Raman	Trans. of TcO_4
110.75	B_{3u}	IR	Rot. of TcO_4
113.04	B_{2u}	IR	Rot. of TcO_4
114.75	B_{1g}	Raman	Rot. of TcO_4
116.89	B_{2g}	Raman	Rot. of TcO_4
122.62	B_{1u}	IR	Rot. of TcO_4
277.58	B_{2u}	IR	Wagg. and Rock. in TcO_4
278.36	B_{1g}	Raman	Twist. and Sci. in TcO_4
281.35	A_u	Silent	Wagg. and Twist. in TcO_4
286.46	A_g	Raman	Wagg. and Sci. in TcO_4
288.13	B_{3u}	IR	Wagg. and Sci. in TcO_4
289.59	B_{2u}	IR	Twist. in TcO_4

Continued on next page

Table 3.13 – *Continued from previous page*

Frequency (cm^{-1})	**Symmetry**	**Mode**	**Assignment**
294.59	B_{3g}	Raman	Twist. in TcO_4
297.76	B_{1u}	IR	Sci. in TcO_4
299.57	A_g	Raman	Sci. in TcO_4
300.52	A_u	Silent	Twist. in TcO_4
301.26	B_{2g}	Raman	Wagg. and Sci. in TcO_4
305.80	B_{2g}	Raman	Sci. in TcO_4
308.31	B_{3u}	IR	Wagg. and Sci. in TcO_4
310.37	B_{1u}	IR	Sci. in TcO_4
320.09	B_{1u}	IR	Sci. in TcO_4
320.67	B_{3u}	IR	Sci. in TcO_4
321.86	A_g	Raman	Sci. in TcO_4
322.72	B_{2g}	Raman	Sci. in TcO_4
323.86	B_{3g}	Raman	Wagg. and Rock. in TcO_4
325.18	B_{1g}	Raman	Wagg. and Rock. in TcO_4
926.07	A_u	Silent	Asym. Str. in TcO_4
927.61	B_{3g}	Raman	Asym. Str. in TcO_4
934.15	A_g	Raman	Str. of Tc-O bonds
935.65	B_{3u}	IR	Str. of Tc-O bonds
936.47	B_{1u}	IR	Str. of Tc-O bonds
938.31	B_{2u}	IR	Asym. Str. of Tc-O bonds
939.72	B_{2g}	Raman	Str. of Tc-O bonds
939.89	B_{1g}	Raman	Asym. Str. of Tc-O bonds
947.05	B_{1u}	IR	Sym. Str. of Tc-O bonds
948.83	A_g	Raman	Sym. Str. of Tc-O bonds
953.27	B_{3u}	IR	Sym. Str. of Tc-O bonds
956.99	B_{2g}	Raman	Sym. Str. of Tc-O bonds
961.72	A_g	Raman	Str. of Tc-O bonds
965.91	B_{2g}	Raman	Asym. and Sym. Str. of Tc-O bonds
968.63	B_{1u}	IR	Str. of Tc-O bonds
985.80	B_{3u}	IR	Str. of Tc-O bonds

3.4 Conclusions

In conclusion, we have carried out a thorough density functional theory study of structural, vibrational and associated IR and Raman frequencies of ABO_4 type transition metal oxides $TlReO_4$ and $TlTcO_4$. In the case of $TlReO_4$, our calculation has been supported by experimental results. DFT total energy calculation of low-temperature tetragonal, room-temperature monoclinic and hypothetical orthorhombic phases shows that our experimentally predicted room-temperature monoclinic phase is energetically more favourable than the earlier proposed orthorhombic structure of $TlReO_4$. Our DFT calculations facilitate the assignment of all the vibrational properties of the low- and room-temperature phases of $TlReO_4$. Calculated BECs show the presence of a mixed-valence character of bonds in both phases. Calculated phonon frequencies allow the assignment of the Raman modes, the determination of the frequencies of mode undetected in experiments, and the identification of the atomic movement associated with each mode. We have obtained the same information for IR and silent modes for the tetragonal phase. The vibrations of $TlReO_4$ can be divided into external and internal modes of the ReO_4 tetrahedron as discussed above. There is a very strong high-frequency mode which we have assigned to the internal stretching vibration of the ReO_4 tetrahedron. This is the first time all the vibration modes of both phases of $TlReO_4$ have been properly assigned. Experimentally obtained Raman spectrum of room-temperature $TlReO_4$ is discussed in comparison with the Raman frequencies of the room- and low-temperature phases, showing that the assignation of external and internal modes is maintained in the room-temperature structure in spite of the increase of the number of modes due to the symmetry decrease caused by the temperature-driven transition. In case of $TlTcO_4$, the structural properties with various exchange-correlation functional have been addressed. After obtaining the ground state structure with the PBE+TS scheme, we have performed the calculation of zone-centered vibrational properties along with understanding of IR and Raman spectra which shows a similar trend like ABO_4 type material. Here we have also addressed the bonding nature of this material from born effective charge (BEC), which tells that this material is ionically bonded with Tl and TcO_4 block whereas TcO_4 block is covalently bonded. Among different types of O atoms, the contribution of O3 atom is found to be prominent in high-intensity IR and Raman modes.

References

[1] G. Voicu, M. Bardoux and R. Stevenson, Ore Geol. Rev. 18, 211 (2001).

[2] A. Brenier, G.H. Jia and C.Y. Tu, J. Phys.: Condens. Matter 16, 9103 (2004).

[3] M. Kobayashi, M. Ishii, Y. Usuki and H. Yahagi, Nucl. Instrum. Methods Phys. Res. A 333, 429 (1993).

[4] M. Nikl et al, J. Appl. Phys. 91, 5041 (2002).

[5] N. Faure, C. Borel, M. Couchaud, G. Basset, R. Templier and C. Wyon, Appl. Phys. B 63, 593 (1996).

[6] H.P. Scott, Q. Williams and E. Knittle, Phys. Rev. Lett. 88, 015506 (2002).

[7] Y. Le Page and G. Donnay, Acta Crystallogr. B 32, 2456 (1976).

[8] P. Rogner and K.J. Range, Z. Anorg. Allg. Chem. 619, 1017 (1993).

[9] D. Errandonea and J. Ruiz-Fuertes, Crystals 8, 71 (2018).

[10] D. Errandonea, A. Munoz, P. Rodriguez-Hernandez, O. Gomis, S.N. Achary, C. Popescu, S.J. Patwe and A.K. Tyagi, Inorg. Chem. 55, 4958 (2016).

[11] J. Beintema, Z. Kristallogr. 97, 300 (1937).

[12] D. Errandonea, J. Chem. Sci. 131, 88 (2019).

[13] D. Errandonea and F.J. Manjon, Prog. Mater. Sci. 53, 711 (2008).

[14] D. Errandonea and A.B. Garg, Prog. Mater. Sci. 97, 123 (2018).

[15] P.K. Jharapla, E.N. Rao and G. Vaitheeswaran, J. Phys.: Condens. Matter 30, 475402 (2018).

[16] S. Mondal, S. Appalakondaiah and G. Vaitheeswaran, J. Appl. Phys. 119, 085702 (2016).

[17] G. Shwetha, V. Kanchana, K.R. Babu, G. Vaitheeswaran and M.C. Valsakumar, J. Phys. Chem. C 118, 4325 (2014).

[18] G. Shwetha, V. Kanchana and G. Vaitheeswaran, Mater. Chem. Phys. 163, 376 (2015).

[19] S. Injac, A.K.L. Yuen, M. Avdeev, F. Orlandi and B.J. Kennedy, Phys. Chem. Chem. Phys. 21(14), 7261 (2019).

[20] C.A. Marjerrison, C. Mauws, A.Z. Sharrna, C.R. Wiebe, S. Derakhshan, C. Boyer, B.D. Gaulin and J.E. Greedan, Inorg. Chem. 55(24), 12897 (2016).

[21] J. Yamaura and Z. Hiroi, Phys. Rev. B: Condens. Matter Mater. Phys. 99(15), 155113 (2019).

[22] O. Fukunaga and S. Yamaoka, Phys. Chem. Miner. 5, 167 (1979).

[23] A. Jayaraman, B. Batlogg and L.G. Van Uitert, Phys. Rev. B 31, 5423 (1985).

[24] A. Jayaraman, B. Batlogg and L.G. Van Uitert, Phys. Rev. B 28, 4774 (1983).

[25] G.H. Cartledge, Br. Corros. J. 1 (8), 293-302 (1966).

[26] E. Holm, Radiochim. Acta 63, 57-62 (1993).

[27] T. Ishida and H. Mazaki, Phys. Rev. B: Condens. Matter Mater. Phys. 20, 131-138 (1979).

[28] I.R. Little-Marenin, S.J. Little, Observations. Astron. J. 84, 1374-1383 (1979).

[29] S. Goriely, World Scientific: Singapore, pp 326-336 (2013).

[30] R.D.W. Kemmitt and R.D. Peacock, The chemistry of manganese, technetium, and rhenium: Pergamon texts in inorganic chemistry; Elsevier: New York, (2013).

[31] E.V. Johnstone, M.A. Yates, F. Poineau, A.P. Sattelberger and K.R. Czerwinski, J. Chem. Educ. 94 (3), 320-326 (2017).

[32] E. Deutsch, K. Libson, S. Jurisson, L.F. Lindoy, Ed.; John Wiley Sons, Inc.: New York, pp 75-139 (1983).

[33] V.I. Spitsin, I.L. Rosenfeld, V.P. Persiantseva, N.N. Zamoshnikova and A.F. Kuzina, Corrosion 21, 211-221 (1965).

[34] R. Faggiani, R.J. Gillespie, C.J.L. Lock, J. Poce, Acta Crystallogr., Sect. B: Struct. Crystallogr. Cryst. Chem. 36 (2), 231-233 (1980).

[35] B. Krebs and K.D. Hasse, Acta Crystallogr., Sect. B:Struct. Crystallogr. Cryst. Chem. 32, 1334-1337 (1976).

[36] M.J. Sarsfield, A.D. Sutton, F.R. Livens, I. May and R.J. Taylor, Acta Crystallogr., Sect. C:Cryst. Struct. Com. 59, I45-I46 (2003).

[37] B.J. McDonald and G.J. Tyson, Acta Crystallogr. 15, 87 (1962).

[38] G. Meyer and R. Hoppe, Z. Anorg. Allg. Chem. 420 (1), 40-50 (1976).

[39] C. Keller and B. Kanellakopulos, In Radiochimica Acta 1, 107 (1963).

[40] J. Weaver, C.Z. Soderquist, N.M. Washton, A.S. Lipton, P.L. Gassman, W.W. Lukens, A.A. Kruger, N.A. Wall and J.S. McCloy, Inorg. Chem. 56 (5), 2533-2544 (2017).

[41] V.P. Tarasov, S.A. Petrushin, V.I. Privalov, K.E. German, S.V. Kryuchkov, Y.A. Buslaev, Koord. Khim. 12, 1227-1236 (1986).

[42] L. Errico, G. Darriba, M. Rentería, Z. Tang, H. Emmerich and S. Cottenier, Phys. Rev. B: Condens. Matter Mater. Phys. 77, 195118 (2008).

[43] H. Migge, MRS Online Proc. Libr. 176, 411-417 (1989).

[44] J.G. Darab and P.A. Smith, Chem. Mater. 8, 1004-1021 (1996).

[45] B. Kanellakopulos, J. Inorg. Nucl. Chem. 28 (3), 813-816 (1966).

[46] G.E. Boyd, J. Chem. Educ. 36 (1), 3 (1959).

[47] K. Ulbricht and H. Kriegsmann, Z. Anorg. Allg. Chem. 358, 193 (1968).

[48] N.M. Roddatis, S.M. Tolmachev, V.V. Ugarov and N.G. Rambidi, J. Struct. Chem. 15, 591 (1974).

[49] A. Jayaraman, G.A. Kourouklis, R.M. Fleming and L.G. Van Uitert, Phys. Rev. B 37, 664 (1988).

[50] L.C. Ming, A. Jayaraman, S.R. Shieh and Y.H. Kim, Phys. Rev. B 51, 12100 (1995).

[51] J.M. Ablett, J.P. Rueff, S.R. Shieh, C.C. Kao and S. Wang, Phys. Rev. B 92, 014113 (2015).

[52] A. Jayaraman, G.A. Kourouklis and L.G. Van Uitert, Phys. Rev. B 36, 8547 (1987).

[53] J.M. Ablett, C.C. Kao, S.R. Shieh, H.K. Mao, M. Croft and T.A. Tyson, High Press. Res. 23, 471 (2003).

[54] D. de Waal and W. Kiefer, Z. Anorg. Allg. Chem. 630, 127 (2004).

[55] A. Jayaraman, G.A. Kourouklis, L.G. Van Uitert, W.H. Grodkiewicz and R.G. Maines, Physica A 156, 325 (1989).

[56] J.G. Darab and P.A. Smith, Chem Mater 8(5), 1004–1021 (1996).

[57] P.L. Gassman, J.S. McCloy, C.Z. Soderquist and M.J. Schweiger, J Raman Spectrosc 45(1), 139–147 (2014).

[58] D.S. Kim, C.Z. Soderquist, J.P. Icenhower, B.P. McGrail, R.D. Scheele, B.K. McNamara, L.M. Bagaasen, M.J. Schweiger, J.V. Crum, J.D. Yeager, J. Matyas, L.P. Darnell, H.T. Schaef, A.T. Owen, A.E. Kozelisky, L.A. Snow and M.J. Steele, Pacific Northwest National Laboratory, Richland (2005).

[59] I.S. Muller, D.A. McKeown and I.L. Pegg, Procedia Mater Sci 7, 53–59 (2014).

[60] I.S. Muller, C. Viragh, H. Gan, K.S. Matlack and I.L. Pegg, Hyperfine Interact 191(1–3), 347–354 (2009).

[61] D.K. Shuh, W. Lukens and C.J. Burns, Lawrence Berkeley National Laboratory, Berkeley (2003).

[62] D.A. McKeown, A.C. Buechele, W.W. Lukens, D.K. Shuh and I.L. Pegg, Environ Sci Technol 41, 431–436 (2007).

[63] D.A. McKeown, A.C. Buechele, W.W. Lukens, D.K. Shuh and I.L. Pegg, Radiochim Acta 95(5), 275–280 (2007).

[64] N. Weinstock and H. Schulze, J. Chem. Phys. 59, 5063 (1973).

[65] H.H. Eysel and B. Kanellakopulos, J. Raman Spectrosc. 24, 119 (1993).

[66] R.H. Busey and O.L. Keller,Jr., J. Chem. Phys. 41, 215 (1964).

[67] D.A. McKeown, A.C. Buechele, W.W. Lukens, D.K. Shuh and I.L. Pegg, Radiochim. Acta 95, 275 (2007).

[68] L.J. Basile, J.R. Ferraro, P. LaBonville, M.C. Wall, Coord. Chem. Rev. 11, 21 (1973).

[69] M.V. Mikelsons and T.C. Pinkerton, Appl. Radiat. Isot. 38, 569 (1987).

[70] A. Müller and W. Rittner, Spectrochim. Acta A. 23, 1831 (1967).

[71] M.J. Sarsfield, A.D. Sutton, F.R. Livens, I. May, R.J. Taylor, Acta Crystallogr. C 59, I45 (2003).

[72] K.I. Petrov, A.F. Kuzina, N.I. Dolgorukova, Y.M. Golovin and V.I. Spitsyn, Dokl. Akad. Nauk SSSR 206, 909 (1972).

[73] D. Errandonea, A. Munoz, P. Rodriguez-Hernandez, J.E. Proctor, F. Sapina and M. Bettinelli, Inorg. Chem. 54, 7524–35 (2015).

[74] P. Botella, S. Lopez-Moreno, D. Errandonea, F.J. Manjon, J.A. Sans, D. Vie and A. Vomiero, J. Phys.: Condens. Matter 32, 385403 (2020).

[75] D. Dash, C.K. Pandey, S. Chaudhary and S.K. Tripathy, Multidiscip. Model. Mater. Struct. 15, 306–16 (2019).

[76] D. Dash, C.K. Pandey, S. Chaudhury and S.K. Tripathy, Chin. Phys. B 27, 017102 (2018).

[77] D. Dash, C.K. Pandey, S. Chaudhury and S.K. Tripathy, Sci. Iranica 26, 1951 (2019).

[78] P. Hohenberg and W. Kohn, Phys Rev B 136 (3B), B864 (1964).

[79] W. Kohn and L.J. Sham, Phys. Rev. 140 (4A), 1133 (1965).

[80] N.D. Woods, M.C. Payne and P.J. Hasnip, J. Phys: Cond. Matt. 31, 45 (2019).

[81] M.C. Payne, M.P. Teter, D.C. Allan, T.A. Arias and J.D. Joannopoulos, Rev. Modern Physics

64 (4), 1045-1097 (1992).

[82] M.D. Segall, P.J.D. Lindan, M.J. Probert, C.J. Pickard, P.J. Hasnip, S.J. Clark and M.C. Payne, J. Phys: Cond. Matt. 14 (11), 2717-2744 (2002).

[83] D.M. Ceperley and B.J. Alder, Phys. Rev. Lett. 45, 566 (1980).

[84] J.P. Perdew and A. Zunger, Phys. Rev. B 23, 5048 (1981).

[85] J.P. Perdew, K. Burke and M. Ernzerhof, Phys. Rev. Lett. 77, 3865 (1996).

[86] A. Tkatchenko and M. Scheffler, Phys. Rev. Lett. 102, 073005 (2009).

[87] H.J. Monkhorst and J.D. Pack, Phys. Rev. B 13, 5188 (1976).

[88] T.H. Fischer and J. Almlof, J. Phys. Chem. 96, 9768 (1992).

[89] C. Chay, M. Avdeev, H.E.A. Brand, S. Injac, T.A. Whittle and B.J. Kennedy, Dalton Trans. 48, 17524 (2019).

[90] B. Kanellakopulos, J. Inorg. Nucl. Chem. 28, 813 (1966).

[91] C. Cazorla and D. Errandonea, Phys. Rev. Lett. 113, 235902 (2014).

[92] A.K. Sagotra, D. Errandonea and C. Cazorla, Nat. Commun. 8, 963 (2017).

[93] L. Kývala and D. Legut, Phys. Rev. B 101, 075117 (2020).

[94] M. Posternak, R. Resta and A. Baldereschi, Phys. Rev. B 50, 8911 (1994).

[95] W. Zhong, R.D. Kingsmith and D. Vanderbilt, Phys. Rev. Lett. 72, 3618 (1994).

[96] F.J. Manjon, D. Errandonea, N. Garro, J. Pellicer-Porres, P. Rodriguez-Hernandez, S. Radescu, J. Lopez-Solano, A. Mujica and A Munoz, Phys. Rev. B 74, 144111 (2006).

[97] A.Z. Grasyuk, Sov. J. Quantum Electron. 4, 269 (1974).

[98] J.W. Otto, J.K. Vassiliou, R.F. Porter and A.L. Ruoff, Phys. Rev. B 44, 9223 (1991).

[99] L. Burtsch and C. Feldmann, Z. Anorg. Allg. Chem. 643, 789 (2017).

[100] S. Mondal, G. Vaitheeswaran, Brendan J Kennedy, Clarissa Chay, Sean Injac and Daniel Errandonea, J. Phys.: Condens. Matter 33, 065403 (2021).

CHAPTER 4

Structure-property correlation study of nitromethane related energetic materials

A detailed theoretical understanding about the crystalline properties of nitromethane related di- and trinitromethane based energetic salts have been discussed in this chapter. In this connection, dinitromethane based potassium dinitromethane (KDNM) and trinitromethane based potassium nitroformate (KNF), methylhydrazinium nitroformate (MHNF), and formamidinium nitroformate (FNF) compounds have been considered. As a first step, the structural properties of these studied materials were tested with different dispersion corrected schemes along with standard DFT pseudopotentials. Though the structural properties of KNF with PBE + TS scheme were found to match well with experimental values, obtained values of these parameters for other studied materials are found in good agreement with the dispersion corrected method of Grimme. Pressure variation study of these parameters for nitroformate related compounds reveal the compressibility nature of these crystals. Mechanical stability, as well as the directional sensitivity of these materials, was understood through the calculation of elastic constants. Studies of Γ*-point vibrational frequencies as well as the IR spectrum of these materials have also been discussed in this work. In the case of KDNM, though the high-frequency IR peak arises due to CH bond stretching, the high-intensity peak is found due to rocking of CH bond along with the asymmetric stretching of NO bonds at 1194.50* cm^{-1}*. On the other hand, the high-intensity IR peak of KNF arises due to the asymmetric stretching of NO bond and the asymmetric stretching of NH bond found to be the main factor for such peaks in MHNF and FNF.*

4.1 Introduction

Energetic materials are normally known for their complex molecular and crystal structures. The very important component of these materials is known as nitro group due to its excellent energetic contribution to such materials. Among the nitro-based energetic materials, nitromethane is known as the simplest organic and yet powerful (secondary) energetic material. This material is widely being used as explosive [1, 2, 3, 4, 5], as monopropellant which can be stored and as an additive fuel in combustion engines [6, 7, 8, 9] due to its low toxicity and environment-friendly nature. These applications are mainly attributed to safe handling due to its insensitive nature, but still the detonation performance of this material matches quite well with RDX. Nitromethane can be found in the liquid phase at room temperature and transforms to crystalline phase either at low temperature and ambient pressure [10] or at room temperature and at 0.3 GPa [11]. This material is found in orthorhombic crystal structure with $P2_12_12_1$ space group and four formula units at 4.2 K [10]. The simple molecular and crystal structure of this material, in comparison to other complex energetic materials, made this material a prototype energetic material. Extensive experimental [12, 13, 14, 15, 16] and theoretical studies [17, 18, 19, 20, 21, 22, 23, 24, 25, 26, 27, 28, 29, 30, 31, 32] have been carried out on this material to have a proper understanding of reaction or initiation mechanism of energetic materials [6, 28]. The study of poly-nitro compounds, in which one carbon atom is attached with many nitro groups, has also found particular interest. In this connection, a report on a detailed understanding of IR and Raman spectra of poly-nitroalkanes is worth mentioning [33]. This kind of study helps to understand different properties of mono- and poly-nitro compounds comparatively, which on the other hand, helps us to find more efficient energetic materials. As a result, knowledge of different important properties of di-, tri- and tetra- nitromethane is also important to have a complete understanding of such kinds of materials. In this connection, Tafipolsky et al. [34] reported ab initio results regarding the structural and vibrational properties of di- as well as of tri- nitromethane. Dinitromethane is known to have very low thermal stability [35] whereas trinitromethane is a low explosive that decomposes at 298 K and detonates easily by friction or impact. Report of a dangerous explosion at the time of preparation of sodium trinitromethanide salt can be seen in literature [36]. On the other hand, tetranitromethane (TNM) can serve as a powerful explosive while mixed with nitrobenzene, which is also known for its well-characterized oxidant nature. The structural properties along with the vibrational frequencies of poly-nitromethanes have theoretically been reported by Vladimiroff [37] and Tafipolsky et al. [34]. Though dinitromethane shows less thermal stability, its salts are known to possess different properties. For example, potassium and ammonium salts of dinitromethane show different storage properties, such as different decomposition temperatures of 220 C and 105-110 C, respectively [38]. Potassium dinitromethane [$KCH(NO_2)_2$]

salt was prepared by Villiers [39], for the first time, in 1884. In this method, potassium bromonitromethane was reduced with hydrogen sulfide, which resulted in very low yield of the desired product. Later, in 1951, Feuer and co-workers [40] have synthesized this salt from chloronitromethane via Ter Meer reaction in 23% overall yield. Grakauska and coworkers [38] in 1978, prepared KDNM in slightly improved yield (33%) starting from methyl-dinitroacetic acid. Recently, Latypov and coworkers [41] reported a three-step methodology for the synthesis of KDNM, starting from barbituric acid, which afforded the final product via dinitrobarbituric acid in 33% (4 steps) and 50% (3 steps) overall yield, respectively. More recently, Kang-zhen and coworkers [42] have synthesized KDNM from FOX-7 in four steps in 32% overall yield. Though both the sodium and potassium dinitromethane salts can be stored at ambient temperature for months, the ammonium dinitromethane salt can be found to decompose spontaneously at an appreciable rate. Also, a recent report on guanidinium dinitromethanide shows that it possesses good thermal stability with exceptionally low sensitivity towards mechanical stimuli among earlier known salts of dinitromethane which are phenylhydrazinium dinitromethanide, [43] guanidinium dinitromethanide, [44] 1-ethyl-3-methylimidazolinium dinitromethanide [45] diethylammonium dinitromethanide, [46] tetraethylammonium dinitromethanide, [47] and piperidinium dinitromethanide [48]. Furthermore, due to the ability to respond in non-linear optics, particularly in second-harmonic generation, organic salts, which are non-centrosymmetric, show utmost importance in the development of novel hybrid materials useful for frequency modulation and data storage applications [49]. In search of convenient candidates in this area, the presence of extended H-bonding and delocalized p-electrons are one of the qualifications which help to cause Y-aromaticity in -CN and -NO_2 groups [50]. Nitroform or trinitromethane is also a well-known polynitro compound and has been studied from the end of the eighteenth-century [51]. Though initially it was thought of as a useful explosive or explosive oxidant due to the presence of high nitrogen and oxygen contents, the main issues with this compound are its low decomposition temperature of 298 K and strong acidity. On the other hand, nitroformate salts have been studied widely [52, 53, 54, 55, 56, 57, 58, 59, 60, 61] which show a great deal of interest with high detonation performances and as eco-friendly oxidizers. In this connection, hydrazinium nitroformate is known as a promising replacement of ammonium perchlorate (AP), which is normally being used as solid rocket propellant [62, 63, 64, 65] and have disadvantages of having low energy, high mechanical sensitivity, and high average molecular weight of burning gas [66, 67]. In order to find improved specific impulse-based propellants, nitroformate salts can play a crucial role which is also advantageous over strongly hygroscopic ammonium dinitramide (ADN) [68, 69]. Along with hydrazinium nitroformate, ammonium nitroformate also shows good energetic properties with crystal density above 1.85 gcm^3, and oxygen balance above 10% [61, 70]. Friction as well as impact sensitivity of guanidinium nitroformate were found to be better than TNT [71] and RDX

[72]. At the same time, it is comparable to RDX energetically. A wide variety of nitroformate salts have been reported in the literature. Heterocyclic nitroformate salts were also studied which can be used as potential energetic materials [58, 61, 62, 73, 74, 75, 76, 77]. Among other nitroformate salts, potassium nitroformate, [53] sodium nitroformate, [78] silver nitroformate, melaminium nitroformate, [79] formamidinium nitroformate [80] and derivatives of HNF were well mentioned in literature. On the other hand, the nitramino group (-$NHNO_2$) [71] is known to reduce this unwanted interaction and at the same time provides hydrogen bonding. This, in turn, reduces sensitivity and enhances detonation performances by forming closed crystal packing and hence increasing density as well as better oxygen balance [81]. This hydrogen bond-forming capability of the nitramino group is found to be unique for the formation of different energetic salts with desired properties [82]. A perfect combination of strong H-bonds and energetic groups is also known as an important criterion in order to obtain desired properties of energetic materials [83]. Though the use of a single nitramino group has been observed to provide low sensitivity along with low detonation performance,[84] addition of more -$NHNO_2$ group is known to provide good detonation properties, but less stability, specifically for dinitramino compounds [85, 86]. Among other nitrogen-based groups, azido and N-oxide groups are worth mentioning. With enhanced nitrogen content, the azido group increases the heat of formation of associated energetic material by 300 to 350 kJ mol^{-1} [87]. The main drawbacks of using this group are high sensitivity toward heat, impact and friction stimuli [88, 89]. The use of N-oxide, on the other hand, provide good oxygen balance and high density with low molecular stability and lower heat of formation [90, 91]. As it can be seen that the contribution of different groups is positive as well as negative in finding high performing and low sensitive energetic materials, a proper combination is very much important for designing perspective. In this context, poly-nitro compounds show high exothermicity of combustion, better density and high detonation process with good oxygen balance. Nitro-based materials are also important in space due to withstanding ability of high temperature and low-pressure [92]. Besides showing its good oxidizing properties, nitro group-based materials form nitrogen gas upon decomposition and hence increase the power of explosion [93]. Some worth-mentioning members of nitro-based energetic materials are TNT, RDX, HMX, and CL-20. Understanding of different energetic properties of such materials through computational methods shows advantageous over dangerous experiments involved with these materials. As the structure-properties correlation is linked with electronic structure and different interactions present in these materials, a lot of information can be found out from such studies, which help in designing potential new energetic materials [94, 95, 96, 97, 98, 99]. Also, as the HNF precursor hydrazine hydrate is known as carcinogenic, an attempt has been made to design nitroformate based benign energetic salts [62]. In this connection, a great deal of information can be obtained from a theoretical understanding of such materials. So as significantly fewer theoretical studies

have been found on such materials, we have attempted to understand different properties of di- and trinitromethane-based materials by conducting a comparative theoretical study. In this regard, we have considered potassium dinitromethane (KDNM), formamidinium nitroformate (FNF), methylhydrazinium nitroformate (MHNF) and potassium nitroformate (KNF) as our studied materials. FNF is reported to be an insensitive RDX replacement [101]. Synthesis [100] as well as characterization of MHNF through element analysis, IR spectroscopy, impact sensitivity, and thermal gravimetric analysis have been reported earlier [94]. Reports on crystal structure, sensitivity, NMR, vibrational, and mass spectra of KNF can also be found in literature [60]. Along with these reports, our comparative theoretic study on these materials will provide a deep insight into such materials and help us to design well desired energetic materials. This chapter is organized as follows: computational details have been discussed in the next section. Then the result and discussion of this study have been presented. In the end, the conclusion of this study is drawn.

4.2 Computational Details

Plane-wave pseudo-potential (PW-PP) method based DFT [102, 103, 104] study has been performed in this work for obtaining a proper theoretical understanding of structural along with the vibrational properties of KDNM. Cambridge Serial Total Energy Package (CASTEP) [105, 106] code has been employed in this consideration. The exchange-correlation contribution has been incorporated through generalized gradient approximation (GGA) [107, 108] and local density approximation (LDA) [109]. Among these approximations, GGA has been implemented through PBE and PW91 schemes. In order to calculate different lattice parameters of our studied materials accurately, different vdW corrected schemes such as LDA+OBS, PW91+OBS, PBE+D2 and PBE+TS have been considered. Though the implementation of these schemes is nearly similar, the TS scheme uses polarizability of bonds present in materials along with the contribution of chemical composition [110]. On the other hand, OBS and Grimme schemes are mainly dependent on chemical compositions. Norm-conserving pseudo-potential with 900 eV for KDNM, 1000 eV for FNF, 950 eV for KNF and 900 eV for MHNF were considered as the plane wave energy cutoff. Brillouin zone sampling of these materials was obtained using Monkhorst-Pack scheme [111]. In this regard, a K-points spacing of 0.04 $Å^{-1}$ with k-grids of $6 \times 4 \times 3$ for KDNM, 0.04 $Å^{-1}$ with k-grids of $4 \times 4 \times 3$ for FNF, a K-points spacing of 0.03 $Å^{-1}$ with k-grids of $5 \times 4 \times 4$ for KNF and a K-points spacing of 0.03 $Å^{-1}$ with k-grids of $4 \times 4 \times 3$ for MHNF have been considered. For obtaining geometry optimization of our studied materials, we have used Broyden-Fletcher-Goldfarb-Shanno (BFGS) algorithm [112]. Other different convergence criteria involved in our calculation for obtaining optimized crystal structures are force minimization (< 0.01 eV/Å) and energy minimization ($< 5 \times 10^{-6}$ eV) on each atom. After obtaining detailed structural information from a normal DFT study, density functional perturbation theory (DFPT), which is based on linear response theory, has been employed to calculate the vibrational properties of this material. Involved valence electrons of constituting atoms are as follows: H ($1s^1$), C ($2s^2 2p^2$), N ($2s^2 2p^3$) and O ($2s^2 2p^4$) and K ($3s^2 3p^6 4s^1$).

4.3 Results and Discussion

4.3.1 Structural properties

Among our studied materials, KDNM crystallizes in a triclinic crystal structure with P-1 space group and with a very high-density value of 2.14 gm/cm^3. The dinitromethane (DNM) ($CH(NO_2)_2$), which is known to consist of 2 -NO_2 group attached with one C atom bonded with potassium ion K^+ to form this salt. The number of molecular formula units and the total number of atoms associated with a single unit cell of KDNM is 2 and 18. In the case of formate based materials, the common building block of our studied materials, nitroformate ($C(NO_2)_3$), is known to form with a single carbon atom and 3 -NO_2 group attached to it. Along with the nitroformate group, the molecular formula of FNF, MHNF and KNF are associated with $CH(NH_2)_2$, $CH_3(NH_2)_2$ and K ion, respectively. The molecular formula unit and number of atoms in the unit cell of these crystalline materials are 2, 4 and 4 and 32, 80 and 44, respectively. Among these studied materials, FNF is found to crystalize in triclinic crystal structure with space group P-1. The other two materials KNF and MHNF crystallize in monoclinic crystal structure with space group *P21/N*. Images of the crystal structure of KDNM oriented in different directions have also been depicted in Figure 4.1. Crystal structures of FNF, MHNF and KNF have been depicted in Figure 4.2. After obtaining a thorough knowledge about the structural properties of these materials from experimental data, a detailed density

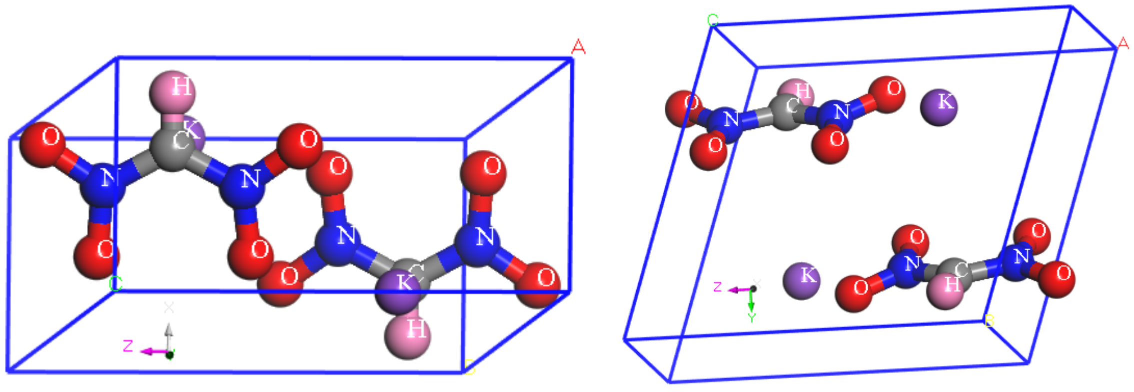

(a) (b)

Figure. 4.1 Crystal structure of KDNM in different orientations (a depicts perpendicular to XZ plane and b depicts perpendicular to ZY plane).

functional theory (DFT) study has been performed on these materials to have a deep insight into different properties associated with the studied materials. As a first step, the effect of various exchange-correlation potentials along with the effect of van der Waals interactions was tested for obtaining exact ground state structural properties. Calculated structural parameters of our studied materials shown in Table 4.1-4.4 clearly indicate a usual trend of the LDA and GGA functionals, respectively, with underestimated and overestimated values. Consideration of different vdW corrected schemes in combination with GGA functionals are found to reduce the error. Though the vdW corrected scheme of OBS with LDA functional is found to deviate more from the result, found only using LDA functional for KDNM. In general, DFT calculations with the inclusion of vdW schemes produce results that are found to be in good accord with experimental structural parameters. Among these schemes, obtained DFT results of KDNM, FNF and MHNF using PBE functional and in combination with vdW corrected Grimme method are found to match well with available experimental data. Whereas, dispersion corrected TS scheme produces very promising results regarding structural parameters of KNF. Due to this reason, these respective schemes have been considered further to investigate other crystalline properties of our studied materials. As a next step, a high-pressure study has been performed on FNF, MHNF and KNF to understand the pressure variation of structural parameters. In this connection, hydrostatic pressure up to 3 GPa in steps of 1 GPa has been applied on these structures. Pressure dependence of lattice parameters and volume of our studied materials are well depicted in Figure 4.3. Calculated pressure coefficient values of lattice parameters for FNF crystal are obtained as 0.76×10^{-4} GPa^{-1}, 1.18×10^{-2} GPa^{-1} and 2.72×10^{-2} GPa^{-1} for crystallographic a-, b- and c- directions, respectively. On the other hand, these corresponding values are 1.01×10^{-2} Gpa^{-1}, 8.56×10^{-3} GPa^{-1} and 9.54×10^{-3}

Table 4.1 Ground state structural details of KDNM with different norm-conserving exchange-correlation functional as well as with different van der Waals corrected schemes along with experimental results.

	Expt.	LDA	LDA+OBS	PBE	PBE+D2	PBE+TS	PW91	PW91+OBS
Space Group	*P1*							
No of atoms	18							
f.u./cell	2							
a (in Å)	4.47	4.22	3.95	4.73	4.36	3.85	4.74	4.37
b (in Å)	6.96	6.73	6.68	7.51	7.09	7.17	7.54	7.28
c (in Å)	7.84	7.74	7.77	7.92	7.99	8.26	7.91	7.94
α(°)	70.54	70.42	68.59	71.68	70.98	66.58	71.67	69.66
β(°)	88.62	88.52	88.21	88.21	88.55	87.46	88.21	88.91
γ(°)	76.55	77.90	80.75	72.68	77.35	80.02	72.45	76.13
Vol (in Å^3)	223.25	202.22	188.35	254.15	227.61	205.94	254.85	229.41
△V(%)		-9.42	-15.63	+13.84	+1.95	-7.75	+14.16	+2.76

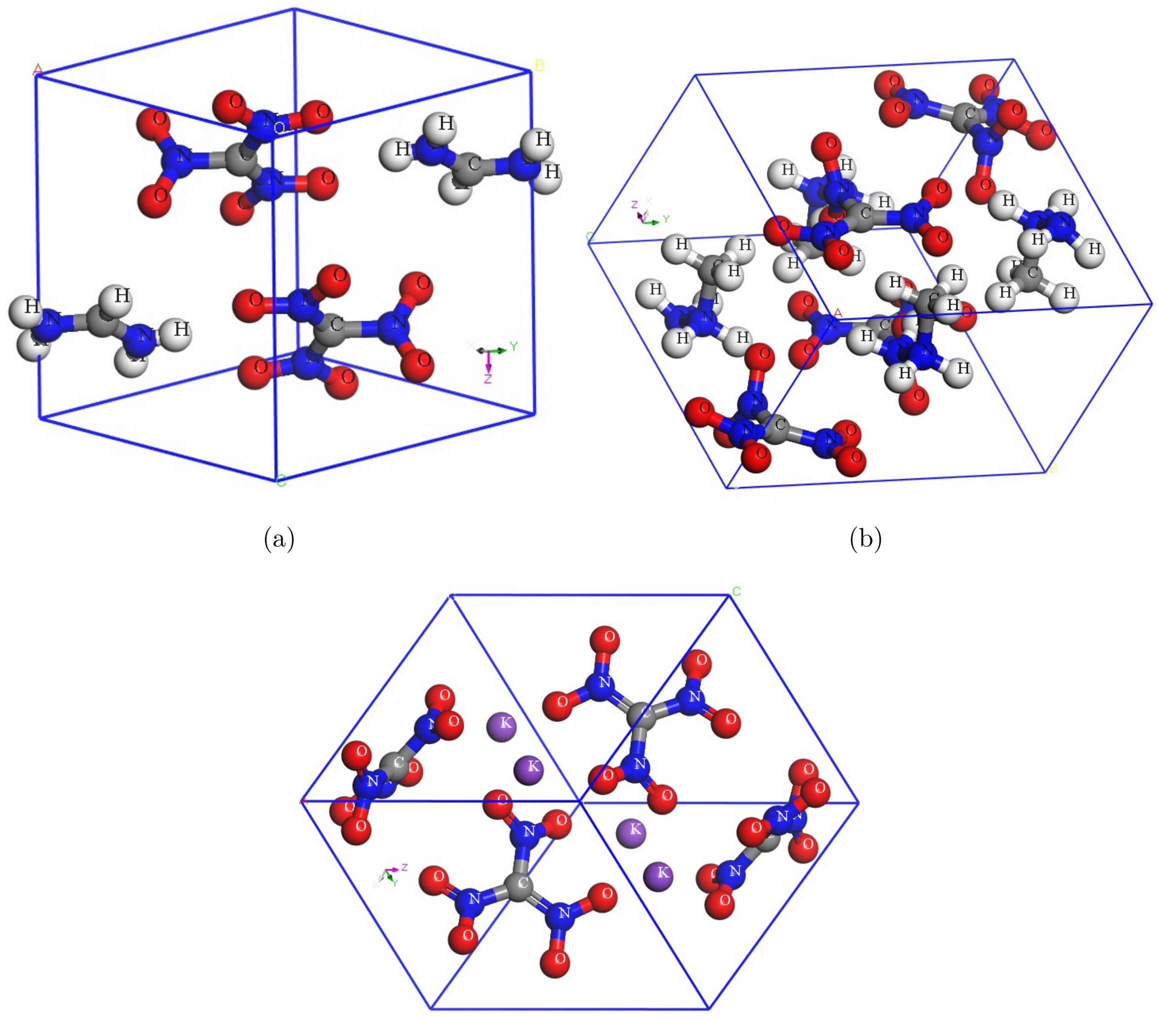

(a)

(b)

(c)

Figure. 4.2 Crystal structure of Formamidinium Nitroformate (a), Methylhydrazinium Nitroformate (b) and Potassium Nitroformate (c)

GPa^{-1} for MHNF and 5.97×10^{-3} GPa^{-1}, 8.81×10^{-3} GPa^{-1} and 8.17×10^{-3} GPa^{-1} for KNF crystals. Variation of volume of these crystals are found as 3.44×10^{-2} GPa^{-1} for FNF, 3.18×10^{-2} GPa^{-1} for MHNF and 2.27×10^{-2} GPa^{-1} for KNF, respectively. These values clearly suggest that the FNF is more and KNF is less compressible. In case of FNF crystal, the order of compressibility of crystallographic a-direction is very less compared to the other two axes. In contrast, the crystallographic c-axis is found to be more compressible. This obtained pressure coefficient value of MHNF also indicates that this material is more compressible along a-directions and less compressible along b axis. Though the order of these pressure coefficient values of KNF crystals is found to be the same but the compressibility of KNF crystal is more along b-crystallographic directions and less along a-axis. The same value of the order of pressure coefficients also indicates that KNF is

Table 4.2 Ground state structural details of FNF with different norm-conserving exchange-correlation functional as well as with different van der Waals corrected schemes along with experimental results.

	Expt.	LDA	LDA+OBS	PBE	PBE+D2	PBE+TS	PW91	PW91+OBS
Space Group	*P1*							
No of atoms	36							
f.u./cell	2							
a (in Å)	6.76	6.58	6.54	7.19	6.71	6.80	7.22	6.64
b (in Å)	7.37	7.16	6.91	7.92	7.50	7.60	8.03	7.60
c (in Å)	8.06	7.87	7.52	9.38	8.30	8.27	9.63	8.35
α(°)	98.98	97.91	95.47	104.93	100.22	100.47	106.53	101.90
β(°)	100.32	100.43	100.31	105.78	100.12	99.54	106.54	99.63
γ(°)	109.95	111.60	112.85	104.62	110.54	110.35	103.57	109.45
Vol(in Å^3)	361.30	330.51	302.55	465.74	372.08	381.69	481.50	376.10
$\triangle$V(%)		-8.52	-16.26	+28.91	+2.98	-5.64	+33.27	+4.10

Table 4.3 Ground state structural details of MHNF with different norm-conserving exchange-correlation functional as well as with different van der Waals corrected schemes along with experimental results.

	Expt.	LDA	LDA+OBS	PBE	PBE+D2	PBE+TS	PW91	PW91+OBS
Space Group	*P21/N*							
No of atoms	80							
f.u./cell	4							
a(in Å)	8.50	8.15	7.87	9.01	8.56	8.58	9.01	8.40
b(in Å)	9.21	8.96	8.82	9.34	9.22	9.27	9.32	9.23
c(in Å)	10.37	10.05	9.75	11.09	10.43	10.56	11.20	10.33
β(°)	108.35	110.03	112.36	105.24	108.55	107.83	105.21	109.27
Vol(in Å^3)	770.73	689.81	626.27	901.26	779.62	800.08	906.46	756.03
$\triangle$V(%)		-10.50	-18.74	+16.94	+1.15	-3.81	+17.61	+1.91

less anisotropic. On the other hand, the deviation of this order of FNF crystal shows its more anisotropic nature. These values also indicate the presence of strong intermolecular interactions in KNF and weak intermolecular interactions in FNF.

4.3.2 Elastic properties

After a detailed understanding of the structural properties of studied materials, knowledge about the elastic properties of these materials can help us to have a deep insight into the present intermolecular interactions in these materials. Elastic properties of energetic materials are known to be correlated to their sensitivity towards explosion as they are linked with the intermolecular interactions present in such materials. Information about these properties also helps us to have a proper understanding about the mechanical stabil-

Table 4.4 Ground state structural details of KNF with different norm-conserving exchange-correlation functional as well as with different van der Waals corrected schemes along with experimental results.

	Expt.	LDA	LDA+OBS	PBE	PBE+D2	PBE+TS	PW91	PW91+OBS
Space Group	*P21/N*							
No of atoms	44							
f.u./cell	4							
a(in Å)	7.54	7.42	7.32	7.82	7.65	7.61	7.83	7.74
b(in Å)	8.04	7.82	7.74	8.59	8.25	8.04	8.61	8.30
c(in Å)	9.03	8.74	8.59	9.61	9.12	9.12	9.65	9.34
β(°)	99.33	100.06	100.80	97.46	99.06	103.69	96.94	98.70
Vol(in Å^3)	540.36	499.68	477.83	639.72	568.86	542.24	645.46	593.49
△V(%)		-7.53	-11.57	+18.39	+5.27	+0.35	+19.45	+9.83

ity of such materials. Keeping this in mind, we have considered the stress-strain method to calculate the elastic constant of studied materials. As KDNM and FNF crystallize in triclinic symmetry and MHNF and KNF crystalize in monoclinic symmetry, a sum of 21 and 13 independent components of elastic constant tensor were obtained respectively. The value of these components is given in the Table 4.5-4.7.

Table 4.5 Ground state independent elastic constant tensor components of KDNM (in GPa).

C11 34.15	C12 16.60	C13 18.82	C14 -0.22	C15 0.99	C16 -13.66
C21 –	C22 20.89	C23 9.42	C24 0.38	C25 -1.30	C26 -6.95
C31 –	C32 –	C33 70.02	C34 1.68	C35 0.96	C36 1.60
C41 –	C42 –	C43 –	C44 4.77	C45 -3.94	C46 -0.24
C51 –	C52 –	C53 –	C54 –	C55 17.06	C56 -0.18
C61 –	C62 –	C63 –	C64 –	C65 –	C66 14.39

Though a direct comparison between these elastic constant components of triclinic and monoclinic crystals cannot be drawn due to their different symmetry, the mechanical stability of these compounds is confirmed. The ordering of the elastic constants along the principal axis for FNF is C22>C11>C33, whereas the ordering of these components for KDNM is C33>C11>C22. This tells that FNF is more sensitive along z-direction and KDNM is more sensitive along y-crystallographic direction due to shock. In case of MHNF and KNF, this ordering is as follows: C22>C33>C11 for MHNF and C11>C22>C33 for

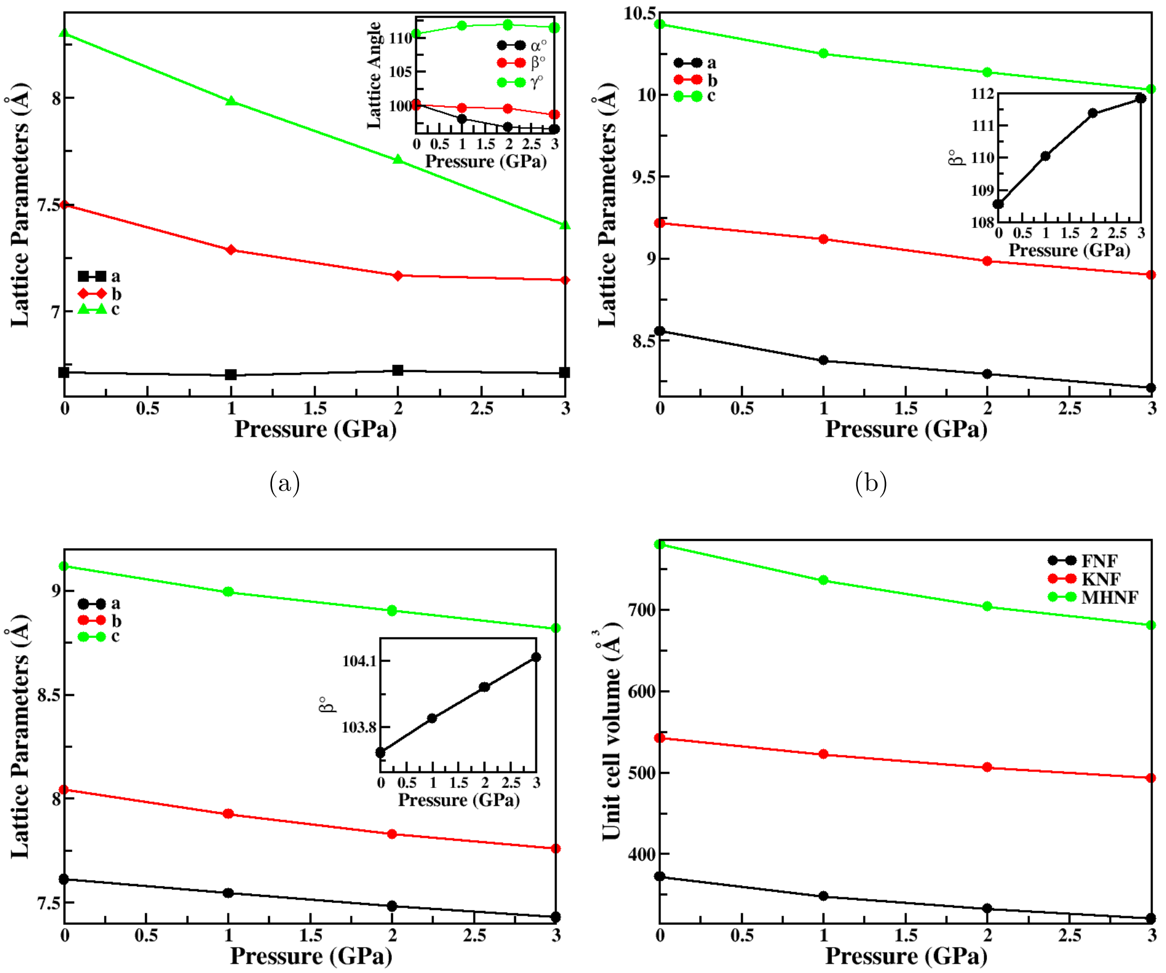

(a)

(b)

(c)

(d)

Figure. 4.3 Pressure variation of lattice parameters and volume of Formamidinium Nitroformate (a), Methylhydrazinium Nitroformate (b) and Potassium Nitroformate (c) crystal structures. Pressure variation of volume has been shown in (d).

KNF. This indicates that the directional shock sensitivity is less along crystallographic y-direction for FNF and MHNF and x-direction for KNF. On the other hand, FNF and KNF are found to be more sensitive along the z-direction, and MHNF is more sensitive along the x-direction. The high bulk modulus value of KNF also indicates its less sensitive nature compared to other studied materials. The calculated polycrystalline bulk modulus of KDNM is found to be 19.17 GPa which is similar to the bulk modulus value of AP (19.69 GPa) [113]. The bulk modulus value of KDNM is relatively large when compared to solid nitromethane (10.32 GPa) [114]. It is interesting to note that the bulk modulus value of KDNM is of the same order as ADN (18.48 GPa) [115] and KDN (20.9 GPa) [116]. This clearly indicates that the bulk modulus value of the above-mentioned oxidizers is similar. After obtaining elastic properties of these materials at 0 GPa, pressure variation

Table 4.6 Ground state independent elastic constant tensor components of FNF (in GPa).

C11 37.23	C12 14.11	C13 18.09	C14 -3.06	C15 15.25	C16 -3.39
C21 –	C22 42.70	C23 11.54	C24 9.22	C25 0.55	C26 -5.85
C31 –	C32 –	C33 22.33	C34 4.56	C35 10.85	C36 6.83
C41 –	C42 –	C43 –	C44 13.32	C45 2.39	C46 7.60
C51 –	C52 –	C53 –	C54 –	C55 19.17	C56 4.09
C61 –	C62 –	C63 –	C64 –	C65 –	C66 13.88

Table 4.7 Ground state independent elastic constant tensor components of MHNF and KNF (in GPa).

	C11	C22	C33	C44	C55	C66	C12	C13	C15	C23	C25	C35	C46
MHNF	30.45	56.45	33.54	7.77	10.04	4.75	7.15	5.88	-3.17	13.31	-2.24	-2.71	-1.92
KNF	55.59	40.64	39.27	16.63	16.51	16.73	18.37	15.36	-4.21	16.35	1.63	-1.46	-0.16

Table 4.8 Obtained value of the Bulk, Shear and Young's Modulus and Poison's Ratio of studied materials.

	Bulk Modulus(GPa)	Shear Modulus(GPa)	Young's Modulus(GPa)	Poison's Ratio
KDNM	19.17	9.44	24.34	0.29
FNF	17.42	8.55	22.05	0.29
MHNF	17.94	9.44	24.08	0.28
KNF	25.85	15.41	38.56	0.25

of elastic properties of nitroformate based energetic materials has also been studied. A clear indication of increment of these values with respect to pressure can be observed from Figure 4.4.

4.3.3 Born effective charge and Vibrational properties

Coupling of electrostatic field and displacement of the lattice is known to be described by born effective charge tensor of any material. This quantity allows us to have more knowledge about vibration as well as optical properties. Linear response theory-based DFPT implemented in CASTEP code has been considered for calculating this quantity of our studied materials. The convergence of related calculation satisfies the acoustic sum rule. Calculated BEC of all the elements of studied materials are given in Table 4.9-4.12. A significant amount of reduction of charge from its nominal charge can be seen for every element of these compounds except the K atom of KDNM and KNF, where an increment

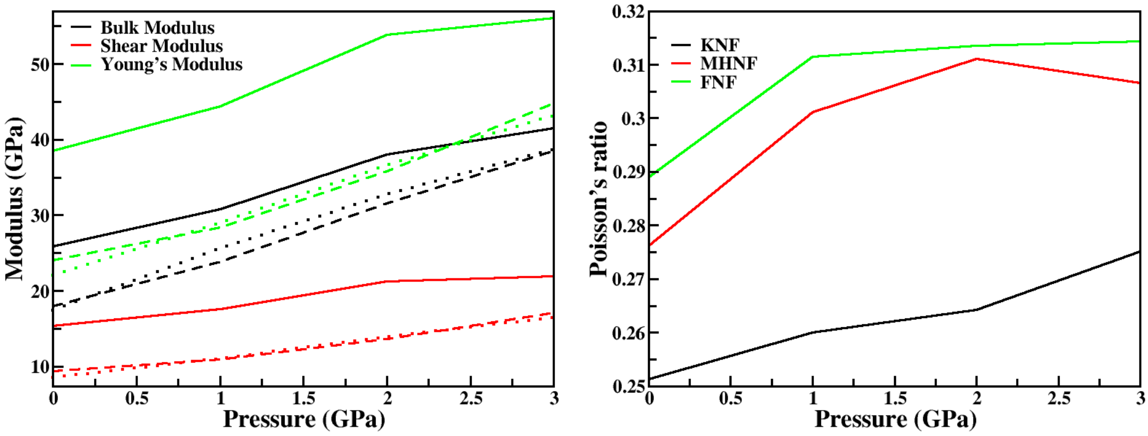

(a) (b)

Figure. 4.4 Pressure variation of Bulk, Shear, Young's Modulus (shown in a) and Poison's ratio (shown in b) of KNF, MHNF, and FNF. (Solid lines, Dashed lines, and dotted lines used in (a) indicate KNF, MHNF, and FNF, respectively).

in the BEC can be observed. This made us to interpret that an ionic bonding can be seen between the di- and trinitromethane groups with the K atom, whereas every element in the di- and trinitromethane are covalently bonded with little presence of ionicity. Other elements present in $CH(NH_2)_2$ and $CH_3(NH_2)_2$ groups are also found to bonded covalently in these respective groups.

Table 4.9 Calculated BECs of K, C, N, H and O atoms of KDNM

Atoms	Ionic	Z^*_{11}	Z^*_{22}	Z^*_{33}
H	1	0.47	0.31	0.00
C	4	-0.25	-0.13	-2.03
N1	-3	1.60	0.69	2.85
N2	-3	1.60	0.71	3.25
O1	-2	-1.44	-0.68	-0.80
O2	-2	-0.84	-0.71	-2.11
O3	-2	-0.99	-0.68	-1.83
O4	-2	-1.42	-0.69	-0.90
K	1	1.26	1.17	1.57

Optimized crystal structure of KDNM, FNF and MHNF with the van der Waals corrected Grimme method and of KNF with TS scheme have been considered for obtaining gamma-point phonon frequencies and associated mode symmetry of these materials. Linear response theory-based density functional perturbation theory (DFPT) approach has been considered in this connection. A sum of 54, 108, 240 and 132 Γ-point phonon modes

Table 4.10 Calculated BECs of C, N, H and O atoms in FNF

Atoms	Ionic	Z^*_{11}	Z^*_{22}	Z^*_{33}
H1	1	0.41	0.93	0.57
H2	1	0.85	0.27	0.56
H3	1	0.15	0.26	0.24
H4	1	0.54	0.76	0.31
H5	1	0.81	0.20	0.56
C1	4	-0.73	-0.41	-0.82
C2	4	0.53	2.15	0.40
N1	-3	1.92	1.79	1.42
N2	-3	1.23	1.53	1.58
N3	-3	1.65	2.13	1.30
N4	-3	-0.91	-1.55	-0.61
N5	-3	-0.66	-1.51	-0.68
O1	-2	-1.30	-1.01	-0.69
O2	-2	-0.92	-1.37	-0.85
O3	-2	-0.91	-0.68	-0.80
O4	-2	-0.58	-1.01	-0.98
O5	-2	-1.47	-0.78	-1.02
O6	-2	-0.61	-1.71	-0.48

was obtained from these calculations for KDNM (contains 36 atoms), FNF (contains 36 atoms), MHNF (contains 80 atoms) and KNF (contains 44 atoms) crystal. Out of these many modes, the first three modes are acoustic, and the rest modes are optical in nature. These optical modes are further known as IR-active and Raman active depending on their symmetry. The irreducible representation of Γ-point phonon modes of these materials can be expressed as:

Γ_{KDNM} = 27 A_u + 27 A_g

Γ_{FNF} = 54 A_u + 54 A_g

Γ_{MHNF} = 60 A_u + 60 B_u + 60 A_g + 60 B_g

Γ_{KNF} = 33 A_u + 33 B_u + 33 A_g + 33 B_g

A proper description of these modes of our studied materials is given in Tables 4.13-4.16. Along with these Γ-point modes, the study of the IR spectrum of these materials has also been presented in this chapter. Figure 4.5-4.8 clearly depicts the IR spectrum of KDNM, FNF, MHNF and KNF mainly divided into three regions (except KNF) for the better understanding.

Table 4.11 Calculated BECs of C, N, H and O atoms in MHNF

Atoms	Ionic	Z^*_{11}	Z^*_{22}	Z^*_{33}
H1	1	0.11	0.02	0.13
H2	1	0.10	0.23	0.06
H3	1	0.08	0.04	0.16
H4	1	0.40	0.93	0.32
H5	1	0.15	1.29	0.41
H6	1	0.32	0.28	0.40
H7	1	0.29	0.31	0.33
C1	4	-0.10	-1.85	0.01
C2	4	0.23	0.04	0.07
N1	-3	-0.07	-0.79	-0.14
N2	-3	-0.52	-0.48	-0.32
N3	-3	2.2	0.37	1.84
N4	-3	0.48	2.82	1.84
N5	-3	0.40	2.99	1.81
O1	-2	-0.49	-1.94	-0.80
O2	-2	-0.40	-0.77	-1.64
O3	-2	-0.45	-0.76	-1.68
O4	-2	-0.36	-2.11	-0.86
O5	-2	-1.39	-0.31	-0.80
O6	-2	-1.00	-0.34	-1.15

Table 4.12 Calculated BECs of K, C, N and O atoms of KNF

Atoms	Ionic	Z^*_{11}	Z^*_{22}	Z^*_{33}
C	4	-1.18	-0.77	-0.95
N1	-3	2.37	0.54	2.20
N2	-3	1.34	1.66	2.08
N3	-3	2.88	2.18	0.10
O1	-2	-1.80	-0.36	-0.59
O2	-2	-0.79	-0.67	-1.43
O3	-2	-0.63	-0.62	-1.70
O4	-2	-1.75	-0.79	-0.32
O5	-2	-1.16	-0.96	-0.53
O6	-2	-0.72	-1.53	-0.27
K	1	1.44	1.32	1.42

Table 4.13 Calculated zone centered vibrational phonon frequencies of triclinic KDNM. Frequencies, associated symmetry along with the assignment of these modes are reported. [Trans. = Translational, Rot. = Rotation, Rock. = Rocking, Twist. = Twisting, Wagg.= Wagging, Sci. = Scissoring, Sym. Str. = Symmetric Stretching and Asym. Str. = Asymmetric stretching.]

Frequency (cm^{-1})	**Symmetry**	**Mode**	**Assignment**
69.54	A_u	IR	Rot.
71.81	A_g	Raman	Trans.
76.49	A_g	Raman	Trans.
93.99	A_g	Raman	Rot.
94.99	A_u	IR	Rot.
98.11	A_u	IR	Rot.
105.17	A_g	Raman	Rot.
113.63	A_u	IR	Rot.
118.53	A_g	Raman	Rot.
131.60	A_g	Raman	Rot. + Twist. in NO_2
136.61	A_g	Raman	Rot. + Twist. in NO_2
137.20	A_u	IR	Rot. + Twist. in NO_2 + trans. of K atoms
145.54	A_g	Raman	Trans. + Twist. in NO_2
149.03	A_g	Raman	Rot. + Twist. in NO_2
153.11	A_u	IR	Twist. in NO_2
165.21	A_g	Raman	Trans. + Twist. in NO_2
178.22	A_u	IR	Trans. + Twist. in NO_2
202.83	A_g	Raman	Twist. in ONCH
212.68	A_u	IR	Twist. in ONCH
278.84	A_g	Raman	Rock. of NO_2
280.92	A_u	IR	Rock. of NO_2
418.87	A_u	IR	Rot. of CHN_2 + Rock. of NO_2
421.93	A_g	Raman	Rot. of CHN_2 + Rock. of NO_2
459.28	A_g	Raman	Sci. of ONCNO and NO_2
461.34	A_u	IR	Sci. of ONCNO and NO_2
707.51	A_g	Raman	Wagg. of CH bond
709.66	A_u	IR	Trans. of CHN_2 + Sci. in NO_2
712.27	A_g	Raman	Wagg. of CH bond + Sci. in NO_2
717.75	A_u	IR	Wagg. of CN bond and NO_2
719.57	A_u	IR	Twist. of NCH

Continued on next page

Table 4.13 – *Continued from previous page*

Frequency (cm^{-1})	**Symmetry**	**Mode**	**Assignment**
720.08	A_g	Raman	Twist. of CN_2
731.76	A_g	Raman	Wagg. of CH
741.32	A_u	IR	Wagg. of CH
765.91	A_g	Raman	Wagg. of CH and Sci. in NO_2
766.44	A_u	IR	Wagg. of CH and Sci. in NO_2
974.13	A_u	IR	Str. of NO and NC bonds
980.63	A_g	Raman	Str. of NO and NC bonds
1064.59	A_u	IR	Rock. of CH + Str. of NO bonds
1074.05	A_g	Raman	Rock. of CH + Str. of NO bonds
1194.50	A_u	IR	Rock. of CH + Asym. Str. of NO bonds
1207.28	A_g	Raman	Rock. of CH + Asym. Str. of NO bonds
1305.10	A_u	IR	Str. of NO and NC bonds
1306.24	A_g	Raman	Rock. of CH + Str. of NO bonds
1318.83	A_u	IR	Rock. of CH + str. of NO bonds
1350.75	A_g	Raman	Asym. Str. of CN bonds + str. of NO bonds
1396.90	A_u	IR	Rock. of CH bond + Asym. Str. of ONC bonds
1408.07	A_u	IR	Rock. of CH + Asym. Str. of NO_2 + str. of CN bond
1411.18	A_g	Raman	Sym. Str. of CN bonds
1413.32	A_g	Raman	Rock. of CH + Asym. Str. of CNO bonds
3132.98	A_g	Raman	Str. of CH bond in opposite direction
3139.55	A_u	IR	Str. of CH bond in same direction

Table 4.14 Calculated zone centered vibrational phonon frequencies of triclinic FNF. The mode assignment, symmetry and frequencies are reported. Rot. = Rotation, Trans. = Translational, Rock. = Rocking, Wagg.= Wagging, Twist. = Twisting, Sci. = Scissoring, Asym. Str. = Asymmetric stretching and Sym. Str. = Symmetric Stretching.

Frequency (cm^{-1})	**Symmetry**	**Mode**	**Assignment**
40.92	A_g	Raman	Rot.
53.39	A_u	IR	Rot.
57.24	A_g	Raman	Rot.
61.32	A_g	Raman	Rot.
73.80	A_u	IR	Rot.
74.06	A_g	Raman	Rot.
77.09	A_u	IR	Rot.
78.13	A_g	Raman	Rot.
82.16	A_g	Raman	Rot. + Twist. in NO_2
85.80	A_u	IR	Rot. of $CHNH_2$ + Twist. in NO_2
86.39	A_g	Raman	Rot. of $CHNO_2$ + Twist. in NO_2
92.74	A_u	IR	Rot.
95.91	A_g	Raman	Rot. of $CHNO_2$ + Twist. in NO_2
105.99	A_u	IR	Rot. of $CHNO_2$ + Twist. in NO_2
108.54	A_g	Raman	Rot. of $CHNO_2$ + Twist. and Rock. in NO_2
109.16	A_g	Raman	Rot. of $CHNH_2$
117.78	A_g	Raman	Trans. of $CHNO_2$
118.17	A_u	IR	Rot. of $CHNH_2$ + Twist. in NO_2
127.84	A_g	Raman	Trans. of $CHNH_2$ + Twist. in NO_2
130.39	A_u	IR	Rot. of $CHNH_2$ + Twist. of NO_2
133.09	A_g	Raman	Rot. of $CHNH_2$
134.07	A_u	IR	Rot. of $CHNH_2$ + Twist. of NO_2
142.35	A_u	IR	Rot. of $CHNH_2$
145.14	A_g	Raman	Rot. of $CHNH_2$ + Rock. of NO_2 + Out of plane Trans. of C atoms
150.41	A_u	IR	Rot. of $CHNH_2$ + Rock. and Wagg. of NO_2 + Out of plane Trans. of C atoms
161.20	A_u	IR	Trans. of $CHNH_2$ + Wagg. of NO_2
162.00	A_g	Raman	Rot. of $CHNH_2$ + Wagg. in NO_2
222.92	A_g	Raman	Rot. of $CHNH_2$ + Rock. and Wagg.

Continued on next page

Table 4.14 – *Continued from previous page*

Frequency (cm^{-1})	**Symmetry**	**Mode**	**Assignment**
			of NO_2
223.89	A$_u$	IR	Rot. of $CHNH_2$ + Rock. and Wagg. of NO_2
242.18	A$_u$	IR	Rot. of $CHNH_2$ (OOP) + Rock. of NO_2 + Sci. of CN
244.15	A$_g$	Raman	Rot. of $CHNH_2$ (OOP) + Rock. of NO_2 + Sci. of CN
266.16	A$_g$	Raman	Rot. of $CHNH_2$ (OOP)
272.04	A$_u$	IR	Rot. of $CHNH_2$ (OOP)
405.29	A$_g$	Raman	Sci. of NO_2 + Str. of CN
405.51	A$_u$	IR	Sci. of NO_2 + Str. of CN
417.75	A$_u$	IR	Sci. of NO_2 + Str. of CN
418.09	A$_g$	Raman	Sci. of NO_2 + Str. of CN
460.05	A$_g$	Raman	Sci. of NO bonds
461.59	A$_u$	IR	Sci. of NO bonds
518.03	A$_g$	Raman	Rock. of NO_2 + Trans. of CN_2 (OOP)
518.15	A$_u$	IR	Rock. of NO_2 + Trans. of CN_2 (OOP)
542.16	A$_u$	IR	Rock. of NH_2 + Sci. of CN_2
543.94	A$_g$	Raman	Rock. of NH_2 + Sci. of CN_2
641.26	A$_g$	Raman	Wagg. of NH_2 + Vib. of N atoms OOP of NO_2 unit
641.98	A$_u$	IR	Sci. and Wagg. of NO_2
643.79	A$_g$	Raman	Wagg. of NH_2 and NO_2
650.46	A$_u$	IR	Wagg. and Twist. of NH_2
694.59	A$_u$	IR	Wagg. of NH_2 and Twist. of CN_2 in CNO_2
696.57	A$_g$	Raman	Twist. of CN_2 in CNO_2
703.97	A$_u$	IR	Wagg. and Twist. of NH_2 + Wagg. of CN_2 in CNO_2
705.90	A$_g$	Raman	Wagg. and Twist. of NH_2 + Wagg. of CN_2 in CNO_2
706.16	A$_u$	IR	Wagg. of NH_2 and CN_2 in CNO_2
721.64	A$_g$	Raman	Twist. of NH_2 + Wagg. of CN_2 in CNO_2
734.00	A$_u$	IR	Twist. of NH_2
749.73	A$_g$	Raman	Wagg. and Twist. in $CHNH_2$ + Sci.

Continued on next page

Table 4.14 – *Continued from previous page*

Frequency (cm^{-1})	**Symmetry**	**Mode**	**Assignment**
			of NO_2 in CNO_2
751.71	A$_g$	Raman	Wagg. of NH_2 + Sci. of NO_2 in CNO_2
751.88	A$_u$	IR	Wagg. and Twist. of NH_2 + Sci. of NO_2
760.59	A$_g$	Raman	Wagg. of NH_2 + Sci. of NO_2 and CN_2
762.72	A$_u$	IR	Wagg. of NH_2 + Sci. of NO_2 and CN_2
809.00	A$_u$	IR	Twist. of NH_2
816.67	A$_g$	Raman	Twist. of NH_2 + Wagg. of CN
835.78	A$_u$	IR	Twist. of NH_2 + Sci. of NO_2 + Str. of CN in CNO_2
836.13	A$_g$	Raman	Twist. of NH_2 + Sci. of NO_2 + Str. of CN in CNO_2
1051.35	A$_g$	Raman	Twist. of NH_2 and CH in CHNH
1053.23	A$_u$	IR	Twist. of NH_2 and CH in CHNH
1056.40	A$_u$	IR	Rock. of NH_2 and CH in $CHNH_2$
1061.01	A$_g$	Raman	Rock. of NH_2 and CH in $CHNH_2$
1103.92	A$_u$	IR	Str. of CN in CNO_2
1104.23	A$_g$	Raman	Str. of CN in CNO_2
1113.38	A$_g$	Raman	Rock. of NH_2 + Str. in CNO_2
1114.35	A$_u$	IR	Rock. of NH_2 + Str. in NO_2
1121.06	A$_u$	IR	Rock. of NH_2 + Str. of CN in $CHNH_2$
1128.78	A$_g$	Raman	Rock. of NH_2 + Str. of CN in CHNH2 + Str. of NO_2
1261.35	A$_g$	Raman	Str. of CN and NO_2 in CNO_2
1268.18	A$_u$	IR	Str. of CN and NO_2 in CNO_2
1305.11	A$_u$	IR	Rock. of CH and NH in $CHNH_2$ + Asym. Str. of NCN in CNO_2
1317.08	A$_g$	Raman	Rock. of CH in $CHNH_2$ + Asym. Str. of NCN in CNO_2
1320.55	A$_g$	Raman	Asym. Str. of ONO in CNO_2
1322.16	A$_u$	IR	Rock. of CH and NH in $CHNH_2$ + Asym. Str. of ONO in CNO_2

Continued on next page

Table 4.14 – *Continued from previous page*

Frequency (cm^{-1})	**Symmetry**	**Mode**	**Assignment**
1323.50	A$_u$	IR	Rock. of CH in CHNH$_2$ + Asym. Str. of ONO in CNO$_2$
1336.78	A$_g$	Raman	Rock. of CH in CHNH$_2$ + Asym. Str. of ONCNO in CNO$_2$
1339.16	A$_g$	Raman	Rock. of CH in CHNH$_2$ + Asym. Str. of ONO in CNO$_2$
1341.48	A$_u$	IR	Rock. of CH in CHNH$_2$ + Asym. Str. of ONO in CNO$_2$
1389.94	A$_u$	IR	Sci. in CHNH$_2$
1395.18	A$_g$	Raman	Sci. in CHNH$_2$ + Asym. Str. of ONO in CNO$_2$
1402.65	A$_g$	Raman	Rock. and Sci. in CHNH$_2$ + Asym. Str. of ONCNO in CNO$_2$
1414.29	A$_u$	IR	Rock. and Sci. in CHNH$_2$ + Asym. Str. of ONCNO in CNO$_2$
1464.27	A$_g$	Raman	Sci. of HNH in CHNH$_2$ + Asym. Str. of ONO in CNO$_2$
1464.97	A$_u$	IR	Asym. Str. of ONO in CNO$_2$
1555.12	A$_g$	Raman	Sci. of NH$_2$
1555.83	A$_u$	IR	Sci. of NH$_2$
1620.82	A$_u$	IR	Sci. of NH$_2$
1621.31	A$_g$	Raman	Sci. of NH$_2$
1692.31	A$_u$	IR	Sci. of NH$_2$ + Asym. Str. of NCN in CHNH$_2$
1699.69	A$_g$	Raman	Sci. of NH$_2$ + Asym. Str. of NCN in CHNH$_2$
3156.16	A$_g$	Raman	Str. of CH + Sym. Str. of NH$_2$
3157.97	A$_u$	IR	Str. of CH + Sym. Str. of NH$_2$
3173.66	A$_g$	Raman	Sym. Str. of NH and CH bonds
3179.23	A$_u$	IR	Sym. Str. of NH and CH bonds
3278.51	A$_u$	IR	Sym. Str. of NH bonds
3280.62	A$_g$	Raman	Sym. Str. of NH bonds
3286.53	A$_u$	IR	Asym. Str. of NH$_2$ bonds
3287.00	A$_g$	Raman	Asym. Str. of NH$_2$ bonds
3393.41	A$_g$	Raman	Asym. Str. of NH$_2$ bonds
3399.71	A$_u$	IR	Asym. Str. of NH$_2$ bonds

Table 4.15 Calculated zone centered vibrational phonon frequencies of MHNF. The mode assignment, symmetry and frequencies are reported. Rot. = Rotation, Trans. = Translational, Rock. = Rocking, Wagg.= Wagging, Twist. = Twisting, Sci. = Scissoring, Asym. Str. = Asymmetric stretching and Sym. Str. = Symmetric Stretching, OOP = out of plane.

Freq. (cm^{-1})	**Sym.**	**Mode**	**Assignment**
44.08	A_g	Raman	Rot.
45.20	A_u	IR	Rot.
47.15	B_g	Raman	Trans.
48.57	B_u	IR	Trans.
55.08	A_u	IR	Rot.
56.60	A_g	Raman	Trans. of $C(NO_2)_3$ + Rot. of CN_2H_7
60.55	A_u	IR	Rot. in both the components
63.19	B_g	Raman	Rot. + Trans.
66.64	A_g	Raman	Trans. of $C(NO_2)_3$ + Rot. of CN_2H_7
67.11	B_g	Raman	Trans.
68.39	B_u	IR	Rot.
68.90	B_g	Raman	Rot. of CN_2H_7
70.38	B_u	IR	Rot.
74.02	A_u	IR	Rot. of CN_2H_7
78.82	A_g	Raman	Trans. and Rock. of NH_2 in CN_2H_7
84.20	B_u	IR	Rot.
84.28	B_g	Raman	Trans. of CN_2H_7 + Rot. of $C(NO_2)_3$
84.91	A_g	Raman	Rot.
85.53	B_u	IR	Rock. of NH_2 in CN_2H_7
88.27	B_g	Raman	Rot.
89.07	A_u	IR	Rot. in $C(NO_2)_3$ + Trans. in CN_2H_7
94.70	A_u	IR	Rot. in CN_2H_7 + Twist. in $C(NO_2)_3$
95.00	B_g	Raman	Rot. in CN_2H_7 + Twist. in $C(NO_2)_3$
95.16	B_u	IR	Rot. in CN_2H_7 + Twist. in $C(NO_2)_3$
97.11	A_g	Raman	Trans. + Twist. in $C(NO_2)_3$
97.57	A_u	IR	Trans. of CN_2H_7 + Twist. of NO_2 in $C(NO_2)_3$
104.92	B_g	Raman	Trans. of CN_2H_7 + Twist. of NO_2 in $C(NO_2)_3$
105.99	A_g	Raman	Rot. of CN_2H_7 + Twist. of NO_2 in

Continued on next page

Table 4.15 – *Continued from previous page*

Freq. (cm^{-1})	**Sym.**	**Mode**	**Assignment**
			$C(NO_2)_3$
108.95	A_u	IR	Trans. of CN_2H_7 + Twist. of NO_2 in $C(NO_2)_3$
109.21	A_g	Raman	Trans. of CN_2H_7 + Twist. of NO_2 in $C(NO_2)_3$
111.16	B_u	IR	Rot. in CN_2H_7 + Twist. of NO_2 in $C(NO_2)_3$
117.43	B_u	IR	Rot. in CN_2H_7 + Twist. of NO_2 in $C(NO_2)_3$
117.59	A_g	Raman	Rock. of NH_2 in CN_2H_7 + Twist. of NO_2 in $C(NO_2)_3$
117.70	B_g	Raman	Rot. in CN_2H_7 + Twist. of NO_2 in $C(NO_2)_3$
121.10	A_g	Raman	Rock. in CN_2H_7 + Twist. of NO_2 in $C(NO_2)_3$
123.69	A_u	IR	Rot. in CN_2H_7 + Twist. of NO_2 in $C(NO_2)_3$
125.38	A_g	Raman	Rot. in CN_2H_7 + Twist. of NO_2 in $C(NO_2)_3$
128.09	B_g	Raman	Rot. in CN_2H_7 + Twist. of NO_2 in $C(NO_2)_3$
128.29	B_u	IR	Rot. in CN_2H_7 + Twist. of NO_2 in $C(NO_2)_3$
133.37	A_u	IR	Rot. in CN_2H_7 + Twist. of NO_2 in $C(NO_2)_3$
140.32	A_u	IR	Rot. in CN_2H_7 + Twist. of NO_2 and Rot. of CNO_2 in $C(NO_2)_3$
140.33	B_u	IR	Rot. in CN_2H_7 + Twist. of NO_2 in $C(NO_2)_3$
141.50	A_u	IR	Rot. in CN_2H_7 + Twist. of NO_2 in $C(NO_2)_3$
143.10	A_g	Raman	Twist. of NO_2 in $C(NO_2)_3$
145.00	B_g	Raman	Rot. in CN_2H_7 + Twist. of NO_2 in $C(NO_2)_3$
147.68	B_g	Raman	Rot. in CN_2H_7 + Twist. of NO_2 in $C(NO_2)_3$

Continued on next page

Table 4.15 – *Continued from previous page*

Freq. (cm^{-1})	Sym.	Mode	Assignment
148.47	B$_u$	IR	Rot. in CN_2H_7 + Twist. of NO_2 in $C(NO_2)_3$
160.92	B$_g$	Raman	Rot. in CN_2H_7 + Rot. of CNO_2 and Wagg. of NO_2 in $C(NO_2)_3$
163.15	A$_g$	Raman	Rot. in CN_2H_7 + Rot. of CNO_2 and wagging of NO_2 in $C(NO_2)_3$
165.00	A$_u$	IR	Rot. in CN_2H_7 + Rot. of CNO_2 and Wagg. of NO_2 in $C(NO_2)_3$
170.68	B$_g$	Raman	Trans. of CN_2H_7 + Rot. of CH_3 in CN_2H_7 + Twist. of NO_2 in $C(NO_2)_3$
171.21	B$_u$	IR	Rot. of CN_2H_7 + Twist. of NO_2 in $C(NO_2)_3$
172.54	B$_u$	IR	Rot. in CN_2H_7 + Rot. of CNO_2, Wagg. and Twist. of NO_2 in $C(NO_2)_3$
173.05	A$_g$	Raman	Rot. in CN_2H_7 + Trans. of c atoms and Twist. of NO_2 in $C(NO_2)_3$
174.65	A$_u$	IR	Trans. of CN_2H_7 + Rot. of CH_3 in CN3H_7 + Twist. of NO_2 in $C(NO_2)_3$
191.17	A$_g$	Raman	Rot. of CN_2H_7
191.95	B$_g$	Raman	Rot. of CN_2H_7
193.04	B$_u$	IR	Rot. of CN_2H_7 + Wagg. of NO_2 in $C(NO_2)_3$
193.24	A$_u$	IR	Rot. of CN_2H_7
198.65	B$_g$	Raman	Rot. in CN_2H_7
211.09	A$_g$	Raman	Rot. of CH_3 and Rock. of NH_2 in CN_2H_7 + Rock. and Wagg. of NO_2 in $C(NO_2)_3$
227.23	A$_u$	IR	Rot. of CH_3 in CN_2H_7 + Sci. of CN_2 in $C(NO_2)_3$
227.59	B$_u$	IR	Rot. of CH_3 in CN_2H_7 + Sci. of CN_2 in $C(NO_2)_3$
229.37	A$_g$	Raman	Rot. of CH_3 in CN_2H_7 + Sci. of CN_2 in $C(NO_2)_3$
232.33	A$_u$	IR	Rot. of CH_3, Rock. of NH_2 in CN_2H_7 + Sci. of CN_2 in $C(NO_2)_3$
233.70	A$_g$	Raman	Rot. of CH_3 in CN_2H_7 + Sci. of CN_2 in $C(NO_2)_3$

Continued on next page

Table 4.15 – *Continued from previous page*

Freq. (cm^{-1})	**Sym.**	**Mode**	**Assignment**
234.43	B_g	Raman	Rot. of CH_3 in CN_2H_7 + Sci. of CN_2 in $C(NO_2)_3$
236.63	B_u	IR	Rot. of CH_3, Rock. of NH_2 in CN_2H_7 + Sci. of CN_2 in $C(NO_2)_3$
243.16	B_g	Raman	Rot. of CH_3 in CN_2H_7
262.78	B_u	IR	Rot. of CH_3, Rock. of NH_2 in oppo. Dir. in CN_2H_7
263.33	A_u	IR	Rot. of CH_3, Rock. of NH_2 in oppo. Dir. in CN_2H_7
279.44	B_g	Raman	Rot. of CH_3, Rock. of NH_2 in oppo. Dir. in CN_2H_7
282.71	A_g	Raman	Rot. of CH_3 + Rock. of NH_2 in oppo. Dir. in CN_2H_7
354.18	A_g	Raman	Rot. of CH_3 and Rock. of two NH_2 in oppo. Dir. in CN_2H_7
356.61	B_g	Raman	Rot. of CH_3 and Rock. of two NH_2 in oppo. Dir. in CN_2H_7
369.74	A_u	IR	Rot. of CH_3 and Rock. of two NH_2 in oppo. Dir. in CN_2H_7
370.81	B_u	IR	Rot. of CH_3 and Rock. of two NH_2 in oppo. Dir. in CN_2H_7
400.90	B_u	IR	Str. of CN bond in $C(NO_2)_3$
401.57	A_u	IR	Str. of CN bond in $C(NO_2)_3$
401.80	B_g	Raman	Str. of CN bond in $C(NO_2)_3$
402.06	A_g	Raman	Str. of CN bond in $C(NO_2)_3$
406.08	A_g	Raman	Rock. of NO_2 in $C(NO_2)_3$
406.11	A_u	IR	Rock. of NO_2 and CN_2 in $C(NO_2)_3$ and NH_2 in CN_2H_7
407.64	B_u	IR	Rock. of NO_2 and CN_2 in $C(NO_2)_3$ and NH_2 in CN_2H_7
408.25	B_g	Raman	Rock. of NO_2 and CN_2 in $C(NO_2)_3$
420.08	B_g	Raman	Sci. of NNC in CN_2H_7
422.84	A_g	Raman	Sci. of NNC in CN_2H_7
431.07	B_u	IR	Sci. of NNC in CN_2H_7
434.04	A_u	IR	Sci. of NNC in CN_2H_7

Continued on next page

Table 4.15 – *Continued from previous page*

Freq. (cm^{-1})	**Sym.**	**Mode**	**Assignment**
462.17	A_g	Raman	Sci. of CNO in $C(NO_2)_3$
463.71	A_u	IR	Sci. of NNC in CN_2H_7 and CNO in $C(NO_2)_3$
464.96	B_u	IR	Sci. of NNC in CN_2H_7 and CNO in $C(NO_2)_3$
465.01	B_g	Raman	Sci. of CNO in $C(NO_2)_3$
522.51	A_u	IR	Rock. of NO_2 and Vib. of other CN_2 (OOP) in $C(NO_2)_3$
522.52	B_u	IR	Rock. of NO_2 and Vib. of other CN_2 (OOP) in $C(NO_2)_3$
522.98	A_g	Raman	Rock. of NO_2 and Vib. of other CN_2 (OOP) in $C(NO_2)_3$
523.18	B_g	Raman	Rock. of NO_2 and Vib. of other CN_2 (OOP) in $C(NO_2)_3$
643.03	B_u	IR	Wagg. of NO_2, Sci. of NO_2 and CN_2 in $C(NO_2)_3$
643.08	B_g	Raman	Wagg. of NO_2, Sci. of NO_2 and CN_2 in $C(NO_2)_3$
643.11	A_u	IR	Wagg. of NO_2, Sci. of NO_2 and CN_2 in $C(NO_2)_3$
643.24	A_g	Raman	Wagg. of NO_2, Sci. of NO_2 and CN_2 in $C(NO_2)_3$
698.01	B_g	Raman	Wagg. of NO_2 and Twist. of CN_2 in $C(NO_2)_3$
698.02	B_u	IR	Wagg. of NO_2 and Twist. of CN_2 in $C(NO_2)_3$
698.06	A_g	Raman	Wagg. of NO_2 and Twist. of CN_2 in $C(NO_2)_3$
698.19	A_u	IR	Wagg. of NO_2 and Twist. of CN_2 in $C(NO_2)_3$
711.42	B_u	IR	Wagg. of NO_2, CN_2 and Vib. of C (OP) in $C(NO_2)_3$
712.00	A_u	IR	Wagg. of NO_2, CN_2 and Vib. of C (OP) in $C(NO_2)_3$
712.60	A_g	Raman	Wagg. of NO_2, CN_2 and Vib. of C (OP) in $C(NO_2)_3$

Continued on next page

Table 4.15 – *Continued from previous page*

Freq. (cm^{-1})	**Sym.**	**Mode**	**Assignment**
712.83	B$_g$	Raman	Wagg. of NO_2, CN_2 and Vib. of C (OP) in $C(NO_2)_3$
745.22	B$_u$	IR	Twist. of CH_2 in CH_3 + Rock. of NH_2 in CN_2H_7 + Wagg., Sci. of NO_2 + Sci. of CN_2 in $C(NO_2)_3$
745.26	B$_g$	Raman	Twist. of CH_2 in CH_3 + Rock. of NH_2 in CN_2H_7 + Wagg., Sci. of NO_2 + Sci. of CN_2 in $C(NO_2)_3$
745.36	A$_u$	IR	Twist. of CH_2 in CH_3 + Rock. of NH_2 in CN_2H_7 + Wagg., Sci. of NO_2 + Sci. of CN_2 in $C(NO_2)_3$
745.82	A$_g$	Raman	Twist. of CH_2 in CH_3 + Rock. of NH_2 in CN_2H_7 + Wagg., Sci. of NO_2 + Sci. of CN_2 in $C(NO_2)_3$
757.22	A$_g$	Raman	Sci. of NO_2 and CN_2 in $C(NO_2)_3$
757.82	B$_u$	IR	Sci. of NO_2 and CN_2 in $C(NO_2)_3$
758.47	A$_u$	IR	Sci. of NO_2 and CN_2 in $C(NO_2)_3$
758.78	B$_g$	Raman	Sci. of NO_2 and CN_2 in $C(NO_2)_3$
831.92	A$_g$	Raman	Sci. of NO_2 and Str. of CN in $C(NO_2)_3$
832.15	B$_g$	Raman	Sci. of NO_2 and Str. of CN in $C(NO_2)_3$
832.28	B$_u$	IR	Sci. of NO_2 and Str. of CN in $C(NO_2)_3$ + Sci. of NH_2 in CN_2H_7
832.56	A$_u$	IR	Sci. of NO_2 and Str. of CN in $C(NO_2)_3$
863.00	A$_g$	Raman	Sci. of CNH, Rock. of CH_3, NH_2 in CN_2H_7
863.78	B$_g$	Raman	Sci. of CNH, Rock. of CH_3, NH_2 in CN_2H_7
867.16	A$_u$	IR	Sci. of CNH and Str. of CN and NN bond + Wagg. of NH_2 in CN_2H_7
868.05	B$_u$	IR	Sci. of CNH and Str. of CN and NN bond + Wagg. of NH_2 in CN_2H_7
873.36	A$_u$	IR	Rock. of CH_2 in CH_3, NH_2 in CN_2H_7
875.47	B$_u$	IR	Rock. of CH_2 in CH_3, NH_2 in CN_2H_7
881.88	B$_g$	Raman	Rock. of CH_2 in CH_3, NH_2 in CN_2H_7
882.97	A$_g$	Raman	Rock. of CH_2 in CH_3, NH_2 in CN_2H_7
985.98	B$_u$	IR	Asym. Str. of CNN, Rock. of CH_3, Wagg. of NH_2 in CN_2H_7
986.51	B$_g$	Raman	Asym. Str. of CNN, Rock. of CH_3,

Continued on next page

Table 4.15 – *Continued from previous page*

Freq. (cm^{-1})	**Sym.**	**Mode**	**Assignment**
			Wagg. of NH_2 in CN_2H_7
987.13	A_g	Raman	Asym. Str. of CNN, Rock. of CH_3, Wagg. of NH_2 in CN_2H_7
989.28	A_u	IR	Asym. Str. of CNN, Rock. of CH_3, Wagg. of NH_2 in CN_2H_7
1068.32	A_g	Raman	Rock. of CH_3 + Wagg. of NH_2 in CN_2H_7
1071.53	B_g	Raman	Rock. of CH_3 + Wagg. of NH_2 in CN_2H_7
1074.36	B_u	IR	Rock. of CH_3 + Wagg. of NH_2 in CN_2H_7
1075.05	A_u	IR	Rock. of CH_3 + Wagg. of NH_2 in CN_2H_7
1101.27	B_u	IR	Str. of CN bond in $C(NO_2)_3$
1101.32	A_g	Raman	Str. of CN bond in $C(NO_2)_3$
1101.57	A_u	IR	Str. of CN bond in $C(NO_2)_3$
1101.75	B_g	Raman	Str. of CN bond in $C(NO_2)_3$ + Twist. of NH_2 in CN_2H_7
1108.64	B_u	IR	Twist. of CH_2 in CH_3 and NH_2 in CN_2H_7
1108.69	A_u	IR	Twist. of CH_2 in CH_3 and NH_2 in CN_2H_7
1110.44	A_g	Raman	Twist. of CH_2 in CH_3 and NH_2 in CN_2H_7
1110.47	B_g	Raman	Twist. of CH_2 in CH_3 and NH_2 in CN_2H_7
1113.18	A_g	Raman	Rock. of NH_2 in CN_2H_7 + Sym. Str. of NO bonds in $C(NO_2)_3$
1117.68	B_g	Raman	Rock. of NH_2 in CN_2H_7 + Sym. Str. of NO bonds in $C(NO_2)_3$
1117.98	A_u	IR	Twist. of NH_2 and CH_2 in CN_2H_7 + Sym. Str. of NO bonds in $C(NO_2)_3$
1122.44	B_u	IR	Twist. of NH_2 and CH_2 in CN_2H_7 + Sym. Str. of NO bonds in $C(NO_2)_3$
1212.33	A_u	IR	Wagg. of NH_2, Rock. of CH_3, Sci. of NNC in CN_2H_7
1214.22	A_g	Raman	Wagg. of NH_2, Rock. of CH_3, Sci. of NNC in CN_2H_7
1214.89	B_g	Raman	Wagg of NH_2, Rock. of CH_3, Sci. of NNC in CN_2H_7

Continued on next page

Table 4.15 – *Continued from previous page*

Freq. (cm^{-1})	**Sym.**	**Mode**	**Assignment**
1215.93	B$_u$	IR	Wagg. of NH$_2$, Rock. of CH$_3$, Sci. of NNC in CN$_2$H$_7$
1259.39	A$_u$	IR	Wagg. of NH$_2$, Rock. of CH$_3$ in CN$_2$H$_7$ + Str. of CN bond in C(NO$_2$)$_3$
1259.70	A$_g$	Raman	Wagg. of NH$_2$, Rock. of CH$_3$ in CN$_2$H$_7$ + Str. of CN bond in C(NO$_2$)$_3$
1264.59	B$_u$	IR	Wagg. of NH$_2$, Rock. of CH$_3$ in CN$_2$H$_7$ + Str. of CN bond in C(NO$_2$)$_3$
1265.37	B$_g$	Raman	Twist. of NH$_2$, CH of CH$_3$ in CN$_2$H$_7$ + Str. of CN bond in C(NO$_2$)$_3$
1273.44	A$_g$	Raman	Twist. of NH$_2$ + Rock. of CH$_3$ in CN$_2$H$_7$
1278.22	B$_u$	IR	Twist. of NH$_2$ + Rock. of CH$_3$ in CN$_2$H$_7$
1281.28	A$_u$	IR	Twist. of NH$_2$ + Rock. of CH$_3$ in CN$_2$H$_7$
1282.71	B$_g$	Raman	Twist. of NH$_2$ + Rock. of CH$_3$ in CN$_2$H$_7$
1309.04	B$_u$	IR	Twist. of NH$_2$ + Wagg. of CH$_3$ in CN$_2$H$_7$ + Str. of CN and NO bonds in C(NO$_2$)$_3$
1311.67	A$_u$	IR	Twist. of NH$_2$ + Sci. of CH bonds of CH$_3$ in CN$_2$H$_7$ + Str. of CN and NO bonds in C(NO$_2$)$_3$
1312.06	B$_g$	Raman	Twist., Wagg. of NH$_2$ in CN$_2$H$_7$ + Str. of CN, NO bonds in C(NO$_2$)$_3$
1312.79	A$_g$	Raman	Twist., Sci. of NH$_2$ + Sci. of CH of CH$_3$ in CN$_2$H$_7$ + Asym. Str. of CN, NO bonds in C(NO$_2$)$_3$
1317.89	A$_u$	IR	Twist. of NH$_2$ + Sci. of CH in CH$_3$ + Asym. Str. of CN, NO bonds in C(NO$_2$)$_3$
1320.48	A$_g$	Raman	Twist. of NH$_2$ + Wagg. of CH in CH$_3$ + Asym. Str. of CN, NO bonds in C(NO$_2$)$_3$
1323.63	B$_u$	IR	Twist. of NH$_2$ + Sci. of CH in CH$_3$ + Asym. Str. of CN, NO bonds in C(NO$_2$)$_3$
1326.36	B$_g$	Raman	Twist. of NH$_2$ + Wagg. of CH in CH$_3$ + Asym. Str. of CN, NO bonds in C(NO$_2$)$_3$
1340.13	A$_g$	Raman	Twist. of NH$_2$ + Rock. in CH$_3$ + Asym. Str. of CN, NO bonds in C(NO$_2$)$_3$
1344.00	B$_g$	Raman	Twist., Wagg. of NH$_2$ + Sci. of CH$_3$ + Asym. Str. of CN, NO bonds in C(NO$_2$)$_3$

Continued on next page

Table 4.15 – *Continued from previous page*

Freq. (cm^{-1})	**Sym.**	**Mode**	**Assignment**
1348.94	A_u	IR	Twist. of NH_2 + Sci. of CH_3 + Asym. Str. of CN, NO bonds in $C(NO_2)_3$
1350.63	B_u	IR	Twist., Wagg. of NH_2 + Sci. of CH_3 + Asym. Str. of CN, NO bonds in $C(NO_2)_3$
1379.55	B_u	IR	Twist., Wagg. of NH_2 + Sci. of CH_3 + Asym. Str. of CN, NO bonds in $C(NO_2)_3$
1379.77	A_g	Raman	Twist., Wagg. of NH_2 + Sci. of CH_3 in CN_2H_7
1382.31	B_g	Raman	Twist., Wagg. of NH_2 + Sci. of CH_3 in CN_2H_7
1383.71	A_u	IR	Twist., Wagg. of NH_2 + Sci. of CH_3 in CN_2H_7
1387.72	A_g	Raman	Wagg. of NH_2 + Sci. of CH_3
1387.75	B_g	Raman	Sci. of CH_3
1388.13	B_u	IR	Sci. of CH_3
1390.32	A_u	IR	Wagg. of NH_2 + Sci. of CH_3
1410.82	B_u	IR	Twist., Wagg. of NH_2 + Sci. of CH_3 + Asym. Str. of NO bonds in $C(NO_2)_3$
1415.99	B_g	Raman	Twist., Wagg. of NH_2 + Sci. of CH_3 + Asym. Str. of NO bonds in $C(NO_2)_3$
1420.33	A_g	Raman	Sci. of CH_3 + Asym. Str. of NO bonds in $C(NO_2)_3$
1420.89	A_u	IR	Twist. of NH_2 + Sci. of CH_3 + Asym. Str. of NO bonds in $C(NO_2)_3$
1424.81	B_g	Raman	Sci. of CH_3 in CN_2H_7
1424.83	B_u	IR	Twist. of NH_2 + Sci. of CH_3
1425.67	A_u	IR	Twist. of NH_2 + Sci. of CH_3 + Asym. Str. of NO bonds in $C(NO_2)_3$
1426.63	A_g	Raman	Twist. of NH_2 + Sci. of CH_3
1431.05	A_u	IR	Twist. of NH_2 + Sci. of CH_3
1438.72	B_u	IR	Twist. of NH_2 + Sci. of CH_3
1441.32	A_g	Raman	Twist., Wagg. of NH_2 + Sci. of CH_3
1442.55	B_g	Raman	Twist., Wagg. of NH_2 + Sci. of CH_3
1451.48	A_u	IR	Twist. of NH_2 + Sci. of CH_3 + Asym. Str. of NO bonds in $C(NO_2)_3$
1458.28	B_u	IR	Twist. of NH_2 + Sci. of CH_3 +

Continued on next page

Table 4.15 – *Continued from previous page*

Freq. (cm^{-1})	**Sym.**	**Mode**	**Assignment**
			Asym. Str. of NO bonds in $C(NO_2)_3$
1460.09	A_g	Raman	Twist. of NH_2 + Sci. of CH_3 + Asym. Str. of NO bonds in $C(NO_2)_3$
1460.60	B_g	Raman	Twist. of NH_2 + Sci. of CH_3
1467.15	A_g	Raman	Twist. of NH_2 + Sci. of CH_3 + Asym. Str. of NO bonds in $C(NO_2)_3$
1469.54	B_u	IR	Twist. of NH_2 in CN_2H_7, Asym. Str. of NO bonds in $C(NO_2)_3$
1475.65	B_g	Raman	Twist. of NH_2 and Sci. of CH_3 + Asym. Str. of NO bonds in $C(NO_2)_3$
1476.22	A_u	IR	Twist. of NH_2 + Sci. of CH_3 + Asym. Str. of NO bonds in $C(NO_2)_3$
1588.98	B_u	IR	Sci. of NH_2 in CN_2H_7
1589.74	A_u	IR	Sci. of NH_2 in CN_2H_7
1594.30	A_g	Raman	Sci. of NH_2 in CN_2H_7
1595.93	B_g	Raman	Sci. of NH_2 in CN_2H_7
1618.51	A_g	Raman	Sci. of NH_2 in CN_2H_7
1624.86	A_u	IR	Sci. of NH_2 in CN_2H_7
1632.15	B_u	IR	Sci. of NH_2 in CN_2H_7
1632.73	B_g	Raman	Sci. of NH_2 in CN_2H_7
2962.17	B_u	IR	Str. of NH + Sym. Str. of CH in CN_2H_7
2963.74	A_g	Raman	Str. of NH + Sym. Str. of CH in CN_2H_7
2964.52	A_u	IR	Str. of NH + Sym. Str. of CH in CN_2H_7
2971.45	B_g	Raman	Str. of NH + Sym. Str. of CH in CN_2H_7
2995.04	B_g	Raman	Str. of NH + Sym. Str. of CH in CN_2H_7
2995.12	A_g	Raman	Str. of NH + Sym. Str. of CH in CN_2H_7
2995.37	A_u	IR	Str. of NH + Sym. Str. of CH in CN_2H_7
2995.63	B_u	IR	Str. of NH + Sym. Str. of CH in CN_2H_7
3100.11	A_g	Raman	Str. of NH + Asym. Str. of CH in CN_2H_7
3100.28	B_g	Raman	Str. of NH + Asym. Str. of CH in CN_2H_7
3102.32	A_u	IR	Str. of NH + Asym. Str. of CH in CN_2H_7
3102.50	B_u	IR	Str. of NH + Asym. Str. of CH in CN_2H_7
3114.38	A_g	Raman	Str. of NH + Asym. Str. of CH in CN_2H_7
3114.44	B_g	Raman	Str. of NH + Asym. Str. of CH in CN_2H_7
3114.89	B_u	IR	Str. of NH + Asym. Str. of CH in CN_2H_7
3114.97	A_u	IR	Sym. Str. of NH +

Continued on next page

Table 4.15 – *Continued from previous page*

Freq. (cm^{-1})	**Sym.**	**Mode**	**Assignment**
			Asym. Str. of CH in CN_2H_7
3119.84	A_g	Raman	Str. of NH + Asym. Str. of CH in CN_2H_7
3119.95	B_g	Raman	Str. of NH + Asym. Str. of CH in CN_2H_7
3127.52	A_u	IR	Str. of NH + Asym. Str. of CH in CN_2H_7
3128.60	B_u	IR	Str. of NH + Asym. Str. of CH in CN_2H_7
3291.44	B_u	IR	Sym. Str. of NH in CN_2H_7
3292.01	A_u	IR	Sym. Str. of NH in CN_2H_7
3292.57	A_g	Raman	Sym. Str. of NH in CN_2H_7
3292.78	B_g	Raman	Sym. Str. of NH in CN_2H_7
3369.30	B_u	IR	Asym. Str. of NH in CN_2H_7
3369.38	A_g	Raman	Asym. Str. of NH in CN_2H_7
3370.48	B_u	IR	Asym. Str. of NH in CN_2H_7
3370.79	B_g	Raman	Asym. Str. of NH in CN_2H_7

Table 4.16 Calculated zone centered vibrational phonon frequencies of KNF. The mode assignment, symmetry and frequencies are reported. Rot. = Rotation, Trans. = Translational, Rock. = Rocking, Wagg.= Wagging, Twist. = Twisting, Sci. = Scissoring, Asym. Str. = Asymmetric stretching and Sym. Str. = Symmetric Stretching, OOP = out of plane.

Freq. (cm^{-1})	**Sym.**	**Mode**	**Assignment**
40.52	B_u	IR	Trans.
43.29	A_g	Raman	Rot.
45.97	A_u	IR	Rot.
55.76	B_g	Raman	Rot.
56.06	A_g	Raman	Trans.
57.73	A_u	IR	Rot.
64.18	B_g	Raman	Trans.
66.98	A_u	IR	Rot. (OOP)
69.13	B_u	IR	$C(NO_2)_3$ Rot. + K atom Trans.
69.77	B_g	Raman	Trans.
72.25	A_u	IR	Trans.
72.71	A_g	Raman	Trans.
81.86	A_g	Raman	Trans.

Continued on next page

Table 4.16 – *Continued from previous page*

Freq. (cm^{-1})	**Sym.**	**Mode**	**Assignment**
84.27	B_u	IR	$C(NO_2)_3$ Rot. + K atom Trans.
84.53	B_g	Raman	$C(NO_2)_3$ Rot. + K atom Trans.
94.16	B_g	Raman	$C(NO_2)_3$ Rot. + K atom Trans.
96.40	A_u	IR	$C(NO_2)_3$ Rot. + K atom Trans.
96.64	B_u	IR	Rot. of NO_2 (OOP) + K atom Trans.
97.02	A_g	Raman	Trans.
100.87	B_u	IR	$C(NO_2)_3$ Rot. (OOP) + K atom Trans.
104.14	A_g	Raman	$C(NO_2)_3$ Rot. (OOP) + K atom Trans.
106.35	B_g	Raman	Trans.
107.47	A_u	IR	Twist. of NO_2 + Trans. K
108.68	A_g	Raman	Twist. of NO_2 + Trans. K
111.98	B_g	Raman	$C(NO_2)_3$ Rot. (OOP) + Trans. K
115.90	B_u	IR	$C(NO_2)_3$ Rot. (OOP) + Trans. K
116.86	A_u	IR	Trans.
120.87	B_u	IR	Trans., Twist. in $C(NO_2)_3$ + Trans. K atoms
123.92	B_g	Raman	Twist. of NO_2 + Trans. K
125.08	A_u	IR	Twist. of NO_2 + Trans. K
130.61	A_g	Raman	Trans., Twist. in $C(NO_2)_3$ +Trans. K
134.41	A_g	Raman	Twist. of NO_2
134.97	B_g	Raman	Trans., Twist. in $C(NO_2)_3$ + Trans. K
136.53	A_u	IR	$C(NO_2)_3$ Rot. (OOP)+ Trans. K
141.86	B_u	IR	Trans.
142.41	A_g	Raman	Twist., Rock. in $C(NO_2)_3$ + Trans. K
146.36	A_u	IR	$C(NO_2)_3$ Rot. (OOP) + Trans. K
148.84	B_u	IR	Twist. in $C(NO_2)_3$ + Trans. K
152.92	B_g	Raman	Trans.
158.54	B_u	IR	Twist. of NO_2
161.83	B_g	Raman	Twist. of NO_2 + Trans. K
165.23	A_u	IR	Twist. of NO_2
167.67	A_g	Raman	Twist. of NO_2 + Trans. of K
172.50	B_g	Raman	Twist. of NO_2 + Trans. of K
175.32	A_g	Raman	Twist. of NO_2 + Trans. of K

Continued on next page

Table 4.16 – *Continued from previous page*

Freq. (cm^{-1})	**Sym.**	**Mode**	**Assignment**
220.68	A_u	IR	Trans. of C atoms OOP
225.55	A_g	Raman	Trans. of C atoms OOP
225.82	B_u	IR	Trans. of C atoms OOP
233.71	B_g	Raman	Trans. of C atoms OOP
255.23	A_u	IR	Rock. of NO_2
259.51	B_u	IR	Rock. of NO_2
260.20	B_g	Raman	Rock. of NO_2
264.09	A_g	Raman	Rock., Trans. in $C(NO_2)_3$
268.37	B_g	Raman	Rock. of NO_2, Sci. of CN
270.67	B_u	IR	Rock. of NO_2, Sci. of CN
273.22	A_g	Raman	Rock. of NO_2, Sci. of CN
274.34	A_u	IR	Rock. of NO_2, Sci. of CN
389.81	B_u	IR	Rock. of NO_2 + Trans. of C atoms OOP
392.14	A_u	IR	Rock. of NO_2 + Trans. of C atoms OOP
393.30	A_g	Raman	Rock. of NO_2 + Trans. of C atoms OOP
394.55	B_g	Raman	Rock. of NO_2 + Trans. of C atoms OOP
432.27	B_g	Raman	Str. of CN bonds
432.36	A_u	IR	Str. of CN bonds
433.26	B_u	IR	Str. of CN bonds
433.65	A_g	Raman	Str. of CN bonds
448.53	A_u	IR	Str. of CN bonds
449.00	B_u	IR	Str. of CN bonds
449.17	A_g	Raman	Str. of CN bonds
450.14	B_g	Raman	Str. of CN bonds
462.32	B_g	Raman	Str. of CN bonds + Rock. of NO_2 + Trans. of C atoms OOP
466.07	B_u	IR	Str. of CN bonds + Rock. of NO_2 + Trans. of C atoms OOP
469.20	A_u	IR	Str. of CN bonds + Rock. of NO_2 + Trans of C atoms OOP
469.29	A_g	Raman	Str. of CN bonds + Rock. of NO_2 + Trans. of C atoms OOP

Continued on next page

Table 4.16 – *Continued from previous page*

Freq. (cm^{-1})	**Sym.**	**Mode**	**Assignment**
684.26	B$_u$	IR	OOP Rot. of CN$_3$ + Wagg. and Sci. in NO$_2$
686.26	B$_g$	Raman	OOP Rot. of CN$_3$ + Wagg. and Sci. in NO$_2$
686.53	A$_g$	Raman	OOP Rot. of CN$_3$ + Wagg. and Sci. in NO$_2$
686.59	A$_u$	IR	OOP Rot. of CN$_3$ + Wagg. and Sci. in NO$_2$
701.22	A$_g$	Raman	Twist. of CN$_2$ + Wagg. of NO$_2$
701.84	B$_g$	Raman	Twist. of CN$_2$ + Wagg. of NO$_2$
704.27	A$_u$	IR	Twist. of CN$_2$ + Wagg. of NO$_2$
706.27	B$_u$	IR	Twist. of CN$_2$ + Wagg. of NO$_2$
726.21	B$_u$	IR	Trans. of C atoms OOP + Wagg. of CN and NO$_2$
726.72	A$_u$	IR	Trans. of C atoms OOP + Wagg. of CN and NO$_2$
729.05	A$_g$	Raman	Trans. of C atoms OOP + Wagg. of CN and NO$_2$
731.07	B$_g$	Raman	Trans. of C atoms OOP + Wagg. of CN and NO$_2$
762.91	A$_u$	IR	Sci. of NO$_2$ + Wagg. of CN, NO$_2$
763.01	A$_g$	Raman	Sci. of NO$_2$ + Wagg. of CN, NO$_2$
763.98	B$_u$	IR	Sci. of NO$_2$ + Wagg. of CN, NO$_2$
764.08	B$_g$	Raman	Sci. of NO$_2$ + Wagg. of CN, NO$_2$
768.65	B$_u$	IR	Sci. of NO$_2$
770.96	A$_g$	Raman	Sci. of NO$_2$
771.55	A$_u$	IR	Sci. of NO$_2$ and CN$_2$
771.70	B$_g$	Raman	Sci. of NO$_2$ and CN$_2$
854.04	A$_u$	IR	Sci. of NO$_2$ + Str. of CN
855.03	A$_g$	Raman	Sci. of NO$_2$ + Str. of CN
855.62	B$_g$	Raman	Sci. of NO$_2$ + Str. of CN
855.99	B$_u$	IR	Sci. of NO$_2$ + Str. of CN
1124.10	A$_g$	Raman	Sym. Str. of NO$_2$
1134.40	B$_u$	IR	Sym. Str. of NO$_2$
1134.52	A$_u$	IR	Sym. Str. of NO$_2$
1135.25	B$_g$	Raman	Sym. Str. of NO$_2$

Continued on next page

Table 4.16 – *Continued from previous page*

Freq. (cm^{-1})	**Sym.**	**Mode**	**Assignment**
1136.35	A$_u$	IR	Sym. Str. of NO$_2$ + Asym. Str. of CN$_2$
1136.74	A$_g$	Raman	Sym. Str. of NO$_2$ + Asym. Str. of CN$_2$
1136.95	B$_u$	IR	Sym. Str. of NO$_2$ + Asym. Str. of CN$_2$
1137.66	B$_g$	Raman	Sym. Str. of NO$_2$ and CN$_2$
1204.90	A$_g$	Raman	Sym. Str. of NO$_2$ + Str. of CN bond
1206.20	A$_u$	IR	Sym. Str. of NO$_2$ + Asym. Str. of CN$_2$
1206.25	B$_u$	IR	Sym. Str. of NO$_2$ + Asym. Str. of CN$_2$
1222.25	B$_g$	Raman	Sym. Str. of NO$_2$ + Sym. and
		Asym. Str. of CN$_2$	
1226.40	A$_g$	Raman	Asym. Str. of CN$_2$
1245.84	B$_u$	IR	Asym. Str. of CN$_2$
1253.68	B$_g$	Raman	Asym. Str. of CN$_2$
1255.19	A$_u$	IR	Asym. Str. of CN$_2$
1339.21	A$_u$	IR	Sym. Str. of CN$_2$ + Str. of NO bonds
1342.47	B$_u$	IR	Sym. Str. of CN$_2$ and NO$_2$ + Str. of NO bonds
1344.60	A$_g$	Raman	Sym. Str. of CN bonds + Str. of NO bonds
1344.69	A$_u$	IR	Asym. Str. of NO bonds
1345.58	B$_g$	Raman	Sym. Str. of CN + Str. of NO bonds
1352.25	B$_u$	IR	Asym. Str. of NO$_2$
1365.45	B$_g$	Raman	Asym. Str. of NO$_2$
1367.72	A$_g$	Raman	Asym. Str. of NO$_2$
1408.10	B$_u$	IR	Asym. Str. of NO$_2$
1410.77	A$_g$	Raman	Asym. Str. of NO$_2$ + Sci. of CN$_2$
1429.58	A$_u$	IR	Asym. Str. of NO$_2$ + Sci. of CN$_2$
1429.61	B$_g$	Raman	Asym. Str. of NO$_2$ + Sci. of CN$_2$
1451.26	B$_g$	Raman	Asym. Str. of NO$_2$ + Sci. of CN$_2$

Continued on next page

Table 4.16 – *Continued from previous page*

Freq. (cm^{-1})	**Sym.**	**Mode**	**Assignment**
1452.02	A_g	Raman	Asym. Str. of NO_2 + Sci. of CN_2
1455.11	A_u	IR	Asym. Str. of NO_2 + Sci. of CN_2
1466.88	B_u	IR	Asym. Str. of NO_2 + Sci. of CN_2

Though Figure 4.5 is mainly divided into three regions, this figure clearly indicates that the IR frequency distribution of KDNM can further be subdivided into different regions. Frequencies below 300 cm^{-1} mainly arise as a result of rotation, translation and twisting of NO_2 group. The intensity of the frequencies from 400 to 600 cm^{-1} is significantly less, which is mainly attributed to the rocking of the NO_2 group. The region from 600 to 700 cm^{-1} is due to wagging of CH bond along with scissoring of NO_2 group. Stretching of NO and NC bonds are found to be the main reason for IR frequencies between 900 to 1000 cm^{-1}. Figure 4.5b shows mainly six peaks among which, the first peak at 1064.59 cm^{-1} is due to rocking of CH bond in association with the stretching of NO bonds. The 2nd peak, which is the highest intensity IR peak of the studied material, found at 1194.50 cm^{-1} is because of the rocking of CH bond along with the asymmetric stretching of NO bonds. Figure 4.9 very well depicts this mode for better understanding. 3rd and 4th peaks are found at 1305.10 and at 1318.83 cm^{-1}, which are due to stretching of NO and NC bonds and rocking of CH along with stretching of NO bond. Rocking of CH bond in addition to asymmetric stretching of ONC bonds and NO_2 and stretching of CN bonds are responsible for 5th and 6th peaks, which can be found at 1396.90 and 1408.07 cm^{-1}. As it is well known that the frequency associated with CH bond stretching will be at higher frequencies due to less mass of H atom, the high-frequency peak is found at 3139.55 cm^{-1}. Depiction of this mode can be seen in Figure 4.9b. Figure 4.6, 4.7 and 4.8 clearly depicts the IR spectrum of FNF, MHNF and KNF, respectively. This IR spectrum of FNF and MHNF are mainly divided into three regions and KNF divided into two regions for a better understanding of these spectrum. These figures also show the pressure variation of the IR spectrum of these studied materials. As shown in Figure 4.6, low-frequency peaks of FNF below 272.04 cm^{-1} mainly arise due to rotation and translation. Peaks between 400 to 550 cm^{-1} are mainly arise due to scissoring and rocking in NO_2 and CN bonds. Wagging and twisting of NO, NH and CN bonds provide the main contribution in the IR peaks in the frequency region 640 to 1130 cm^{-1}. IR peaks of FNF in between 1260 to 1700 cm^{-1} frequency range are found due to stretching of CN bonds, rocking of CH and NH bonds and scissoring of NH_2 group.

The high-frequency IR spectrum of FNF (shown in Figure 4.6c) is mainly contributed due

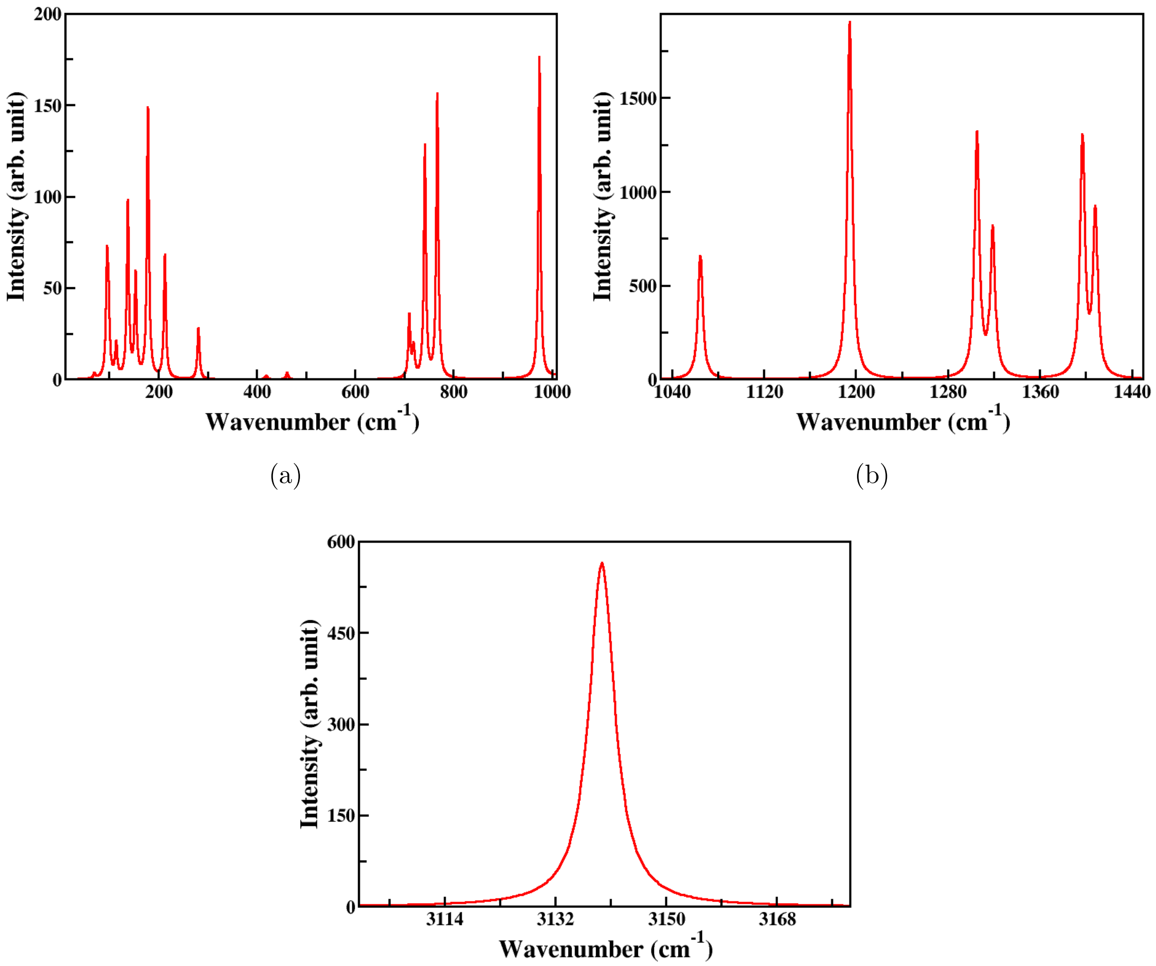

(a) (b)

(c)

Figure. 4.5 Calculated IR spectrum of triclinic KDNM in three different frequency ranges (a denotes frequency range from 0 to 1000 cm^{-1}, b denotes 1010 to 1440 cm^{-1} frequency range and c depicts the frequency range from 3114 to 3168 cm^{-1}).

to the symmetric and asymmetric stretching of NH and CH bonds present in the material. High-intensity IR peak of this material is found due to the asymmetric stretching of NH bonds. The effect of pressure on the IR spectrum of FNF has also been studied in this work and shown in the same figure with different colours indicating different pressure. Basically, a blue shift can be observed for the low-frequency IR peaks. Though the high-intensity IR peak initially shows a redshift up to 2 GPa, it shows a blue shift for 3 GPa. In case of MHNF (shown in Figure 4.7), the low-frequency range is due to rotation, translation, twisting and rocking up to 283 cm^{-1}. In the frequency range from 350 to 524 cm^{-1}, the contribution of rocking, scissoring and stretching of NO and CN bonds to the IR peaks is predominant. Wagging of NO, scissoring and twisting of NO and CN bonds show the main contribution in the frequency range from 643 to 759 cm^{-1}. Scissoring

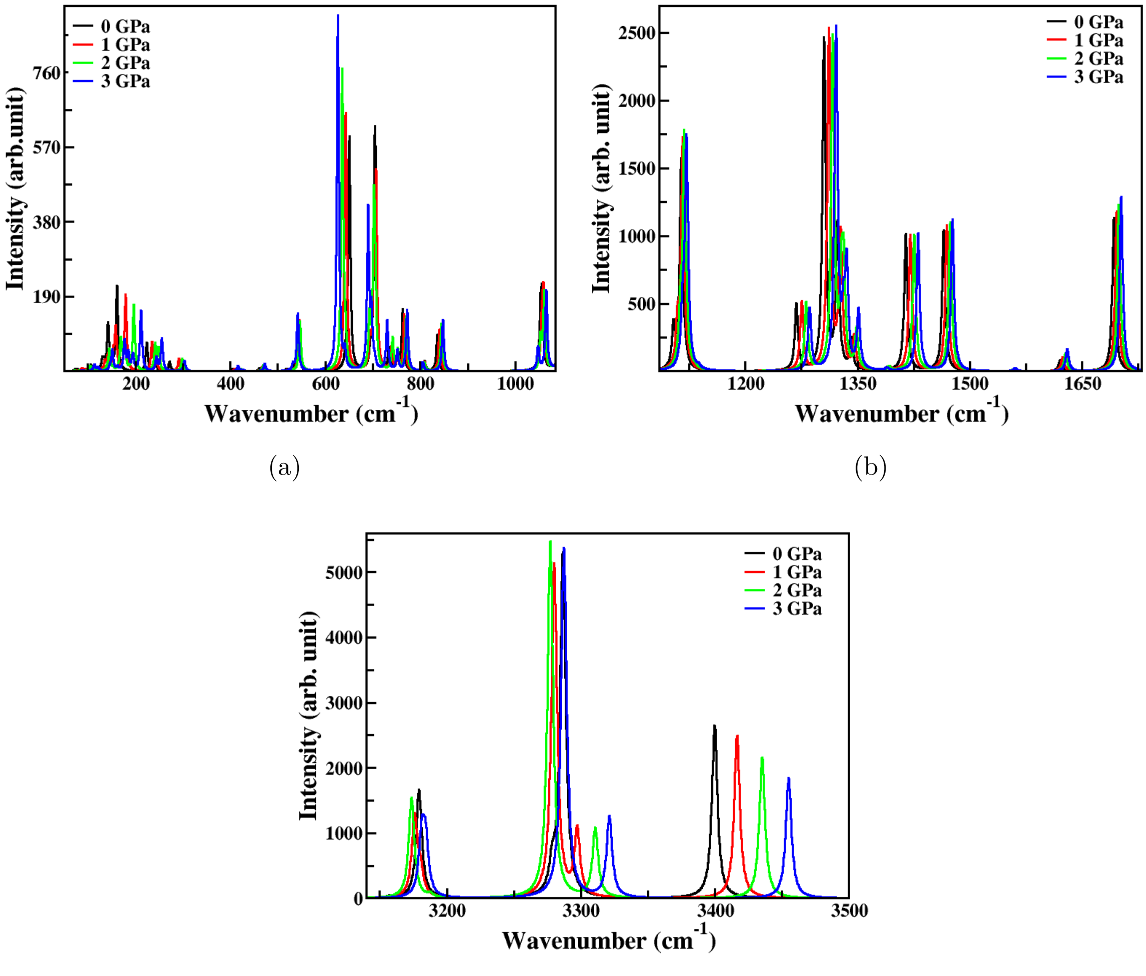

(a) (b)

(c)

Figure. 4.6 Calculated IR spectrum of triclinic FNF in three different frequency ranges.

and stretching of NO and CN bonds along with the rocking of CH and NH bonds in the frequency range 831 to 883 cm^{-1} is prominent. IR peaks in 985 to 990 cm^{-1} frequency range is mainly due to the asymmetric stretching of CN bonds and rocking of CH and wagging of NH bonds.

In the frequency range from 1068 to 1123 cm^{-1}, rocking, wagging, twisting of CH and NH bonds and stretching of CN and NO bonds can be observed. IR peaks of MHNF from 1212 to 1477 cm^{-1} are found because of the wagging, rocking and twisting of NH and CH bonds along with scissoring of CN and CH bonds and asymmetric stretching of CN and NO bonds present in this material. A prominent presence of scissoring of NH bond in the 1588 to 1633 cm^{-1} frequency range can be observed. IR peaks of this material in the high-frequency range from 2962 to 3371 cm^{-1} are found mainly due to the scissoring of NH bonds and symmetric and asymmetric stretching of NH and CH bonds. Pressure variation study of the IR spectrum of this material clearly indicates the blue shift of the

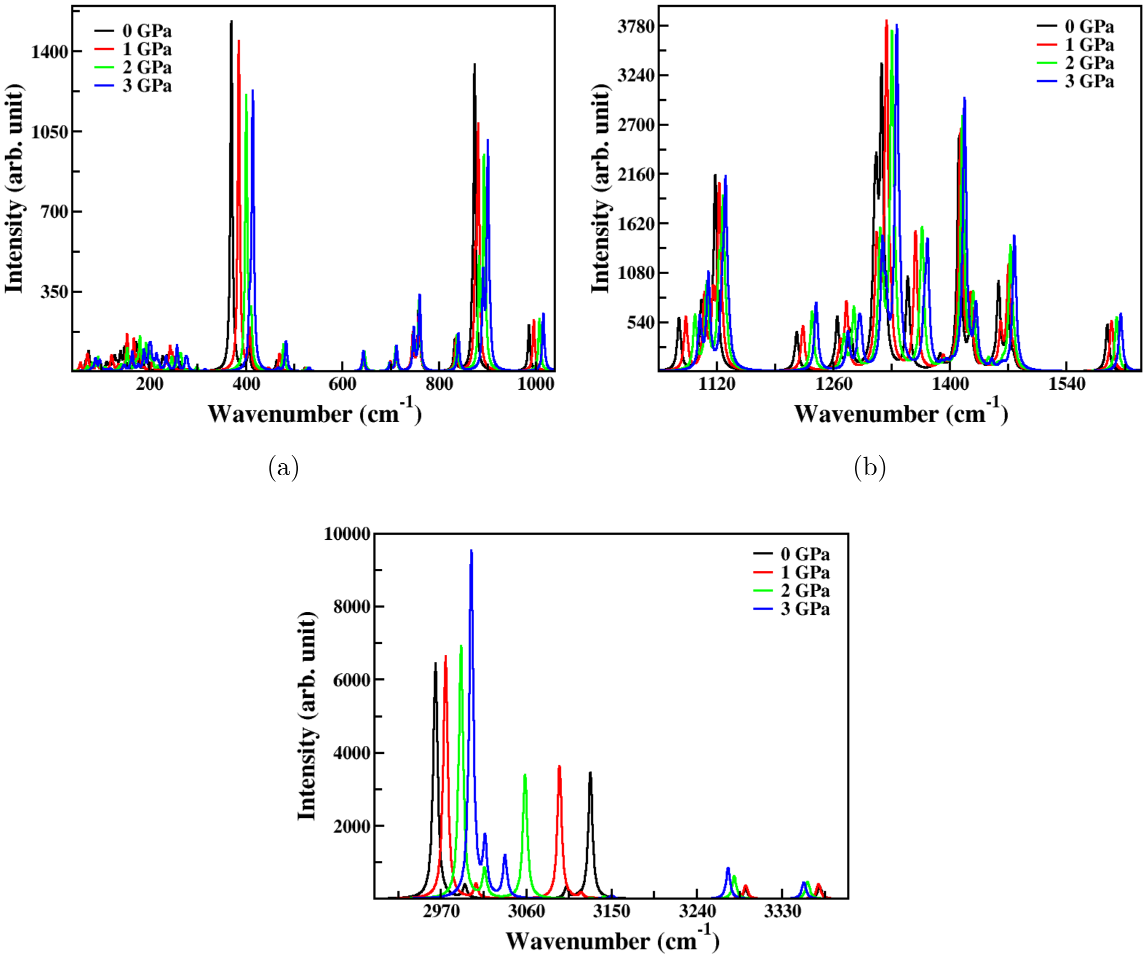

(a)

(b)

(c)

Figure. 4.7 Calculated IR spectrum of MHNF in three different frequency ranges.

whole spectrum throughout the frequency range except high-frequency IR peaks. These two peaks above 3240 cm^{-1}, which are found due to symmetric and asymmetric stretching of NH bonds, show redshift indicating the strengthening of H-bonding.

Figure 4.8 depicts the IR spectrum of KNF at 0 GPa as well as at high pressure up to 3 GPa in steps of 1 GPa. The absence of lighter elements like H atom in this material will confirm that IR peaks above 3000 cm^{-1} cannot be seen for KNF, and the whole IR spectrum is divided into two regions. Low-frequency peaks below 300cm^{-1} are found for the rotation, translation, twisting and rocking. Rocking of NO and stretching of CN bonds are the main reason for the IR peaks of FNF in the frequency range from 380 to 470 cm^{-1}. Wagging, twisting and scissoring of NO, CN bonds and stretching of CN bonds between 684 to 856 cm^{-1} are main contributor in IR peaks. Symmetric and asymmetric stretching of NO and CN bonds shows the main contribution in the IR peaks of KNF above 1124 cm^{-1}. Pressure variation of this IR spectrum clearly shows a blue shift over

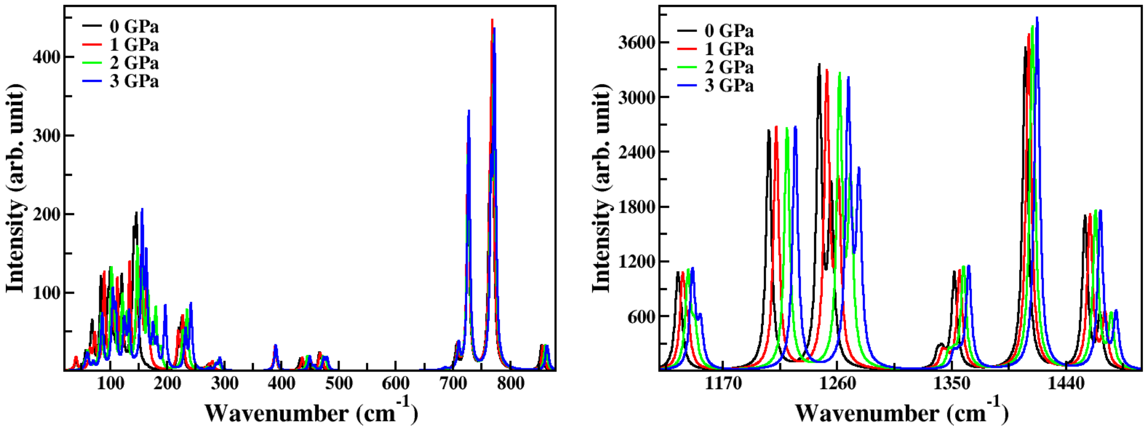

(a)

(b)

Figure. 4.8 Calculated IR spectrum of KNF in two different frequency ranges.

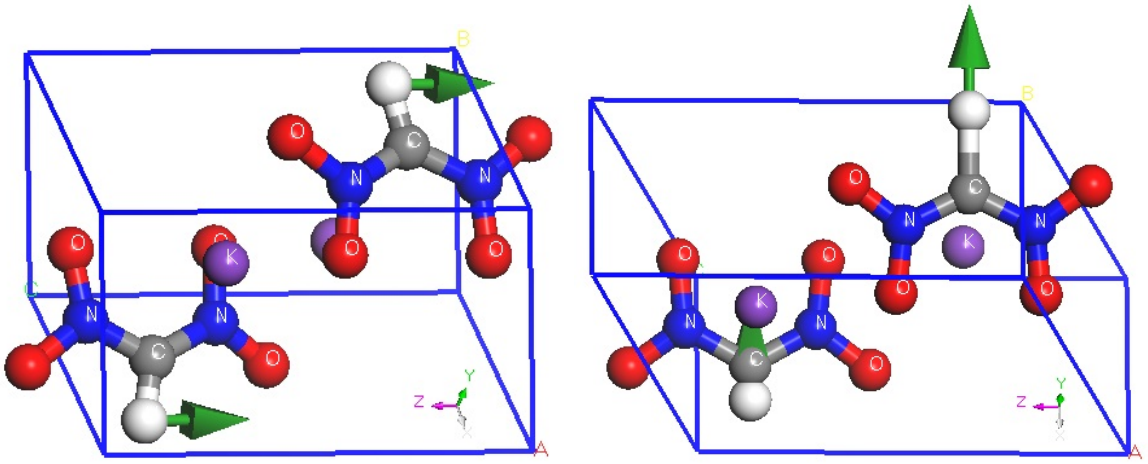

(a)

(b)

Figure. 4.9 High intensity IR mode of KDNM at 1194.50 cm-1 (a) and high frequency IR mode of KDNM at 3139.55 cm-1 (b).

all frequency range except IR peaks from 700 to 800 cm^{-1}.

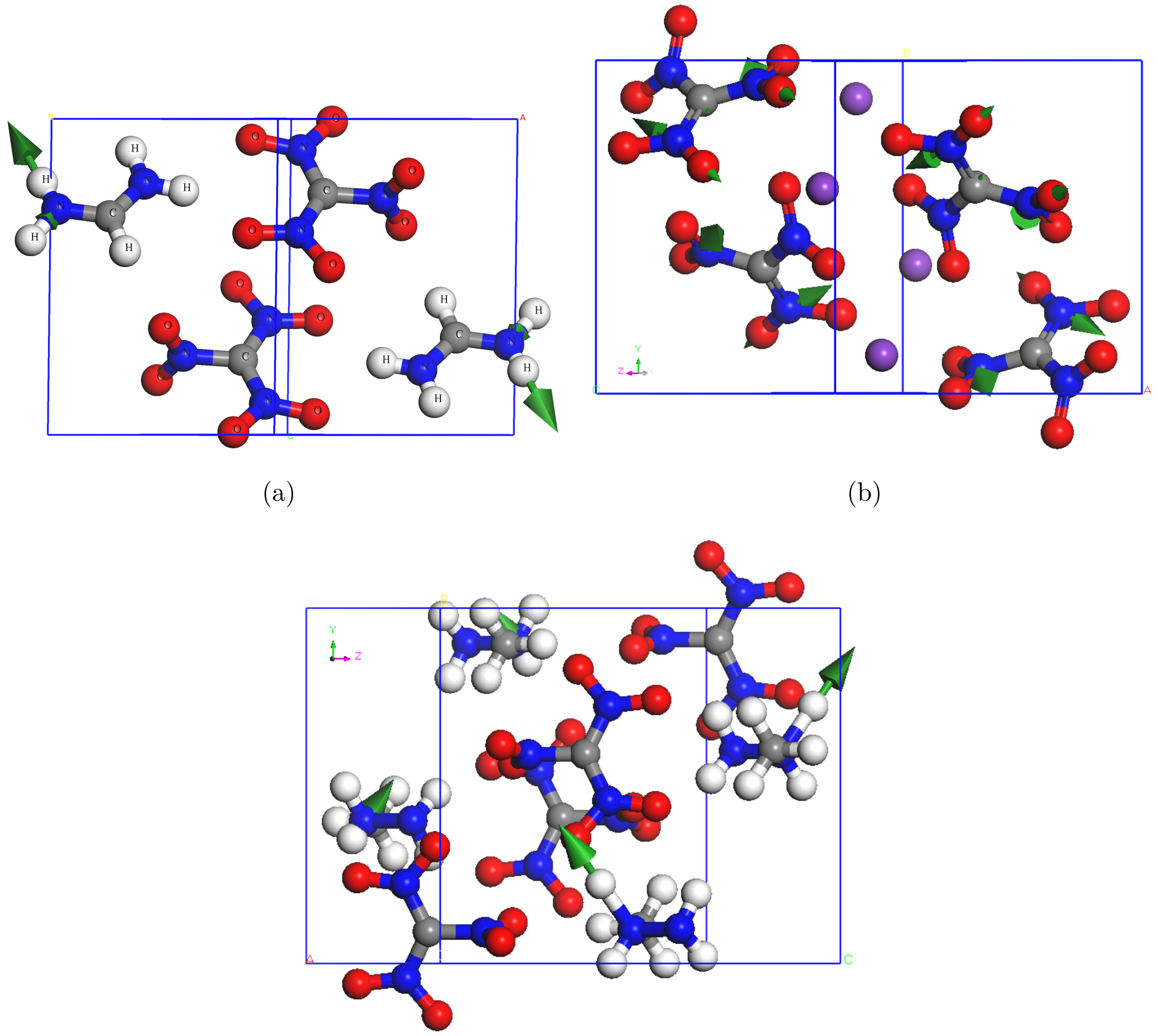

(a) (b)

(c)

Figure. 4.10 High intensity IR modes of (a) FNF, (b) KNF and (c) MHNF.

4.4 Conclusions

In conclusion, we can say that we have performed a thorough density functional theory study of di- and trinitromethane based energetic materials KDNM, FNF, MHNF and KNF. Understanding structural properties with different functionals tells the importance of van der Waals interaction in calculating the other properties of these materials. Obtained ground state structural parameters with varying combinations of functional and dispersion corrected schemes show that the dispersion corrected Grimme along with PBE pseudopotential works well for KDNM, FNF and MHNF. On the other hand, PBE + TS scheme provide structural parameters of KNF, which match well with experimental details. The pressure variation study clearly indicates that the KNF is less and FNF is more compressible in the studied pressure range. This also helps us to understand that the presence of intermolecular interactions in KNF is stronger compared to FNF. The study of elastic properties of these materials also supports this statement by providing higher value of bulk modulus for KNF and less for FNF. Proper understanding of these elastic constants along different crystallographic directions indicates that the FNF and KNF crystal is more sensitive along the z-direction, whereas the MHNF and KDNM crystals are more sensitive along x-direction and y-direction, respectively. Study of Born effective charge of these materials tells the presence of ionic bonding in KNF and KDNM crystals. On the contrary, more covalent bonding is found to be present in FNF and MHNF crystals. The study of vibrational properties provides knowledge about different vibration modes and the importance of stretching NO bonds in KDNM. In case of nitroformate-based materials, this study at 0 GPa as well as at high pressure indicates a blue shift for whole IR peaks except high-frequency peaks of FNF and MHNF, which are mainly due to symmetric and asymmetric stretching of NH bonds present in these compounds.

References

[1] J. Chang, P. Lian, D.Q. Wei, X.R. Chen, Q.M. Zhang and Z.Z. Gong, Phys. Rev. Lett. 105, 188302 (2010).

[2] H. Liu, J.J. Zhao, D.Q. Wei and Z.Z. Gong, J. Chem. Phys. 124, 124501 (2006).

[3] J.-C. Xu and J.-J. Zhao, Acta Phys. Sin. 58(6), 4144-4149 (2009).

[4] E.J. Reed, J.D. Joannopoulos and L.E. Fried, Phys. Rev. B. 62, 16500 (2000).

[5] S. Courtecuisse, F. Cansell, D. Fabre and J.P. Petitet, J. Chem. Phys. 108, 7350 (1998).

[6] S. Appalakondaiah, G. Vaitheeswaran and S. Leb‘egue, J. Chem. Phys. 138, 184705 (2013).

[7] S. Courtecuisse, F. Cansell, D. Fabre and J.P. Petitet, J. Chem. Phys. 102, 968 (1995).

[8] G.-X. Dong, S.-H. Ge and D.-H. Li, J. At. Mol. Phys. 2, 181-189 (2015).

[9] G.-X. Dong, X.-L. Cheng, S.-H. Ge and D.-H. Li, J. At. Mol. Phys. 31, 687-694 (2014).

[10] S.F. Trevino, E. Prince and C.R. Hubbard, J Chem. Phys. 73, 2996 (1980).

[11] D.T. Cromer, R.R. Ryan and D. Schiferl, J. Phys Chem. 89, 2315-2318 (1985).

[12] S.F. Trevino and W.H. Rymes, J. Chem. Phys. 73, 3001 (1980).

[13] F.L. Yarger and B. Olinger, J. Chem. Phys. 85, 1534 (1986).

[14] V.M. Groˇsev, F. Stelzer and D. Jocham, J. Mol. Struct. 476, 181-189 (1999).

[15] J.-P. Pinan-Lucarr´e, R. Ouillon, B. Canny, Ph. Pruzan and P. Ranson, J. Raman Spectrosc. 34, 819-825 (2003).

[16] M. Citroni, F. Datchi, R. Bini, M.D. Vaira, P. Pruzan, B. Canny and V. Schettino, J. Phys.

Chem. B 112, 1095-1103 (2008).

[17] D.C. Sorescu, B.M. Rice and D.L. Thompson, J. Phys. Chem. B 104, 8406-8419 (2000).

[18] D. Margetis, E. Kaxiras, M. Elstner, Th. Frauenheim and M.R. Manaa, J. Chem. Phys. 117, 788 (2002).

[19] M.R. Manaa, E.J. Reed, L.E. Fried, G. Galli and F. Gygi, J. Chem. Phys. 120, 10146 (2004).

[20] F.J. Zerilli, J.P. Hooper and M.M. Kuklja, J. Chem. Phys. 126, 114701 (2007).

[21] I.I. Oleynik, M. Conroy and C.T. White, AIP Conf. Proc. 955, 401 (2007).

[22] M.W. Conroy, M.M. Budzevich, Y. Lin, I.I. Oleynik and C.T. White, AIP Conf. Proc. 1195, 805 (2009).

[23] M.W. Conroy, I.I. Oleynik, S.V. Zybin and C.T. White, J. Phys. Chem. A 113, 3610-3614 (2009).

[24] A. Siavosh-Haghighi, R. Dawes, T.D. Sewell and D.L. Thompson, J. Phys. Chem. B 114, 17177-17186 (2010).

[25] W. Slough and W.F. Perger, Chem. Phys. Lett. 498, 97-100 (2010).

[26] F. Guo, H. Zhang and X. Cheng, J. Theor. Comput. Chem. 9, 315-325 (2020).

[27] A.C. Landerville, M.W. Conroy, M.M. Budzevich, Y. Lin, C.T. White and I.I. Oleynik, Appl. Phys. Lett. 97, 251908 (2010).

[28] F. Guo, X.-L. Cheng and H. Zhang, J. Phys. Chem. A 116, 3514-3520 (2012).

[29] C. Jing, Z. XiaoLin, Z. GuoPing and W. Li, Sci. China Phys. Mech. Astron. 56, 1874-1881 (2013).

[30] Z. Li and C. Lang, Acta Phys. Sin. 62, 138201 (2013).

[31] Z. Li and C. Lang, Acta Phys. Sin. 63, 098105 (2014).

[32] F. Guo, H. Zhang, C.Y. Zhang, X.-L. Cheng and H.-O. Hu, J. Theor. Comput. Chem. 14, 1550013 (2015).

[33] V.A. Shlyapochnikov, Nauka, Moscow 136 pp (1989).

[34] M.A. Tafipolsky, I.V. Tokmakov and V.A. Shlyapochnikov, J. Mol. Struct. 510, 149-156 (1999).

[35] A.L. Laikhter, T.I. Cherkasova and V.V. Semenov, Bull. Acad. Sci. USSR Div. Chem. Sci. 40, 2463 (1991).

[36] A.K. Macbeth, Ber. Dtsch. Chem. Ges. 46, 2537 (1913).

[37] T. Vladimiroff, J. Mol. Struct. Theochem. 452, 233-236 (1998).

[38] V. Grakauskas and A.M. Guest, J. Org. Chem. 43, 3485–3488 (1978).

[39] R. Villiers, Bull. Soc. Chim. Fr. 41, 281 (1884).

[40] H. Feuer, G.B. Backman and J.P. Kispersky, J. Am. Chem. Soc. 73, 1360 (1951).

[41] A. Langlet, N.V. Latypov, U. Wellmar, U. Bemm and P. Goede, J. Org. Chem. 67, 7833-7838 (2002).

[42] S. Qian, W.X. Hui, X. Kang-zhen, L.Y. Feng, S.J. Rong and Z.F. Qi, Chinese J. Enger. Mater. 24, 874-879 (2016).

[43] P. Duden, Ber. Deut. Chem. Ges. 26, 3003-3011 (1893).

[44] N.V. Latypov, A. Langlet, U. Wellmar and P. Goede, 31st International Annual Conference of ICT, pp 11/1–11/10 (2000).

[45] H. Brand, J.F. Liebman, A. Schulz, P. Mayer and A. Villinger, Eur. J. Inorg. Chem. 21, 4294–4308 (2006).

[46] V.A. Kokorekiha, L.G. Feoktistov, S.A. Shevelev and A.A. Fainzil'berg, Elektrokhimiya 6, 1849–1853 (1970).

[47] A.F. Baskakova, V.I. Slovetskii, S.A. Shevelev, V.I. Erashko and A.A. Fainzil'berg, Izv. Akad. Nauk, Ser. Khim. 11, 2404–42408 (1969).

[48] V.I. Slovetskii, A.F. Toshcheva, A.A. Fainzil'berg, S.A. Shevelev and V.I. Erashko, Izv. Akad. Nauk, Ser. Khim. 5, 1054–1060 (1968).

[49] H. Ratajczak, J. Baran, J. Barycki, S. Debrus, M. May, A. Pietraszko, H.M. Ratajczak, A. Tramer and J. Venturini, J. Mol. Struct. 555, 149–158 (2000).

[50] T.N.G. Row, Coord. Chem. Rev. 183, 81–100 (1999).

[51] A. Hantzsch and A. Rinckenberger, Ber. 32, 628 (1899).

[52] N.I. Golovina and L.O. Atovmyan, Zh. Strukt. Khim. 8, 307–311 (1967).

[53] N.V. Grigor'eva, N.V. Margolis and I.N. Shokhor, Zh. Strukt. Khim. 7, 278–280 (1966).

[54] N.V. Grigor'eva, N.V. Margolis and I.N. Shokhor, Zh. Strukt. Khim. 9, 550–552 (1968).

[55] M.J. Brookes and N.J. Jonathan, Chem. Soc. 9, 2266–2269 (1968).

[56] M. Krishnan, P. Sjoberg and P. Politzer, J. Chem. Soc. 9, 1237–1242 (1989).

[57] H.L. Ammon, C.S. Choi and A. Bashir-Hashemi, Acta Cryst. C C45, 319–321 (1989).

[58] J.C. Bryan, M.N. Burnett and A.A. Gakh, Acta Cryst. C C54, 1229–1233 (1998).

[59] M. Göbel, T.M. Klapötke and P. Mayer, Z. Anorg. Allg. Chem. 632, 1043–1050 (2006).

[60] M. Göbel and T.M. Klapötke, Z. Anorg. Allg. Chem. 633, 1006–1017 (2007).

[61] Y.E. Huang, H.X. Gao, B. Twamley and J.M. Shreeve, Eur. J. Inorg. Chem. 14, 2025–2030 (2007).

[62] H.F.R. Schöyer, W.H.M. Welland-Veltmans and J. Louwers, J. Propul. Power 18, 131–137 (2002).

[63] H.F.R. Schöyer, W.H.M. Welland-Veltmans and J. Louwers, J. Propul. Power 18, 138–145 (2002).

[64] G.K. Willians and T.B. Brill, Combust. Flame 102, 418–426 (1995).

[65] M.A. Bohn, J. Pyrol. 26, 65–94 (2007).

[66] Z. Yang, F. Gong, L. Ding, Y. Li, G. Yang and F. Nie, Propellants Explos Pyrotech 42, 809–815 (2017).

[67] J.E. Balzer, C.R. Siviour, S.M. Walley, W.G. Proud and J.E. Field, Proc R Soc Lond A Math Phys Eng Sci 460, 781–806 (2004).

[68] S. Venkatachalam, G. Santhosh and K. Ninan, Propellants Explos Pyrotech 29, 178–187 (2004).

[69] P. Kumar, Def Technol 14, 661–673 (2018).

[70] L. Yang, J. Zhang, T. Zhang, J. Zhang and Y. Cui, J Hazard Mater 164, 962–967 (2009).

[71] H. Wei, C. He, J. Zhang and J.M. Shreeve, Angew. Chem., Int. Ed. 54(32), 9367-9371 (2015).

[72] G.T. Liu and H.X. Qu, J Nanjing Univ Sci Technol, (2002).

[73] V. Forquet, C.M. Sabate, H. Chermette, G. Jacob, E. Labarthe, H. Delalu and C. Darwich, Chem. Asian J. 11(5), 730-744 (2016).

[74] H.S. Jadhav, M.B. Talawar, D.D. Dhavale, S.N. Asthana and V.N. Krishnamurthy, Indian J. Chem. Technol. 12 (2), 187-192 (2005).

[75] T.M. Klapötke, P.C. Schmid, S. Schnell and J. Stierstorfer, J. Mater. Chem. A 3 (6), 2658-1668 (2015).

[76] T.T. Vo, D.A. Parrish and J.M. Shreeve, J. Am. Chem. Soc. 136(34), 11934-11937 (2014).

[77] J.-T. Wu, J.-G. Zhang, X. Yin, Z.-Y. Cheng and C.-X. Xu, New J. Chem. 39 (7), 5265-5271 (2015).

[78] J.R. Lovett and N.J. Edison, Nitroform Salt of Certain Metals[P]. US 3562309, (1971).

[79] A. Gunasekaran and J.H. Boyer, Heteroatom Chemistry 3, 611 (1992).

[80] A.F. Baxter, I. Martin, K.O. Christe and R. Haiges, J Am Chem Soc 140, 15089–15098 (2018).

[81] J. Zhang and J.M. Shreeve, J. Am. Chem. Soc. 136 (11), 4437-4445 (2014).

[82] J. Zhang, S. Dharavath, L.A. Mitchell, D.A. Parrish and J.M. Shreeve, J. Am. Chem. Soc. 138 (24), 7500-7503 (2016).

[83] C. He, P. Yin, L.A. Mitchell, D.A. Parrish and J.M. Shreeve, Chem. Commun. 52 (52), 8123-8126 (2016).

[84] D. Kumar, G.H. Imler, D.A. Parrish and J.M. Shreeve, J. Mater. Chem. A 5 (32), 16767-16775 (2017).

[85] P. Yin, J. Zhang, L.A. Mitchell, D.A. Parrish and J.M. Shreeve, Angew. Chem., Int. Ed. 55, 12895-12897 (2016).

[86] Y. Tang, J. Zhang, L.A. Mitchell, D.A. Parrish and J.M. Shreeve, J. Am. Chem. Soc. 137 (51), 15984-15987 (2015).

[87] A. Devi, V.D. Ghule and A. Nirwan, ChemistrySelect 3 (30), 8651-8655 (2018).

[88] Y. Tang, C. He, P. Yin, G.H. Imler, D.A. Parrish and J.M. Shreeve, Eur. J. Org. Chem. 2018 (19), 2273-2276 (2018).

[89] P. Yin, J. Zhang, D.A. Parrish and J.M. Shreeve, Chem. - Eur. J. 20 (50), 16529-16536 (2014).

[90] H. Wei, H. Gao and J.M. Shreeve, Chem. - Eur. J. 20 (51), 16943-16952 (2014).

[91] H. Wei, J. Zhang and J.M. Shreeve, Chem. - Asian J. 10 (5), 1130-1132 (2015).

[92] Y. Liu, X.D. Gong, L.J. Wang, G.X. Wang and H.M. Xiao, J. Phys. Chem. A 115, 1754-1762 (2011).

[93] J. Akhavan, The chemistry of explosives, 2nd edn. Royal Society of Chemistry, London (2004).

[94] R. Lu, S. Wang and Y. Lu, Chem. Phys. Lett. 505, 87-91 (2011).

[95] T. Endo, T. Morita and K. Nishikawa, Chem. Phys. Lett. 517, 162-165 (2011).

[96] X. Hu, Q. Lin, J. Gao, Y. Wu and Z. Zhang, Chem. Phys. Lett. 516, 35-39 (2011).

[97] W. Bensch, T. Bredow, H. Ebert, P. Heitjans, S. Indris, S. Mankovsky and M. Wilkening, Prog. Solid State Ch. 37, 206-225 (2009).

[98] S. Xia and S. Bobev, J. Am. Chem. Soc. 129, 4049-4057 (2007).

[99] T. Shimizu, T. Urakubo, P. Jin, M. Kondo, S. Kitagawa and N. Kamigata, J. Organomet. Chem. 539, 171-175 (1997).

[100] J.R. Thornton, Salts of nitroform with hydrazines. US3297747A, (1963).

[101] P. Hohenberg and W. Kohn, Phys. Rev. 136 (3B), B864 (1964).

[102] P. Hohenberg and W. Kohn, Phys. Rev. 136 (3B), B864 (1964).

[103] W. Kohn and L.J. Sham, Phys. Rev. 140 (4A), 1133 (1965).

[104] N.D. Woods, M.C. Payne and P.J. Hasnip, J. Phys: Cond. Matt. 31 (45) (2019).

[105] M.C. Payne, M.P. Teter, D.C. Allan, T.A. Arias and J.D. Joannopoulos, Rev. Modern Physics 64 (4), 1045-1097 (1992).

[106] M.D. Segall, P.J.D. Lindan, M.J. Probert, C.J. Pickard, P.J. Hasnip, S.J. Clark and M.C. Payne, J. Phys: Cond. Matt. 14 (11), 2717-2744 (2002).

[107] J.P. Perdew and A. Zunger, Phys. Rev. B 23 (10), 5048-5079 (1981).

[108] J.P. Perdew, K. Burke and M. Ernzerhof, Phys. Rev. Lett. 77 (18), 3865-3868 (1996).

[109] D.M. Ceperley and B.J. Alder, Phys Rev Lett. 45 (7), 566-569 (1980).

[110] A. Tkatchenko and M. Scheffler, Phys. Rev. Lett. 102 (7), 073005 (2009).

[111] H.J. Monkhorst and J.D. Pack, Phys. Rev. B 13 (12), 5188-5192 (1976).

[112] T.H. Fischer and J. Almlof, J. Phys. Chem. 96 (24), 9768-9774 (1992).

[113] N. Yedukondalu and G. Vaitheeswaran, J. Phys. Chem. C 123, 2114-2126 (2019).

[114] S. Appalakondaiah and G. Vaitheeswaran, AIP Conf. Proc. 1512, 830 (2013).

[115] N. Yedukondalu, D. Ghule, Vikas and G. Vaitheeswaran, J. Chem. Phys. 145, 064706 (2016).

[116] P.K. Jharapla, G. Vaitheeswaran, M.K. Gupta and R. Mittal, Mater. Chem. Phys 267, 124645 (2021).

CHAPTER 5

Understanding of structure-property correlation study of cage-structured energetic materials

We present a thorough density functional theory (DFT) based computational study of crystalline properties of cubane caged potential energetic material octonirocubane (ONC). As expected for a layered molecular solid, van der Waals (vdW) corrections are inevitable and the same has been incorporated to capture the ground state properties more accurately. Study of Born effective charge (BEC) and zone centered phonon frequencies using density functional perturbation theory (DFPT) reveals the important role of N2, N4 type nitrogen and associated oxygen atoms in contributing to the high-intensity Infrared (IR) modes. From the calculated electronic band structure, we can conclude that ONC is an insulator with a bandgap of 5.31 eV. The optical properties of ONC are found to be nearly isotropic in low energy regions in spite of a strong anisotropic crystal structure.

5.1 Introduction

Towards the finding of novel high energy density materials (HEDMs), an enhanced interest can be seen in nitrogen-based materials, such as homonuclear polynitrogen compounds [1] and poly-nitro compounds. Nitro groups in such materials are especially known for providing sufficient oxygen during the process of combustion and hence considered as very special energetic groups. Moreover, incorporation of these groups makes energetic materials less vulnerable against external stimuli such as temperature or pressure [2]. Recent studies on highly nitrated cage hydrocarbons found great attention over normal poly-nitro compounds because of their compact structure, large strain energy, and positive oxygen balance [3, 4, 5, 6, 7, 8]. Normally it is seen that the density of any cage compound with compact structure is higher than its other non-caged analogs. Furthermore, large strain energy in these compounds can be responsible for their high heat of formation (HOF) over conventional energetic materials like 1,3,5,7-tetranitro-1,3,5,7-tetraazacyclooctane (HMX) or hexahydro-1,3,5-trinitro-1,3,5-triazine (RDX). As a result, these compounds become potential energetic materials with positive HOF, large density, outstanding detonation performance, and good thermal stability [9, 10, 11, 12, 13]. Among these cage-based explosives, most familiar energetic materials are 2,4,6,8,10,12-hexanitro-2,4,6,8,10,12-hexaazaisowurtzitane (CL-20), octanitrocubane (ONC) and 2,4,6,8,9,10-hexa -nitrohexaazaadamantane (HNHAA) [3, 14, 15, 16]. Based on the skeleton of caged structure of isowurtzitane, cubane, adamantane [17, 18, 19, 20, 21, 22, 23, 24, 25, 26] and prismane, [27, 28] other new caged energetic materials are developed. Though these types of materials are known for their good energetic properties associated with low sensitivity, they are very difficult to synthesize due to the complexity involved in these materials. Also, the presence of more nitro groups makes them susceptible to external stimuli. In this connection, the successful synthesis of polynitro cubane's such as tetra-, penta-, hexa-, hepta-, and octanitrocubane has gained considerable interest as ONC shows high explosive properties than well-established high energy material CL-20 [29]. Theoretical study by Zhang et al. on ONC also confirms the high performance of ONC with high detonation velocity (∼10 km/s) and high detonation pressure (∼50 GPa) of ONC [30]. Cubane cage of this material is known to possess a high HOF of 622.1 kJ/mol along with a density of 1.29 g/cm^3 and is thermally stable with decomposition temperature $>$ 220 °C [31, 32]. The strain energy associated with ONC is reported to be 1101.03 kJ/mol which is quite higher than other caged structures [33]. ONC is also well known for its molecular symmetry which has been achieved by the replacement of hydrogen atom from platonic hydrocarbon with -NO_2 substitution. It is also reported to lose its three-fold symmetry at each corner of the cubane cage. To date, a lot of studies based on theoretical approaches have been performed on this material. The study of interaction between the -NO_2 groups in this material has also been reported [34]. Kortus et al. reported electronic structure as well as the vibrational properties of ONC with the all-electron Gaussian orbital-based density functional theory calculation [35]. High heat of formation (HOF) of ONC has been evaluated by the Benson's group activity method which has also been predicted accurately using corrected Parametric Method 3 (PM3) [36, 37]. The semi-empirical molecular orbital (MO) methods have been used by Owens to study the decomposition of ONC [38]. A recent computational study on ONC also reveals information about its IR spectra, thermodynamic properties, detonation properties and pyrolysis mechanism at different levels [39]. Although it is well known that the molecule is the main key of any explosive material, but the exact performance of any energetic material will only depend on its solid-state environment in the crystalline form. The main focus of this work is to study the crystalline properties of ONC through the *ab-initio* approach. Here we have addressed the structural properties as well as the elastic properties of this material to have a better understanding of the impact sensitivity of this material. This work also reports about the zone centered phonon frequencies along with the born effective charge (BEC) of this material and as the bandgap of any energetic material plays a vital role for electrical discharge related detonation, a more accurate value of bandgap of this material has been calculated using well known TB-mBJ potential [40]. This chapter is organized as follows: the next section is attributed to molecular and crystal structure with computational details involved in this study. After that, the result and discussion related to this study has been considered and finally, the conclusion of this work is drawn.

5.2 Structural details of ONC and the Computational Details

The molecular structure of ONC shown in Figure 5.1a contains 8 -NO_2 groups, each attached to each corner of its strained cubane cage. The skeleton of the cubane (C_8H_8) cage shaped as cube formed by carbon atoms at each corner of this cube and one hydrogen atom is associated with each carbon atom. So, each carbon atom at the corner of this cubane is bound with its three neighbour corner carbon atoms, and internuclear angles of C-C-C are nearly 90°. Which is a huge deviation from normal tetravalent angle 109.5°results from the sp^3-hybridized carbons [29]. This deviation is very expensive energetically, and the structure is strained by about 166 kcal/mol corresponding to a substantial weakening of its bonds. These deformed bond angles make cubane a potential compound for storing energy where each strained bond is considered as a potential site for energy storage. Though this cubane is known to be a meta-stable compound, it can form molecular crystalline solid at room temperature with 1.29 g/cm^3 density and melting point of 130 °C. These cubane based polynitrocubanes are formed by replacing one or more hydrogen atoms from the cubane structure by -NO_2 groups. Among these polynitrocubanes, ONC is the one in which all the hydrogens are replaced by -NO_2 groups. Basically, one ONC molecule is made up of 4 types of carbon atoms, four types of nitrogen atoms and eight types of oxygen atoms. Among these atoms, the 2nd and 4th types of atoms are arranged in the opposite edges of the cubane, whereas the 1st and 3rd types of atoms are arranged diagonally in this cubane cage. Each type of nitrogen atom in the -NO_2 group contains further two types of oxygen atoms, such as type A and type B. A complicated arrangement of these ONC molecules in the crystalline form is shown in the Figure 5.1(b)-(d). Crystalline bc-plane, shown in Figure 5.1d clearly depicts that the type 2 and type 4 atoms are aligned along the c-axis of the crystal and opposite edges of the ONC molecule. Crystallographic ac-plane, which has been shown in Figure 5.1b shows that type 1 and 3 atoms are arranged diagonally in the molecule and type 3 and 1 atoms are aligned along the crystallographic c-axis. It is also noted that 4 ONC molecules will be found in a unit cell of the crystal structure of ONC which is monoclinic. A primitive crystal structure of ONC has been considered for all the calculations in this study. This primitive cell contains 2 ONC molecules in it. Different alignment of this crystal perpendicular to a-, b-, and c- axis clearly indicate a presence of layer along the c-axis. Figure 5.1b indicates that B type of oxygen atoms form nearest layers along this crystallographic axis. This initial inspection of crystal structure suggests the presence of van der Waals interaction in this material, which led us to consider vdW corrected DFT calculation for this material. For calculating different crystalline properties of ONC, *ab-initio* simulations have been carried out considering the above-mentioned structural details as input parameters. In this respect, two approaches have been used, which are projector augmented wave (PAW) and full-potential linear augmented plane wave (FP-LAPPW) method. Among these two methods, FP-LAPW is considered for calculating electronic and optical properties, whereas the rest of the prop-

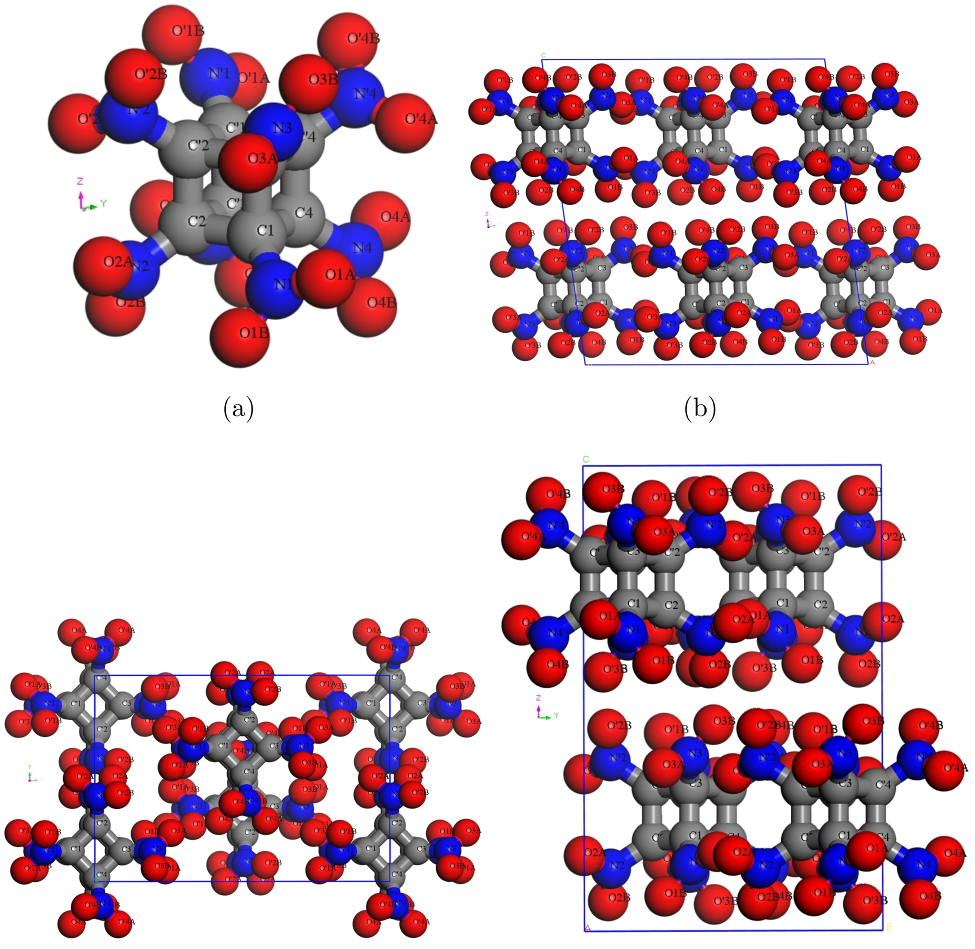

(a)

(b)

(c)

(d)

Figure. 5.1 Molecular structure (shown in a) and crystal structure of ONC aligned in different crystallographic directions.

erties discussed in this article have been computed through the PAW method. Density functional theory (DFT) [41, 42] based PAW method implemented in Vienna *ab-initio* simulation package [43] is considered in this work. The generalized gradient approximation (GGA) [44] was used to treat electron-electron interactions. The Broyden-Fletcher-Goldgarb-Shanno (BFGS) minimization scheme [45] has been used for structural relaxation. The convergence criteria for structural optimization of ONC crystal structure were performed with a kinetic energy cutoff of 600 eV and we have used Monkhorst Packing [46] as (4×3×3) for gamma centered grid. The valence electronic configurations of the atoms considered here are as follows: C: [$2s^22p^2$], N: [$2s^22p^3$], and O: [$2s^22p^4$]. The self-consistent energy convergence was set to 1×10^{-8} eV/atom. The convergence criterion for the maximal force between atoms was set to 0.01 eV/Å. While calculating the elastic constants, this maximal residual force was set to 1×10^{-4} eV/Å. Knowing the presence of a prominent effect of van der Waals interaction in this material, two vdW-corrected methods have been considered to get the correct ground state structure which are Grimme or D2 and Tkatchenko-Scheffler (TS) methods. The basic difference between these two methods is that the TS method considers a correction due to polarizability of the inter-atomic bonds, whereas the Grimme method does not [47]. Calculation of electronic band structure, the density of states and optical properties have been accomplished using the FP-LAPW implemented in WIEN2k [48]. Exchange-correlation interaction has been treated through the GGA scheme. It is well known that normal DFT calculation with standard LDA and GGA functional always underestimate bandgap with respect to the experimental value. In this regard, the Tran-Blaha modified Beche-Johnson density functional (TB-mBJ) [40] which includes the kinetic energy density to improve bandgap has been considered. Calculated bandgap with this functional for semiconductors and insulators are reported to match nearly accurately with experimental results [49, 50]. Threshold energy of -6 Ry has been considered as separation energy between core and valence electrons. In order to have the proper size of the basis set, a cut off of RK_{max} has been chosen to 7 and the value of G_{max} is considered 14. A set of 500 and 5000 k points are used for calculating the electronic band structure and optical properties of this material. For calculating the electronic band structure, K-path in the irreducible first Brillouin zone is L-M-A-Γ-Z-V.

5.3 Results and Discussion

5.3.1 Structural properties of ONC

Crystalline properties of any material mainly depend on two factors which are the composition of the material and the arrangement of these compositions in the crystal. It is quite obvious that different properties can be achieved with the different arrangements or with different crystal structures with the same composing elements. According to the above-mentioned facts, we have considered the study of ground-state structural properties of ONC. In this connection, we have calculated the lattice parameters, volume and associated bond lengths of this material at the ambient condition as well as under pressure. As mentioned in the previous section and shown in Figure 5.1, the consideration of van der Waals corrected DFT calculation in this study is very clear.

Table 5.1 Calculated ground state structural parameters such as lattice parameters, angle and volume of ONC (with and without van der Waals correction) along with experimental results.

Parameters	Expt	PBE	D2	TS	TS-HI
a(in Å)	12.78	13.11	12.78	12.84	12.84
b(in Å)	8.84	9.05	8.72	8.77	8.84
c(in Å)	13.92	14.43	13.72	13.91	13.98
β(°)	98.03	97.99	98.05	98.05	97.98
Vol(in Å^3)	1558.17	1695.86	1514.95	1551.00	1571.67
$\triangle$V(%)		+8.84	-2.77	-0.46	+0.87

It has been a well-established concept in DFT calculation that LDA functional will always underestimate calculated lattice parameters and volume, whereas PBE functional will overestimate. Van der Waals corrected TS, TS-HI, and D2 method of Grimme have been used along with normal PBE functionals in this consideration. Our calculated lattice parameters and volume at equilibrium with PBE functional as well as with van der Waals corrected TS, TS-HI and D2 methods are given in Table 5.1. These results close to experimental values justify the well speculative idea of considering van der Waals interaction from the first look of crystal structure shown in Figure 5.1. Among these vdW-corrected methods, TS is found to be more accurate in calculating the structural parameters than other vdW methods and which is the reason it has been considered for carrying out further calculations on ONC to get different properties of this material. As a next step, the pressure variation study of lattice parameters and volume has been addressed to have a proper idea about the compressibility and other related structural properties of this material. In this regard, a hydrostatic pressure up to 5 GPa in steps of 0.5 GPa has been applied to the optimized crystal structure at ambient condition. Results related to this high-pressure calculation have been depicted in Figure 5.2. Pressure variation of lattice parameters shown in Figure 5.2 indicates that the crystallographic c-axis is more compressible than the other two axes which is quite obvious and also can be anticipated from the Figure 5.1. The presence of layers along the c-axis explains the existence of weak intermolecular interaction in this direction which in turn leads to the above anticipation. The order of compressibility of different lattice parameters is as follows: c > b > a.

After having a proper understanding of the compressibility nature of different crystallographic axis, the pressure-volume data has been considered for calculating the bulk modulus and its pressure derivative. For this reason, the third-order Birch-Murnaghan

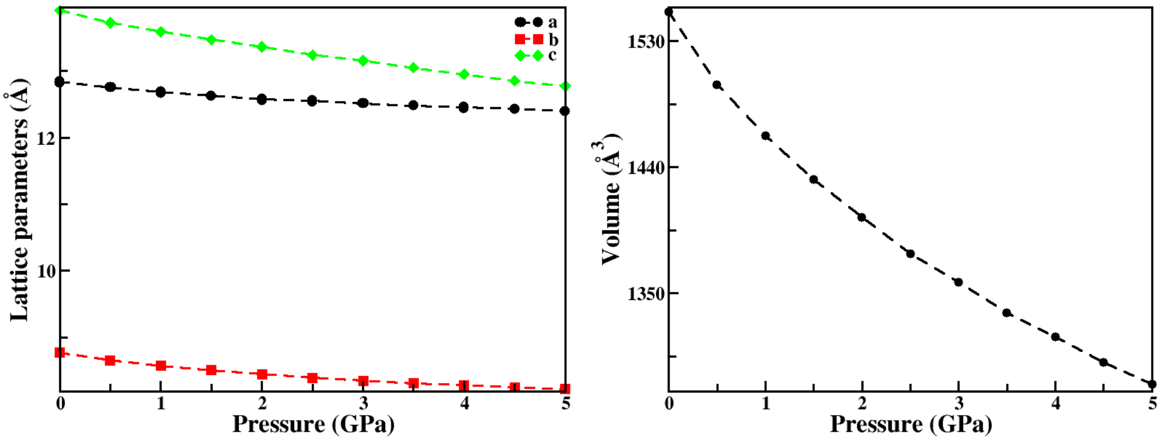

(a) (b)

Figure. 5.2 Pressure variation of lattice parameters (shown in a) and volume (shown in b) of ONC.

equation of states (BM-EOS) [52] has been used to fit the pressure-volume data and bulk modulus and its pressure derivative are calculated. The calculated bulk modulus and the derivative of this quantity with respect to pressure are 12.19 GPa and 8.78, respectively. These values indicate high compressibility along with the increased stiffness nature of ONC. A similar trend of result for bulk modulus and its pressure derivative of similar kind of secondary energetic material has also been found in literature [53, 54, 55, 56, 57] in support of our calculated bulk modulus and its pressure derivative.

5.3.2 Elastic properties

Knowledge of elastic properties of any material is known to be linked with the interactions present in that material and at the same time, these present interactions are also responsible for mechanical energy transfer in a material. This phenomenon in energetic materials is related to the detonation initiation mechanism of such kind of materials. The initiation of the detonation process is mainly dependent on the constituting composition of the molecule and the interaction present in the material. This fact is further supported by the experimental work done by Dick on the directional dependency of shock-initiated sensitivity of energetic material pentaerithrytol tetranitrate (PETN) [58]. This directional dependence is related to the strength of interactions present in the material which in turn is related to the elastic constants of the material. Hence elastic constants of energetic material are very useful parameters for predicting the directional sensitivity of that material. In this regard, the lowest sensitivity of energetic material PETN is reported along the a-axis of this material whereas the stiffest elastic constant of this material is also the C11.

In this connection, a stress-strain method has been applied on ONC crystal to obtain the

Table 5.2 Comparison of experimental value of elastic constants Cij of well-known energetic material RDX and β-HMX and calculated Cij of ONC at the optimized volume. Unit of elastic constants is in GPa.

C_{ij}	C11	C12	C13	C15	C22	C23	C25	C33	C35	C44	C46	C55	C66
ONC	22.12	8.8	8.49	1.89	18.87	2.45	-1.62	15.67	0.43	5.76	-1.22	7.44	6.19
RDX	36.67	1.38	1.67	–	25.67	9.17	–	21.64	–	11.99	–	2.72	7.6
β-HMX	18.41	6.37	10.50	-1.1	14.41	6.42	0.83	12.44	1.08	4.77	2.75	4.77	4.46

elastic constant values of this material so that a proper idea about the sensitivity of this material can be predicted qualitatively. In order to accomplish this qualitative study of the sensitivity of ONC due to shock, a comparative study has been carried out with similar kind of well-known secondary energetic materials such as orthorhombic cyclotrimethylene trinitramine (RDX) [59] and monoclinic cyclotetramethylene tetranitamine β-HMX [60] and the related elastic constant values are tabulated in Table 5.2. Though a direct comparison is not possible between orthorhombic RDX and monoclinic ONC, a lot of information can be predicted speculatively. These tabulated results clearly show a much lower value of C11, C22 and C33 of ONC than RDX but slightly higher than β-HMX. Elastic constants C25 and C46 of ONC are found to be negative but these constants are also found to satisfy the Born's stability criteria regarding the monoclinic structure and this confirms the mechanical stability of this material. Ordering of these elastic constants along the principal directions is as follows: C11 $>$ C22 $>$ C33. Bulk modulus calculated from this elastic constant calculation is also found to agree with the bulk modulus found from 3rd order BM-EOS. Though a much lower value in the principle elastic constants of ONC can be seen compared to RDX, C12 and C13 values of ONC are found to be higher than the corresponding values of RDX. As the elastic constants of β-HMX are smaller than those of RDX, previous studies on elastic constants relevance to detonation [59] suggest a highly sensitive nature of β-HMX than RDX to detonation which is initiated by shock-wave. Higher value of elastic constants C12, C13 of β-HMX suggests that the sensitivity due to shear deformation along crystallographic b- and c-direction of RDX will be higher than β-HMX and the high sensitivity of RDX along c-direction has also been correlated with the less value of C33 of RDX. Considering these well-established facts, the sensitivity of ONC can be predicted qualitatively to be higher than RDX but lower than β-HMX. Directional dependence of sensitivity along the c-axis is high whereas lower in magnitude along the a-axis. It can also be mentioned that the b- and c-axis are not vulnerable to the specific shear deformation like RDX.

5.3.3 Born effective charges (BECs) and vibrational properties

To have a better understanding of the vibrational and optical properties of any material, Born effective charge is a very useful fundamental quantity. The quantity itself defines coupling of electrostatic field with the displacement of the lattice. In this study linear response method implemented in VASP has been used for the purpose of computing BEC's of ONC. All diagonal Born effective charge values for C, N and O atoms of ONC have been presented in Table 5.3 and 5.4. The convergence of this calculation is found to satisfy the acoustic sum rule which is $\sum_k Z^*_{k,ij} = 0$. It is well known that the less deviation of BEC of any atom from its ionic charge concludes the presence of ionic bond around that atom. Whereas the reduced value of BEC implies the delocalization of charges along the present bonds and hence the presence of covalent bond around that atom. From this point of view, we can easily say that carbon atoms in ONC are covalently bonded in cubane cage as carbon atoms in ONC show a significant reduction in BEC value. On the contrary, an increment on BEC for N and O atoms can be seen from their nominal charges. This observation helps us to conclude that all the bonds between carbon atoms are covalent in nature but the bonding character of N and O atoms within NO2 is a mixture of ionic and covalent. It can also be seen that BEC tensor is having a criterion on its elements which is $Z^*_{11} \neq Z^*_{22} \neq Z^*_{33}$.

Table 5.3 Calculated BECs of C and N atoms of ONC.

Atoms	Ionic	Z^*_{11}	Z^*_{22}	Z^*_{33}
C1	4	0.01650	0.23561	-0.37395
C'1	4	-0.12886	0.10142	-0.45482
C2	4	0.31715	0.35306	0.44478
C'2	4	0.27426	0.49773	0.39910
C3	4	-0.32030	-0.19577	0.60929
C'3	4	-0.16422	-0.33328	0.58420
C4	4	0.40899	-0.43264	-0.31906
C'4	4	0.35904	-0.42949	-0.30283
N1	-3	1.40624	0.44294	2.65368
N'1	-3	1.48314	0.73419	2.66233
N2	-3	0.45173	0.37392	1.60388
N'2	-3	0.46808	0.09162	1.72558
N3	-3	1.37328	1.03755	0.80332
N'3	-3	1.15415	1.24020	0.74871
N4	-3	0.44775	1.74449	0.68435
N'4	-3	0.41172	1.79506	0.59940

As it is well known that the strength of the polarizability of any material is correlated to the deviation of BECs of the constituent elements of that material, results given in Table 5.3 and 5.4 tell that the constituent oxygen atoms of ONC are responsible for making this material more polarizable.

A further study of directional dependence of the strength of polarizability indicates a less

Table 5.4 Calculated BECs of oxygen atoms of ONC.

Atoms	Ionic	Z^*_{11}	Z^*_{22}	Z^*_{33}
O1A	-2	-0.72252	-0.08438	-1.00057
O’1A	-2	-0.73242	-0.15432	-0.99939
O1B	-2	-0.52104	-0.56047	-1.40683
O’1B	-2	-0.49529	-0.70854	-1.39354
O2A	-2	-0.45482	-0.6541	-0.68332
O’2A	-2	-0.44382	-0.57664	-0.7151
O2B	-2	-0.34741	-0.0747	-0.98198
O’2B	-2	-0.39164	0.07973	-1.05834
O3A	-2	-0.83319	-0.90013	-0.33493
O’3A	-2	-0.75967	-0.9265	-0.33471
O3B	-2	-0.31399	-0.47629	-0.63676
O’3B	-2	-0.25105	-0.57926	-0.61086
O4A	-2	-0.44159	-0.33843	-0.2515
O’4A	-2	-0.44381	-0.34056	-0.21977
O4B	-2	-0.39841	-0.46809	-0.74386
O’4B	-2	-0.40797	-0.49394	-0.69649

and mixed deviation of BECs of C1, C2, C3 and C4 type of atoms in different directions. N1 and N2 atoms show a similar order of deviation of BECs such as c > a > b but N3 and N4 type of nitrogen atoms show similar order as b > a > c. In the case of oxygen atoms, less deviation can be seen along the c-axis whereas O1B, O2A, O3B, and O4B atoms show high deviation along a-axis and other types of oxygen atoms show high deviation along b-axis. Atomic vibrations in a periodic solid can be considered as the standing elastic waves which are equivalent to normal modes of vibrations. In this connection, if N atoms in a primitive unit cell are vibrating in 3D space, 3N degrees of freedom have to be considered and this will give 3N vibrational modes for the system. This phonon is the quantization of these vibrational modes and is known as quasi-particles that follow Bose-Einstein statistics. These vibrational modes in a periodic crystal can further be divided in two ways. When the atomic displacement vectors are in same phase, it gives acoustic modes and when they are in out of phase, such kinds of vibrations are called optical modes. For 3D periodic solid, we will have three acoustic modes, and 3N-3 modes will be optical. These optical modes are further involved in the IR and Raman spectra of the material. The reason for IR activity in any material is induced dipole moment due to the change in the atomic positions and the reason for Raman activity is the induced dipole moment due to deformation of the electron shell which is related to the polarizability tensor. These normal phonon modes are also related to the irreducible representation of the point group of the material.

Table 5.5 Calculated vibrational frequencies of ONC. (All the frequencies are given in (cm^{-1})).

A_g		A_u		B_g		B_u	
40.2144	687.2089	7.1733	687.6215	40.6496	646.4334	5.5119	645.2871
54.7118	751.4861	44.7771	750.6956	47.1942	685.362	4.0405	683.7639
69.8720	759.694	74.9180	757.8374	48.1158	752.8252	34.7256	753.8019
85.4648	766.7309	79.0017	766.56	69.4056	762.7501	68.3323	763.1618
96.4849	807.7717	86.1550	809.721	77.9637	766.4615	72.9598	766.3322
101.1518	829.7617	102.3837	831.1221	90.5060	790.7901	84.0760	784.0059
107.608	883.1611	103.3379	882.2596	95.6214	831.8212	85.8747	832.4619
114.7376	890.976	112.6625	891.0082	100.8112	844.4865	100.9558	839.6992
131.9189	898.0246	116.4877	898.1112	112.388	884.6569	111.4515	886.1531
140.9194	963.0654	132.161	966.6455	125.5883	898.0166	117.3405	898.3411
152.7888	973.8654	141.1286	974.4535	138.9551	972.0067	132.3287	972.7964
158.9598	1019.344	161.4222	1016.68	144.5368	1006.689	140.6656	1007.44
169.2401	1121.23	168.7692	1124.065	147.665	1118.726	145.0218	1121.529
251.1474	1128.548	249.4351	1130.364	153.5745	1143.974	150.5989	1142.409
266.983	1148.2	264.2749	1148.203	244.9989	1146.702	244.6874	1145.041
272.2505	1160.258	269.4734	1162.212	257.8432	1161.807	256.3302	1164.402
291.7749	1301.744	288.9441	1298.076	270.0034	1296.497	266.3985	1294.154
357.0169	1313.719	353.1964	1309.987	296.1439	1304.836	293.443	1304.622
366.6732	1314.285	363.6425	1312.968	353.3716	1318.523	351.6591	1315.58
380.216	1339.125	379.7907	1337.297	363.2657	1328.132	361.6926	1321.124
464.4417	1591.114	464.284	1597.843	428.226	1574.847	427.5711	1583.273
546.7315	1602.09	546.4778	1608.505	467.8925	1602.339	467.992	1590.689
622.7525	1627.637	620.3693	1627.069	547.1336	1609.792	545.5406	1621.535
633.8634	1669.657	633.4594	1679.368	619.6753	1620.208	619.5216	1627.114

It is well accepted that these ground-state vibrational modes provide a lot of information regarding the interaction present in any material. Along with this information, knowledge of IR and Raman spectra can help us to have a deep insight about our concerned material. In this connection, we have not only done the analysis of BECs for ONC but also calculated the zone center phonon frequencies using density functional perturbation theory (DFPT) within the framework of harmonic approximation. As ONC has 64 atoms in a primitive unit cell, we have found 192 zone centre phonon modes. It can be seen that the mechanical representation of these vibrational modes is as follows:

$M = 48A_g + 48A_u + 48B_g + 48B_u$

All the phonon frequencies related to different representations are given in Table 5.5. Among these modes, $A_u + 2B_u$ are acoustic modes and the rest $48A_g + 47A_u + 48B_g + 46B_u$ are optical whereas $47A_u + 46B_u$ modes are IR active modes and $48A_g + 48B_g$

modes are Raman active modes. As the assignment of all these 192 modes are extremely difficult and the BEC calculations show N2, N4 and oxygen O2A atoms play a crucial role in BEC, vibrational modes related to these atoms can be considered to contribute mainly to the vibrational properties of ONC. It is quite obvious that a direct comparison cannot be drawn in between the earlier reported IR active modes by Kortus et al. with the presented result in this work as the previous report is based on molecular level calculation, whereas our calculation considers crystalline ONC along with van der Waals interaction. This consideration gives the reliability of our calculation compared to earlier reported vibrational modes. Report by Kortus et al. shows that the highest frequency of IR active mode is found at 1591 cm^{-1} whereas our result shows it at 1679.37 cm^{-1}. As no other report or experimental results are available on this property of ONC, our calculation shows its importance in this concern.

5.3.4 Electronic band structure

Information about the exact bandgap of any energetic material is very important as this parameter is associated with the electric discharge phenomenon and the consequent detonation of such material. In this regard, the use of TB-mBJ potential along with the normal GGA functional has proven to produce nearly the exact bandgap of any material with less computational time whereas standard LDA or GGA functionals are always known to underestimate the bandgap. As a result, the electronic band structure of monoclinic ONC is computed using full-potential linear augmented plane wave method with normal GGA functional as well as with the addition of TB-mBJ potential has been calculated which has been shown in Figure 5.3a. The bandgap without TB-mBJ potential is 3.09 eV while the bandgap after the incorporation of TB-mBJ potential has shown a large increment with a value of 5.31 eV. This band structure is showing an indirect nature of bandgap with valence band top (VBT) at V and conduction band bottom (CBB) at Γ. It can also be seen from the Figure 5.3a that these bands are less dispersed and flat in nature.

In this consideration, no report can be found regarding the bandgap of this material except the HOMO-LUMO gap of 3.25 eV by Kortus et al. [35] which is near to the bandgap found in this work for bulk ONC with GGA functional. From this result, the importance of the incorporation of TB-mBJ potential in this work can easily be understood. Along with the electronic band structure of ONC, the total and partial density of states (DOS) of this material have also been considered in this study. This DOS and PDOS of ONC are shown in Figure 5.3b. A sum of 16 inequivalent atoms has been considered in this concern. It can easily be seen from this DOS that a strong covalent bonding is present in between all carbon atoms in the cage. This also indicates the presence of a mixture of covalent and ionic bonding with nitrogen and corresponding carbon atoms. In case of nitrogen and oxygen atoms a slight deviation in overlapping in the DOS can be seen which

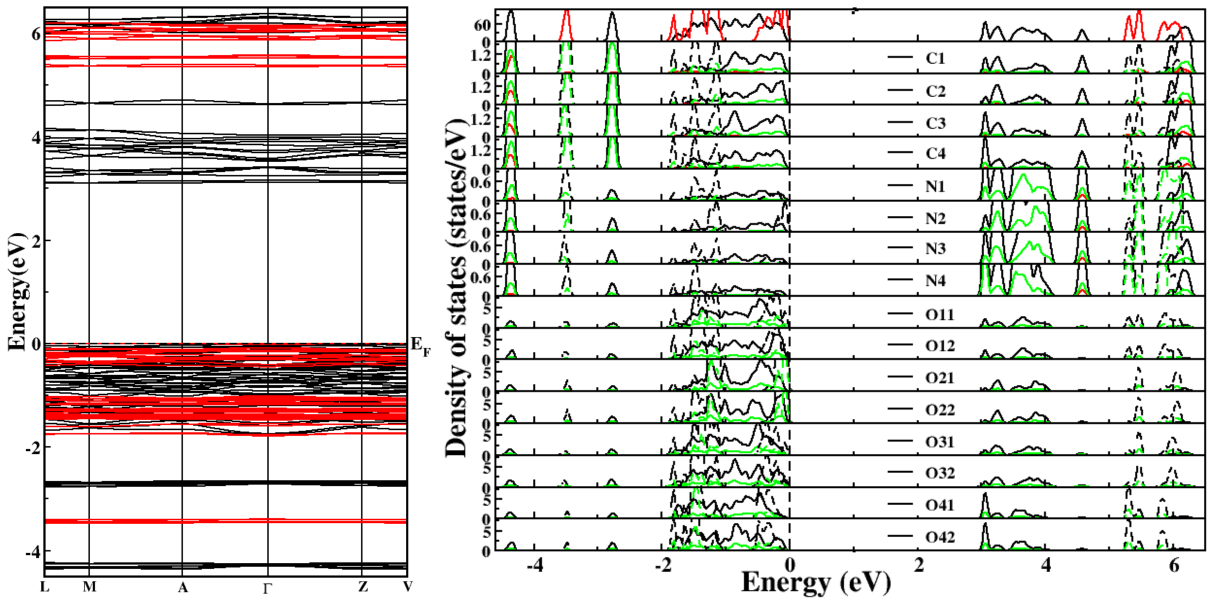

(a) (b)

Figure. 5.3 Electronic band structure (shown in a: black and red colour denote band structure without and with TB-mBJ potential) and density of states [shown in b: solid and dashed line represent partial density of states without and with TB-mBJ potential (black: atomic, red: s-electronic and green: p-electronic contributions) whereas total DOS without and with TB-mBJ is represented by black and red colour, respectively] along with the contributing inequivalent atoms of atoms of ONC.

indicates the presence of ionic nature in the bond associated with these atoms. Though the density of states using normal GGA functional clearly shows that the valence band near Fermi level is mainly composed of carbon and oxygen contribution, the inclusion of TB-mBJ potential shows a shift of density of states of carbon atoms towards more negative energy leaving the fact that the main contribution near the Fermi level is due to the oxygen atoms. The main contribution in the bottom of the conduction band is found due to O4 type oxygen atoms. Calculation of BEC has also shown a large deviation in O2 and O4 types of oxygen atoms which helps us to understand the importance of O2 and O4 types of oxygen atoms in this material.

5.3.5 Optical properties

The optical properties of ONC have been studied with more accurate TB-mBJ potential in addition to normal GGA functional which is implemented in the FP-LAPW method. Calculated complex dielectric function, absorption spectra, refractive index, reflection spectra and energy loss function spectra with respect to photon energy have been shown in Figure 5.4 and 5.5. In order to calculate the optical properties, knowledge of dielectric function is very important. In this connection, the imaginary part of the dielectric function can be evaluated with the help of the equation 5.1.

$$\epsilon_2(\omega) = \frac{Ve^2}{2\pi\hbar m^2\omega^2} \int d^3k \sum | < \psi_c|p|\psi_v > |^2 \delta(E_c - E_v - \hbar\omega) \tag{5.1}$$

Where ψ_c and ψ_v denote the conduction and valence band wave functions, respectively, p denotes the momentum operator and photon frequency is denoted by ω. In general, the dielectric function is denoted as $\epsilon(q, \omega)$ where q and ω indicate momentum transfer in photon-electron interaction and the photon energy transfer, respectively. But as we are considering negligible momentum transfer from initial to final state according to electric-dipole approximation, q = 0 in these calculations. Though this dielectric function $\epsilon(\omega)$ is contributed by intra- and interband transitions, interband transitions are mainly considered in these calculations as intraband transitions are important for metals. As it is well known that the contribution of the indirect interband transitions which involve phonon scattering to $\epsilon(\omega)$ is small compared to direct interband transitions, [61] we have considered only direct interband transitions. By integrating all possible transitions from occupied to unoccupied states with fixed k-vector over Brillouin zone, direct interband contribution to imaginary dielectric function $\epsilon_2(\omega)$ can be calculated within the random phase approximation [62] which has been shown in equation 5.1. For obtaining the full information about the dielectric function, Kramers-Kronig transformation is found to be useful which is normally used to extract the real dielectric function.

$$\epsilon_1(\omega) = 1 + \frac{2}{\pi} P \int_0^\infty \frac{\epsilon_1(\omega')\omega' d\omega'}{(\omega')^2 - (\omega)^2} \tag{5.2}$$

Here P denotes the principal value of the integral. Knowledge of imaginary and real dielectric functions helps to calculate other optical properties such as reflectivity R(ω), refractivity n(ω), energy-loss function L(ω) etc. The relation to obtaining the reflectivity R(ω) is as follows

$$R(\omega) = |\frac{(\sqrt{\epsilon(\omega)} - 1)}{(\sqrt{\epsilon(\omega)} + 1)}|^2 \tag{5.3}$$

In case of energy-loss function L(ω), the relation is

$$L(\omega) = |\frac{(\epsilon_2(\omega)}{\epsilon_1(\omega)^2 + \epsilon_2(\omega)^2}|^2 \tag{5.4}$$

Refractivity function n(ω) can be expressed as

$$n(\omega) = \frac{1}{\sqrt{2}[\sqrt{\epsilon_1(\omega)^2 + \epsilon_2(\omega)^2} + \epsilon_1(\omega)^2]^{\frac{1}{2}}} \tag{5.5}$$

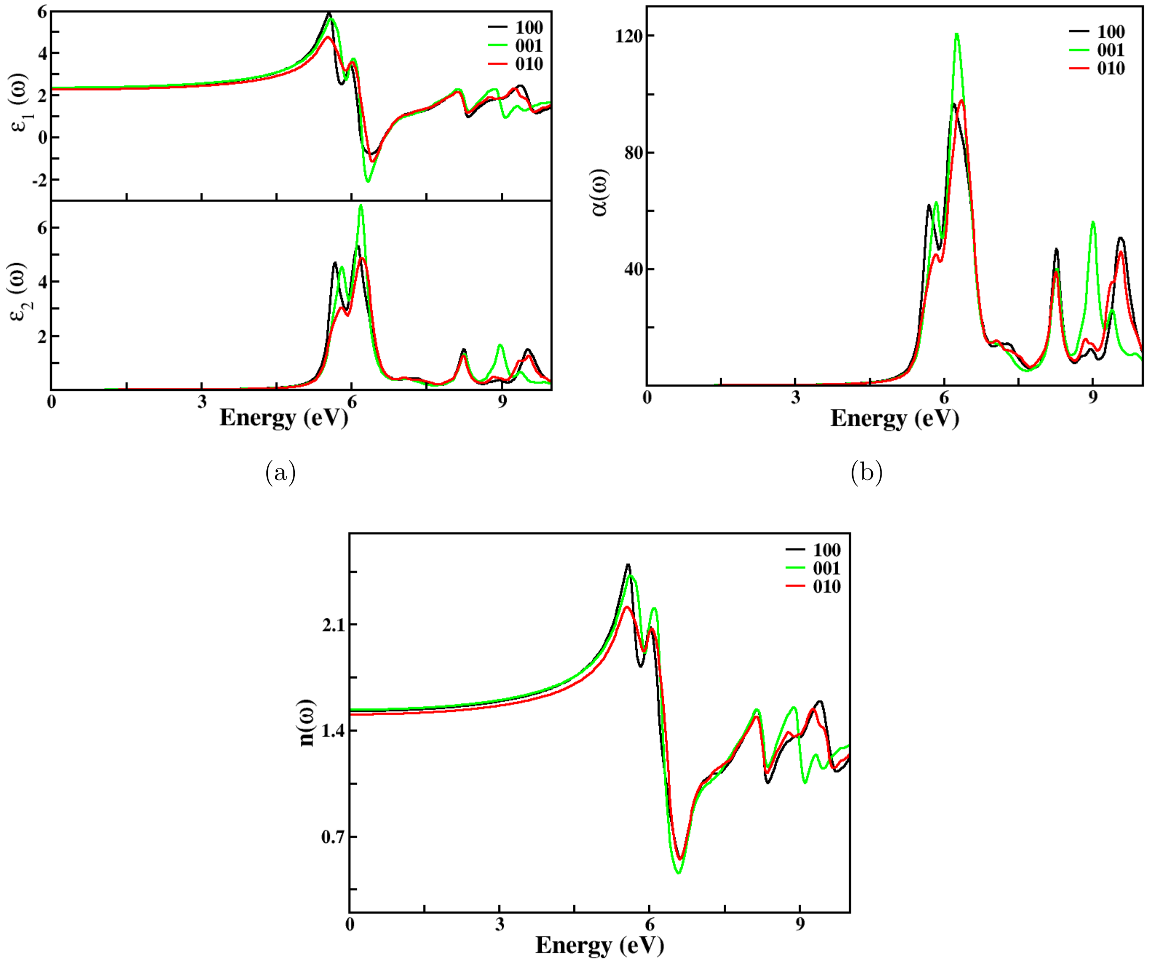

(a)

(b)

(c)

Figure. 5.4 Optical properties of ONC. (a) dielectric function (upper panel shows $\epsilon_1(\omega)$ and lower panel shows $\epsilon_2(\omega)$), (b) absorption spectra and (c) refractive index.

The real and imaginary dielectric function shown in Figure 5.4a (upper panel and lower panel, respectively) show optical anisotropy, especially in the high energy range. Static dielectric constant along different directions follows as: zz (high) $>$ xx (medium) $>$ yy (low). Static values of $\epsilon_1(\omega)$ for xx, yy and zz directions are 2.33, 2.26 and 2.36, respectively, which are nearly equal and show optically isotropic behaviour in the low energy range. The fluctuation of the real part of dielectric function can be found high at 6 eV which leads to the high value of imaginary parts of dielectric functions. In both the cases, c-axis show higher optical activity compared to other axes. In order to calculate the absorption spectra of this material, this imaginary part of the dielectric constant has been evaluated from the real part of the dielectric function with the help of the Kramers-Kroning relation.

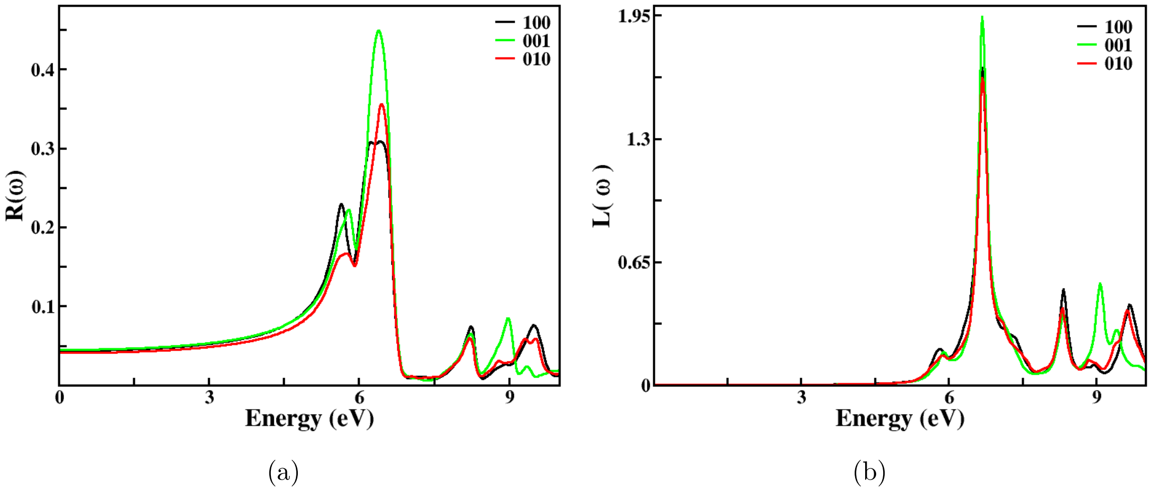

(a)

(b)

Figure. 5.5 Optical properties of ONC: (a) reflectivity and (b) energy loss function.

Absorption spectra of ONC depicted in Figure 5.4b clearly show that the first absorption peak is in the xx-direction at nearly 5.2 eV photon energy. Though this absorption spectra shows nearly isotropic nature in the low energy region it becomes anisotropic in the high energy range. All the high-intensity absorption peaks can be seen in the zz-direction which indicates the importance of oxygen atoms (specially B type of oxygen atoms) aligned in this direction. Static value of n(ω) along different direction are as follows: 1.54 (nzz) > 1.53 (nxx) > 1.51 (nyy) whereas the static value of R(ω) along different directions are as follows: 0.045 (nzz) > 0.044 (nxx) > 0.041 (nyy). The reflectivity is shown in Figure 5.5a in three crystallographic directions which indicates that the value of this parameter is always high along the c-axis. Similarly, energy loss function L(ω) of this material has been studied in this work which is related to the energy loss of electrons while travelling inside a material. The value of this parameter along the c-axis is found to be higher compared to other axes.

5.4 Conclusions

In summary, we have optimized the monoclinic structure of novel high energetic material octanitrocubane (ONC) with normal PBE functional as well as with van der Waals corrected DFT to obtain the ground state structural as well as elastic properties of ONC. van der Waals corrected TS method is found to be more suitable for producing experimental results. Lattice parameter $'c'$ of this material is found to be more compressible than the other two axes which had been anticipated from the study of the crystal structure. The calculated bulk modulus is found to be 12.19 GPa which is similar to other secondary energetic materials. The study of elastic constants of this material reveals that the c-axis is more sensitive, and the a-axis is less sensitive to shock initiation. Also, this material is more sensitive than RDX but less sensitive than β-HMX. Analysis of BECs of ONC tells the presence of mixed ionic and covalent bonding among nitrogen (N2, N4) and oxygen (O2A) atoms. After that, zone centred phonon frequencies of this material have been evaluated in this study, and 192 vibrational frequencies of ONC have been reported. In the end, the bandgap of this material has been calculated using well-known semi-local TB-mBJ potential and found to be 5.31 eV. The density of state shows a presence of strong covalent bonding in the carbon cage of this material. In the low energy range, optical isotropy can be seen, which becomes anisotropic at high energy. An extensive study of structural, elastic, vibrational, electronic and optical properties clearly indicates the involvement of 2- and 4-type of atoms in different properties of this material which are arranged in bc-plane of the material.

References

[1] A. Vij, W.W. Wilson, V. Vij, F.S. Tham, J.A. Sheehy and K.O. Christe, J. Am. Chem. Soc. 123, 6308 (2001).

[2] D. Kumar and A.J. Elias, RESONANCE 24, 1253 (2019).

[3] A.K. Sikder and N. Sikder, J. Hazard. Mater. 112 (2004).

[4] L.E. Fried, M.R. Manaa, P.F. Pagoria and R.L. Simpson, Annu. Rev. Mater. Res. 31, 291 (2001).

[5] Q. Wu, W.H. Zhu and H.M. Xiao, RSC Adv. 4, 3789 (2014).

[6] M.B. Talawar, R. Sivabalan, T. Mukundan, H. Muthurajan, A.K. Sikder, B.R. Gandhe and A.S. Rao, J. Hazard. Mater. 161, 589 (2009).

[7] Y. Pan and W.H. Zhu, J. Phys. Chem. A 121, 9163 (2017).

[8] L.A. Paquette, J.W. Fischer and P. Engel, J. Org. Chem. 50, 2524 (1985).

[9] S. Rajkumar, R.S. Choudhari, A. Chowdhury and I.N.N. Namboothiri, Thermochimica Acta 563, 38 (2013).

[10] S. Lal, S. Rajkumar, A. Tare, S. Reshmi, A. Chowdhury and I.N.N. Namboothiri, Chem. Asian J. 9, 3533 (2014).

[11] S. Lal, L. Mallick, S. Rajkumar, O.P. Oommen, S. Reshmi, N. Kumbhakarna, A. Chowdhury and I.N.N. Namboothiri, J. Mater. Chem. A 3, 22118 (2015).

[12] L. Mallick, S. Lal, S. Reshmi, I.N.N. Namboothiri, A. Chowdhury and N. Kumbhakarna, New J. Chem. 41, 920 (2017).

[13] B. Shyamala, S. Lal, A. Chowdhury, I.N.N. Namboothiri and N. Kumbhakarna, Combustion

and Flame 197, 111 (2018).

[14] A.T. Nielsen, R.A. Nissan, D.J. Vanderah, C.L. Coon, R.D. Gilardi, C.F. George and J. Flippen-Anderson, J. Org. Chem. 55, 1459 (1990).

[15] F. Wang, H.C. Du, J.Y. Zhang and X.D. Gong, J. Phys. Chem. A 115, 11788 (2011).

[16] X.J. Xu, H.M. Xiao, X.H. Ju, X.D. Gong and W.H. Zhu, J. Phys. Chem. A 110, 5929 (2006).

[17] X.J. Xu, W.H. Zhu and H.M. Xiao, J. Mol. Struct.: THEOCHEM 853, 1 (2008).

[18] Y. Pan, W.H. Zhu and H.M. Xiao, Comput. Theor. Chem. 1114, 77 (2017).

[19] V. Ghule, P. Jadhav, R. Patil, S. Radhakrishnan and T. Soman, J. Phys. Chem. A 114, 498 (2010).

[20] Q. Wu, W.H. Zhu and H.M. Xiao, J. Mol. Model. 20, 2483 (2014).

[21] Y. Pan, W.H. Zhu and H.M. Xiao, Can. J. Chem. 91, 1243 (2013).

[22] J.Y. Zhang, H.C. Du, F. Wang, X.D. Gong and Y.S. Huang, J. Mol. Model. 18, 165 (2012).

[23] J.Y. Zhang, F. Wang and X.D. Gong, Struct. Chem. 24, 1339 (2013).

[24] Y.F. Ling, X.L. Ren, W.P. Lai and J. Luo, Eur. J. Org. Chem. 2015, 1541 (2015).

[25] J.Y. Zhang, H.C. Du, F. Wang, X.D. Gong and Y.S. Huang, J. Phys. Chem. A 115, 6617 (2011).

[26] Y. Wang, C. Qi, J.W. Song, X.Q. Zhao, C.H. Sun and S.P. Pang, J. Mol. Model. 19, 1079 (2013).

[27] W.-J. Chi and Z.-S. Li, C. R. Chim. 18, 1270 (2015).

[28] W. Chi and Z. Li, RSC Adv. 5, 7766 (2015).

[29] P.E. Eaton, M.X. Zhang, R. Gilardi, N. Gelber, S. Iyer and R. Surapaneni, Propellants, Explos., Pyrotech. 27, 1 (2002).

[30] F. Wang, H. Du, J. Zhang and X. Gong, J. Phys. Chem. A 115, 11788 (2011).

[31] P.E. Eaton, Angew. Chem., Int. Ed. 31, 1421 (1992).

[32] B.D. Kybett, S. Carroll, P. Natalis, D. Bonnell, J. Margrave and J.L. Franklin, J. Am. Chem. Soc. 88, 626 (1966).

[33] X.W. Fan, L. Qiu and X.H. Ju, Struct. Chem. 20, 1039 (2009).

[34] D.A. Hrovat, W.T. Borden, P.E. Eaton and B. Kahr, J. Am. Chem. Soc. 123, 1289 (2001).

[35] J. Kortus, M.R. Pederson and S.L. Richardson, Chem. Phys. Lett. 322, 224 (2000).

[36] R.J. Schmitt and J.C. Bottaro, AD-A201416 (1988).

[37] J. Zhang, H.M. Xiao and X.D. Gong, J. Phys. Org. Chem. 14, 583 (2001).

[38] F.J. Owen, J. Mol. Struct. (THEOCHEM) 460, 137 (1999).

[39] J. Zhang and H.M. Xiao, J. Chem. Phys. 116, 10674 (2002).

[40] F. Tran and P. Blaha, Phys. Rev. Lett. 102, 226401 (2009).

[41] P. Hohenberg and W. Kohn, Phys. Rev. 136, B864 (1964).

[42] W. Kohn and L.J. Sham, Phys. Rev. 140, A1133 (1965).

[43] G. Kresse and J. Furthmuller, Phys. Rev. B 54, 11169 (1996).

[44] J.P. Perdew, S. Burke and M. Ernzerhof, Phys. Rev. Lett. 77, 3865 (1996).

[45] T.H. Fischer and J. Almlof, J. Phys. Chem. 96, 9768 (1992).

[46] H.J. Monkhorst and J.D. Pack, Phys. Rev. B 13, 5188 (1976).

[47] (a) A. Tkatchenko and M. Scheffler, Phys. Rev. Lett. 102, 073005 (2009); (b) S. Grimme, J. Comp. Chem. 27, 1787 (2006).

[48] P. Blaha, K. Schwarz, G.K.H. Madsen, D. Kvasnicka and J. Luitz, ISBN 3-9501031-1-2 (2001).

[49] D.J. Singh, Phys. Rev. B 82, 155145 (2010).

[50] D.J. Singh, Phys. Rev. B 82, 205102 (2010).

[51] P.E. Eaton, R.L. Gilardi and M.X. Zhang, Adv. Mater. 12, 1143 (2000).

[52] F.D. Murnaghan, Proc. Natl. Acad. Sci. U.S.A. 30, 244 (1944).

[53] S. Appalakondaiah, G. Vaitheeswaran and S. Lebegue, J. Phys. Chem. A 119, 6574 (2015).

[54] C.-S. Yoo and H. Cynn, J. Chem. Phys. 111, 10229 (1999).

[55] J.C. Gump and S.M. Peiris, J. Appl. Phys. 97, 053513 (2005).

[56] L.L. Stevens, N. Velisavljevic, D.E. Hooks and D.M. Dattelbaum, Propellants, Explos., Pyrotech. 33, 286 (2008).

[57] R.S. McWilliams, Y. Kadry, M.F. Mahmood, A.F. Goncharov and J.C. Jenkins, J. Chem. Phys. 137, 054501 (2012).

[58] J.J. Dick, Appl. Phys. Lett. 44, 859 (1984).

[59] J.J. Haycraft, L.L. Stevvens and C.J. Eckhardt, J. Chem. Phys. 124, 024712 (2006).

[60] L.L. Stevens and C.J. Eckhardt, J. Chem. Phys. 122, 174701 (2005).

[61] N.V. Smith, Phys.Rev.B 3, 1862 (1971).

[62] H. Ehrenreich and M.H. Cohen, Phys.Rev. 115, 786 (1959).

CHAPTER 6

Understanding of structure-property correlation of heterocyclic energetic materials

This chapter presents a theoretical insight about the structure-property correlation of heterocyclic furazan based energetic materials 4,4′-Bis(nitramino)azofurazan (DNAF) and Bis(nitrofurazano)furazan (BNFF-1). Obtained ground state structural parameters of these materials using dispersion corrected schemes are found to match well with experimental data. Pressure variation study of structural properties clearly indicates that DNAF is highly compressible along the b-axis, while the c-axis of BNFF-1 is more compressible. Pressure variation of unit cell volume of these crystals also helps us to evaluate their corresponding bulk modulus and pressure derivative of the bulk modulus. The variation of the intramolecular bond lengths of DNAF with pressure shows that the bond between the nitrogen atoms in the nitramine group is more compressible than other bonds. The study of elastic constants and related properties of these materials has also been carried out to know the impact and frictional sensitivity. In the end, electronic band structure calculation has been performed as the information about this quantity has been found to be very useful due to its correlation with the photodecomposition process of energetic materials.

6.1 Introduction

A recent trend in the development of modern high energy materials has been achieved by replacing the traditional method of using nitro group with nitrogen-rich heterocycles [1]. Indeed, heterocycles are found to be more efficient than the multiple uses of nitro groups as the presence of excessive nitro groups may increase the risk of handling such materials [2]. Also, as desired properties of energetic materials can be achieved to a greater extent with these nitrogen-rich heterocyclic compounds, these compounds are considered as a good substitute for widely used nitroether-, nitramine-, and nitroaromatic-based compounds [3]. Among those different heterocycles, tetrazoles, triazoles, pyrazoles, imidazoles, oxadiazoles, furazan, furoxan, etc., are normally used [4, 5] in modern energetic materials. These materials possess important energetic properties such as positive oxygen balance (OB), high heat of formation (HOF) and high density. The presence of different bonding between nitrogen, carbon and oxygen atoms in these structures are the main reason for these attributes [6]. Also, the ring-strain energy stored in these materials improves their detonation properties [7] and helps to achieve better thermal stability. Earlier studies have shown that the furazan and tetrazole structures are more efficient in comparison to the other heterocyclic structures in high energetic materials [8]. In this connection, the use of furazan group instead of the nitro group has shown an increment in density by 0.06-0.088 g/cm^3, in HOF by 200 kJ/mol, and in detonation velocity by 300 ms^{-1}, respectively [9]. This has brought interest in the community to look forward to finding furazan based energetic materials [10]. These properties, which are making furazan a potential candidate of interest, are due to the presence of two doubly bonded carbon and nitrogen atoms and two singly bonded nitrogen and oxygen atoms in the ring [11, 12]. It is also found that the enhancement of detonation parameters with less sensitivity can be achieved by the use of azo moiety as it includes a larger endothermic HOF in energetic materials [13]. In addition to the azo moiety, better detonation properties can be achieved by using different energy-rich functional groups such as nitro ($-NO_2$), nitrato ($-ONO_2$), nitramine ($-NNO_2$), and azido ($-N_3$) in heterocyclic furazan based energetic materials [14]. A better structural modification can also be expected from $-NHNO_2$ functionality along with the furazan ring to have an advanced energetic anion [15]. The importance of this nitramine group for attaining the desired performance cannot be denied according to present knowledge on energetic material [16] as the nitro and amino groups present in the same molecule can generate extensive intra- and intermolecular hydrogen bonding, reducing their sensitivity. Though hydrogen bonding is a major factor for determining the sensitivity of energetic materials, a lot more other parameters related to these materials are also involved in the complex process of detonation. Dependence of impact sensitivity on bandgap narrowing, stored energy content, crystal habit and the quantification of these parameters are well explained by Bondarchuk [17]. A recent report by Shreeve et al. [18] on the synthesis of DNAF in the nitraminofurazan group mentioned its great detonation performances. Also, based on these furazan and furoxan heterocyclic rings, Bis(nitrofurazano)furoxan (BNFF) was first synthesized by Zhang et al. [19]. This material shows good performance but high sensitivity towards shock-wave due to its active coordination oxygen of furoxan ring. As a result, Zhang et al. synthesized bis(nitrofurazano)furazan (BNFF-1) [20] to achieve less sensitivity along with high performance. Though these materials have shown their potential to become high energy materials, studies on these materials are still very scarce. In this connection, a complete structure-property relation study on these materials can help us to have a thorough understanding of such materials. Therefore, an initiative has been taken in this work to understand the structure-property relation of these materials through density functional theory calculations. Here the structural properties along with the elastic and electronic properties of the crystalline phase have been addressed. Two well-known energetic materials RDX [21], and β-HMX [22] have been considered for the comparison of elastic constants to understand the sensitivity of these materials. The arrangement of this chapter is as follows: the crystal structure and computational details are presented in the next section. Then, our results and corresponding discussions on these materials are given, and our conclusions for this study are drawn.

6.2 Crystal structure and computational Details

To have a preliminary idea about different interactions present in these materials, crystal structure in different orientations as well as the molecular structure are presented. Shreeve et al. [18] has shown that DNAF exists in monoclinic structure with $P2_1/c$ space group where associated molecules are made up of two furazan, two nitramine and one azo building blocks. It can be easily visualised from Figure 6.1a, that the presence of intramolecular hydrogen bonding between the nitramine hydrogen atom and the azo nitrogen atom ((N(8′)–H(6))/(N(8)–H(6′))) contributes significantly to the structural stability of this molecule. The arrangement of this molecule in the crystal structure is clearly shown in Figure 6.1b, c and d with different orientations. The presence of different intermolecular interactions in this material can be explained from these orientations. Stacking of these molecules along a-axis can be seen from the Figure 6.1b, whereas the presence of intermolecular hydrogen bonding along c-axis is depicted in both Figure 6.1b and c. The hydrogen atom of nitramine group and its nearest nitrogen atom of the furazan group of other molecules form this intermolecular hydrogen bonding. Except these interactions, the role of intramolecular azo bond is found to be prominent in between different layers of this material. Figure 6.1d depicts a zigzag arrangement of these molecules in ab-plane which tells about the presence of edge-to-face and face-to-face stacking interaction in this material. This figure also confirms the absence of intermolecular hydrogen bonding in this plane which in turn predicts that the effect of inclusion of van der Waals interaction will be more for lattice parameter a and b than lattice parameter c. In case of BNFF-1, three furazan groups along with two nitro groups can be seen in the molecular structure shown in Figure 6.2a. The crystal structure of this compound depicted in Figure 6.2b clearly shows the presence of stacking interactions in this material. To obtain different properties of these materials, Vienna Ab-initio Simulation Package (VASP) [23] has been used. This package implements density functional theory [24, 25] within the projector augmented wave (PAW) [26] method. The treatment of electron-electron interactions is considered with the generalized gradient approximation (GGA) [27] and the method of Grimme [28] and TS scheme have been used to include missing vdW corrections. The structure optimization has been done using the Broyden-Fletcher-Goldgarb-Shanno (BFGS) [29] minimization scheme. This TS correction scheme will include the correct polarizability of the inter-atomic bonds over Grimme [30]. To ensure a sufficient convergence, the Brillouin zone integration using a Monkhorst-Pack grid [31] was done with a Γ-centered (5×6×6) grid for DNAF and with a grid of (3×2×1) for BNFF-1. While the plane wave energy cutoff was set to 600 eV for both the materials. The valence electronic configurations used in these calculations are C: [$2s^2 2p^2$], N: [$2s^2 2p^3$], O: [$2s^2 2p^4$] and H: [$1s^1$]. The convergence criteria for this calculation were set accordingly: energy convergence = 1×10^{-8} eV/atom, maximal residual force = 0.01 eV/Å. In case of calculating the elastic constants, this maximal residual force was set to 1×10^{-4} eV/Å for DNAF and to 1×10^{-3} eV/Å for BNFF-1. The used K-path for band structure calculation of BNFF-1 crystal is: Γ-Z-T-Y-S-X-U-R.

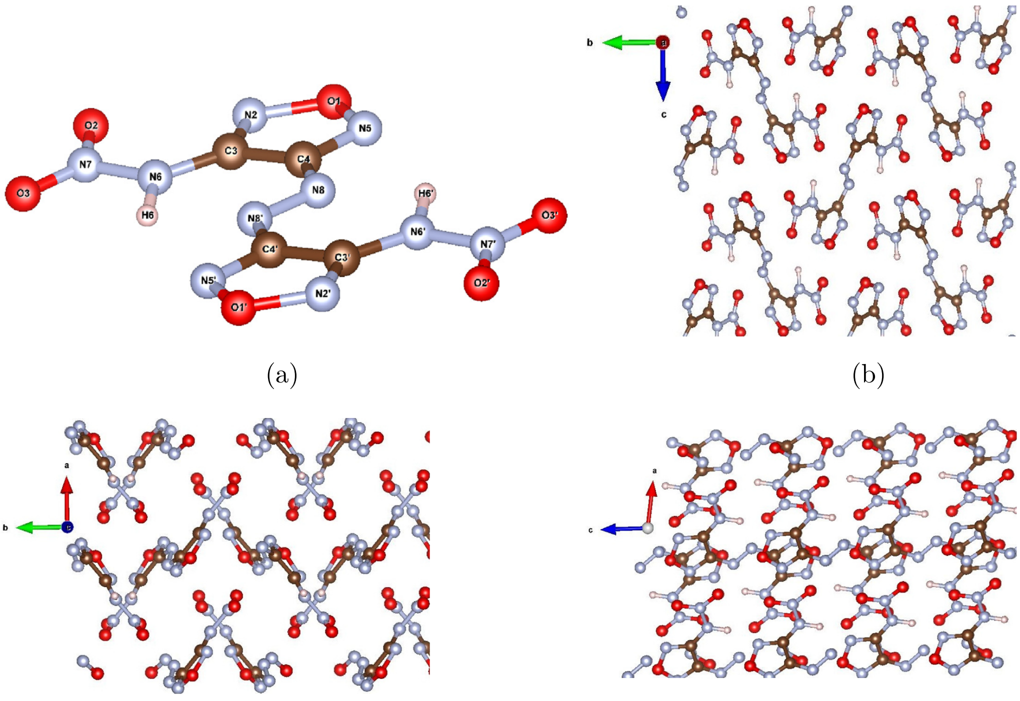

(a)

(b)

(c)

(d)

Figure. 6.1 Molecular structure (shown in a) and Crystal structure of 4,4′-Bis(nitramino)azofurazan shown in (b) bc plane, (c) ca plane and (d) ab plane.

In order to have a precise band structure of DNAF use of the GW approximation [32, 33, 34, 35, 36, 37] has been considered which is implemented in VASP. The convergence of our calculations was reached when 220 states were used to sum over bands for polarizability as well as for self-energy formulas and in order to calculate polarizability matrices a cut-off

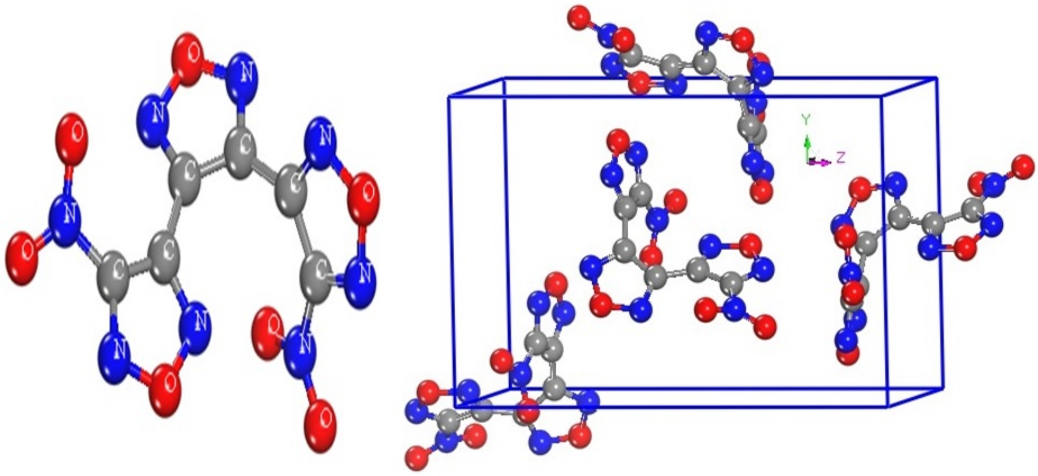

(a) (b)

Figure. 6.2 Molecular structure (a) and crystal structure (b) of BNFF-1 in yz plane.

up to 150 eV has been considered. To understand intermolecular interaction in DNAF, hirshfeld surface with its fingerprint at ambient pressure as well as at high pressure have been calculated using CrystalExplorer [38]. Hisrhfeld surface is based on the electron distribution of the promolecule ($\rho_{promolecule}(r)$) which is considered to be the sum of spherical atoms for molecule and the procrystal ($\rho_{procrystal}(r)$) which is the corresponding sum over the crystal and is defined using an implicit weight function $\omega(r) = 0.5$ [39, 40]. Here $\omega(r)$ is expressed as:

$$\omega(r) = \frac{\rho_{promolecule}}{\rho_{procrystal}} \tag{6.1}$$

Distance information of external (d$_e$) and internal atoms (d$_i$) to the surface is summarized in a 2-D histogram and is called the fingerprint plot of the surface. This kind of fingerprint provides the relative contribution of different intermolecular interactions [40, 41].

6.3 Results and Discussion

6.3.1 Structural properties

The structure of a material is intimately linked to its properties and vice versa. In this section, we present a thorough study of the different structural parameters like lattice parameters and unit cell volume of these materials at ambient and at high pressure. A thorough understanding of different bond angles and bond lengths associated with DNAF and especially intra-, intermolecular hydrogen bonds of this compound have also been presented. The structures shown in Figure 6.1 clearly depicts the presence of layers in DNAF, therefore we can expect a prominent effect of van der Waals interactions. Our calculated lattice parameters, angles, volume at equilibrium using the PBE functional and the van der Waals corrected D2 and TS methods are presented in Table 6.1. As expected, the PBE functional is overestimating significantly the lattice parameters and volume, while the results obtained with the D2 and TS methods are found to be close to the experimental values. In the following, we have used exclusively the D2 method since this method is reproducing more closely the experimental values than the TS method for this particular compound.

Table 6.1 Calculated structural parameters of monoclinic crystal DNAF at 0 GPa along with previously reported result (see in Ref. [18]).

Parameters	Expt.	PBE	D2	TS
a(in Å)	5.63	6.13	5.69	5.75
b(in Å)	9.12	9.55	9.06	9.26
c(in Å)	9.55	9.93	9.60	9.59
$\beta(°)$	97.91	101.18	98.78	98.77
Vol(in Å^3)	485.52	570.69	488.95	504.65
$\triangle$V(%)		+17.54	+0.71	+3.94

The calculated ground state lattice parameters of BNFF-1 are given in Table 6.2. The deviation in optimized lattice parameters and volume of BNFF-1 with PBE (∼5%, >10%) and G06 (∼1%,∼2%), TS (∼0.5%, ∼1%) confirms the importance of van der Waals correction to normal DFT calculation for this material. However, the results given in Table 6.2 clearly explain that the TS method is more suitable than Grimme(D2) [30] for calculating the structural properties of BNFF-1. Since the same damping function is used in both dispersion correction methods, the obtained difference in the structural optimization can be attributed to the fact that TS scheme accounts for the effect of hybridization states on the bond polarizability for calculating the dispersion coefficients. Hence, all further calculations are performed on TS equilibrium BNFF-1 structure. After obtaining the ground state structural parameters of these materials, a pressure variation study has been performed on these materials to understand the compressibility nature of different structural parameters.

The pressure variation of volume and lattice parameters of DNAF are shown in Figure 6.3, and clearly depicts that the lattice parameter b is more compressible than the other two lattice parameters. The calculated coefficients of pressure for a, b, and c lattice parameters are 11.930, 13.037 and 7.307 GPa$^{-1}\times10^{-3}$, respectively. These values indicate that the ordering of compressibility of the lattice parameters follows b > a > c. Bulk modulus as well as its derivative with respect to pressure have been calculated from the pressure-volume curve. Third-order Birch Murnaghan equation of state (EOS) [43] has been employed in this process. Our calculated bulk modulus value for DNAF is 15 GPa, whereas its derivative related pressure is found to be 10.54. Though the high

Table 6.2 Calculated structural parameters of orthorhombic BNFF-1 at 0 GPa with and without van der Waals corrected DFT.

Parameters	Expt.a	PBE	D2	TS
a(in Å)	7.149	7.497	7.131	7.190
b(in Å)	9.789	10.250	9.702	9.82
c(in Å)	15.284	15.899	15.204	15.325
Vol(in Å^3)	1069.63	1221.67	1051.85	1083.00
△V(%)		+14.2	-1.7	+1.2

compressibility of this compound can be confirmed from its low bulk modulus value, higher pressure derivative value of bulk modulus indicates stiff quality of this crystalline material with increasing pressure. A previous study on similar kind of C–H–N–O based energetic materials by Appalakondaiah et al. [44] supports our result, while the known experimental values for energetic materials such as β-HMX (12.4 GPa (10.4) [45], 21.0 GPa (7.4) [46]), TATB (15.7 GPa (8.0) [47]), and TAG-MNT (14.6 GPa (4.8) [48]) are in a similar range.

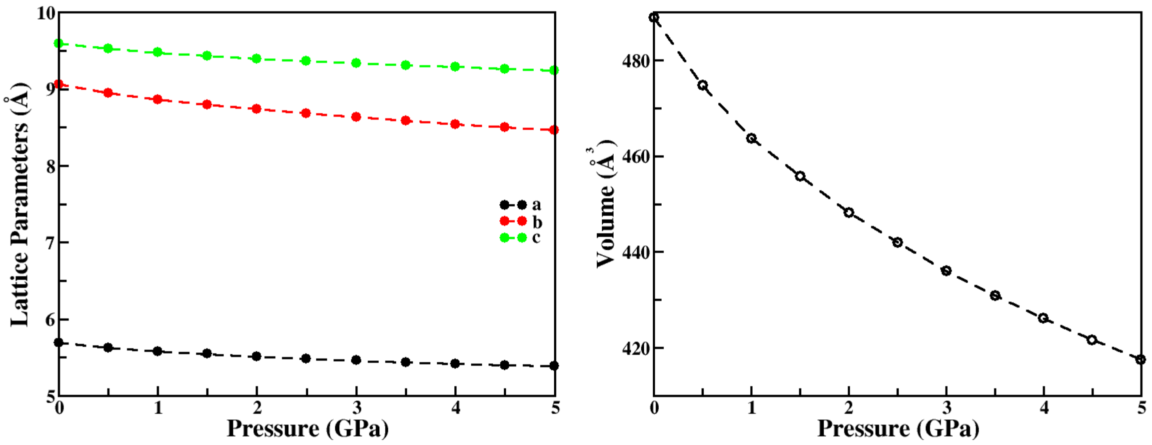

(a) (b)

Figure. 6.3 Pressure variation of lattice parameters (showed in a) and Pressure variation of the volume (showed in b) of DNAF.

In order to obtain the single-crystal bulk modulus value of BNFF-1, we calculated the equation of state (EOS) in 0-5 GPa range with 0.5 GPa step size. The corresponding variations in the lattice parameters and volume with respect to applied pressure are shown in Figure 6.4. It can be clearly seen from the Figure 6.4, that the c axis is more compressible than other two axes. The calculated first-order pressure coefficient for lattice parameters a, b, c are 12.87, 11.51 and 14.63 GPa$^{-1}\times10^{-3}$ respectively, indicating the ordering of compressibility as c > a > b. The pressure versus volume curve is fitted to the third-order

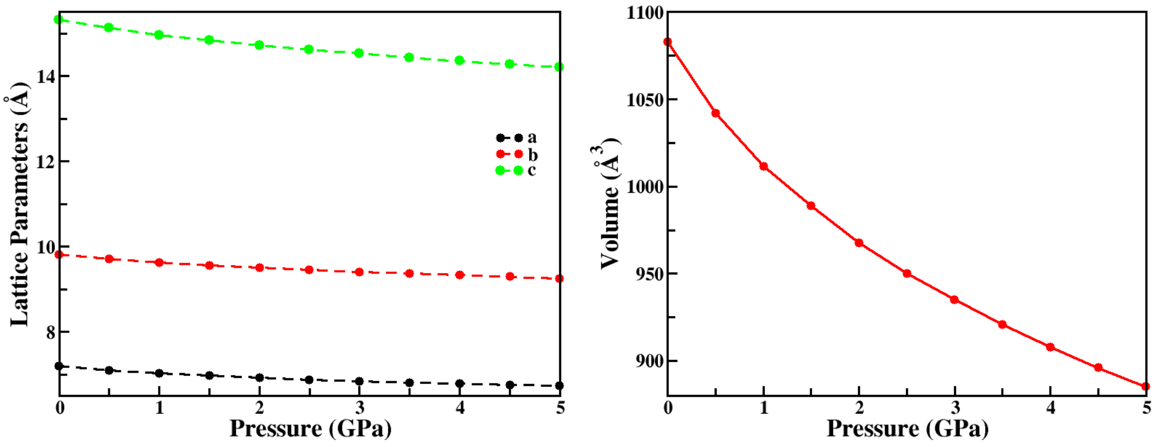

(a)

(b)

Figure. 6.4 Variation of lattice parameters (a, b, c in Å), volume (Å^3) with respect to pressure at PBE+ TS level of BNFF-1.

birch murnaghan equation of states to calculate bulk modulus and pressure derivative. Resulted bulk modulus value (11.43 GPa) is in the range of the secondary energetic materials and its high-pressure derivative value (8.17) shows its more compressible nature. As mentioned earlier in this section, an analysis of intra- and intermolecular bonding of DNAF has also been carried out in this work to support the result found from the unit cell parameter calculation. Along with intramolecular bonds between carbon, nitrogen, hydrogen and oxygen atoms present in the crystal, intermolecular hydrogen bonding has also been considered in our analysis for its major contribution to the cohesion of crystal structure. Obtained values of intramolecular bonds with different functionals at equilibrium is presented in Table 6.3. As expected, the prominent effect of the vdW correction cannot be seen for these bonding. To have a proper understanding of the pressure effect on intramolecular bonds, evaluation of these bond lengths is considered up to 5 GPa, where 0.5 GPa is the size of each step. Fig. 5 shows this evaluation result which clearly depicts high compressible nature of N–N bond of the amine group than the other intramolecular bonds. Our calculated intermolecular distances at equilibrium are reported in Table 6.4. Here, N(2A)–N(6B) denotes the nearest intermolecular distance for face-to-face stacking, whereas N(7A)–C(4B) and N(7A)–N(5B) are the distances to consider for edge-to-face stacking, while N(2A)–H(6B) corresponds to intermolecular hydrogen bonding. It is clear from these data that the vdW interactions take a significant role in the strength of the interatomic distances and therefore in the cohesion of the crystal.

The effect of pressure on intermolecular hydrogen bonding has also been studied here. Figure 6.6 shows the pressure variation of intermolecular nearest distances related to hydrogen bonding. From this figure, it can be seen that N6–H6 which is donor hydrogen

Table 6.3 Intramolecular bond lengths calculated with GGA and different vdW corrections along with reported experimental value (see in Ref. [18]).

Intramolecular bonding	Expt.	PBE	D2	TS
N(8)–N(8′)(in Å)	1.26	1.27	1.27	1.27
N(8)–C(4) (in Å)	1.40	1.38	1.38	1.38
C(4)–C(3) (in Å)	1.44	1.45	1.45	1.45
C(4)–N(5) (in Å)	1.31	1.32	1.32	1.32
C(3)–N(2) (in Å)	1.31	1.32	1.32	1.32
N(5)–O(1) (in Å)	1.35	1.35	1.35	1.34
N(2)–O(1) (in Å)	1.40	1.41	1.40	1.40
C(3)–N(6) (in Å)	1.38	1.37	1.37	1.37
N(6)–N(7) (in Å)	1.38	1.40	1.39	1.39
N(6)–H(6) (in Å)	0.82	1.03	1.04	1.03
N(7)–O(2) (in Å)	1.22	1.23	1.23	1.23
N(7)–O(3) (in Å)	1.22	1.23	1.23	1.23
H(6)–N(8′) (in Å)	2.43	2.30	2.31	2.31

Table 6.4 Intermolecular distances of nearest atoms with GGA and different vdW functionals along with experimental data(see in Ref. [18]).

Intermolecular bonding	Expt.	PBE	D2	TS
N(2A)–H(6B)(in Å)	2.21	2.23	2.05	2.08
N(2A)–N(6B)(in Å)	2.96	3.08	2.95	2.96
N(6B)–H(6B)-N(2A)	147.9	139.4	143.0	141.5
N(6A)–H(6A)–N(8′A)	112.0	114.3	112.8	112.6
N(7A)–C(4B)(in Å)	3.56	3.88	3.55	3.65
N(7A)–N(5B)(in Å)	3.18	3.53	3.17	3.24

bond (D–H), is not varying with pressure whereas the N(2A)–H(6B) intermolecular distance which is acting as acceptor hydrogen bond (H–A), is decreasing with pressure. Also, the intramolecular hydrogen bond (N(8′)–H(6)) is slightly decreasing with pressure. This decrease of the H–A bond length corresponds to densification of the intermolecular hydrogen bonding network and consequently leads to strengthening intermolecular bonding. Though the previous discussion is mainly concerned about the intra- and intermolecular bond lengths and provides a good description of intramolecular interactions, it cannot explain intermolecular interactions in a proper way. Hirshfeld surface analysis has been considered in this respect to have more insight into intermolecular interactions present in this material.

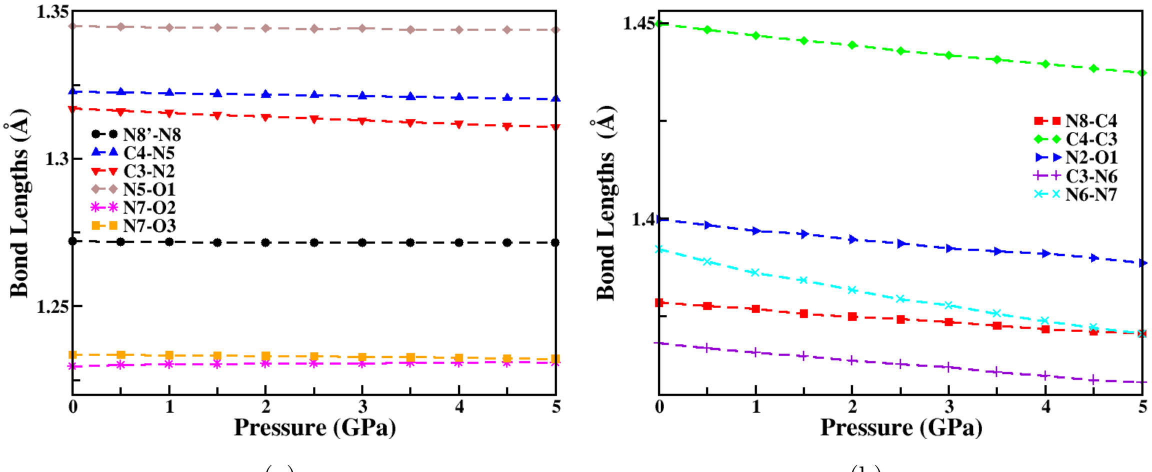

(a) (b)

Figure. 6.5 Variation of intramolecular bond lengths of DNAF with pressure.

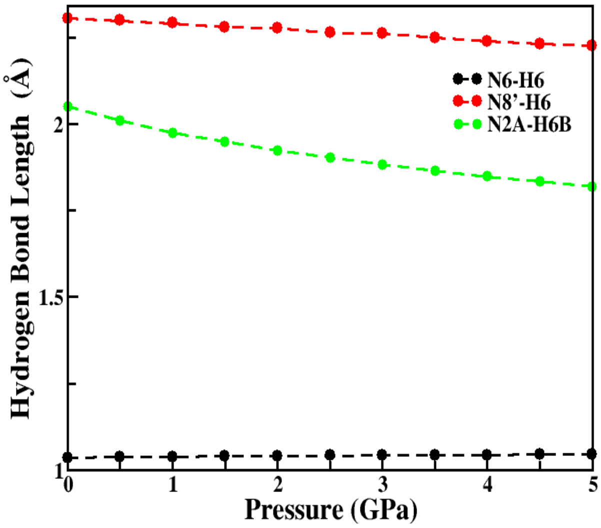

Figure. 6.6 Variation of (N6–H6) (black), (N2A–H6B) (green) and intramolecular hydrogen bond (N8′–H6) (red) length of DNAF with pressure.

This study has been done at 0 GPa as well as at high pressure up to 5 GPa in steps of 1 GPa to understand the pressure effect on these interactions. The hirshfeld surfaces and the corresponding fingerprints of the material are given in Figures 6.7-6.15.

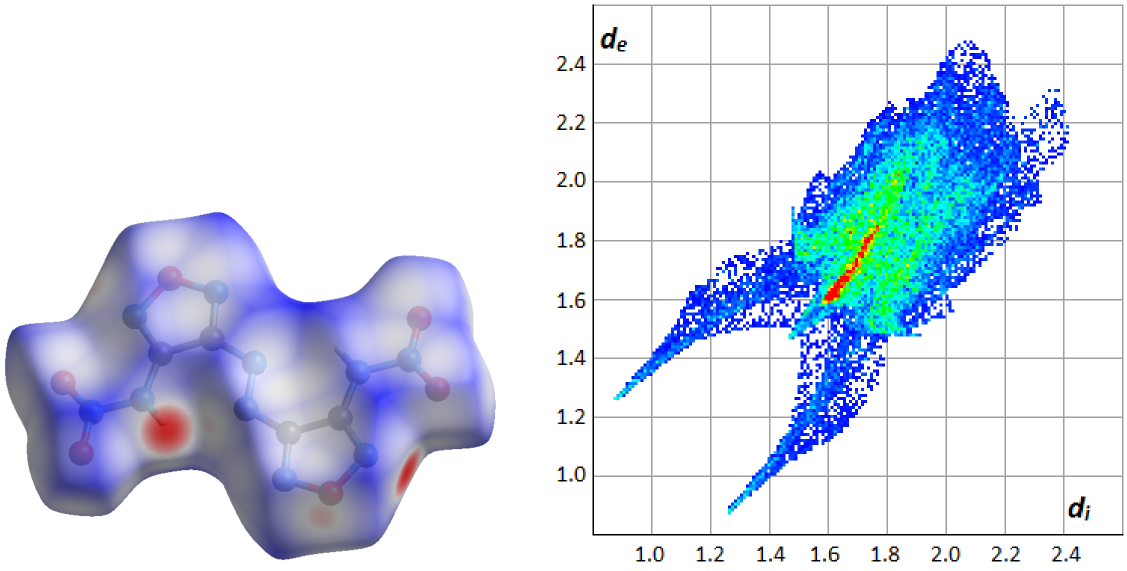

(a) (b)

Figure. 6.7 Hirshfeld surface (a) and finger print (b) of the intermolecular interaction of DNAF at 0 GPa.

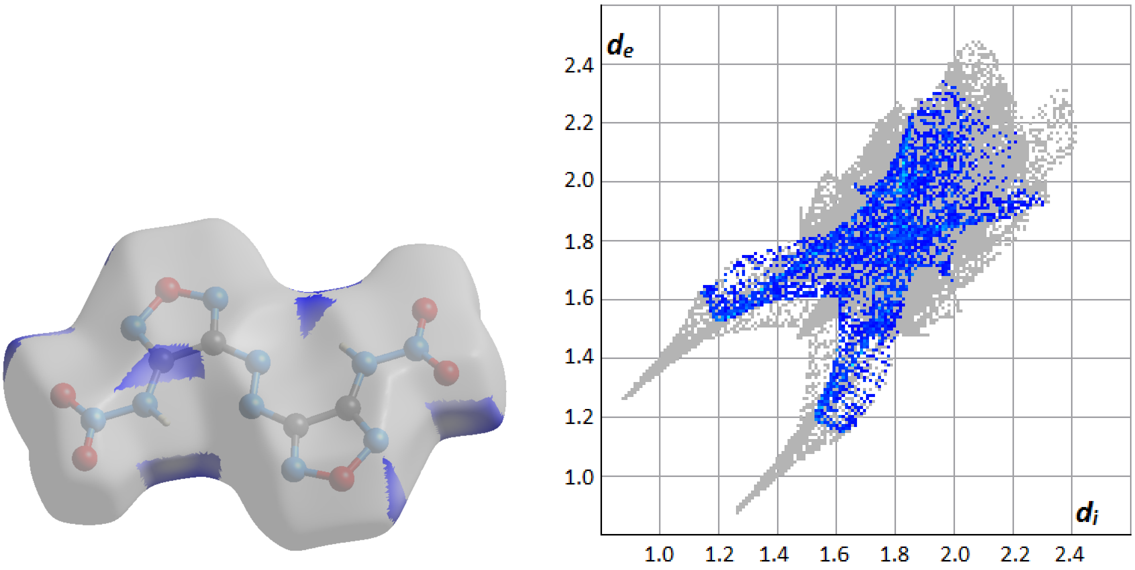

(a) (b)

Figure. 6.8 Contribution of O–H intermolecular interactions in DNAF at 0 GPa shown through Hirshfeld surface (a) and finger print (b).

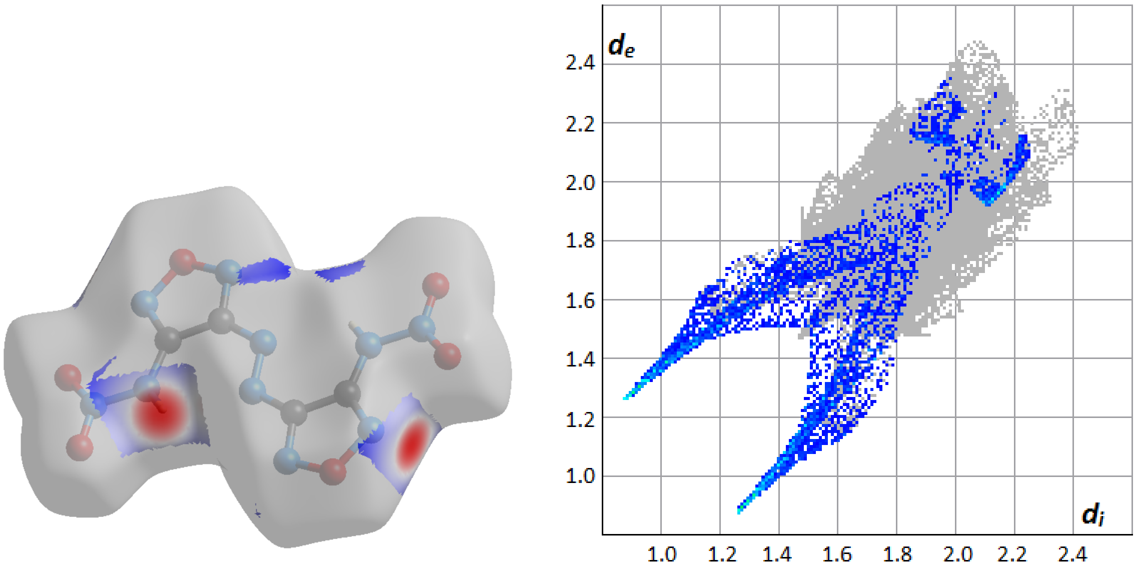

(a) (b)

Figure. 6.9 Contribution of N–H intermolecular interactions in DNAF at 0 GPa shown through Hirshfeld surface (a) and finger print (b).

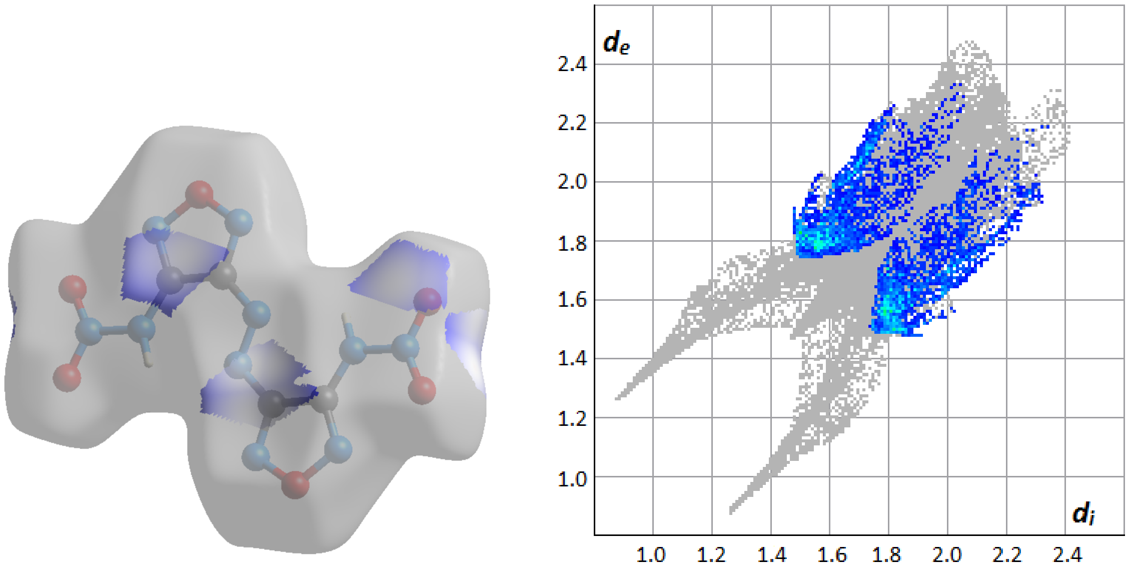

(a) (b)

Figure. 6.10 Contribution of O–C intermolecular interactions in DNAF at 0 GPa shown through Hirshfeld surface (a) and finger print (b).

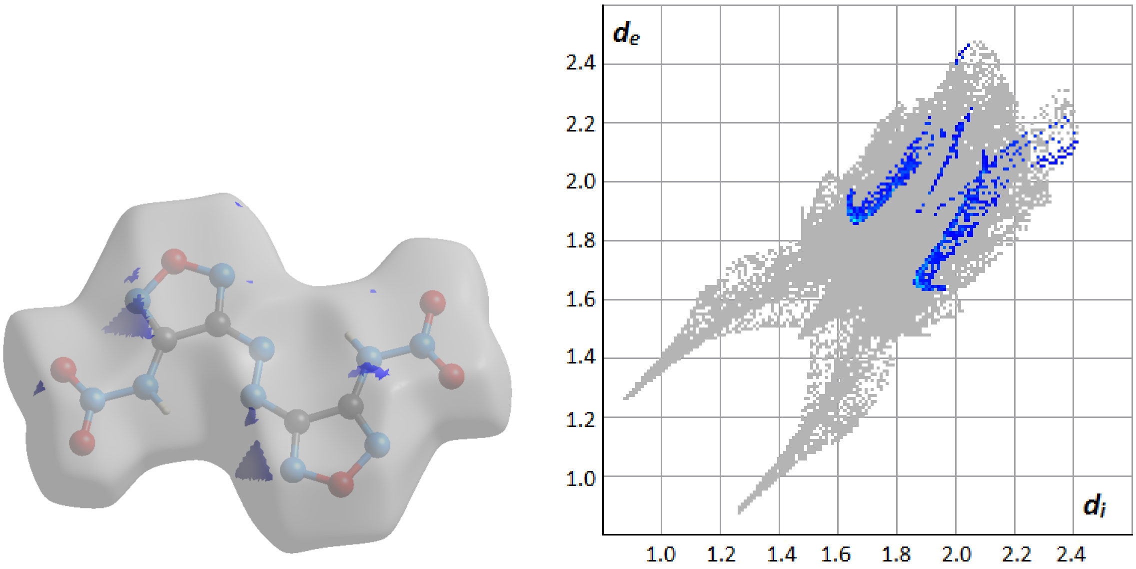

(a) (b)

Figure. 6.11 Contribution of C–N intermolecular interactions in DNAF at 0 GPa shown through Hirshfeld surface (a) and finger print (b).

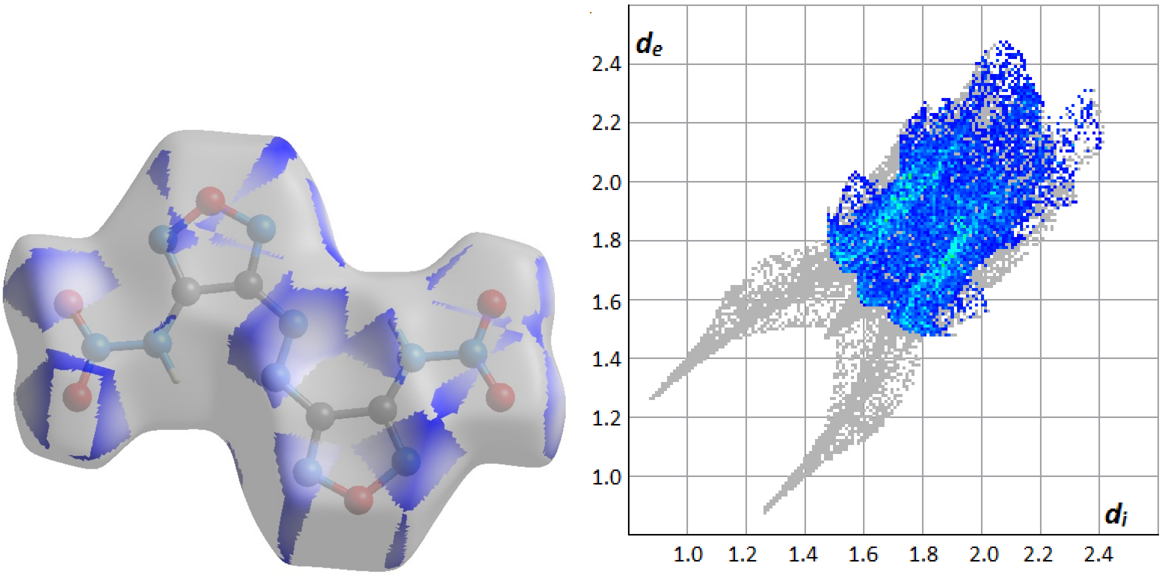

(a) (b)

Figure. 6.12 Contribution of O–N intermolecular interactions in DNAF at 0 GPa shown through Hirshfeld surface (a) and finger print (b).

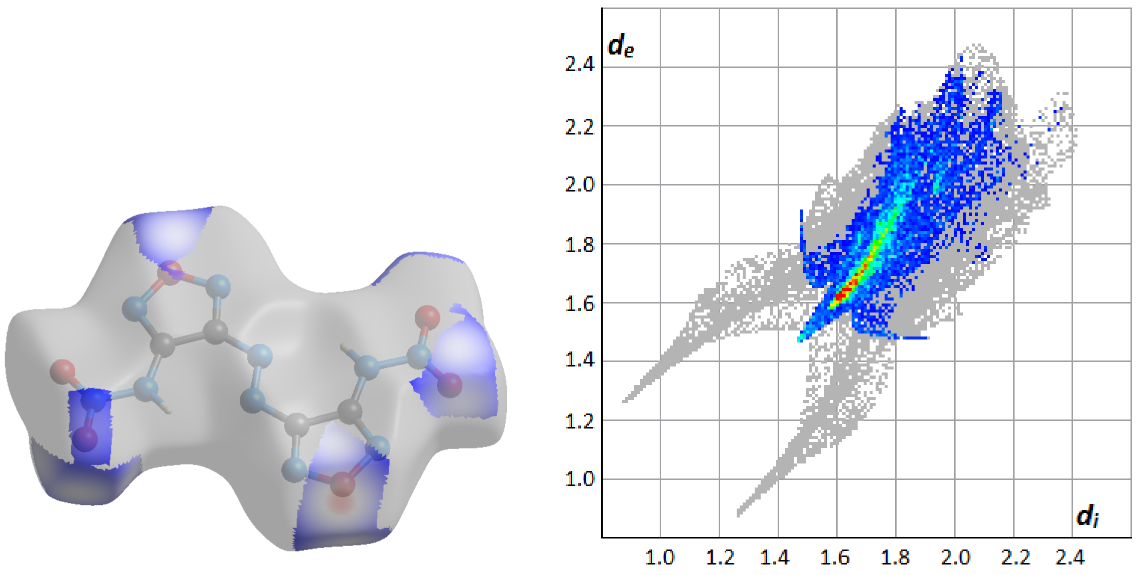

(a) (b)

Figure. 6.13 Contribution of O–O intermolecular interactions in DNAF at 0 GPa shown through Hirshfeld surface (a) and finger print (b).

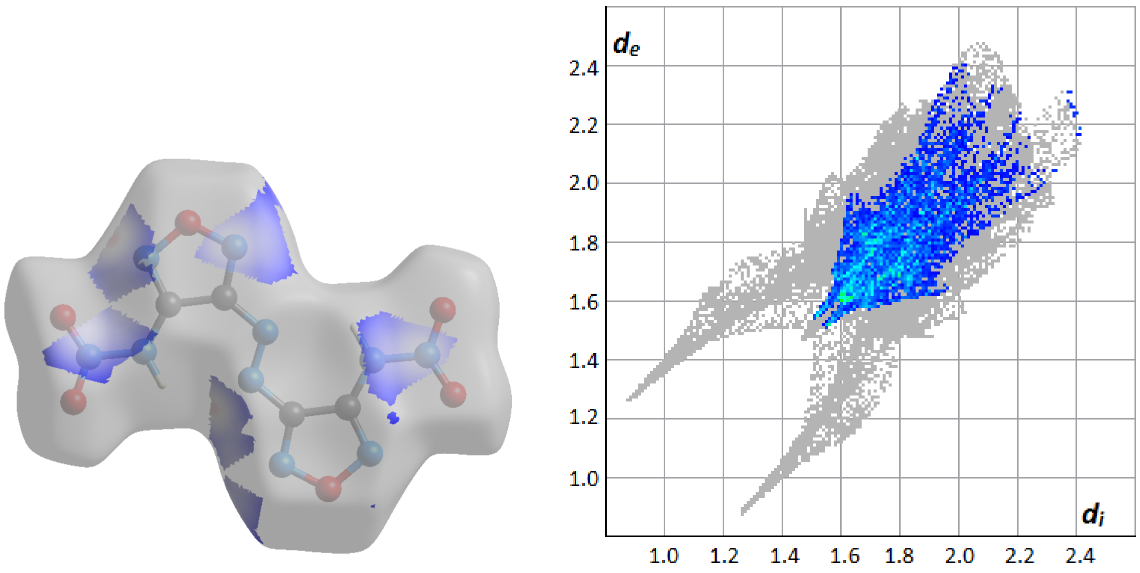

(a) (b)

Figure. 6.14 Contribution of N–N intermolecular interactions in DNAF at 0 GPa shown through Hirshfeld surface (a) and finger print (b).

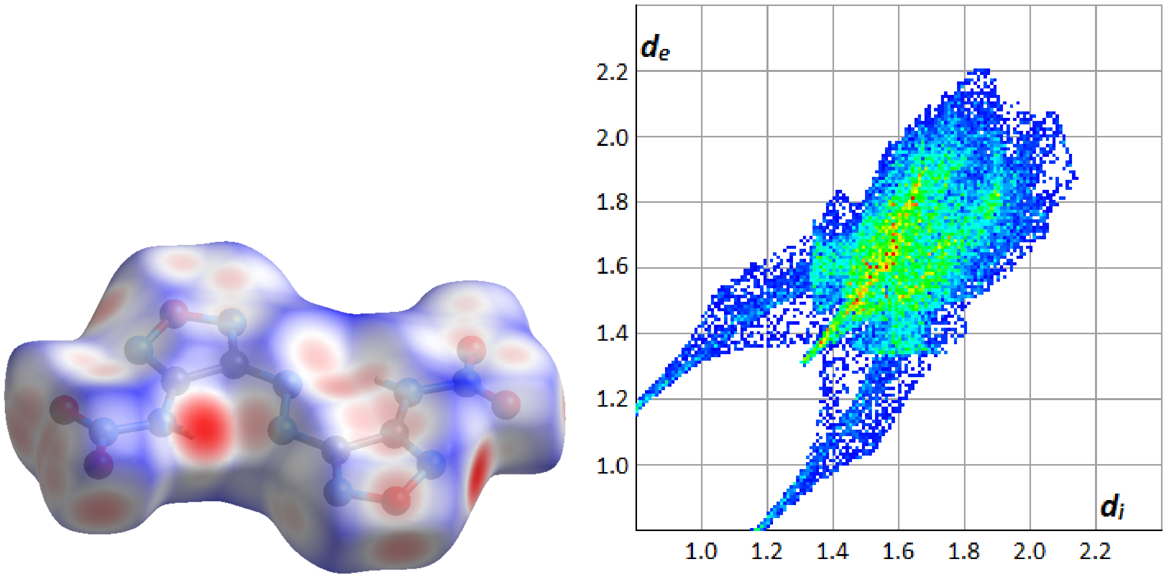

(a) (b)

Figure. 6.15 Hirshfeld surface (a) and finger print (b) of the intermolecular interaction of DNAF at 5 GPa.

It is clear from the hirshfeld surfaces shown in Figures 6.7a and 6.15a that as the pressure increases, blue regions are decreasing and the red regions are increasing, indicating the shortening of the intermolecular distances. This result is quite obvious as the application of pressure is considered to achieve the denser packing of the crystal. More information regarding different interactions can be obtained from the fingerprint plots associated to different interactions. A pair of spikes, seen in the fingerprint plot 6.9b, represents the hydrogen bonding interaction present in the crystal and the de distance of these spikes are becoming shorter with elevated pressure. These fingerprints with increased pressure also depict no variation of the shape of the fingerprints indicating similar intermolecular interaction up to 5 GPa. Percentage of different interactions and variation of these interactions with pressure have also been calculated and shown in Figure 6.16.

Results at 0 GPa clearly shows that the significant contribution in the intermolecular interactions is due to O–N, O–O, N–N, C–O, H–O, and H–N interactions. Among these interactions N–N and H–N interactions are found to increase with pressure whereas other interactions are found to decrease. Increasing nature of H–N interactions supports the strengthening of intermolecular hydrogen bonding in the material. It can also be seen that, though the contribution from C–N interaction at 0 GPa is very less, it is increasing with pressure. Along with the calculation of percentage area study due to different intermolecular interactions, study of hirshfeld surface at high pressure, shown in Figure 6.15 clearly depicts the increment of red coloured concave area around nitrogen atom of

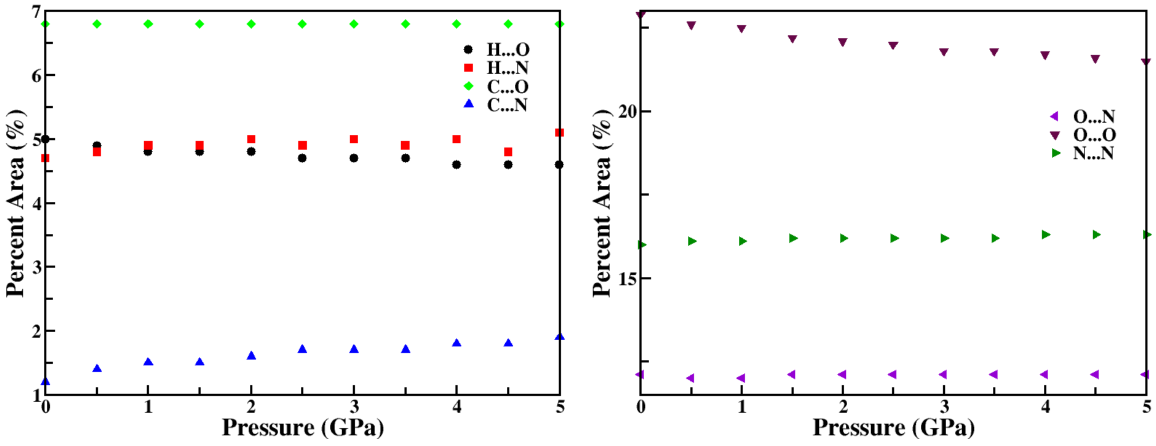

(a) (b)

Figure. 6.16 Pressure variation of percentage contribution on Hirshfeld surface of different intermolecular interaction present in the crystal.

furazan ring and the red coloured area at the end of the nitro group of the nitramine group. This concludes the presence of stacking interaction in the crystal.

6.3.2 Elastic properties

The study of elastic constants is instrumental to understanding interactions taking place in different directions of a crystal. These interactions are the main reason for the transfer of mechanical energy in between different lattice points which in turn is the reason to initiate the decomposition reaction and then leads to the subsequent detonation. It is known that the understanding of the whole detonation process is quite difficult compared to the detonation initiation. This detonation initiation is considered as a collective property of energetic materials which depends mainly on three parameters: intermolecular interactions, molecular arrangements, and the composition of the molecule. Studies have shown that the strength of these interactions between different molecules can be observed on the macroscopic properties of the material. In this respect, a detailed study on pentaerithrytol tetranitrate (PETN) [49] by Dick proved the strong directional dependent nature of shock sensitivity to detonation. As this directional dependence is due to the strength of the lattice interactions in different directions, shock sensitivity can be correlated with the elastic constants of the material and sensitivity of such materials can be predicted through these elastic constants. Indeed, this is the behaviour of the PETN high energy material, where the lowest sensitivity is found to be along the crystallographic ‘a’ axis with its stiffest elastic constant being C11. Using the stress-strain method, different elastic constant values for monoclinic DNAF and orthorhombic BNFF-1 have been obtained (see Table 6.5) and compared them with the elastic constants of cyclotrimethylene trinitramine (RDX) and cyclotetramethylene tetranitamine (β-HMX) found from Brillouin scattering spectroscopy. The elastic constants of RDX and β-HMX, which are secondary energetic materials, are considered to compare the sensitivity of studied materials with respect to RDX and β-HMX. As RDX is an orthorhombic system, a direct comparison between DNAF and RDX is not possible but some observation could be done based on the prominent elastic constants. The elastic constants of DNAF are similar in magnitude to the values found for RDX but with different ordering. Although C35 is found here to be negative but of small magnitude, Born's stability criteria for this monoclinic structure confirms the mechanical stability of the material [50]. A similar situation was found earlier for monoclinic LiN_3 [51]. The decreasing elastic constant ordering along principal directions is C33 $>$ C22 $>$ C11. Also, the elastic constant calculation shows a lowering in bulk modulus value to 10 GPa compared to the value found from pressure-volume data using Birch-Murnaghan EOS. Values of C11, C22, and C33 elastic constants of RDX shown in Table 6.5 are significantly higher than the corresponding values of β-HMX but similar to those of DNAF. However, the highest elastic constant value of DNAF along z-axis (C33) is large compared to the highest elastic constant value of RDX along x-axis (C11) and the values of C12 and C13 are also sizeably different. As the elastic constants of β-HMX are smaller than those of RDX, previous studies on elastic constant's relevance to detonation [49] suggest a high sensitive nature of β-HMX than RDX to detonation which is initiated by shock-wave. Higher value of elastic constants C12, C13 of β-HMX suggests that RDX will be more affected than β-HMX due to shear deformation along crystallographic b- and c-direction and the high sensitivity of RDX along c-direction has also been correlated with the less value of C33 than C33 of RDX. According to this knowledge, we can infer in a qualitative way that the sensitivity of DNAF is nearly equal to RDX and less than β-HMX. Directional dependence of sensitivity along a-axis is high whereas lower in magnitude along the c-axis. It can also be said that the b and c-axis are not susceptible to the specific shear deformation like RDX. The result, shown in Table 6.5 also confirms that the least sensitive c-direction of DNAF is even less compared to least sensitive a-direction of RDX, which is making this material a potential candidate for its future use as a secondary energetic material.

Table 6.5 Comparisons between elastic constants of DNAF, BNFF-1 and from Brillouin scattering spectroscopy for RDX (see in Ref. [21]) and β-HMX (see in Ref. [22]).

Elastic Constants	C11	C12	C13	C15	C22	C23	C25	C33	C35	C44	C46	C55	C66
DNAF	19.18	13.82	6.88	1.70	20.72	10.22	3.94	36.84	-0.58	8.35	3.68	8.02	14.76
BNFF-1	30.03	16.51	8.28	–	27.03	8.6	–	33.53	–	3.16	–	5.05	5.33
RDX	36.67	1.38	1.67	–	25.67	9.17	–	21.64	–	11.99	–	2.72	7.6
β-HMX	18.41	6.37	10.50	-1.1	14.41	6.42	0.83	12.44	1.08	4.77	2.75	4.77	4.46

As BNFF-1 crystallizes in orthorhombic structure, we found 9 independent elastic constants and they are tabulated in Table 6.5. The calculated elastic constants satisfy the Born's stability criteria for orthorhombic crystal structure hence BNFF-1 is mechanically stable. The BNFF-1 is found to show different mechanical stiffness as follows C33 $>$ C11

> C22. The elastic constants results tell that BNFF-1 is stiffer in y, z directions than RDX except in x-direction. The overall bulk modulus values inform that BNFF-1 show similar hardness as RDX (B=11.99 GPa) [21] and hence both possess similar mechanical sensitivity. Further, the calculated Hills [52] polycrystalline bulk modulus is found to be 17.46 GPa. This difference could be due to the force minimization criteria.

6.3.3 Electronic band structure

In order to understand the electronic contribution of different atoms in a material, electronic band structure calculation is normally being performed. It is known that a valence to conduction band transition of an electron can easily be correlated to the electronic bandgap of any material. In this connection, a low bandgap helps in the initiation of the decomposition reaction and consequently the detonation process of the energetic material [53]. This in turn indicates the importance of knowing proper bandgap of energetic materials. However, the value of the bandgap of the presently studied materials is unknown, both theoretically and experimentally. At the same time, density functional theory in the generalized gradient approximation tends to underestimate the bandgap, and therefore cannot be used for this purpose. In this connection, electronic band structure of DNAF and BNFF-1 has been studied using GW approximation [29, 30] and TB-mBJ potential, respectively.

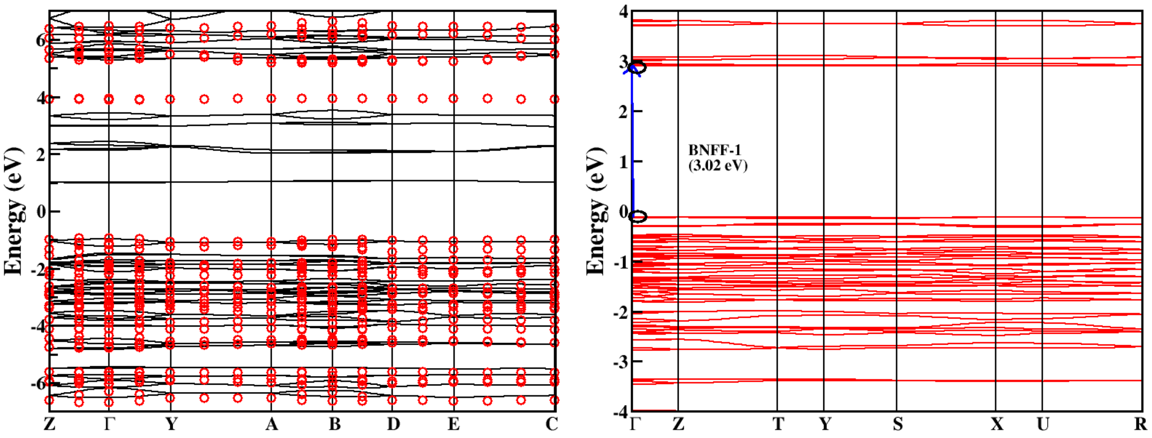

(a) (b)

Figure. 6.17 Electronic band structure of DNAF (a) and BNFF-1 (b).

The GW approximation is known for obtaining a reliable description of electronic band structure and bandgap of any studied material and our results regarding DNAF is presented in Figure 6.17a. The effect of the GW correction is seen by a significant opening of the bandgap in comparison with the results obtained with GGA (the top of the valence bands at the GGA and GW levels have been superposed to each other). Though a Γ-point direct bandgap nature is found for both the approximations, the bandgap value of 4.9 eV from GW approximation is really higher than the value of 1.9 eV found from normal GGA. However, since the dispersion present in the last valence and first conduction band is limited, this direct bandgap is very close in energy to other direct and indirect transitions. This large bandgap value (4.9 eV) confirms that electrons cannot easily be excited to the conduction bands, which makes this material a potential candidate as energetic material by increasing its electric discharge sensitivity. In connection with BNFF-1, when compared to conventional PBE functional, the TB-mBJ potential is known to reproduce experimental band gaps with less computational cost when compared to different hybrid functional [54]. Using the recently implemented TB-mBJ potential using the PAW method in VASP code, we have calculated the electronic bandgap of BNFF-1 for the PBE+TS optimized structure. The calculated band gap for BNFF-1 with GGA and TB-mBJ are 3.02 and 4.35 eV, respectively. The preliminary electronic band structure along Γ-Z-T-Y-S-X-U-R k-path in the first Brillouin zone using GGA functional depicted in Figure 6.17b for reference, which indicates a direct bandgap of BNFF-1 along Γ-Γ point. The bands near the Fermi level in the valance band and conduction band are found to be flat, hence BNFF-1 is an optically active material.

6.4 Conclusions

To conclude, we have studied the high energy material 4,4′-Bis(nitramino) azofurazan and BNFF-1 with density functional theory. The structural properties are well described with the vdW corrected methods of Grimme for DNAF and with the TS scheme for BNFF-1. The compressibility of DNAF and BNFF-1 is found to be high along b axis and c axis, respectively. Hirshfeld surface analysis has shown a clear presence of strong intermolecular hydrogen bonding in DNAF. Also, a detailed description of the sensitivity of studied materials along different directions have been evaluated from the elastic constant's calculation and the comparison with the elastic constants of well-established energetic material has given us the confirmation about the sensitivity of these materials in a qualitative way which shows that the sensitivity of DNAF is nearly equal to that of RDX but lower than that of β-HMX. Finally, the quasiparticle bandgap and TB-mBJ bandgap for DNAF and BNFF-1 show that the obtained value is much larger than the one found with GGA and confirms the low sensitivity due to electron transfer and subsequent decomposition for these compounds.

References

[1] H. Wei, J. Zhang, C. He and J.M. Shreeve, Chem. Eur. J. 21, 8607–8612 (2015).

[2] X. Jin, B. Hu, W. Lu, S. Gao, Z. Liu and C. Lv, RSC Adv. 4, 6471–6477 (2014).

[3] H. Gao and J.M. Shreeve, Chem. Rev. 111, 7377 (2011); M. Göbel, K. Karaghiosoff, T.M. Klapötke, D.G. Piercey and J. Stierstorfer, J. Am. Chem. Soc. 132, 17216 (2010); A.A. Dippold and T.M. Klapötke, J. Am. Chem. Soc. 135, 9931 (2013); Y. Zhang, D.A. Parrish and J.M. Shreeve, J. Mater. Chem. A 1, 585 (2013); N. Fischer, D. Fischer, T.M. Klapötke, D.G. Piercey and J. Stierstorfer, J. Mater. Chem. 22, 20418 (2012); T.M. Klapötke and M.S. Carles, Chem. Mater. 20, 3629 (2008).

[4] G.-H. Tao, B. Twamley and J.M. Shreeve, J. Mater. Chem. 19, 5850–5854 (2009); Y. Zhang, Y. Huang, D.A. Parrish and J.M. Shreeve, J. Mater. Chem. 21, 6891–6897 (2011); V. Thottempudi, H. Gao and J.M. Shreeve, J. Am. Chem. Soc. 133, 6464–6471 (2011); H. Gao, C. Ye, O.D. Gupta, J.-C. Xiao, M.A. Hiskey, B. Twamley and J.M. Shreeve, Chem. Eur. J. 13, 3853–3860 (2007); Z. Fu, R. Su, Y. Wang, Y.-F. Wang, W. Zeng, N. Xiao, Y. Wu, Z. Zhou, J. Chen and F.-X. Chen, Chem. Eur. J. 18, 1886–1889 (2012); H. Huang, Z. Zhou, L. Liang, J. Song, K. Wang, D. Cao, W. Sun, C. Bian and M. Xue, Chem. Asian J. 7, 707–714 (2012).

[5] R. Kinney and H.J. Harwood, J. Am. Chem. Soc. 49, 514 (1927); R.A. Olofson and J.S. Michelman, J. Org. Chem. 30, 1854 (1965); A.B. Sheremetev, V.O. Kulagina and E.A. Ivanova, J. Org. Chem. 61, 1510 (1996); A.B. Sheremetev and J. Hetercycl. Chem. 32, 371 (1995); A.B. Sheremetev, V.O. Kulgina, N.S. Aleksandrova, D.E. Dmitriev, Y.A. Strelenko, V.P. Lebedev and Y.N. Matyushin, Propellants Explos. Pyrotech. 23, 142 (1998); A.B. Sheremetev, E.V. Mantseva, D.E. Dmitriev and F.S. Sirovskii, Russ. Chem. Bull. 111, 659 (2002); M.B. Talawar, R. Sivabalan, N. Senthilkumar, G. Prabhu and S.N. Asthana, J. Hazard. Mater. 113, 11 (2004); J.P. Agrawal and R.D. Hodgson, Organic Chemistry of Explosive, John Wiley & Sons, West Sussex, 2007.

[6] D.E. Chavez, M.A. Hiskey and R.D. Gilardi, Angew. Chem. Int. Ed. 39, 1791–1793 (2000); D.M.

Badgujar, M.B. Talawar, S.N. Asthana and P.P. Mahulikar, J. Hazard. Mater. 151, 289–305 (2008); Y.-H. Joo and J.M. Shreeve, J. Am. Chem. Soc. 132, 15081–15090 (2010); F. Boneberg, A. Kirchner, T.M. Klapotke, D.G. Piercey, M.J. Poller and J. Stierstorfer, Chem. Asian J. 8, 148–159 (2013); A.A. Dippold and T.M. Klapotke, Chem. Asian J. 8, 1463–1471 (2013); J. Zhang and J.M. Shreeve, J. Am. Chem. Soc. 136, 4437–4445 (2014).

[7] V. Thottempudi, F. Forohor, D.A. Parrish and J.M. Shreeve, Angew. Chem. Int. Ed. 51, 9881–9885 (2012).

[8] O.M. Suleimenov and T.K. Ha, Chem. Phys. Lett. 290, 451–460 (1998).

[9] C. Zhang, J. Mol. Struct. 765, 77–83 (2006).

[10] M.B. Talawar, J.K. Niar, S.M. Pundalik, R.S. Satpute and S. Venugopalan, J. Hazard. Mater. 136, 978–981 (2006).

[11] V. Thottempudi, P. Yin, J. Zhang, D.A. Parrish and J.M. Shreeve, Chem.-Eur. J. 20, 542–548 (2014).

[12] J.M. Veauthier, D.E. Chavez, B.C. Tappan and D.A. Parrish, J. Energy Mater. 28, 229–249 (2010).

[13] V. Thottempudi, H. Gao and J.M. Shreeve, J. Am. Chem. Soc. 133, 6464–6471 (2011); V. Thottempudi and J.M. Shreeve, J. Am. Chem. Soc. 133, 19982–19992 (2011); P. Yin, D.A. Parrish and J.M. Shreeve, Chem. Eur. J. 20, 6707–6712 (2014); T. Abe, Y.-H. Joo, G.-H. Tao, B. Twamley and J.M. Shreeve, Chem. Eur. J. 15, 4102–4110 (2009); P.W. Leonard, D.E. Chavez, P.F. Pagoria and D.L. Parrish, Prop. Explos. Pyrotechnol. 36, 233–239 (2011).

[14] Y.-H. Joo and J.M. Shreeve, Chem. Commun. 46, 142–144 (2010); Y. Zhang, D.A. Parrish and J.M. Shreeve, J. Mater. Chem. A 1, 585–593 (2013); Y. Zhang, D.A. Parrish and J.M. Shreeve, Chem. Eur. J. 18, 987–994 (2012); T. Abe, G.-H. Tao, Y.-H. Joo, Y. Huang, B. Twamley and J.M. Shreeve, Angew. Chem. Int. Ed. 47, 7087–7090 (2008); T.M. Klapötke, D.G. Piercey and J. Stierstorfer, Chem. Eur. J. 17, 13068–13077 (2011); A.A. Dippold and T.M. Klapötke, Chem. Eur. J. 18, 16742–16753 (2012).

[15] V. Thottempudi, H. Gao and J.M. Shreeve, J. Am. Chem. Soc. 133, 6464–6471 (2011).

[16] V. Thottempudi and J.M. Shreeve, J. Am. Chem. Soc. 133, 19982–19992 (2011).

[17] S.V. Bondarchuk, J. Mol. Graphics Model. 89, 114–121 (2019); S.V. Bondarchuk, CrysEngComm 20, 5718–5725 (2018); S.V. Bondarchuk, New J. Chem. 43, 1459–1468 (2019); S.V. Bondarchuk, J. Phys. Chem. A 122 (24), 5455–5463 (2018); S.V. Bondarchuk, Int. J. Quantum Chem. 117, e25430 (2017).

[18] J. Zhang and J.M. Shreeve, J. Phys. Chem. C 119, 12887–12895 (2015).

[19] Y. S. Zhou, B. Z. Wang, J. K. Li, C. Zhou, L. Hu, Z. Q. Chen and Z. Z. Zhang, Acta Chim. Sinica 69, 1673 (2011).

[20] Y. Zhang, B. Wang, Y. Zhou, K. Xu, S. Jia, and F. Zhao, Propellants Explos. Pyrotech. 39, 809-814 (2014).

[21] J.J. Haycraft, L.L. Stevvens and C.J. Eckhardt, J. Chem. Phys. 124, 024712 (2006).

[22] L.L. Stevens and C.J. Eckhardt, J. Chem. Phys. 122, 174701 (2005).

[23] G. Kresse and J. Furthmüller, Phys. Rev. B 54, 11169 (1996).

[24] P. Hohenberg and W. Kohn, Phys. Rev. 136 (3B), B864–B871 (1964).

[25] W. Kohn and L.J. Sham, Phys. Rev. 140 (4A), A1133–A1138 (1965).

[26] P.E. Blöchl, Phys. Rev. B 50, 17953 (1994).

[27] J.P. Perdew, S. Burke and M. Ernzerhof, Phys. Rev. Lett. 77, 3865 (1996).

[28] S. Grimme, J. Comput. Chem. 27, 1787 (2006).

[29] T.H. Fischer and J. Almlof, J. Phys. Chem. 96, 9768 (1992).

[30] (a) A. Tkatchenko and M. Scheffler, Phys. Rev. Lett. 102, 073005 (2009).; (b) S. Grimme, J. Comp. Chem. 27, 1787 (2006).

[31] H.J. Monkhorst and J.D. Pack, Phys. Rev. B 13, 5188 (1976).

[32] L. Hedin, Phys. Rev. 139 A, 796 (1965).

[33] L. Hedin, S. Lundquist, H. Ehrenreich, F. Seitz and D. Turnbull (Eds.), Solid State Physics, vol. 23, Academic, New York, (1969).

[34] S. Lebègue, B. Arnaud, M. Alouani and P.E. Blöchl, Phys. Rev. B 67, 155208 (2003).

[35] R.H. Scheicher, D.Y. Kim, S. Lebègue, B. Arnaud, M. Alouani and R. Ahuja, Appl. Phys. Lett. 92, 201903 (2008).

[36] T.A. Pham, H.-V. Nguyen, D. Rocca and G. Galli, Phys. Rev. B 87, 155148 (2013).

[37] Y. Ping, D. Rocca and G. Galli, Chem. Soc. Rev. 42, 2437 (2013).

[38] S.K. Wolff, D.J. Grimwood, J.J. McKinnon, M.J. Turner, D. Jayatilaka and M.A. Spackman, CrystalExplorer 3.1, University of Western Australia, Australia, (2012).

[39] M.A. Spackman and D. Jayatilaka, CrystEngComm 11, 19 (2009).

[40] M.A. Spackman and J.J. McKinnon, CrystEngComm 4, 378 (2002).

[41] P.A. Wood, J.J. McKinnon, S. Parsons, E. Pidcock and M.A. Spackman, CrystEngComm 10, 368 (2008).

[42] W. Fickett and W.C. Davis, Courier Corporation: Mineola, NY, USA, 403 (2012).

[43] F.D. Murnaghan, Proc. Natl. Acad. Sci. U.S.A. 30, 244 (1944).

[44] S. Appalakondaiah, G. Vaitheeswaran and S. Lebègue, J. Phys. Chem. A 119, 6574–6581 (2015).

[45] C.-S. Yoo and H. Cynn, J. Chem. Phys. 111, 10229–10235 (1999).

[46] J.C. Gump and S.M. Peiris, J. Appl. Phys. 97, 053513 (2005).

[47] L.L. Stevens, N. Velisavljevic, D.E. Hooks and D.M. Dattelbaum, Propellants Explos. Pyrotech. 33, 286–295 (2008).

[48] R.S. McWilliams, Y. Kadry, M.F. Mahmood, A.F. Goncharov and J.C. Jenkins, J. Chem. Phys. 137, 054501 (2012).

[49] J.J. Dick, Appl. Phys. Lett. 44, 859 (1984).

[50] F. Mouhat and F.-X. Coudert, Phys. Rev. B. 90, 224104 (2014).

[51] K. Ramesh Babu, Ch. Bheema Lingam, Surya P. Tewari and G. Vaitheeswaran, J. Phys. Chem. A 115, 4521–4529 (2011).

[52] R. Hill, Proc. R. Soc. London, Ser. A 65, 350 (1952).

[53] S. Appalakondaiah, G. Vaitheeswaran and S. Lebègue, Chem. Phys. Lett. 10, 605 (2014).

[54] E. Narsimha Rao, A. H. Reshak, S. Auluck and G.Vaitheeswaran, Phys. Chem. Chem. Phys. 19, 31255 (2017).

CHAPTER 7

Conclusions

7.1 Summary and Conclusions

In conclusion, we have carried out a thorough density functional theory study of transition metal oxides and energetic materials with different molecular structures.

In case of transition metal oxides, we studied mainly the structural, vibrational and associated IR and Raman frequencies of ABO_4 type transition metal oxides $TlTcO_4$ and $TlReO_4$. In case of $TlTcO_4$, first the structural properties with various exchange-correlation functional have been addressed. After obtaining the ground state structure with the PBE+TS scheme, we have performed the zone-centered vibrational properties calculation along with understanding of IR and Raman spectra which shows a similar trend like ABO_4 type material. Here we have also addressed the bonding nature of this material from born effective charge (BEC) which tells that this material is ionically bonded with Tl and TcO_4 block whereas TcO_4 block is covalently bonded. Among different types of O atoms, contribution of O3 atom is found to be prominent in high-intensity IR and Raman modes. In case of $TlReO_4$, our obtained results are found to be consistent with our recently reported experimental results. DFT total energy calculation of low-temperature tetragonal, room-temperature monoclinic and hypothetical orthorhombic phases shows that our experimentally predicted room-temperature monoclinic phase is energetically more favourable than the earlier proposed orthorhombic structure of $TlReO_4$. Our DFT calculations facilitate the assignment of all the vibrational properties of the low- and room-temperature phases of $TlReO_4$. Calculated BECs show the presence of a mixed-valence character of bonds in both phases. Calculated phonon frequencies allow the assignment of the Raman modes, the determination of the frequencies of mode undetected in experiments, and the identification of the atomic movement associated with each mode. We have obtained the same information for IR and silent modes for the tetragonal phase. The vibrations of $TlReO_4$ are found to be divided into external and internal modes of the ReO_4 tetrahedron. The strong high-frequency mode is assigned to the internal stretching vibration of the ReO_4 tetrahedron. This is the first time all the vibration modes of both phases of $TlReO_4$ have been properly assigned. Our reported experimental Raman spectrum of room-temperature $TlReO_4$ is discussed in comparison with the calculated Raman frequencies of the room- and low-temperature phases, showing that the assignation of external and internal modes is maintained in the room-temperature structure in spite of the increase of the number of modes due to the symmetry decrease caused by the temperature-driven transition.

In case of di- and trinitromethane based energetic materials KDNM, FNF, MHNF and KNF, all the structural properties with different functionals and vdW schemes have been calculated initially. Obtained ground state structural parameters with different combinations of functional and dispersion corrected schemes show that the dispersion corrected Grimme along with PBE pseudopotential works well for KDNM, FNF and MHNF. On the other hand, PBE + TS scheme provide structural parameters of KNF which match well with experimental details. Pressure variation study of NF based salts clearly indicates that the KNF is less and FNF is more compressible in the studied pressure range. This also helps us to understand that the presence of intermolecular interactions in KNF is stronger compared to FNF. The study of elastic properties of these materials also supports this statement by providing higher value of bulk modulus for KNF and less for FNF. Proper understanding of these elastic constants along different crystallographic directions indicates that the FNF and KNF crystal is more sensitive along the z-direction, whereas the MHNF and KDNM crystals are more sensitive along x-direction and y-direction, respectively. Study of Born effective charge of these materials tells the presence of ionic bonding in KNF and KDNM crystals. On the contrary more covalent bonding is found to be present in FNF and MHNF crystals. The study of vibrational properties provides the knowledge about different modes of vibration and the importance of stretching NO bonds in KDNM. In case of NF-based materials, this study at 0 GPa as well as at high pressure indicates a blue shift for whole IR peaks except high-frequency peaks of FNF and MHNF, which are mainly due to symmetric and asymmetric stretching of NH bonds present in these compounds.

In case of cage structured energetic material, octanitrocubane (ONC) the ground state structural as well as elastic properties with normal PBE functional in addition with van der Waals corrected TS scheme have been obtained. Lattice parameter 'c' of this material is found to be more compressible than the other two axes which had been anticipated from the study of the crystal structure. The calculated bulk modulus is found to be 12.19 GPa which is similar to other secondary energetic materials. The study of elastic constants of this material reveals that the c-axis is more sensitive and a-axis is less sensitive to shock initiation. Also, this material is more sensitive than RDX but less sensitive than β-HMX. Analysis of BECs of ONC tells the presence of mixed ionic and covalent bonding among nitrogen (N2, N4) and oxygen (O2A) atoms. After that, zone centred phonon frequencies of this material have been evaluated in this study, and 192 vibrational frequencies of ONC have been reported. In the end, the bandgap of this material has been calculated using well-known semi-local TB-mBJ potential and found to be 5.31 eV. The density of state shows a presence of strong covalent bonding in the carbon cage of this material. In the low energy range, optical isotropy can be seen which becomes anisotropic at high energy. An extensive study of structural, elastic, vibrational, electronic and optical properties clearly indicates the involvement of 2- and 4-type of atoms in different properties of this material which are arranged in bc-plane of the material.

In case of heterocyclic based materials, we have studied 4,4′-Bis(nitramino) azofurazan and BNFF-1. The structural properties are well described with the vdW corrected methods of Grimme for DNAF and with the TS scheme for BNFF-1. The compressibility of DNAF and BNFF-1 is found to be high along b axis and c axis, respectively. Hirshfeld surface analysis has shown a clear presence of strong intermolecular hydrogen bonding in DNAF. Also, a detailed description of the sensitivity of studied materials along different directions have been evaluated from the elastic constant's calculation and the comparison with the elastic constants of well-established energetic material has given us the confirmation about the sensitivity of these materials in a qualitative way which shows that the sensitivity of DNAF is nearly equal to that of RDX but lower than that of β-HMX. Finally, the quasiparticle bandgap and TB-mBJ bandgap for DNAF and BNFF-1 show that the obtained value is much larger than the one found with GGA and confirms the low sensitivity due to electron transfer and subsequent decomposition for these compounds.

7.2 Future Work

We have mainly restricted our study to ground state crystalline properties studied materials. This can be further expanded to the high-pressure study of studied materials as this kind of study will provide more knowledge about the different properties of such materials. In this connection, the pressure-induced phase transition study of $TlReO_4$ will provide a deep insight and help to understand the microscopic phenomena related to this transformation. High-pressure behaviour of the bandgap value of energetic materials can provide the understanding about metallization and hence the detonation of such materials.

List of Publications

Journal Papers:

1. **S. Mondal**, G. Vaitheeswaran, Brendan J Kennedy, Clarissa Chay, Sean Injac and Daniel Errandonea, *Crystal structure and phase transition of TlReO4: a combined experimental and theoretical study*, J. Phys.: Condens. Matter 33, 065403 (2021).

2. **S. Mondal**, G. Vaitheeswaran, M K Gupta and Ranjan Mittal, *Structural, elastic, vibrational and optical properties of energetic material octanitrocubane studied from first-principles theory*, J. Phys.: Condens. Matter 32, 425502 (2020).

3. **S. Mondal**, D. Rocca, S. Lebegue, G. Vaitheeswaran, *Structural, elastic, and quasiparticle bandstructure of 4,4-Bis(nitramino)azofurazan from first principles theory*, Computational Materials Science 169, 109081 (2019).

Publications not included in the thesis:

1. **S. Mondal**, S. Appalakondaiah and G. Vaitheeswaran, *High pressure structural, electronic, and optical properties of polymorphic* $InVO_4$ *phases*, J. Appl. Phys. 119, 085702 (2016).

2. Uppara Ugandhar, Tokala Navaneetha, Junaid Ali, **Subrata Mondal**, Ganapathy Vaitheeswaran and Viswanathan Baskar, *Assembling Homometallic* Sb_6 *and Heterometallic* Ti_4Sb_2 *Oxo Clusters*, Inorg. Chem. 59, 6689–6696 (2020).

3. Prathap Kumar Jharapla1, **Subrata Mondal** and Ganapathy Vaitheeswaran, *Comparative DFT study of vibrational, electronic, and optical properties of energetic alkali metal salts based on nitrogen-rich 5-aminotetrazole*, J Comput Chem. 42,

180-191 (2021).

4. Bryce G. Mullens, Maxim Avdeev, Helen E. A. Brand, **S. Mondal**, G. Vaitheeswaran and Brendan J. Kennedy, *Insights into the structural variations in* $SmNb_{1-x}Ta_xO_4$ *and* $HoNb_{1-x}Ta_xO_4$ *combined experimental and computational studies*, Dalton Trans. 50, 9103–9117 (2021).

5. Supratik Mukherjee, Aiswarya T, **Subrata Mondal** and G Vaitheeswaran, *Electronic structure, phonons and optical properties of baryte type scintillators* $TlXO_4$ *(X = Cl, Br)*, J. Phys.: Condens. Matter, (2021) (Accepted, DOI: 10.1088/1361-648X/ac4347)

Manuscripts under preparation:

- **S. Mondal**, Sohan Lal, Neeraj Kumbhakarna, Arindrajit Chowdhury, Irishi N. N. Namboothiri and G. Vaitheeswaran, *Experimental and Theoretical Study on the Structural and Energetic Properties of Potassium Dinitromethane* (2021).

- **S. Mondal**, J. Prathap Kumar, and G. Vaitheeswaran, *Comparative DFT study of crystalline properties of Nitroformate-based energetic saltsComparative DFT study of crystalline properties of Nitroformate-based energetic salts* (2021).

Achievements/Recognitions:

∗ ***Best poster presentation award***

- **S. Mondal** and G. VaitheeswaranLeela, *Study of structural, elastic and electronic properties of crystalline octanitrocubane using van der Waals corrected density functional approach*, **Sorbonne-JNCASR School on Advanced Computational Material Science** jointly organized by Sorbonne University, Paris and JNCASR, Bangalore, 29th Jan - 02nd Feb, (**2018**).

Schools/Workshops:

- **10th International High Energy Materials Conference and Exhibit (HEMCE)**, 11-13th February (**2016**).

- **15th Indian Theoretical Chemistry Symposium** organized by School of Chemistry, University of Hyderabad during 14th Dec – 17th Dec, (**2016**).

- **National Conference on Recent Trends in Condensed Matter Physics** organized by Bose Institute during 31st Oct – 3rd Nov, (**2017**).

- **Workshop on Development of Binders and Plasticizers for Energetic Applications** organized by Advanced Centre of Research in High Energy Materials, University of Hyderabad on Dec 25th (**2017**).

- **Sorbonne-JNCASR School on Advanced Computational Material Science** jointly organized by Sorbonne University, Paris and JNCASR, Bangalore, 29th Jan - 02nd Feb, (**2018**).
- **Workshop on Functional Magnetic Materials** organized by UGC Networking Resource Centre, School of Physics, University of Hyderabad during 26th Feb – 3rd March, (**2018**).
- **CSR lecture on Numerical Methods and Computer Programming (NMCP2018)** organized by UGC-DAE Consortium for Scientific Research, Indore during 6th Aug – 10th Aug, (**2018**).

Conference Proceedings:

- **S. Mondal**, J. Prathap Kumar, E. Narsimha Rao, and G. Vaitheeswaran, *Structure-property correlations of bis(nitrofurazano) furazan(BNFF-1): A density functional theory study*, AIP Coference Proceedings 2115, 030391 (2019).

Conference Presentations (National/International):

- **15th Indian Theoretical Chemistry Symposium** organized by School of Chemistry, University of Hyderabad during 14th Dec – 17th Dec, (**2016**). (POSTER)
- **National Conference on Recent Trends in Condensed Matter Physics** organized by Bose Institute during 31st Oct – 3rd Nov, (**2017**). (POSTER)
- **Sorbonne-JNCASR School on Advanced Computational Material Science** jointly organized by Sorbonne University, Paris and JNCASR, Bangalore, 29th Jan - 02nd Feb, (**2018**). (POSTER)

Structure-Property Correlation Study of Transition Metal Oxides and Energetic Solids

by Subrata Mondal

G. Vaitheeswaran

Dr. G.S. Vaitheeswaran
Associate Professor
School of Physics
University of Hyderabad
Hyderabad-500 046. (TS) INDIA

Submission date: 28-Dec-2021 04:48PM (UTC+0530)
Submission ID: 1736080919
File name: Thesis_Subrata_new_withref.pdf (15.12M)
Word count: 58216
Character count: 275208

Structure-Property Correlation Study of Transition Metal Oxides and Energetic Solids

ORIGINALITY REPORT

32%	12%	27%	3%
SIMILARITY INDEX	INTERNET SOURCES	PUBLICATIONS	STUDENT PAPERS

PRIMARY SOURCES

1 S. Mondal, D. Rocca, S. Lebègue, G. Vaitheeswaran. "Structural, elastic, and quasiparticle bandstructure of 4,4'-Bis(nitramino)azofurazan from first principles theory", Computational Materials Science, 2019 — 7%

Publication

This paper belongs to student's first author paper included in chapter-6

G. Vaitheeswaran

Dr. G.S. Vaitheeswaran
Associate Professor
School of Physics
University of Hyderabad
Hyderabad-500 046. (TS) INDIA

2 Subrata Mondal, Ganapathy Vaitheeswaran, Mayanak Kumar Gupta, Ranjan Mittal. "Structural, elastic, vibrational and optical properties of energetic material Octanitrocubane studied from first-principles theory", Journal of Physics: Condensed Matter, 2020 — 7%

Publication

This paper belongs to student's first author paper included in chapter-5

G. Vaitheeswaran

Dr. G.S. Vaitheeswaran
Associate Professor
School of Physics
University of Hyderabad
Hyderabad-500 046. (TS) INDIA

3 S Mondal, G Vaitheeswaran, M K Gupta, Ranjan Mittal. "Structural, elastic, vibrational and optical properties of energetic material octanitrocubane studied from first-principles theory", Journal of Physics: Condensed Matter, 2020 — 5%

This paper belongs to student's first author paper included in chapter-5

G. Vaitheeswaran

Dr. G.S. Vaitheeswaran
Associate Professor
School of Physics
University of Hyderabad
Hyderabad-500 046. (TS) INDIA

Publication

4 **iopscience.iop.org**
Internet Source
3%

This article is student's first author paper chapter-3
G. Vaitheeswaran

Dr. G.S. Vaitheeswaran
Associate Professor
School of Physics
University of Hyderabad
Hyderabad-500 046. (TS) INDIA

5 **S. Mondal, J. Prathap Kumar, E. Narsimha Rao, G. Vaitheeswaran. "Structure-property correlations of bis(nitrofurazano) furazan(BNFF-1): A density functional theory study", AIP Publishing, 2019**
Publication
1%

This article is student's first author paper chapter-6
G. Vaitheeswaran

Dr. G.S. Vaitheeswaran
Associate Professor
School of Physics
University of Hyderabad
Hyderabad-500 046. (TS) INDIA

6 **Submitted to University of Hyderabad, Hyderabad**
Student Paper
1%

This refers to the standard Physics terms such as FLAPW method, structural properties etc which are commonly used by my earlier students. G. Vaitheeswaran

Dr. G.S. Vaitheeswaran
Associate Professor
School of Physics
University of Hyderabad
Hyderabad-500 046. (TS) INDIA

7 **Landt, Lasse. "Electronic Structure and Optical Properties of Pristine and Modified Diamondoids", Technische Universität Berlin, 2010.**
Publication
1%

8 **Subrata Mondal, Ganapathy Vaitheeswaran, Brendan J Kennedy, Clarissa Chay, Sean Injac, Daniel Errandonea. " Crystal structure and phase transition of TlReO : A combined experimental and theoretical study ", Journal of Physics: Condensed Matter, 2020**
Publication
1%

This article is student's first author paper chapter-3
G. Vaitheeswaran

Dr. G.S. Vaitheeswaran
Associate Professor
School of Physics
University of Hyderabad
Hyderabad-500 046. (TS) INDIA

9 **arxiv.org**
Internet Source
1%

This article is also student's first author paper included in chapter-3
G. Vaitheeswaran

Dr. G.S. Vaitheeswaran
Associate Professor
School of Physics
University of Hyderabad
Hyderabad-500 046. (TS) INDIA

74	Internet Source	<1 %
75	digitalcommons.unl.edu Internet Source	<1 %
76	wiki.abinit.org Internet Source	<1 %
77	ynu.repo.nii.ac.jp Internet Source	<1 %

Exclude quotes	On	Exclude matches	< 14 words
Exclude bibliography	On		

Structure-Property Correlation Study of Transition Metal Oxides and Energetic Solids

ORIGINALITY REPORT

37%	19%	28%	5%
SIMILARITY INDEX	INTERNET SOURCES	PUBLICATIONS	STUDENT PAPERS

PRIMARY SOURCES

1 S. Mondal, D. Rocca, S. Lebègue, G. Vaitheeswaran. "Structural, elastic, and quasiparticle bandstructure of 4,4'-Bis(nitramino)azofurazan from first principles theory", Computational Materials Science, 2019
Publication — 7%

This paper belongs to student's first author paper included in chapter-6
G. Vaitheeswaran

Dr. G.S. Vaitheeswaran
Associate Professor
School of Physics
University of Hyderabad
Hyderabad-500 046. (TS) INDIA

2 Subrata Mondal, Ganapathy Vaitheeswaran, Mayanak Kumar Gupta, Ranjan Mittal. "Structural, elastic, vibrational and optical properties of energetic material Octanitrocubane studied from first-principles theory", Journal of Physics: Condensed Matter, 2020
Publication — 7%

This paper belongs to student's first author paper included in chapter-5
G. Vaitheeswaran

Dr. G.S. Vaitheeswaran
Associate Professor
School of Physics
University of Hyderabad
Hyderabad-500 046. (TS) INDIA

3 S Mondal, G Vaitheeswaran, M K Gupta, Ranjan Mittal. "Structural, elastic, vibrational and optical properties of energetic material octanitrocubane studied from first-principles theory", Journal of Physics: Condensed Matter, 2020 — 5%

This paper belongs to student's first author paper included in chapter-5
G. Vaitheeswaran

Dr. G.S. Vaitheeswaran
Associate Professor
School of Physics
University of Hyderabad
Hyderabad-500 046. (TS) INDIA

Publication

4 iopscience.iop.org 3%
Internet Source

This article is student's first author paper chapter -3
G. Vaitheeswaran

Dr. G.S. Vaitheeswaran
Associate Professor
School of Physics
University of Hyderabad
Hyderabad-500 046. (TS) INDIA

5 S. Mondal, J. Prathap Kumar, E. Narsimha Rao, G. Vaitheeswaran. "Structure-property correlations of bis(nitrofurazano) furazan(BNFF-1): A density functional theory study", AIP Publishing, 2019 2%
Publication

This article is student's first author paper chapter - 6
G. Vaitheeswaran

Dr. G.S. Vaitheeswaran
Associate Professor
School of Physics
University of Hyderabad
Hyderabad-500 046. (TS) INDIA

6 arxiv.org 1%
Internet Source

This article is also student's first author paper included in chapter-3
G. Vaitheeswaran

Dr. G.S. Vaitheeswaran
Associate Professor
School of Physics
University of Hyderabad
Hyderabad-500 046. (TS) INDIA

7 Submitted to University of Hyderabad, Hyderabad 1%
Student Paper

This refers to the standard Physics terms such as FLAPW method, structural properties etc which are commonly used by my earlier students.
G. Vaitheeswaran

Dr. G.S. Vaitheeswaran
Associate Professor
School of Physics
University of Hyderabad
Hyderabad-500 046. (TS) INDIA

8 link.springer.com 1%
Internet Source

9 Landt, Lasse. "Electronic Structure and Optical Properties of Pristine and Modified Diamondoids", Technische Universität Berlin, 2010. 1%
Publication

10 Gabriel R Schleder, Antonio C M Padilha, Carlos Mera Acosta, Marcio Costa, Adalberto Fazzio. "From DFT to machine learning: recent approaches to materials science–a review", Journal of Physics: Materials, 2019 1%
Publication

11	Subrata Mondal, Ganapathy Vaitheeswaran, Brendan J Kennedy, Clarissa Chay, Sean Injac, Daniel Errandonea. " Crystal structure and phase transition of TlReO : A combined experimental and theoretical study ", Journal of Physics: Condensed Matter, 2020 Publication	1 %
12	pubs.rsc.org Internet Source	1 %
13	www.hanford.gov Internet Source	<1 %
14	Supratik Mukherjee, Aiswarya T, Subrata Mondal, Ganapathy Vaitheeswaran. "Electronic structure, phonons and optical propertiesof baryte type scintillators TlXO4 (X=Cl, Br)", Journal of Physics: Condensed Matter, 2021 Publication	<1 %
15	aip.scitation.org Internet Source	<1 %
16	www.sal.wisc.edu Internet Source	<1 %
17	van de Walle, Axel. "First-Principles Alloy Thermodynamics", Multiscale Modeling From Atoms to Devices, 2010. Publication	<1 %

This article belong to student's first author paper - chapter 3

G. Vaitheeswaran

Dr. G.S. Vaitheeswaran
Associate Professor
School of Physics
University of Hyderabad
Hyderabad-500 046 (TS) INDIA

142	Internet Source	<1 %
143	www.electrochemsci.org Internet Source	<1 %
144	www.iphy.ac.cn Internet Source	<1 %
145	www.phys.ttu.edu Internet Source	<1 %
146	cjcp.ustc.edu.cn Internet Source	<1 %
147	digitalcommons.unl.edu Internet Source	<1 %
148	www.ippt.gov.pl Internet Source	<1 %
149	www.isan.troitsk.ru Internet Source	<1 %
150	www.tsijournals.com Internet Source	<1 %
151	ynu.repo.nii.ac.jp Internet Source	<1 %

Exclude quotes	On	Exclude matches	< 14 words
Exclude bibliography	Off		